A statistical analysis of the auroral boundaries; their response to geomagnetic dynamics and their use in auroral forecast verification

Michaela K. Mooney

A dissertation submitted in partial fulfillment

of the requirements for the degree of

Doctor of Philosophy

of

University College London.

Mullard Space Science Laboratory, Department of Space and Climate Physics

University College London

February 24, 2022

I, Michaela K. Mooney, confirm that the work presented in this thesis is my own. Where information has been derived from other sources, I confirm that this has been indicated in the work.

Abstract

The aurora and associated current systems are hazardous to space and ground-based infrastructure. In this thesis, the auroral boundaries determined from satellite images have been used to evaluate the performance of an operational auroral forecast model and explore the location and dynamics of the auroral boundaries in the context of the wider magnetosphere.

The performance of the OVATION-Prime 2013 auroral forecast model is compared against the observed auroral boundaries. The analysis shows that the model performs well at predicting the location of the auroral oval, however the performance is reduced during periods of higher geomagnetic activity and in the high latitude nightside auroral oval. The model also underpredicts the probabilities of aurora occurring. The results of this analysis provide a benchmark against which future generations of auroral forecast models can be assessed.

The lower model performance in the high latitude nightside sectors is likely due to substorm activity and so the statistical motion of the poleward auroral boundary and open-closed field line boundary (OCB) during substorms is analysed. The results show that the OCB does not contract uniformly after substorm onset. In sectors closest to the onset sector, the OCB contracts immediately while in sectors further from onset the OCB contracts later, distorting the shape of the OCB. However, the total nightside flux content of the polar cap decreases immediately at onset, in contrast to recent studies.

Finally, the alignment between the equatorward auroral boundary and the plasmapause is explored. The statistical locations of the equatorward auroral boundary and the ionospheric projection of the plasmapause are compared. The two

boundaries are found to be statistically offset in all sectors by 4 – 11°, suggesting that the equatorward auroral boundary does not map to the plasmapause. However, the separation between the two boundaries decreases with increasing levels of geomagnetic activity.

Acknowledgements

Firstly, I would like to thank my supervisors Colin Forsyth, Jonny Rae, Mike Marsh, Suzy Bingham and David Jackson for their continuous support and guidance throughout my PhD. Thank you for all the great opportunities that you have helped to create for me, from securing the NERC funding, the MSSL - Met Office partnership to the conferences, travel opportunities and involvement in the SMILE consortium. I owe a special thanks to Colin as my primary supervisor for his patience over the last four years and everything he has taught me about the aurora, magnetosphere and statistical analysis. I hope I've been a good first PhD student! In addition, I'm also grateful for everyone in the plasma group and wider solar system groups. I've learned a huge amount from you all, in different ways, both professionally and personally and I'm grateful to have been part of such an excellent and supportive research community.

I owe thanks to NERC and the Met Office for funding this research, and also to the people and institutes who have provided the data used in this research.

I gained a huge amount from doing science outreach during my PhD. I would like to thank Will and the wider Orbyts team for encouraging me to be part of Orbyts and I wish the program every success in the future! It was a joy to work with Dr Sian Clark and the many great students at St Richard Reynolds Catholic College. Thank you all for your hard work and enthusiasm to learn about the aurora and wider magnetosphere.

I would also like to thank the Space Girls Frankie, Jenny and Divya. I could not have wished for a better or more capable group of friends/flatmates/house party co-hosts to have over the last four years. Although I'm very sad that we are all

going our separate ways, I wish you all the best in your future careers and I hope we stay friends for many more years.

I would like to thank my office mates, both past and more recent. My fellow Auroral Explorers, Jasmine and Nadine who have been excellent role models and 108 (Frankie, Affelia, Richard, Qasim and Seong-Yeop) for the fun, good company and the occasional distractions throughout my PhD. I would also like to thank all the students and everyone else at MSSL for making the department such a great place to be over the past 4 years.

Finally, my biggest thanks goes to my family. My mum, dad, my sister Natasha, my grandparents and Ali who have always encouraged me and often had more faith in me than I had in myself. Ali, thank you for your continuous support over the years and thank you for your keen assistance in proofreading this thesis! I'd like to give a special mention to my granny Gladys who is firm in her belief that I will go to space one day.

Contents

List of Figures

List of Tables

Chapter 1

Impact Statement

The aurora is the most visible space weather phenomenon at Earth and is of interest to many members of the public, with auroral alert services such as AuroraWatch UK having over 112,000 Twitter followers to date. Space weather, including the aurora, poses a significant threat to infrastructure that society relies on and was added to the UK National Risk Register in 2012. The high-energy, charged particles precipitating into the upper atmosphere and ionosphere that cause the bright auroral emission also disrupt radio communication networks used by emergency responders and aircraft for long range communication and tracking, resulting in flight diversions and significant costs to airlines. Meanwhile, the associated auroral current systems can cause ground-induced currents (GICs) which can damage electricity supply networks and increase the rate of corrosion in oil and gas pipelines. Space weather research and modelling efforts provide stakeholder industries with advanced warning of disruption due to space weather to mitigate the risk of space weather impact on essential services.

The research in this thesis presents a rigorous evaluation of the operational implementation of the OVATION-Prime 2013 auroral forecast model. Evaluation techniques that are routinely used in weather forecast verification, but not yet widely applied to space weather forecast models, are used to assess the model's ability to predict the location and probability of the auroral occurrence. The analysis provides quantitative benchmarks against which future developments in auroral modelling can be assessed and can inform space weather forecasters about the operational

performance and biases of the auroral model. This analysis has been carried out in collaboration with the Met Office and has been published in Space Weather.

An increased understanding of the auroral oval boundaries and their dynamics in response to large-scale processes in the magnetosphere will help to improve space weather modelling capabilities for use in both scientific studies and operational forecasting centres. The research presented in this thesis also explores the statistical analysis of the auroral boundaries. The analysis examines the detailed motion of the poleward auroral boundary during substorms and shows that the boundary does not respond uniformly in all nightside local time sectors. In sectors near the substorm onset sector, the auroral boundary moves immediately poleward while the boundary in sectors further from the onset sector continues to expand equatorward until the closure of flux convects round to these sectors. This research has been published in the Journal of Geophysical Research.

The dynamics of the equatorward auroral boundary and how it relates to the wider magnetospheric structure is poorly understood. There is significant evidence of a close association between the equatorward auroral boundary and the plasmapause, under certain conditions. However, the analysis presented in this thesis shows that on average, the equatorward auroral boundary maps to a region outside the plasmapause. A better understanding of the sharp decrease in the auroral emission at the equatorward auroral boundary is required. The open questions highlighted from this study are timely in relation to the upcoming international magnetospheric science mission, SMILE, which will provide a global view of the solar wind – magnetosphere – ionosphere interaction and will help improve our understanding of the auroral oval and dynamics in the larger context of the magnetosphere.

Chapter 2

Introduction

The Sun is the largest and most massive body in the solar system. The Sun's mass generates a huge gravitational force that causes all the planets and planetary bodies in the solar system to orbit around it. Due to the high temperatures of the Sun, its matter exists as a highly ionised plasma. The Sun also has a very strong and complex intrinsic magnetic field which has far reaching consequences throughout the solar system. The solar wind is a constant stream of charged plasma particles that expands radially outward from the Sun's atmosphere and carries the intrinsic solar magnetic field to the outer edges of the solar system. Planets that have an internal magnetic field, such as the Earth, are largely protected from the solar wind. The planetary magnetic field creates a protective cavity, known as a magnetosphere, which diverts the majority of the solar wind around the planet. However, the interaction between the solar wind and the magnetosphere drives geomagnetic activity. When this activity results in disruption or damage to technology or daily services at Earth, it is termed space weather. The most visible space weather phenomenon is the aurora, which can be enhanced during strong space weather events.

The research in this thesis primarily focuses on understanding the large-scale structure and dynamics of the aurora in the wider context of the magnetosphere in the hope that the knowledge can be applied to future generations of auroral forecast models which can help to mitigate the impact of future space weather events at Earth.

In this Chapter, the background physics that governs the interaction between

plasma particles and electromagnetic fields is introduced. An overview of the Earth's magnetosphere is then provided in which each region of the magnetosphere is briefly introduced and the large-scale processes that govern the dynamics of the magnetosphere and coupling between regions is described in detail. Finally, the current understanding of the source regions of the particles which cause the aurora and the physical processes which result in the auroral emission are summarised.

2.1 Basic Plasma Physics

2.1.1 The Quasi-neutrality and Collective Behaviour of Plasmas

A plasma is a distinct state of matter consisting mostly of electrically charged particles but may also contain some neutral particles. The particles in a plasma are free to move. The presence of charged particles means that electric and magnetic fields can play a critical role in the dynamics of the plasma.

Although plasma particles are electrically charged, plasmas generally have an approximately equal number of positive and negatively charged particles, making plasmas effectively electrically neutral, termed *quasi-neutral*, on large scales when they are in a steady state. Plasmas maintain quasi-neutrality by either having similar ionisation and recombination rates or alternatively by having very low number densities of particles such that the recombination rate between ions and electrons or between charged particles and neutrals is sufficiently low, as is often the case in space plasmas. Many plasmas, particularly plasma populations in the magnetosphere are generally considered to be collisionless.

A collection of charged particles, such as in a plasma, generate large-scale electric and magnetic fields. The behaviour of particles in a plasma is determined by both local, near-neighbour particles and more distant particles in the plasma. Similar to a gas, the individual plasma particles are free to move independently from one another with the average kinetic energy of each particle exceeding the average electrostatic potential from its nearest neighbours. However, plasmas also exhibit *collective behaviour* where the plasma responds as a whole. Collective behaviour results in the particles in a plasma moving in an organised way which is determined

by the large-scale electromagnetic forces generated from all the particles in the plasma and external fields. For example, plasmas react collectively to maintain or restore charge neutrality. If a localised charge imbalance occurs in a plasma, the electrons and ions in the immediate vicinity of the charge imbalance immediately reconfigure. The electrostatic potential created by the movement of the electrons and ions counters the electrostatic potential of the charge disturbance, acting to shield the rest of the plasma from the local charge imbalance and restore the local charge neutrality. This process is known as *Debye shielding*. The electrons respond much more quickly to the charge imbalance because the mass of an electron is much smaller than the mass of a proton. The redistribution of plasma is generally simplified to only consider the displacement of the electrons in response to a charge imbalance with the ions in the plasma remaining stationary, whereas in reality, the ions would experience an equal but opposite force but the acceleration would be ~ 2000 times slower. An illustration of Debye shielding in a plasma in response to a localised charge imbalance is shown in Figure 2.1.

The influence of the charge imbalance is reduced by a factor of $\frac{1}{e}$, where e is the base of the natural logarithm, at the Debye length (λ_D) of the plasma which is defined by Equation 2.1, where ε_0 is the permittivity of free space, k_B is the Boltzman constant, T_e is the electron temperature, n_e is the number density of electrons and q_e is the electron charge.

$$\lambda_D = \sqrt{\frac{\varepsilon_0 k_B T_e}{n_e q_e^2}} \tag{2.1}$$

Debye shielding is an example of the *collective behaviour* of a plasma. For a plasma to exhibit collective behaviour, there must be a high enough number density of plasma particles within a Debye sphere (a sphere with radius equal to the Debye length) to shield a charge disturbance and return the plasma to quasi-neutrality. The number of plasma particles in the Debye sphere, known as the plasma parameter, is described by Equation 2.2 where N_D is the number of particles in a Debye sphere, n_e is the electron density and λ_D is the Debye length.

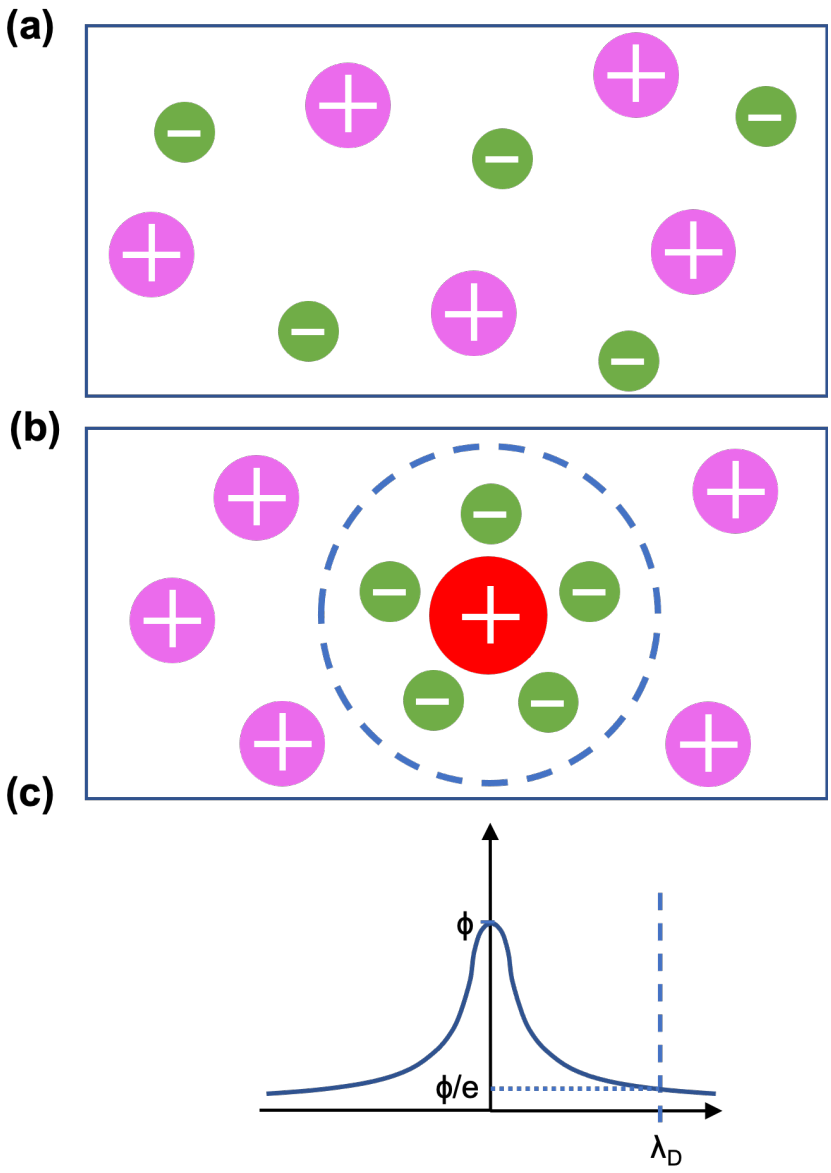

Figure 2.1: A cartoon illustration of Debye shielding in a plasma. Panel (a) shows a quasi-neutral plasma before the introduction of a charge imbalance. Panel (b) shows the response of the plasma to shield the localised charge imbalance ϕ, illustrated by the red positive charge. Panel (c) shows the electric potential of the charge imbalance with distance from the charge. At a radius of the Debye length (λ_D), the potential from the charge imbalance ϕ is reduced by a factor of $\frac{1}{e}$.

$$N_D = \frac{4\pi}{3} n_e \lambda_D^3 \tag{2.2}$$

When the electrons in the plasma are displaced from their equilibrium position

the charge separation creates an electric field that acts as a restoring force to return the electrons towards their initial equilibrium position. However, the action of the restoring force causes the particles to overshoot their equilibrium position and the direction of the restoring force reverses, resulting in the oscillation of the particles about their equilibrium position at the plasma frequency (ω_s), defined in Equation 2.3 where n_s, m_s and q_s, refer to the number density, mass and charge of the particle, respectively and the subscript s is generalised to any plasma particle species.

$$\omega_s = \sqrt{\frac{n_s q_s^2}{\varepsilon_0 m_s}} \tag{2.3}$$

As previously mentioned, a plasma may contain some neutral particles however for a collisionless plasma the collision frequency between the charged and neutral particles must be less than the natural plasma frequency, ω_s, such that the neutral particles do not interfere with or impede the collective behaviour of the plasma. This is generally true of collisionless plasmas in the magnetosphere but not the case in the collisional ionospheric plasma where there is a higher number density of neutral particles.

2.1.2 Single Particle Motion

The main constituents of a plasma are electrically charged and so plasmas interact with electric and magnetic fields. The following section describes the motion of a single plasma particle in response to uniform and non-uniform electric and magnetic fields.

2.1.2.1 Particle Motion in Uniform Electromagnetic Fields

The Lorentz force describes the force a charged particle experiences in an electromagnetic field. The Lorentz force is given by Equation 2.4 where q is the charge of the particle in the electromagnetic field, **E** and **B** are electric and magnetic field vectors, respectively and **v** is the particle velocity vector.

$$F_L = q(\mathbf{E} + \mathbf{v} \times \mathbf{B}) \tag{2.4}$$

The motion of a particle in an electromagnetic field can be examined by considering the forces from the electric and magnetic fields separately.

If the charged particle is exposed to a uniform electric field but no magnetic field, the particle will be continually accelerated. Electrons and ions are accelerated in different directions in the electric field, due to their opposing charge. Positively charged ions are accelerated in the direction of the electric field while negative electrons are accelerated in the opposite direction. The acceleration of the particle is inversely proportional to the mass of the particles which results in a much faster acceleration of the electrons compared to the heavier, positive ions. The force on the particle due to the electric field is shown in Equation 2.5 where m and q are the mass and charge of the particle, respectively, **a** is the acceleration of the particle due to the electric field and **E** is the electric field vector.

$$m\mathbf{a} = q\mathbf{E} \tag{2.5}$$

In the case where the charged particle is exposed to a uniform external magnetic field but no electric field, the resulting motion of the particle depends on the initial velocity of the particle. If the particle is initially at rest, the vector cross product from Equation 2.4 ($\mathbf{v} \times \mathbf{B}$) is zero and thus there is no force applied to the particle and the particle remains at rest. However, if the initial velocity of the charged particle is non-zero and the initial velocity has a component which is not parallel to the magnetic field direction, the force on the particle is directed perpendicular to both the particle velocity and magnetic field direction. The resulting motion is the gyration of the particle around the magnetic field axis. A cartoon illustration of the resulting motion is shown in panel (a) of Figure 2.2. The radius and period of the gyro-orbit are defined in Equations 2.6 and 2.7, respectively where r_L is the gyroradius, also known as the Larmor radius, ω_c is the gyroperiod or cyclotron period, m is the mass of the particle, $v_\perp$ is the velocity perpendicular to the magnetic field vector, q is the particle charge and B is the magnitude of the magnetic field vector.

$$r_L = \frac{mv_\perp}{q\mathbf{B}} \tag{2.6}$$

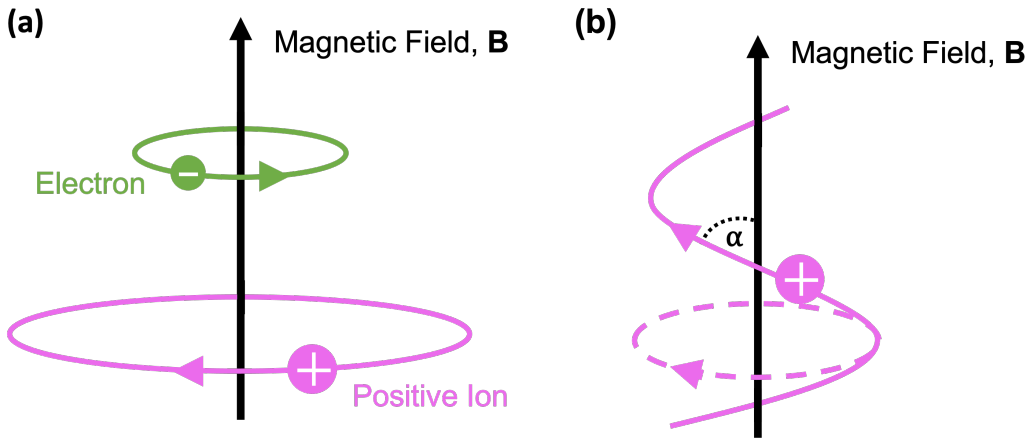

Figure 2.2: An illustration of single particle motion in a uniform magnetic field. Panel (a) shows the resulting gyromotion for a particle which has a non-zero initial velocity in the direction perpendicular to the magnetic field for electrons in green and positive charges in pink. Panel (b) shows the resulting motion for particles which non-zero initial velocity components both perpendicular and parallel to the magnetic field direction.

$$\omega_c = \frac{q\mathbf{B}}{m} \tag{2.7}$$

As the gyroradius of the particle is dependant on both the charge and the mass of the particle, ions and electrons gyrate in different directions around the magnetic field, with ions gyrating anti-clockwise when viewed in the direction of the magnetic field, with a larger gyroradius and electrons gyrating clockwise when viewed in the direction of the magnetic field, with a smaller gyroradius.

If the charged particle initially has a non-zero velocity component parallel to the magnetic field direction, the particle moves in a helical path around a guiding centre as illustrated in panel (b) in Figure 2.2. The force of the magnetic field only acts perpendicular to the particle velocity and magnetic field direction, resulting in the gyromotion. There is no force from the magnetic field in the direction parallel to the particle velocity and so the non-zero parallel velocity component of the particle is unchanged by the magnetic field and the particle continues to move along the magnetic field direction while gyrating around the magnetic field, resulting in a helical path. The pitch angle, α is the angle between the particle velocity and the magnetic field vectors and can be calculated from the ratio of the velocity compo-

nents perpendicular ($v_\perp$) and parallel ($v_\parallel$) to the magnetic field direction, as shown in Equation 2.8.

$$tan(\alpha) = \frac{v_\perp}{v_\parallel} \tag{2.8}$$

Returning to the Lorentz equation (Equation 2.4), if the charged particle is exposed to a uniform electric field with a component which is perpendicular to the magnetic field, the particle is accelerated by the electric field and can be accelerated from rest. The combined motion of both the electric and magnetic field causes the charged particle to gyrate around a guiding centre while drifting in the direction perpendicular to both the electric and magnetic field directions, as illustrated in Figure 2.3. This is known as the $\mathbf{E} \times \mathbf{B}$ drift and is defined in Equation 2.9 where $\mathbf{E}$ and $\mathbf{B}$ are the electric and magnetic field vectors, respectively and B is the magnitude of the magnetic field. Note that the $\mathbf{E} \times \mathbf{B}$ drift is independent of the particle's charge, mass and initial velocity, thus all charged particles drift in the same direction with the same drift velocity.

$$\mathbf{v}_{\mathbf{E}\times\mathbf{B}} = \frac{\mathbf{E} \times \mathbf{B}}{B^2} \tag{2.9}$$

2.1.2.2 Particle Motion in Non-Uniform Magnetic Fields

Non-uniformities in the magnetic field, including gradients or curvatures, can also introduce drifts in the motion of a charged particle in the magnetic field. If a charged particle experiences a spatial gradient in the magnetic field perpendicular to the magnetic field direction, the particle drifts in the direction perpendicular to both the magnetic field vector and the gradient in the magnetic field. The gradient in the magnetic field causes the Larmor radius of the particles gyromotion to vary as the particle drifts, with smaller gryoradii in regions of stronger magnetic fields for a particle with a fixed energy. An illustration of particle gradient drift is shown in Figure 2.4. The magnetic gradient drift velocity $\mathbf{v}_{\nabla\mathbf{B}}$ is defined in Equation 2.10 where $W_\perp$ is the perpendicular component of the particle kinetic energy, $\mathbf{B}$ is the magnetic field vector, $\nabla\mathbf{B}$ is the gradient in the magnetic field and q is the particle

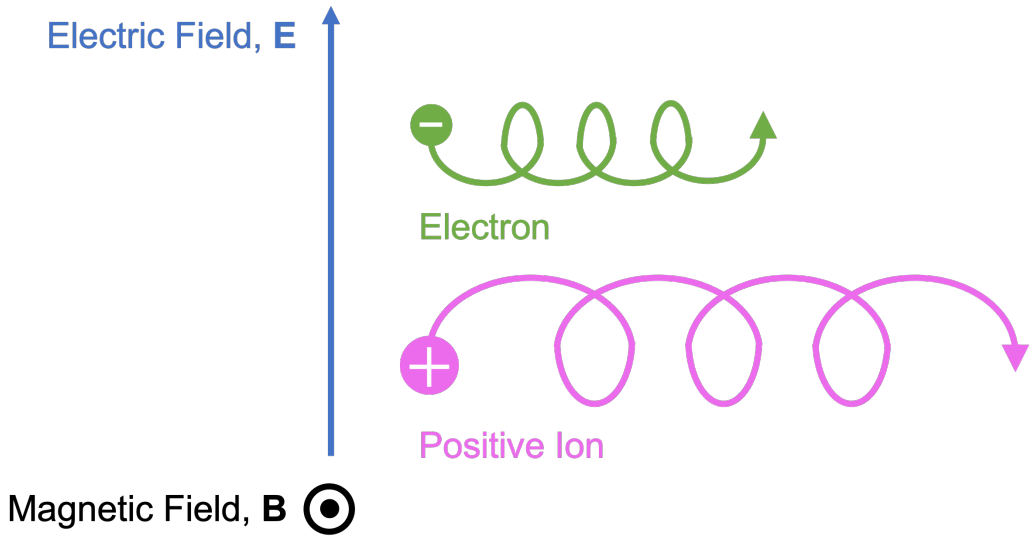

Figure 2.3: A cartoon illustrating the resulting motion of positive and negatively charged particles in uniform electric and magnetic fields. In this figure, the electric (E) and magnetic (B) field directions are perpendicular to each other and the magnetic field direction points out of the page.

charge. Due to the dependence on particle charge, electrons and ions gradient drift in opposite directions.

$$\mathbf{v}_{\nabla \mathbf{B}} = \left(\frac{2W_{\perp}}{B}\right) \frac{\mathbf{B} \times \nabla \mathbf{B}}{qB^2} \tag{2.10}$$

If the charged particle is moving along a curved magnetic field the particle experiences a centrifugal force that is directed outward from the centre of curvature of the field. This results in a curvature drift of the charged particle in the direction perpendicular to the magnetic field vector and the centrifugal force. The curvature drift velocity ($\mathbf{v_c}$) is defined by Equation 2.11 where $W_{\parallel}$ is the parallel component of the particle kinetic energy, R_c is the radius of curvature of the magnetic field line, $\mathbf{B}$ is the magnetic field vector and q is the particle charge. The curvature drift is dependent on the charge of the particles which causes electrons and ions to curvature drift in opposite directions.

$$\mathbf{v_c} = \left(\frac{2W_{\parallel}}{R_c^2}\right) \frac{\mathbf{R_c} \times \mathbf{B}}{qB^2} \tag{2.11}$$

In the case where the magnetic field strength varies due to the curvature of the

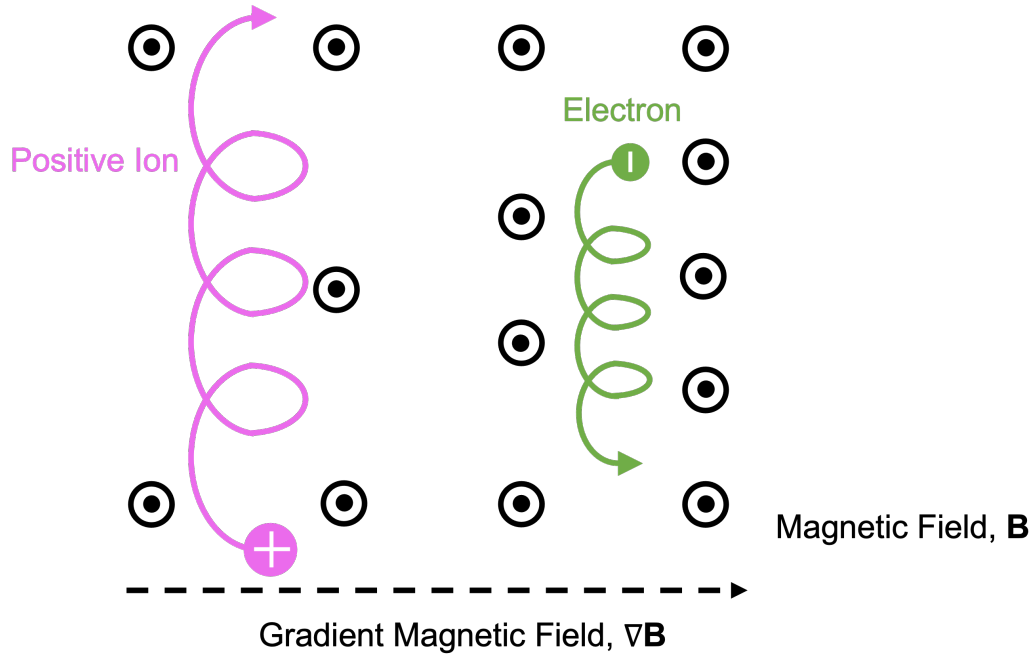

Figure 2.4: A cartoon illustrating the resulting motion of a positive and negative charge in a non-uniform magnetic field which has a gradient in the strength of the magnetic field. The magnetic field is pointing out of the page and is increasing in strength from left to right.

magnetic field, such as in a dipolar or dipole-like field, charged particles experience a combined gradient, curvature and $\mathbf{E} \times \mathbf{B}$ drift motion. The velocity of a charged particle in an electromagnetic field is comprised of the sum of the velocity contributions from the $\mathbf{E} \times \mathbf{B}$ drift, the magnetic field gradient and curvature drifts, as shown in Equation 2.12. For high energy particles, the particle motions are dominated by the gradient and curvature drift motions, whereas lower energy particle motions are dominated by the $\mathbf{E} \times \mathbf{B}$ drift motion.

$$v = \underbrace{\frac{\mathbf{E}\times\mathbf{B}}{B^2}}_{\substack{\mathbf{E}\times\mathbf{B} \\ drift}} + \underbrace{\left(\frac{2W_\perp}{B}\right)\frac{\mathbf{B}\times\nabla\mathbf{B}}{qB^2}}_{\substack{Gradient \\ drift}} + \underbrace{\left(\frac{2W_\parallel}{R_c^2}\right)\frac{\mathbf{R_c}\times\mathbf{B}}{qB^2}}_{\substack{Curvature \\ drift}} \tag{2.12}$$

If a particle is in a non-uniform magnetic field which is very slowly varying with time or not changing at all, in the absence of an electric field, the particle kinetic energy is the sum of the particle energy components in the directions perpendicular and parallel to the magnetic field.

The magnetic moment of the gyrating particle, μ is defined in Equation 2.13 where $W_\perp$ is the perpendicular component of the particle energy and B is the strength of the magnetic field. The magnetic moment is a conserved quantity if the magnetic field changes over timescales that are longer than the particle gyroperiod.

$$\mu = \frac{W_\perp}{B} \tag{2.13}$$

If the particle experiences a gradient in the magnetic field strength and gyrates into a region where the magnetic field strength increases, the perpendicular component of the particle kinetic energy increases proportionally to conserve the magnetic moment. The parallel component of the particle's energy along the magnetic field direction decreases to conserve the total kinetic energy of the particle. If the magnetic field strength is high enough, the parallel velocity of the particle can be reduced to zero such that the particle stops moving along the magnetic field. The particle motion is reversed and the particle gyrates back to the region of lower magnetic field strength. The velocity component parallel to the field begins to increase as the perpendicular component decreases. The reflection of the particle in regions of high magnetic field strength is known as a magnetic mirror. Gyrating particles can become trapped between regions of strong magnetic fields, known as a magnetic bottle. The point where the particle mirrors in the magnetic field depends on the pitch angle of the particle's gyration in the region of minimum magnetic field strength and the minimum and maximum magnitude of the magnetic field strength. Figure 2.5 shows an illustration of the motion of a charged particle trapped in a magnetic bottle.

2.2 Magnetohydrodynamics: The Fluid Description of a Plasma

Single particle motion is useful to understand the interaction between individual charged particles and external magnetic and electric fields. However, to study the macroscopic properties of a body of plasma, a simplification can be made which

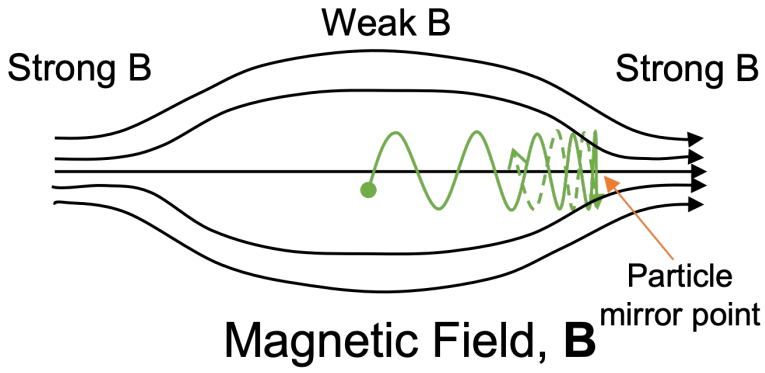

Figure 2.5: A cartoon of a charged particle trapped in a magnetic bottle. The orange arrow indicates the mirror point in the magnetic field where the parallel velocity of the particle decreases to zero and then reverses direction.

treats the plasma as a conducting, magnetised fluid, known as magnetohydrodynamics (MHD), which averages across the single particle motions.

2.2.1 The MHD Equations

The basic laws of electromagnetism that are central to the MHD description of a plasma are defined in Equations 2.14 - 2.17 and are collectively known as Maxwell's equations. In Equations 2.14 - 2.17, the symbols have their usual meanings where **E** and **B** are the electric and magnetic field vectors, respectively, ρ is the charge density, **j** is the current density and ε_0 and μ_0 are the permittivity and permeability of free space, respectively.

Poisson's law, defined in Equation 2.14, shows that the net electric flux associated with the volume of space surrounding any charge density is non-zero. In other words, any charge density in space is either a source or sink of electric field, depending on whether the charge is positive or negative. In contrast, Gauss' law, defined in Equation 2.15, shows that the magnetic flux in a volume of space is always conserved i.e. the magnetic flux into a volume of space is equal to the magnetic flux out of the same volume. This also dictates that magnetic monopoles cannot exist. Faraday's law, in Equation 2.16, demonstrates an inherent link between evolving magnetic and electric fields in that a magnetic field that evolves with time is related to a circulating electric field. Equally, a circulating electric field is related to a time-

evolving magnetic field. Finally, Ampère's law, defined in Equation 2.17, illustrates that a circulating magnetic field is associated with a conduction current (**j**) or a displacement current associated with an electric field evolving with time ($\varepsilon_0 \frac{\partial \mathbf{E}}{\partial t}$) and vice versa.

- **Poisson's Law:**

$$\nabla \cdot \mathbf{E} = \frac{\rho}{\varepsilon_0} \tag{2.14}$$

- **Gauss' Law:**

$$\nabla \cdot \mathbf{B} = 0 \tag{2.15}$$

- **Faraday's Law:**

$$\nabla \times \mathbf{E} = -\frac{\partial \mathbf{B}}{\partial t} \tag{2.16}$$

- **Ampère's Law:**

$$\nabla \times \mathbf{B} = \mu_0 \left(\mathbf{j} + \varepsilon_0 \frac{\partial \mathbf{E}}{\partial t} \right) \tag{2.17}$$

MHD is further governed by a set of equations which describe the plasma in terms of its macroscopic properties including particle number density (n), velocity (**v**), charge density (ρ), current density (**j**), pressure (**P**), the electric and magnetic fields (**E** and **B**, respectively), magnetic diffusivity (η), number density of electrons (n_e), electron mass (m_e), polytropic index (γ) and time (t). In the MHD framework, mass, charge, momentum and energy are conserved quantities as demonstrated in Equations 2.18 - 2.21. Equation 2.22 defines the spatial and temporal evolution of a current.

- **Mass Conservation**

$$\frac{\partial n}{\partial t} + \nabla \cdot (n\mathbf{v}) = 0 \tag{2.18}$$

- **Charge Conservation**

$$\frac{\partial \rho}{\partial t} + \nabla \cdot \mathbf{j} = 0 \tag{2.19}$$

- **Equation of Motion**

$$\rho\left(\frac{\partial \mathbf{v}}{\partial t}+\mathbf{v}\cdot\nabla\mathbf{v}\right)=-\nabla\cdot\mathbf{P}+\rho\mathbf{E}+\mathbf{j}\times\mathbf{B} \tag{2.20}$$

- **Equation of State**

$$\left(\frac{\partial}{\partial t}+\mathbf{v}\cdot\nabla\right)\left(\mathbf{P}\rho^{-\gamma}\right)=0 \tag{2.21}$$

- **Generalised Ohm's Law**

$$\mathbf{E}+\mathbf{v}\times\mathbf{B}=\underbrace{\eta\mathbf{j}}_{\substack{Resistive\\ term}}-\underbrace{\left(\frac{\nabla\cdot\mathbf{P}}{n_e}\right)}_{\substack{Electron\\ pressure}}+\underbrace{\frac{m_e}{n_e^2}\frac{\partial\mathbf{j}}{\partial t}}_{\substack{Electron\\ inertia}}+\underbrace{\frac{\mathbf{j}\times\mathbf{B}}{n_e}}_{\substack{Lorentz\\ force}} \tag{2.22}$$

A few assumptions can be applied to simplify the MHD and Maxwell equations. The first assumption is that plasmas are quasi-neutral, and in the case of ideal MHD there is no distinction between plasma species i.e. between ions and electrons, so the net charge density (ρ) is zero. Poisson's law can then be simplified to $\nabla\cdot\mathbf{E}=0$ and the $\rho\mathbf{E}$ term in the equation of motion is also often neglected. Secondly, the fluid motions of a plasma are assumed to be slow compared to the characteristic time and length scales of a plasma. In Ampère's Law, this means that the displacement current ($\varepsilon_0\frac{\partial\mathbf{E}}{\partial t}$) is assumed to be insignificant, compared to the conduction current and thus Ampère's law can be simplified to $\nabla\times\mathbf{B}=\mu_0\mathbf{j}$. In the Generalised Ohm's Law, the electron pressure, electron inertia and Lorentz force terms are also averaged out over large time and length scales and so they can also be neglected. A final assumption in ideal MHD is that the fluid is a perfect conductor which means that the diffusivity is zero ($\eta=0$) and this term can also be neglected from the Generalised Ohm's Law. These assumptions are generally valid when considering plasmas in the solar wind and Earth's magnetosphere. Applying these assumptions to the generalised form of Ohm's Law in Equation 2.22 greatly simplifies Ohm's law to:

$$\mathbf{E}+\mathbf{v}\times\mathbf{B}=0. \tag{2.23}$$

2.2.2 Magnetic Forces

The $\mathbf{j} \times \mathbf{B}$ term in Ampère's Law (Equation 2.17) can be further expanded to examine the forces acting on a magnetic field line in more detail which results in Equation 2.24 where the symbols have the same meanings as previously defined. The first term on the right hand side defines the magnetic pressure, which is a lateral pressure arising due to a gradient in the magnetic flux density. The magnetic pressure acts perpendicularly to the magnetic field line and opposes the squashing of the magnetic field. The second term on the right hand side defines the magnetic tension force which acts axially along the field line, opposing the bending of magnetic field lines. The magnetic pressure and tension forces are important in later discussions of magnetic processes such as reconnection, which is discussed further in Section 2.5.1.

- **Magnetic Forces**

$$F_m = \underbrace{-\nabla_\perp \frac{B^2}{2\mu_0}}_{\substack{Magnetic \\ pressure}} + \underbrace{\frac{B^2}{\mu_0}\frac{R_c}{R_c^2}}_{\substack{Magnetic \\ tension}} \tag{2.24}$$

2.2.3 The Convection and Diffusion of a Plasma

By combining the simplified expression for Ohm's law in the case of ideal MHD (Equation 2.23), and Ampère's law (Equation 2.17), an expression which illustrates the relationship between the plasma mass motion and the magnetic field can be defined, known as the MHD induction equation (Equation 2.25).

- **MHD Induction Equation**

$$\frac{\partial B}{\partial t} = \underbrace{\nabla \times (\mathbf{v} \times \mathbf{B})}_{Convection} + \underbrace{\frac{\eta}{\mu_0}\nabla^2 \mathbf{B}}_{Diffusion} \tag{2.25}$$

The first term on the right hand side ($\nabla \times (\mathbf{v} \times \mathbf{B})$) describes the convection of the magnetic field by the motion of the plasma particles, in other words the motion of the magnetic field and particles is strongly linked. The second term on the right hand side ($\frac{\eta}{\mu_0}\nabla^2 \mathbf{B}$) describes the diffusion of the magnetic field through

the plasma particles, in other words, the motion of the particles and magnetic fields being independent. The ratio of the convection and diffusion terms defines the magnetic Reynold's number (Equation 2.26), where the symbols are the same as previously defined and L is the length scale.

- **Magnetic Reynold's Number**

$$R_m = \frac{Convection}{Diffusion} = \frac{\mu_0 v L}{\eta} \tag{2.26}$$

From the assumptions that were previously stated in the ideal MHD framework, the plasma is assumed to be a perfect conductor and so the magnetic diffusivity term (η) is very small. Hence, in the ideal MHD case, the convective motion dominates which means that the motion of the magnetic field is associated with the motion of the plasma particles. This is known as the *frozen-in flux theorem*.

An interesting consequence of the frozen-in flux theorem is that two plasma populations from different sources in close proximity to one another are prevented from mixing. If two bodies of convection-dominated plasma come together the magnetic fields cannot overlap and so the plasma particles which are tied to the magnetic flux tubes cannot mix. Plasmas can only mix in regions where the frozen-in flux theorem breaks down and the diffusion term becomes significant again which can occur in boundary regions between plasma populations. If the magnetic Reynold's number is approximately unity, neither convection nor diffusion are dominant and both processes need to be taken into consideration. This situation can arise on short length scales such as thin current sheets. The frozen-in flux theorem and the limits under which it breaks down will be important in Section 2.5.1 in the discussion of magnetic reconnection and the interaction between the Earth's magnetosphere and the solar wind.

Similar to the Reynold's number, the plasma β parameter is the ratio of plasma pressure to magnetic pressure as defined in Equation 2.27. The plasma β parameter ties into the frozen-in flux theorem in that it also helps to describe whether the magnetic field is dominated by the plasma motion in the high β regime, for example

in the Earth's plasma sheet, or the plasma motion is dominated by the magnetic field in the low β regime, for example in the magnetotail lobes.

- **Plasma β Parameter**

$$\beta = \frac{Plasma\ Pressure}{Magnetic\ Pressure} = \frac{2\mu_0 P}{B^2} \tag{2.27}$$

2.3 The Earth's Magnetosphere

Magnetised bodies in the solar system, such as Earth, have a magnetosphere in which the magnetic field of the body is the dominant force acting on the plasma. Figure 2.6 shows a schematic diagram of the magnetic field structure of the Earth's magnetosphere, illustrating the main features. To a first approximation, Earth's intrinsic magnetic field is dipolar and is thought to be generated by the motion of the molten iron core of the Earth, however as the magnetic field expands into space, it is deformed by its interaction with the solar wind. The magnetosphere is filled with plasma. The majority of the plasma originates from the upper atmosphere where atmospheric particles are ionised and frozen-in to the magnetic field, filling up the magnetic flux tubes; however, some of the plasma is also captured by the magnetosphere from its solar neighbourhood. In the following sections, the structure of the magnetosphere is outlined and the external processes that influence the magnetospheric structure are discussed.

2.3.1 The Ionosphere

The ionosphere is the upper region of the atmosphere where the particle population transitions from the neutral atmosphere to the fully ionised plasma of the magnetosphere. The ionosphere extends from approximately 60 km to over 1000 km in altitude. The temperature and plasma density vary significantly with height in the ionosphere. The plasma temperature of the ionosphere is low and generally less than 0.13 eV. The plasma density ranges from $\sim 10^3 - 10^6$ cm^{-3}. The atmospheric neutral particles are mainly ionised by the incident solar ultraviolet (UV) radiation (photoionisation) on the dayside. Secondary ionisation sources, such as precipitat-

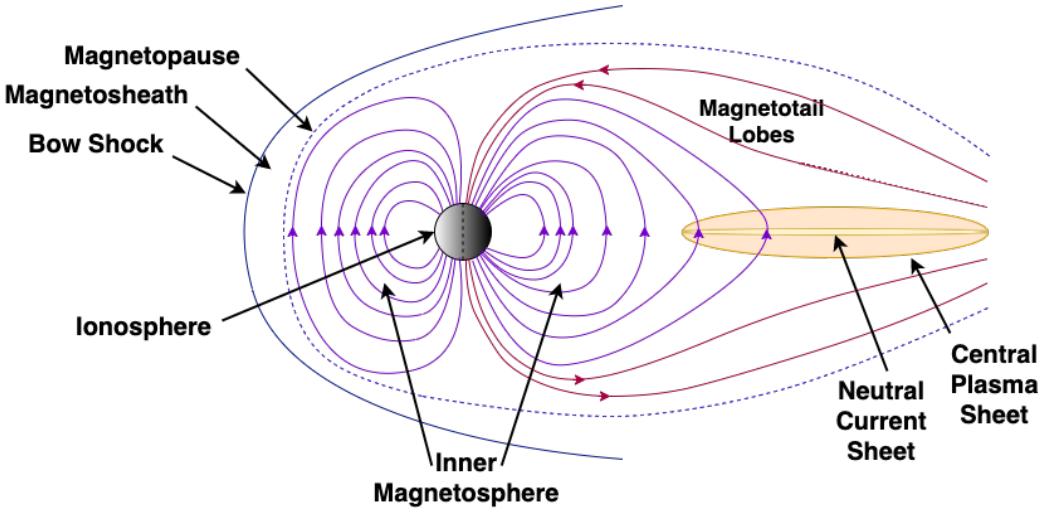

Figure 2.6: A cartoon illustrating the main regions of the magnetosphere. Solid purple/red lines indicate closed/open magnetic field lines.

ing auroral particles from the magnetotail or highly energetic solar particles ejected during eruptive solar events, also ionise the neutral particle population, however the rate of ionisation by these secondary methods is more variable. The ionosphere has a high neutral particle population. This leads to a higher collision rate between ions and neutral particles which de-couples the ions from the magnetic field. The plasma in the ionosphere is therefore not a fully ionised plasma and the ideal MHD framework cannot be applied to the ionospheric plasma. At higher altitudes in the ionosphere the number density of neutral particles decreases, reducing the number of collisions between ions and neutral particles and the plasma becomes fully ionised. Ion outflows from the ionosphere are a large source of magnetospheric plasma.

The ionosphere is in hydrostatic equilibrium such that the Earth-directed gravitational force balances the upwards pressure gradient force, as shown in Equation 2.28 where P is the pressure, g is the acceleration due to Earth's gravity, k is the Boltzmann constant, T is the temperature, m is the particle mass and z is the height from the Earth's surface.

$$\frac{dP}{P} = -\frac{gMdz}{kT} \tag{2.28}$$

Due to the smaller mass of electrons compared to ions, the electrons have a

higher scale height i.e. the altitude at which the atmospheric pressure decreases by a factor of e is higher for electrons than protons. The resulting altitudinal charge separation in the ionosphere is known as the ambipolar electric field which drives the lighter ions such as H^+ and He^+ up along the magnetic field lines. Ion outflows have been measured in the low to middle latitudes, the auroral regions, the polar cap (the area of open magnetic field lines at the magnetic poles) and at the dayside cusp region (Kronberg et al., 2014). In the polar cap, low energy ions outflow along the open field lines into the magnetotail lobes (Kronberg et al., 2014). At low to middle latitudes, ions outflow along closed field lines into the inner magnetosphere where they become trapped on closed drift paths, mirroring between the stronger magnetic field regions near the poles and forming a cold ($\sim$ 1 eV), dense plasma population, known as the plasmasphere (Kronberg et al., 2014). The ionospheric plasma fills the magnetic flux tubes, becomes frozen-in to the magnetic field and co-rotates with the Earth. Due to the low energies of the particles, the cold plasmaspheric particle motions are dominated by the $\mathbf{E} \times \mathbf{B}$ drift.

2.3.1.1 The Aurora

Charged plasma particles in the Earth's magnetosphere are trapped between the strong magnetic field regions near the poles, known as a magnetic bottle as described in Section 2.1.2.2. In the polar regions, the magnetic field lines thread the ionosphere where the neutral particle density increases along the field line. A trapped particle may encounter and collide with a neutral particle before it reaches its mirror point. Collisions with neutral particles can change the pitch angle of the trapped particle trajectory which can result in the particle being scattered into the *loss cone* where it is no longer trapped in the magnetic field. The loss cone defines a range of pitch angles which have mirror points at low altitudes such that the particle is lost to the atmosphere before it is reflected back along the field line at the mirror point. Plasma particles from the loss cone precipitate along closed magnetic field lines and into the upper atmosphere where they undergo collisions with atmospheric particles. The main source of the precipitating particles is thought to be the nightside plasma sheet, with some plasma also precipitating in the dayside from the

cusp and magnetosheath.

Initially, the precipitating particles have such high energy that they completely ionise the atmospheric particle that they collide with, creating a cascade of free electrons. These free electrons undergo further collisions, losing energy and freeing more electrons until they eventually have insufficient energy to ionise neutral particles and collisionally excite atmospheric atoms and ions (e.g. Oxygen and Nitrogen). The resulting de-excitation emits a photon of radiation which is observed as aurora at altitudes of $\sim$ 100 km, with different wavelengths of light emitted depending on the particle species and de-excitation energy. Typically, electrons with energies in the range of $1-10$ keV precipitate to altitudes of $100-150$ km before colliding with ionospheric particles. Lower energy electrons of <1 keV can travel along the field lines to altitudes of $\sim$ 200 km and higher energy particles can penetrate to altitudes of $\sim$ 80 km. Precipitating protons can also emit radiation via charge exchange in which a precipitating proton captures an electron, producing a neutral Hydrogen atom and emitting a photon. The auroral emission is observed in the infrared, visible, UV and X-ray. The UV emission production mechanisms will be discussed in more detail in Chapter 4. The source regions of the auroral particles and the dynamics of the aurora will be discussed in more detail in Sections 2.5, 2.6 and 2.7.

2.3.2 The Inner Magnetosphere: The Plasmasphere, Radiation Belts and Ring Current

The inner magnetosphere (within ~ 6 R_E) is dominated by three distinct, trapped, particle populations; the high energy radiation belt particles, the ring current particles and the very low energy plasmaspheric particles. From Faraday's law in Equation 2.16, a time varying magnetic field is related to a rotational electric field. The rotation of the Earth's dipole magnetic field has a corresponding co-rotational electric field which is the dominating electric field in the inner magnetosphere.

The plasmasphere is a dense ($\sim$ 10^3 cm^{-3}, Baumjohann and Treumann, 2012) torus of cold plasma (<1 eV, Goldstein, 2007; Delzanno et al., 2021), located in the inner magnetosphere extending from the ionosphere out to $\sim 3-6$ R_E (Lemaire

and Gringauz, 1998). The plasmasphere is populated by particles from the upper ionosphere that drift up along field lines to higher altitudes. The plasmaspheric particle population is dominated by protons and electrons with a small percentage (5 - 20%) of Helium (He^+) ions, which varies with geomagnetic activity (Delzanno et al., 2021; Darrouzet et al., 2009; Sandel et al., 2000) and a heavy ion population of mainly Oxygen and Nitrogen ions, contributing $\sim 3\%$ of the particle population (Delzanno et al., 2021; Grew et al., 2007; Dandouras, 2013). The outer boundary of the plasmasphere, the plasmapause, is identified by a sharp particle number density gradient. The plasmasphere often has a plume feature that forms in the dusk local time sectors and stretches towards the dayside. The plume is known as the plasmaspheric drainage plume as a significant amount of the cold plasmaspheric particle population is lost via the plume. The plumes develop during periods of enhanced geomagnetic activity, such as magnetospheric storms, which causes the plasmasphere to contract to smaller radii.

The radiation belts are split into an inner and an outer radiation belt, separated by the slot region between $\sim 2 - 4$ R_E. The radiation belt particle population is a lower density plasma (~ 1 cm^{-3} Baumjohann and Treumann, 2012), compared to the plasmaspheric plasma but the radiation belt particles have much higher energies. The inner radiation belt within $\sim 2\,R_E$ consists of high energy ions (10 MeV - 1 GeV). The outer radiation belt is located between $\sim 3 - 7$ R_E and consists of high energy electrons (> 100 keV). The outer radiation belt is highly variable and sensitive to the level of geomagnetic activity. The high energy radiation belt particles coexist in the inner magnetosphere with the cold plasmapsheric particle population. However, the two populations are well ordered by magnetospheric wave activity. The spatial distribution of the important wave activity in the inner magnetosphere is illustrated in Figure 2.7, from Thorne (2010). The majority of the wave activity occurs outside the plasmapause. Chorus waves, which are discrete, coherent whistler mode waves, are observed outside the plasmapause in the midnight through dawn to the noon local time sectors. Inside the plasmapause, incoherent whistler mode hiss waves are observed in the dayside local time sectors and drainage plume region.

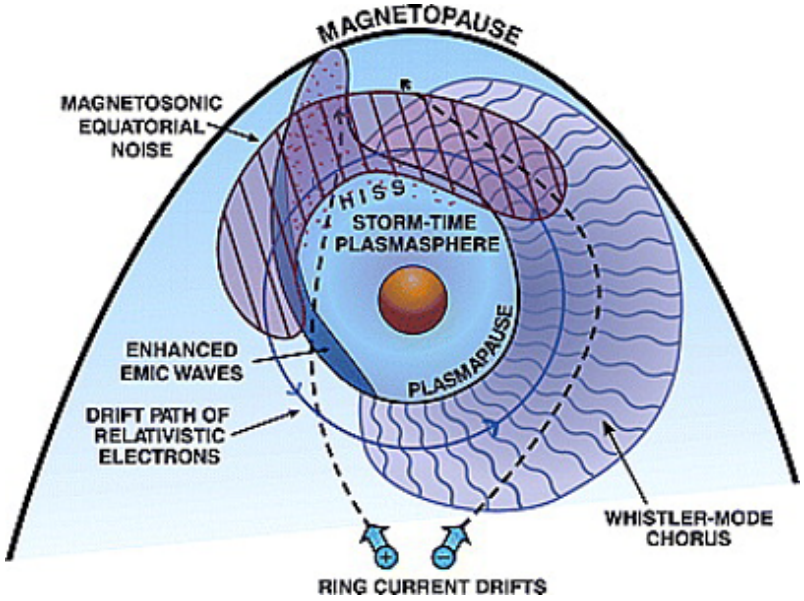

Figure 2.7: Figure from Thorne (2010): "Schematic illustration of the spatial distribution of important waves in the inner magnetosphere, in relation to the plasmasphere and the drift-paths of ring-current (10–100 keV) electrons and ions and relativistic ($\geq$ 0.3 MeV) electrons."

Electromagnetic ion cyclotron (EMIC) waves, which are discrete electromagnetic waves, are also enhanced at the edge of the drainage plume. The wave activity in the inner magnetosphere is a large source of both energisation and loss of the radiation belt particles. The plasmasphere and radiation belt particle populations are known to interact via wave-particle interactions; however, a discussion of this is outside the scope of this work. Due to the high energies of the particles in the radiation belts, the particle motions are dominated by gradient and curvature drifts, trapping the particles on closed drift shells which form the characteristic belt structures around the Earth. The gradient and curvature drift of the ions and electrons in the outer radiation belt is dependent on the energy and charge of the particles, causing the positively charged ions to drift westwards and the negatively charged electrons to drift eastwards.

The ring current is a westward directed current generated by drifting trapped, charged particles which are predominantly ions with energies between 1 keV to a few hundred keV in the equatorial plane of the inner magnetosphere, between $\sim 4-9$ R_E (Daglis et al., 1999; Le et al., 2004). Ring current ions originate from

the ionosphere and the solar wind. Ions from the ionosphere populate the nightside plasma sheet which are then injected into the inner magnetosphere during periods of strong magnetospheric convection and during substorms. The ring current is then enhanced during geomagnetic storms and substorms (Sandhu et al., 2018, 2021). The associated ring current magnetic field opposes the geomagnetic field inside the ring current location, but enhances the geomagnetic field outside the ring current. H^+ ions are the dominant ion species in the ring current; however, the O^+ ion content increases during geomagnetically active periods, constituting up to $\sim 20\%$ during active times (Daglis et al., 1993). After the enhanced geomagnetic activity, the ring current decays due to charge exchange with cold, neutral Hydrogen particles in the upper atmosphere, Coulomb collisions with plasmaspheric Hydrogen and wave-particle interactions (Fok et al., 1995; Daglis et al., 1999). Charge exchange is the most important loss mechanism for the high energy ring current particles of a few hundred keV while Coulomb collisions are a more significant loss mechanism for the lower energy particles of ~ 10 keV. Coulomb collisions can pitch angle scatter ring current ions into the loss cone where they precipitate into the ionosphere.

2.4 Solar Wind - Magnetospheric Coupling

2.4.1 The Solar Wind

The solar wind is a stream of plasma particles that expands radially outward from the Sun into interplanetary space. The solar wind plasma originates from the base of the solar atmosphere, known as the corona. The visible surface of the Sun, known as the photosphere, has an effective temperature of ~ 6000 K; however, the temperature of the solar corona reaches temperatures on the order of 10^6 K. The outward thermal pressure in the corona exceeds the gravitational force of the Sun, allowing the ionised coronal plasma to expand radially outwards from the Sun into interplanetary space where it forms the solar wind. The solar corona has a low particle density of $\sim 10^{14}$ m^{-3} compared to $\sim 10^{23}$ m^{-3} at the photosphere (Meyer-Vernet, 2007) and a weaker magnetic field of approximately 10^{-4} T (Meyer-Vernet, 2007). In the high latitude regions of the lower corona, the plasma pressure dominates over

the magnetic pressure (plasma $\beta >> 1$). As a result, the magnetic field is dragged with the convection of the plasma particles, in other words, the magnetic field is frozen-in to the plasma. The magnetic field, which is frozen-in to the solar wind plasma, expands outwards and becomes the interplanetary magnetic field (IMF). The radial expansion of the solar wind in addition to the solar rotation results in the IMF forming a spiral structure in interplanetary space, known as the Parker Spiral (Parker, 1958).

2.4.2 The Outer Magnetosphere

The terrestrial magnetosphere acts to shield Earth from the incoming solar wind. Due to the frozen-in flux theorem, the plasmas associated with the two magnetic field regimes of the magnetosphere and the IMF are prevented from mixing directly. As a result, the magnetosphere forms a magnetic cavity around Earth that largely diverts the solar wind and IMF around the Earth. As previously mentioned, the Earth's intrinsic magnetic field is approximately dipolar; however, the magnetospheric structure is distorted by the solar wind. The ram pressure of the solar wind compresses the dayside magnetosphere to a distance of $\sim 11 - 15$ R_E (Fairfield, 1971), where 1 R_E $=$ 6371 km is 1 Earth radius. The nightside magnetosphere expands into the wake of the deflected solar wind and is stretched out into a long magnetotail which can extend to distances of $\sim$ 1000 R_E (Russell, 1972; Milan et al., 2004).

2.4.2.1 The Bow Shock, Magnetosheath and Magnetopause

As the solar wind reaches the dayside magnetosphere, the solar wind is travelling at supersonic speeds which results in the creation of a bow shock upstream of the magnetosphere. At the bow shock, the solar wind is largely deflected around the magnetosphere and the solar wind downstream of the shock front is slowed to subsonic speeds. The kinetic energy of the solar wind is converted into thermal and magnetic energy and so the density and temperature of the solar wind plasma downstream of the bow shock increases and the magnetic field strength downstream of the shock also increases. The region downstream of the bow shock is called the mag-

netosheath and consists of the hot, dense, slowed solar wind plasma population. In the magnetosheath region, the plasma is still convection dominated and thus is still frozen-in to the magnetic field and cannot directly mix with the magnetospheric plasma. From Ampère's law, at the boundary between the solar wind plasma population in the magnetosheath and the magnetospheric plasma a thin current sheet forms, known as the magnetopause or Chapman and Ferraro current (Chapman and Ferraro, 1931). The magnetopause current flows dawnwards and closes through the nightside plasma current sheet. Upstream of the magnetopause, the convection of the solar wind plasma dominates the motion of the IMF and so the plasma β in this region is very high ($\beta >> 1$). In contrast, in the Earth's magnetosphere, the magnetic field dominates the motion of the plasma ($\beta << 1$). In the magnetopause current sheet separating these two regions, the plasma β tends towards unity, allowing the two plasma populations in the magnetosheath and magnetosphere to interact via magnetic reconnection which will be discussed later in Section 2.5.1.

2.4.2.2 The Magnetotail

The magnetotail, at the nightside of the Earth, consists of a northern and southern lobe separated by a central plasma sheet and the neutral sheet or current sheet, as shown in Figure 2.6. The magnetotail stores energy and plasma deposited in the magnetosphere from the interaction with the solar wind. The magnetic field in the lobe regions is considered to be *open* and connected to the solar wind. The foot points of the magnetotail lobes map down to the cusp regions and the polar caps in the north and south poles in the ionosphere. The central plasma sheet is a hot plasma population that maps down to the auroral oval, where plasma particles from the nightside plasma sheet precipitate into the ionosphere near the poles. This is discussed further in Section 2.6 and 2.7. The current sheet separates the plasma populations and oppositely directed magnetic field in the northern and southern lobe regions. Magnetic reconnection can occur in the neutral sheet which acts to remove some of the stored energy and plasma in the magnetotail.

2.5 Magnetospheric Dynamics

2.5.1 Magnetic Reconnection

Due to the frozen-in theorem introduced in Section 2.2, to a first approximation the two plasma populations originating from the solar wind and the Earth's magnetosphere are prohibited from mixing at the dayside magnetopause where the two magnetic field regimes meet. On small length scales, such as the thin magnetopause current sheet, the frozen-in flux theorem breaks down allowing the plasma particles to move independently of the magnetic field. The magnetic Reynold's number approaches unity as both diffusion and convection processes are important. On these small length scales, magnetic field lines can diffuse into the narrow current sheet where the magnetic field lines from the two regimes can undergo magnetic reconnection. In the diffusion region, the frozen-in theorem breaks down because plasma particles become *unmagnetised* (Nakamura et al., 2006). The size of the larger, ion diffusion region is comparable to the ion gyro-radius scale. As the magnetic field regimes diffuse into this region, the ions become unmagnetised but the electrons, with smaller gyro-radii continue to convect into the smaller, electron diffusion region where the electrons then become unmagnetised (Nakamura et al., 2006). Figure 2.8 shows a cartoon illustrating x-line reconnection and the relative sizes of the ion and electron diffusion regions. In the diffusion region, the magnetic field lines then *break* and reconnect with one of the magnetic field lines from the other regime (Paschmann, 2008). After reconnection, the two resulting magnetic field lines are strongly kinked. Magnetic tension acts to straighten out the kinks in the magnetic field lines and the magnetic field lines exit the diffusion region perpendicular to the direction in which they entered (Paschmann, 2008), as indicated by the outflow regions in Figure 2.8. The two plasma populations which were associated with each magnetic field regime now co-exist on the new magnetic field line and are essentially mixed. Reconnection allows the exchange of energy, mass and momentum between different plasma populations (Paschmann, 2008).

Magnetic reconnection is most efficient between oppositely directed magnetic field components. During reconnection between the IMF in the solar wind and the

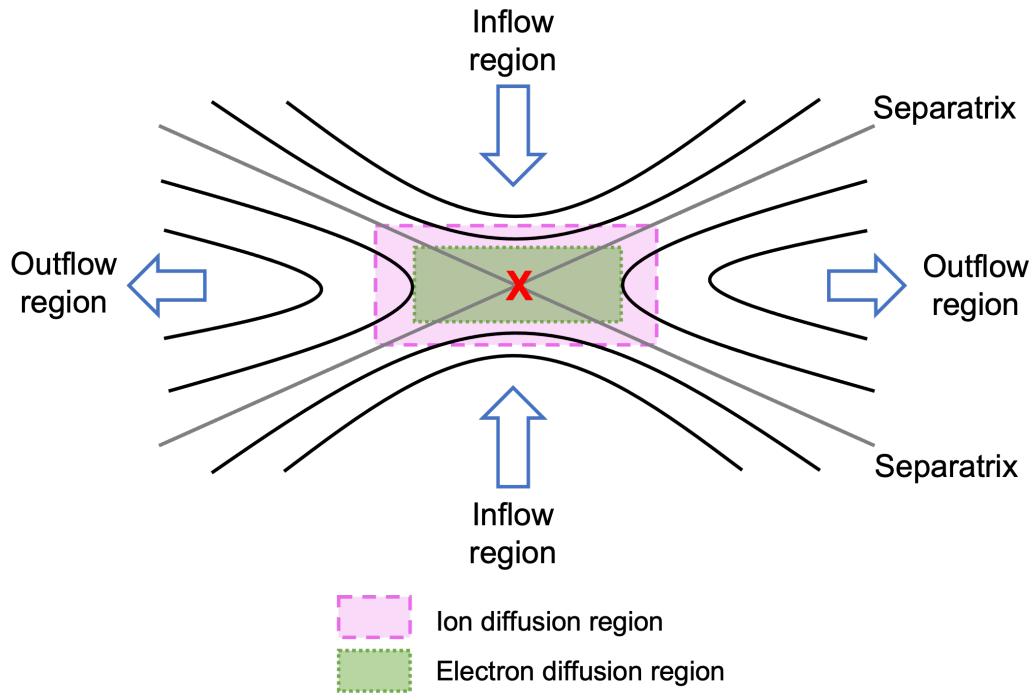

Figure 2.8: An illustration of magnetic reconnection between two magnetic field regimes. The black solid lines indicated magnetic field lines. The grey solid lines indicate the separatrices between different magnetic field regimes. The larger pink box indicates the ion diffusion region and the smaller green box indicates the electron diffusion region. The red X in the centre indicates where the magnetic field lines break and reconnect with field lines from the other magnetic field regime. The newly reconnected field lines then exit, perpendicular to the direction of inflow. The blue arrows indicate the perpendicular inflow and outflow of the magnetic field lines.

Earth's magnetosphere, the most important component of the IMF is the B_z component. A negative B_z component of the IMF is anti-parallel to the geomagnetic field. Reconnection with southward oriented (negative B_z component) occurs at the subsolar point on the dayside magnetosphere. Under northward IMF conditions, reconnection can occur in the lobe regions of the magnetosphere where the magnetospheric field lines have a large anti-parallel component with the northward IMF (Russell, 1972; Song and Russell, 1992).

2.5.2 Magnetosphere-Ionosphere Coupling: The Dungey Cycle

The Dungey Cycle, proposed by Dungey (1961), describes the interaction between the Earth's magnetosphere and the interplanetary magnetic field frozen-in to the solar wind. An illustration of the Dungey Cycle is shown in Figure 2.9. During re-

connection with southward IMF at the dayside magnetosphere, terrestrial magnetic field lines are *opened* to the solar wind such that the newly opened magnetic field lines have one foot point connected down in the ionosphere, in the polar cap and the other end point is connected out in the solar wind. The opening of magnetic field lines increases the open magnetic flux content of the magnetosphere and allows the solar wind plasma into the magnetosphere. From Faraday's law in Equation 2.16, a time varying magnetic field is related to a rotational electric field. The motion of the magnetic field in response to solar wind driving has a corresponding electric field, known as the convection electric field that is superimposed on the co-rotation electric field. In the ionosphere, the convection electric field sets up in a twin-vortex flow of plasma. The open end of the magnetic field line that is still connected out in the solar wind is dragged anti-sunward by the solar wind electric field past the Earth and into the magnetotail lobe regions. The addition of open flux to the magnetotail lobes increases the magnetic pressure in the lobe regions, compressing the magnetic field at the nightside current sheet where a reconnection x-line can form. Reconnection in the nightside current sheet occurs between the anti-parallel fields of the northern and southern lobes and results in the closure of the open field lines in the magnetotail, reducing the open flux content of the magnetosphere. The newly closed magnetic field line dipolarises and moves towards the Earth. From there, the newly closed field lines are convected sunward by the convection electric field completing the convection pattern in the ionosphere and restoring the structure of the dayside magnetosphere for the cycle to continue. A strong or prolonged period of southward IMF can erode the closed field lines, compressing the dayside magnetosphere towards Earth (Aubry et al., 1970; Russell, 1972; McPherron et al., 1973) and can build up a significant amount of magnetic energy and pressure which is stored in the magnetotail.

The magnetospheric convection electric field is superimposed on the co-rotation electric field which dominates in the inner magnetosphere. In the outer magnetosphere, the convection electric field dominates particle motions. This is significant for particle trajectories injected towards Earth from the magnetotail. Ini-

tially their particle motions are determined by the convection electric field but as the particles come closer to the inner magnetosphere, the particles begin to co-rotate with the Earth.

2.5.2.1 The Dynamics of the Auroral Oval

The aurora forms a ring of emission around both the northern and southern magnetic poles, known as the auroral oval. The poleward boundary of the auroral oval is approximately co-located with, although not directly equivalent to, the open-closed field line boundary (OCB) where the magnetic field lines transition from being closed equatorward of this boundary and *open*, i.e. connected to the solar wind, poleward of this boundary. The polar cap, encircled by the OCB, is the region where the footpoints of the open magnetic field lines of the cusp and magnetotail lobe regions connect to the ionosphere. The dynamics of the polar cap are dominated by the ionospheric convection pattern which occurs as a consequence of the Dungey Cycle. The area of the polar cap can be used as a measure of the magnetospheric open flux content which is an indicator of how much energy imparted from the solar wind is being stored in the magnetosphere.

In the ionosphere, the flux content of the polar caps, F_{PC}, varies due to imbalances in the rates of dayside and nightside reconnection (Siscoe and Huang, 1985; Cowley and Lockwood, 1992; Milan et al., 2007; Walach et al., 2017), as defined in Equation 2.29 where $\Phi_D(t)$ and $\Phi_N(t)$ are the rates of dayside and nightside reconnection, respectively.

$$\frac{dF_{PC}(t)}{dt} = \Phi_D(t) - \Phi_N(t) \tag{2.29}$$

As the open flux content of the magnetosphere increases in response to dayside reconnection, magnetic flux is distributed around the polar cap by excited plasma flows via polar cap convection (Cowley and Lockwood, 1992) and the polar cap and OCB expand to lower latitudes, towards the equator. A return convection flow is set up in response to nightside reconnection, redistributing the reduction in open flux. The decrease in the open flux content leads to a reduction in the polar cap

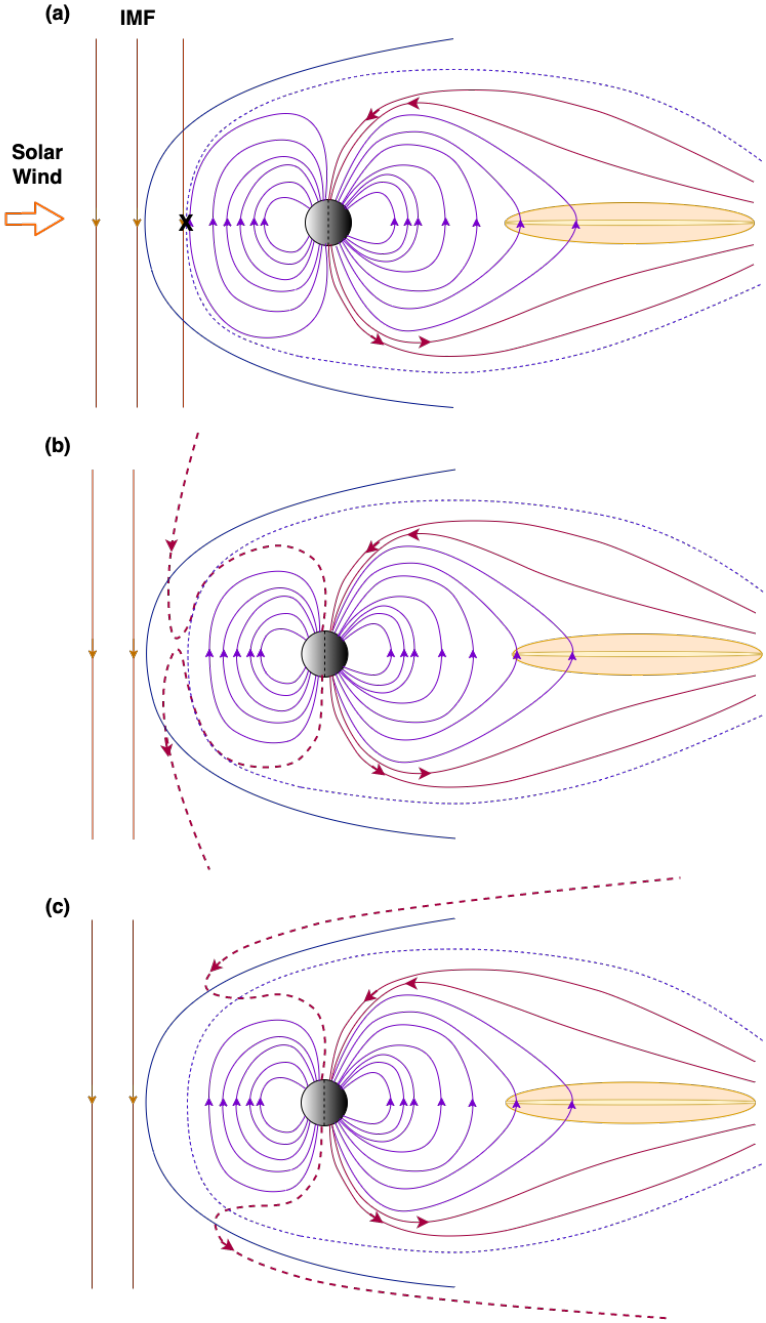

Figure 2.9: A schematic illustration of the Dungey Cycle. (a) Dayside reconnection occurs at the subsolar point during periods of southward directed IMF, indicated by the X. (b) Dayside reconnection results in the opening of previously closed magnetic field lines in the magnetosphere. (c) The newly opened magnetic field lines convect anti-sunward across the polar cap as the open ends of the field line are dragged past the Earth in the solar wind.

area and the OCB contracts towards the pole. The changing size of the polar cap in response to reconnection is known as the expanding and contracting polar cap

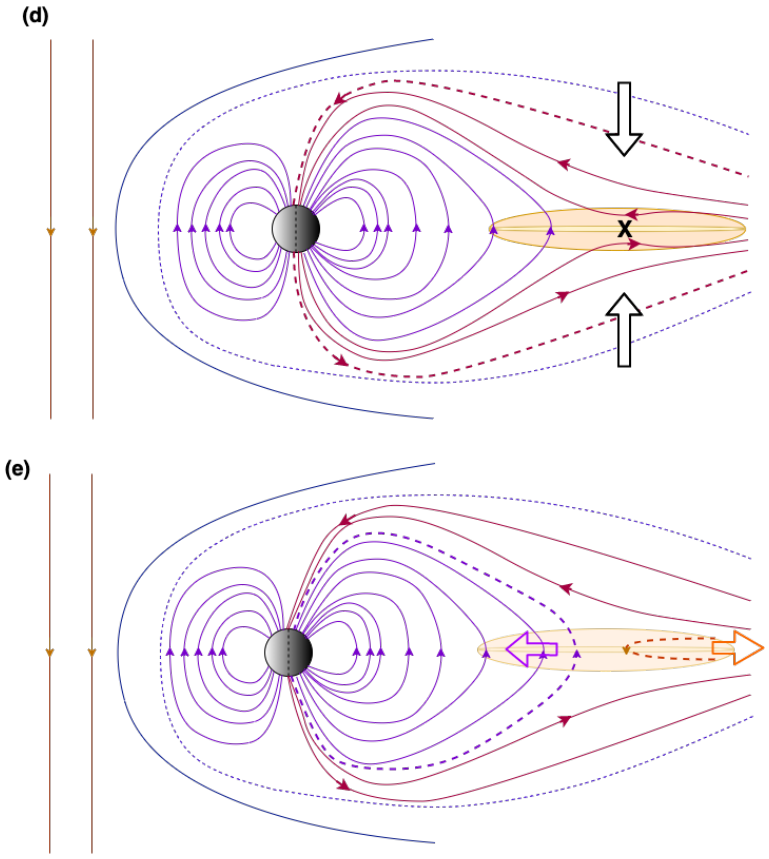

Figure 2.9: A schematic illustration of the Dungey Cycle [continued]. (d) The newly opened field lines are dragged into the magnetotail lobes where magnetic reconnection can occur in the nightside current sheet, indicated by the X. (e) After nightside reconnection, the newly closed field lines dipolarise and convect back towards Earth and a plasmoid is ejected down the magnetotail and out to the solar wind.

(ECPC) paradigm, proposed by Cowley and Lockwood (1992) and is a key concept in magnetospheric dynamics.

2.5.2.2 Substorms

If the open flux content of the polar cap is increasing as a result of dayside reconnection occurring faster than nightside reconnection, a large amount of open flux can accumulate in the polar cap. Without nightside reconnection closing and redistributing flux back round to the dayside magnetosphere at a fast enough rate, that open magnetic flux builds up in the magnetotail (McPherron et al., 1973). The magnetic energy built up in the tail can be explosively released via a large-scale reconfiguration of the magnetic field, known as a substorm.

Substorms have three distinct phases: growth, expansion and recovery (Akasofu, 1964; McPherron, 1970). The duration of a substorm is on the order of 3 hours, on average (Tanskanen, 2009; Forsyth et al., 2015) over which approximately 10^{15} J of energy stored in the magnetosphere is released (Tanskanen et al., 2002). During the growth phase, it is generally considered that the rate of dayside reconnection dominates over the rate of nightside reconnection. As a consequence, the open magnetic flux accumulates in the magnetosphere, which results in an increase of the polar cap area at ionospheric altitudes and an equatorward motion of the OCB (Milan et al., 2008; Boakes et al., 2011). The duration of the substorm growth phase has been observed to vary between less than 40 minutes to over an hour (Coumans et al., 2007; Forsyth et al., 2015).

The beginning of the substorm expansion phase is termed *substorm onset* and has traditionally been identified by a sudden brightening in one of the equatorward arcs in nightside auroral oval (Akasofu, 1964). At some time close to this onset, nightside reconnection begins on closed field lines in the inner magnetosphere. After 5 - 15 minutes reconnection progresses onto open field lines (Baker et al., 1996). At this point, if nightside reconnection dominates over dayside reconnection, it will result in the decrease of the open magnetic flux content (Boakes et al., 2011) and the poleward contraction of the OCB. The auroral oval in the substorm onset sector widens with the poleward contraction of the poleward auroral boundary and the OCB forming the auroral bulge. During the expansion phase, the auroral bulge is observed to expand eastward and westward, with the westward expansion observed to be faster, corresponding to the *westward travelling surge* (Kidd and Rostoker, 1991; Gjerloev et al., 2007). In the magnetotail, a large portion of closed magnetic field, called a plasmoid, is ejected from the distant magnetotail into the solar wind, during the expansion phase. The substorm expansion phase has an average duration on the order of 20 minutes (Chu et al., 2015; Forsyth et al., 2015).

The substorm recovery phase is often reported to be the relaxation of the magnetosphere to its initial, pre-substorm state but there are significant dynamics ongoing during this time (Opgenoorth et al., 1994; Farr et al., 2010). The substorm re-

covery phase has a duration of 30-40 minutes on average, (Chu et al., 2015; Forsyth et al., 2015) but it can last longer. During the recovery phase, although the open flux content is expected to continue to decrease to a quiescent level, the morphology of the auroral oval can change between the expansion and recovery phases, with the morning sector aurora brightening during the recovery phase, while the evening sector aurora continues to decay (Opgenoorth et al., 1994).

The *typical* substorm generally follows the growth-expansion-recovery pattern and is termed an *isolated substorm*, however a second substorm onset can occur during the expansion phase, before the magnetosphere has fully recovered from the initial substorm onset. If the upstream IMF conditions are favourable, the magnetosphere can return to a growth phase after the expansion phase (Forsyth et al., 2015; Milan et al., 2021). Alternatively, the magnetosphere may also enter a driven state of steady magnetospheric convection between the substorm expansion and recovery states where the rates of dayside and nightside reconnection are approximately equal and there is no net change in the open flux content of the magnetosphere (Kissinger et al., 2011; Walach and Milan, 2015; Walach et al., 2017; Milan et al., 2021).

The triggering of the substorm expansion phase onset is not fully understood. The two main competing frameworks for substorm onset are the Near-Earth Neutral Line (NENL) model and the Current Disruption (CD) model. The significant difference between the two models is the order in which tail reconnection and disruption of the cross-tail magnetospheric current occur. It may be the case that both methods are capable of triggering a substorm expansion phase (Lopez, 2000; Murphy et al., 2014). The work presented in this thesis is largely concerned with the auroral boundaries and their associated motion during substorms and so the exact onset mechanism is peripheral to the discussion and only included for completeness.

Substorms have a global impact on the magnetosphere. During the expansion phase, high energy particles from the magnetotail are injected into the inner magnetosphere. Substorms also energise the radiation belt and the ring current particle populations (Forsyth et al., 2015; Sandhu et al., 2018; Forsyth et al., 2020b) and

the intense auroral activity and associated ionospheric currents can induce ground currents which pose a significant space weather risk to ground-based infrastructure (Freeman et al., 2019).

2.6 Auroral Precipitation

This section discusses the physical processes that produce the auroral emission in more detail, including the mechanisms that accelerate and scatter particles into the ionosphere and produce either discrete or diffuse auroral emission.

Particles which precipitate into the ionosphere due to scattering processes in the magnetosphere produce diffuse and unstructured aurora. Electrons and ions can also be accelerated into the ionosphere, producing either broadband or discrete aurora, depending on the acceleration mechanism. Newell et al. (2009) categorised 11 years of particle precipitation profiles measured by the polar orbiting Defence and Meteorological Satellite Programme (DMSP) satellites between 1 January 1988 through 31 December 1998 into monoenergetic, broadband, diffuse and ion aurora, based on the signatures observed in the precipitating energy flux observations. The ion aurora was not subdivided into different categories by Newell et al. (2009) based on whether the energy flux profiles were diffuse or discrete aurora.

One source of aurora is electrons which are accelerated downwards into the ionosphere by quasi-static electric fields aligned with the magnetic field. This method of acceleration results in electrons being accelerated to a narrow range of energies and is referred to as *monoenergetic* precipitation. The resulting aurora from the accelerated precipitating electrons forms discrete auroral arcs, which produce a signature *inverted V* structure in spectrograms. An example spectrogram of an inverted V observed by DMSP is shown in Figure 2.10a. Ions can also be accelerated downwards into the ionosphere by field-aligned quasi-static electric fields which produce black filament structures in the aurora (Marklund et al., 2011). The broadband aurora results from electrons which are accelerated by dispersive Alfvén waves (e.g. Chaston et al., 2003; Watt and Rankin, 2010) resulting in the electrons being accelerated to a broadband range of energies, as shown in Figure 2.10b.

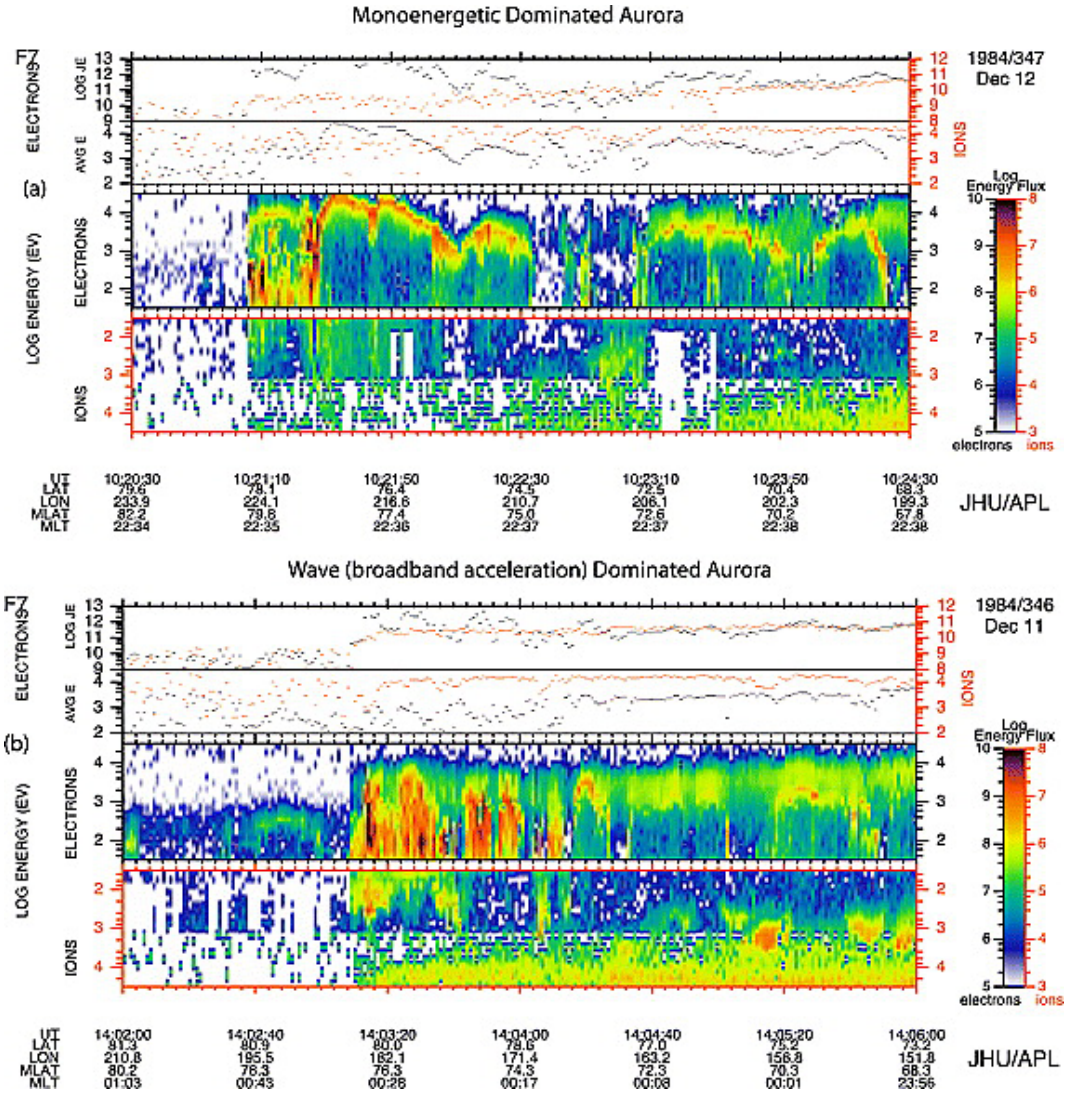

Figure 2.10: Figure from Newell et al. (2009). '(a) A spectrogram of DMSP F7 particle data showing a monoenergetic aurora dominated crossings of the nightside oval. (b) An example in which broadband acceleration is dominant.'

The diffuse electron precipitation category was used to capture all other electron precipitation that was not identified as being accelerated monoenergetic or broadband aurora. The diffuse electron category hides a lot of the underlying physics behind the particle precipitation mechanisms. Unsurprisingly, due to the catch-all nature of this category, Newell et al. (2009) found that the majority of precipitating energy flux spectra were categorised as diffuse aurora which contributes $\sim 71 - 84\%$ of the total energy flux from particles precipitating into the ionosphere.

The precipitating ions are pitch angle scattered into the atmosphere when the ion gyroradius is on the order of the radius of curvature of the magnetic field. On the nightside, the ions are pitch angle scattered as they cross the magnetotail current sheet (Sergeev et al., 1983). On the dayside, ions are pitch angle scattered at the magnetopause and magnetosheath boundary layers, leading to the dayside cusp emission which will be discussed further in Section 2.7.2.

Categorising the particle precipitation profiles by location illustrates the physical processes that cause particles to precipitate into the ionosphere and contribute to the auroral emission on average, in each latitudinal and local time sector of the auroral oval and provides information about the source regions of the precipitating particles. Newell et al. (2009) also looked at the contribution of energy and number flux of each category of particle precipitation under low and high periods of solar wind driving of the magnetosphere to analyse which types of auroral processes lead to more or less significant contributions to the auroral flux under different conditions. The energy flux contribution from each category of particle precipitation increased by a factor of at least 2 between low and high solar wind driving. The contribution of broadband aurora to the overall energy flux was found to increase by a factor of 8 between low and high solar wind driving conditions. Based on these average particles precipitation maps, Newell et al. (2009) developed the OVATION-Prime auroral oval model which will be discussed in more detail in Sections 3.1.2 and Chapter 5. The categories defined by Newell et al. (2009) are limited and hide some of the underlying physics such as ion acceleration processes and physical processes that result in the diffuse auroral emission. Another limitation of this study is that the DMSP Special Sensor J (SSJ) instrument has an upper limit of 30 keV and so precipitating particles which have energies greater than this limit are not captured, although Newell et al. (2009) extrapolated the diffuse and ion spectra assuming a Maxwellian distribution for the energy flux profile to try to account for this.

2.7 Auroral Morphology

As previously discussed, the auroral oval forms a ring of emission around the magnetic poles in both hemispheres. The term auroral oval is often used to refer to a narrow band of discrete, structured auroral emission which sits within a wider band of diffuse aurora, covering a broader range of latitudes. However, this broader band of diffuse aurora is also referred to as the auroral oval. In this thesis, the term auroral oval refers to the broad oval of diffuse auroral emission. Similarly, the auroral boundaries are the poleward and equatorward limits of the diffuse auroral emission.

2.7.1 The Nightside Aurora

Morphological mapping links various types of auroral emission observed in different local time and latitudinal regions of the auroral oval to the source regions of the magnetosphere that are thought to be responsible for the auroral emission. Morphological mapping uses natural tracers which are characteristic properties or features of the plasma that are largely retained regardless of the altitude the observation is made, such that the source region of the plasma can be approximately identified. Morphological mapping is expected to be valid for slowly varying magnetospheric conditions.

Combining the results of many studies, Feldstein and Galperin (1985) presented a generalised morphology of the auroral emission and the respective magnetospheric source regions of the precipitating particles. A schematic illustration of the auroral oval emission is shown in Figures 2.11a and 2.11b during low and disturbed geomagnetic activity levels, respectively, adapted from Figure 24a in Feldstein and Galperin (1985). The level of geomagnetic activity is defined by Kp. At very high latitudes over the pole, the polar cap is largely void of any auroral emission with some very weak emission, known as polar rain observed. The darker blue band in both Figures 2.11a and 2.11b illustrates the band of diffuse and structured (discrete) aurora and the broader dotted band which extends both poleward and equatorward of the discrete aurora represents the diffuse aurora. In Figure 2.11b during higher levels of geomagnetic activity some low latitude aurora is observed in the midnight to dawn sectors which is thought to be caused by particles precipi-

tating from the plasmasphere after substorm activity (Feldstein and Galperin, 1985). During low periods of geomagnetic activity, in the poleward diffuse aurora, auroral structures such as sunward aligned polar arcs can also be observed (Feldstein and Galperin, 1985).

Figures 2.11c and 2.11d show the source regions of the precipitating particles which are responsible for causing the auroral emission in each region of the ionospheric auroral oval illustrated in Figures 2.11a and 2.11b. Figure 2.11e illustrates the source regions in the magnetotail which are colour coded to match the ionospheric projections in Figures 2.11c and 2.11d. In general, particles precipitating to higher latitudes in the ionosphere tend to originate from sources further down the magnetotail, whereas particles precipitating at lower latitudes originate from magnetic field regimes closer to the Earth. As previously mentioned, the polar cap does not have a significant amount of auroral flux and is thought to map to the magnetotail lobes. The diffuse aurora poleward of the discrete emission band is thought to be mapped to the high latitude plasma sheet (also called the plasma sheet boundary layer) (Feldstein and Galperin, 1985; Galperin and Feldstein, 1996) which is indicated by the dark pink in Figures 2.11c and 2.11d. The band of discrete and structured aurora indicated by dark blue in Figures 2.11a and 2.11b originates from the low latitude or central plasma sheet which is closer to Earth than the high latitude boundary layer, indicated by the light pink region in Figures 2.11c and 2.11d. The equatorward edge of the discrete aurora is thought to map to the region of the tail where the magnetic field lines in the magnetotail transition from being dipolar to more stretched. This region of the magnetotail is also linked to the stable trapping boundary where the magnetospheric particle pitch angle distributions transition from being isotropic on dipolar field lines to a loss cone on more stretched magnetic field lines. The lower latitude diffuse auroral emission in the duskward and dawnward local time sectors is thought to originate from different source regions in the inner magnetosphere, as indicated by the two shades of light blue in Figures 2.11c and 2.11d. In the dawn sectors, the precipitating particles are thought to originate from the outer radiation belt. Wave-particle interactions play a significant role in

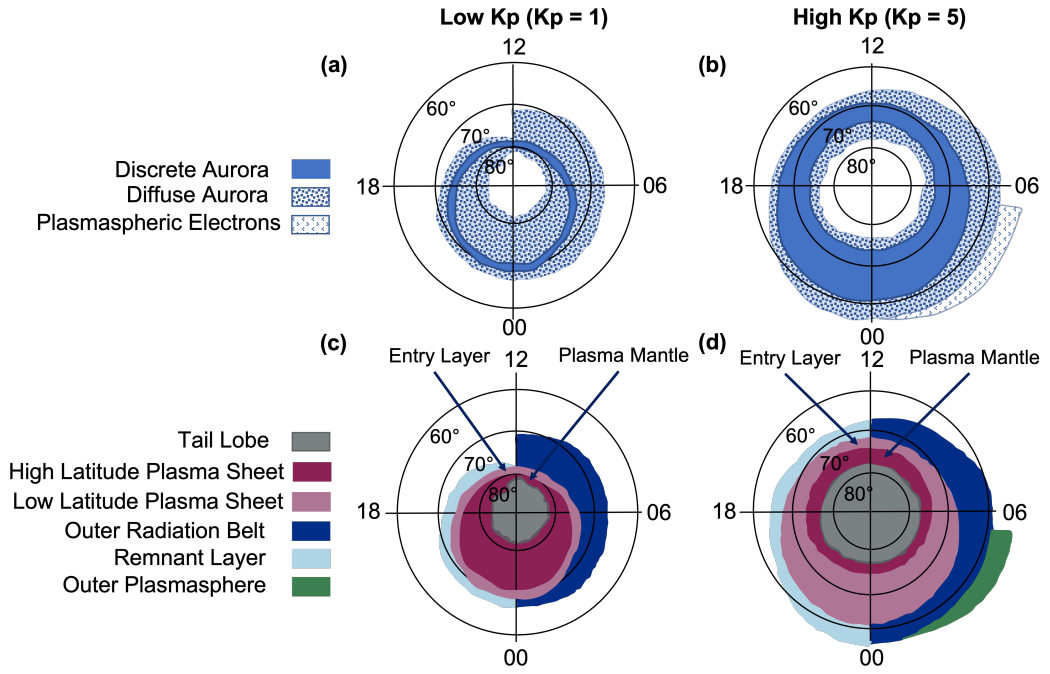

Figure 2.11: Figure adapted from Feldstein and Galperin (1985) showing the magnetospheric source regions of auroral precipitation in different regions of the ionosphere.

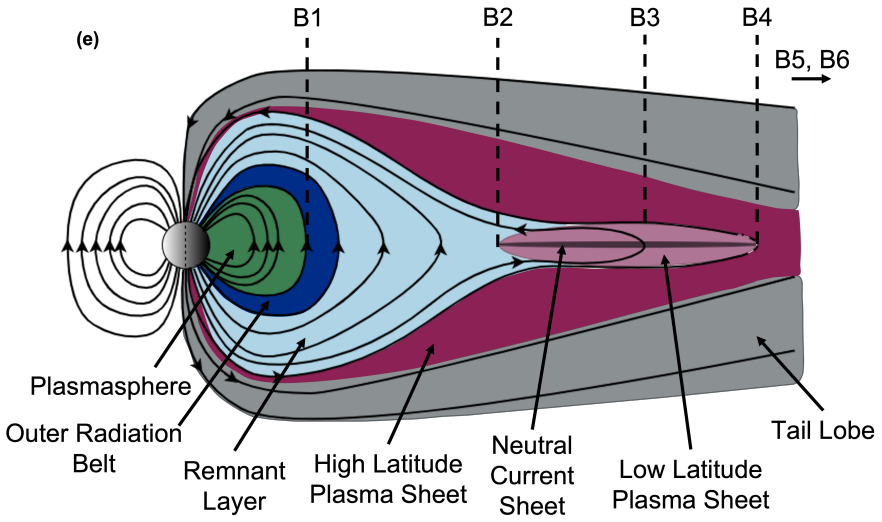

Figure 2.11: A schematic illustration of the magnetotail source regions of precipitating particles and the approximate magnetotail locations that link to the auroral boundaries defined by Newell et al. (1996). The colours in each region match the colours in the ionospheric projections shown in panels c and d.

the loss of particles from the outer radiation belt. In the dawn sector regions, outer radiation belt particles could be scattered into the atmosphere by wave-particle interactions such as chorus waves. This will be discussed in further detail in Section

3.2.3. During more disturbed periods of geomagnetic activity, a low latitude band of emission is observed in the post-midnight to dawn sectors which is thought to originate from the outer plasmasphere as a result of substorm activity (Feldstein and Galperin, 1985). In the dusk sectors, the lower latitude diffuse emission is thought to originate from the remnant layer. The remnant layer is a region of the magnetotail between the plasmapause and the nightside plasma sheet which can exist depending on the time history of the magnetotail. If the convection rate in the magnetosphere has been high, the convection dominated region of the magnetotail moves in closer to Earth, bringing hot plasma inwards which precipitates into the ionosphere. As the convection weakens, the convection dominated plasma sheet retreats further down tail and the depleted magnetic flux tubes begin to refill in the remnant layer between the old and new convection boundaries, resulting in this transition region. Figures 2.11c and 2.11d also indicate the entry layer and plasma mantle as source regions of dayside auroral precipitation. The dayside aurora is discussed in more detail in the following section.

Newell et al. (1996) used in-situ particle precipitation low-altitude measurements from DMSP to define a series of observed boundaries in the auroral emission which indicate transitions in the auroral structure, for example between structured and unstructured aurora. Newell et al. (1996) linked some of the boundaries to transitions between different regions of the magnetosphere which largely agree with the general source regions described by Feldstein and Galperin (1985); Galperin and Feldstein (1996). The magnetotail regions which correspond to the Newell et al. (1996) boundaries are indicated in Figure 2.11e.

The B1 boundary is the equatorward boundary of the auroral emission. In the magnetosphere, the B1 boundary is thought to correspond to the zero-energy particle drift orbit where the particle motions are co-rotation dominated. Theoretically, this boundary coincides with the plasmapause location where the particle motions inside the plasmasphere are co-rotation dominated and outside the plasmapause are convection-dominated. The B1 boundary corresponds with the equatorward edge of the diffuse aurora in Figure 2.11 which was thought to map to the remnant layer be-

tween the plasmapause and the nightside plasma sheet in the dusk sectors (Feldstein and Galperin, 1985; Galperin and Feldstein, 1996). The B2 boundaries correspond to the highest precipitating particle average energy flux. The highest average energy electron flux is associated with the Earthward edge of the main plasma sheet while the highest average energy flux is associated with the Earthward edge of the central plasma sheet. The B3a and B3b identify the most poleward and most equatorward mono-energetic auroral peaks respectively, corresponding to the most poleward and equatorward locations of electron acceleration. The B2 and B3 boundaries defined by Newell et al. (1996) are similar to the boundaries of the discrete auroral emission described by Feldstein and Galperin (1985); Galperin and Feldstein (1996) and map to similar magnetospheric source regions as suggested by Feldstein and Galperin (1985); Galperin and Feldstein (1996). The B4 boundary distinguishes the transition between unstructured and structured aurora on spatial scales of $\geq 5-10$ km which was proposed to map to the boundary between the lower latitude central plasma sheet (unstructured auroral emission) and the higher latitude boundary plasma sheet (structured auroral emission). The B5 boundary identifies the poleward boundary of the main auroral emission where the auroral flux decreases significantly over a short distance (by an order of magnitude over a spatial scale of $\sim 0.2^{\circ}$). The B6 boundary is the poleward boundary of the sub-visual drizzle which is poleward of the main auroral emission boundary (B5) but the emission is distinctly different from polar rain. Although not explicitly defined by Newell et al. (1996), both the B5 and B6 boundaries have been approximated to be the ionospheric footpoint of the the open-closed field line boundary (e.g. Newell et al., 2002; Hubert et al., 2006). Given the close association with the open-closed field line boundary, the sub-visual drizzle observed poleward of the B5 main auroral boundary may result from particles precipitating on newly closed field lines which are reconnecting in the distant magnetotail. A similar diffuse emission poleward of the discrete auroral oval is also illustrated in Figure 2.11 from Feldstein and Galperin (1985) which was expected to map to the high latitude boundary plasma sheet. The boundary definitions and their respective boundary in the magnetosphere are summarised in

Table 2.1. Crossing the auroral oval from low to high latitudes, the boundaries were labeled B1 to B6 where B1 is the most equatorward boundary and B6 is the most poleward boundary of the auroral emission. Although the B1 and B6 boundaries are the furthest poleward and equatorward boundaries, the B2 - B4 boundaries are not strictly found at increasingly higher latitudes, for example, the B3 boundary may be located poleward of the B4 boundary. In addition, not all boundaries were identified in every DMSP spacecraft pass over the auroral oval. Many of the boundaries were sub-divided to identify the equivalent boundaries in both the electron and ion data. Overall, the boundaries determined from in-situ particle observations by Newell et al. (1996) largely agree with the morphological mapping from Feldstein and Galperin (1985).

As mentioned previously, morphological mapping is valid for slowly varying magnetospheric conditions however, the magnetosphere is highly dynamic and is constantly responding to the interaction with solar wind and internal drivers such as substorms. Morphological mapping provides a general guide of the main sources of particles which precipitate into the auroral oval. The formation of the remnant layer is a good example that the time history of the magnetosphere is significant to the source regions of auroral precipitation. Similarly, some weak auroral emission that is not polar rain is observed poleward of the diffuse edge of the auroral oval which maps near the open-closed field line boundary. The weak poleward auroral emission may be due to particles precipitating on newly closed field lines as it takes time for the information that the field line has reconnected downtail to be communicated along the length of the field line.

One interesting question that arises from the morphological mapping is, why is there a sharp equatorward boundary in the auroral emission, below which the auroral precipitation does not occur at lower latitudes? In the inner magnetosphere, the plasmasphere contains a population of cold plasma. These particles would not have enough energy to excite auroral emission if they precipitated into the ionosphere, however the plasmaspheric population is co-located with the ring current and radiation belt particles which are much more energetic and can excite auroral emission

when they precipitate. This equatorward auroral boundary and its associated dynamics will be explored further in Chapter 3.

2.7.2 The Dayside Aurora

Newell and Meng (1992) identified the source regions of particles precipitating into the dayside auroral emission by studying the properties of precipitating particles measured at low altitude by DMSP. Newell and Meng (1992) identified three distinct auroral particle populations at high latitudes on the dayside, between $\sim 75 - 80^{\circ}$ and between 08 - 16 MLT, centred on the noon sector on average; the cusp, mantle and low latitude boundary layer (LLBL). Figure 2.12 shows a schematic of the average locations in the ionosphere of each of these precipitating particle populations, adapted from Figure 2 of Newell and Meng (1992).

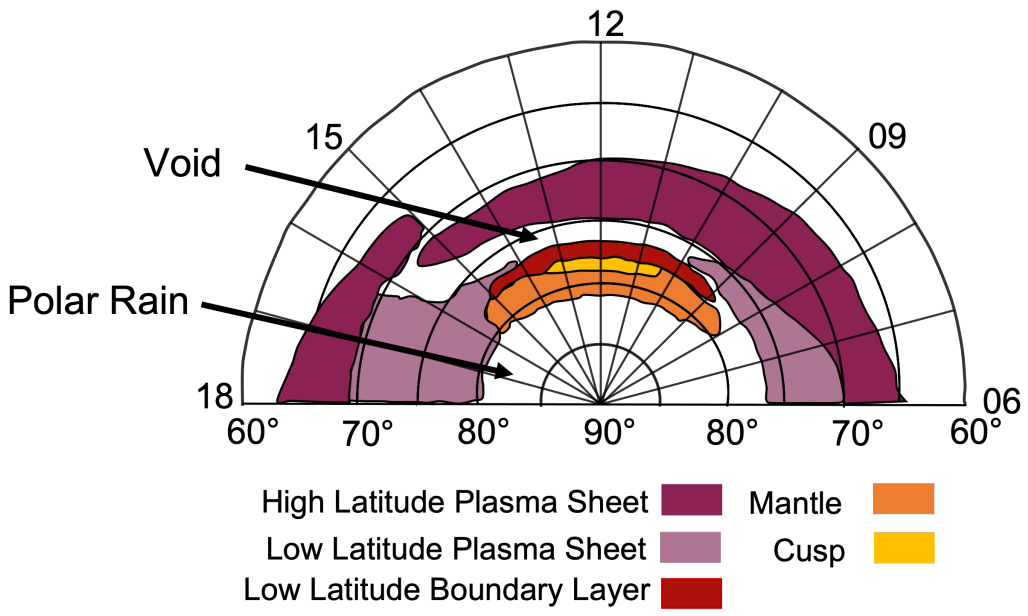

Figure 2.12: Illustration of the source regions of particles precipitating into the dayside ionosphere and contributing to the auroral emission, adapted from Newell and Meng (1992).

The highest latitude mantle population is observed just poleward of the main dayside auroral oval. The mantle particle population has the lowest ion energy of no more than a few hundred eV (Newell et al., 1991a). The field lines associated with the mantle precipitation are generally found to be convecting anti-sunward.

Table 2.1: A summary of the auroral boundary identifications and their respective boundary in the magnetosphere, as defined by Newell et al. (1996).

Boundary Label	Boundary Definition	Magnetospheric Boundary
B6	The poleward boundary of the weak subvisual drizzle, poleward of the main auroral emission boundary.	
B5	B5e, B5i, Poleward boundary of the main auroral oval where the electron and ion precipitation flux decreases sharply, respectively.	
B4	Boundary between structured and unstructured electron precipitation on spatial scales of $\geq$ 5 - 10 km.	May represent boundary between the boundary plasma sheet and the central plasma sheet.
B3	B3a, B3b most equatorward and most poleward mono-energetic auroral peak, respectively.	Furthest poleward and equatorward electron acceleration sites.
B2	B2e, B2i maximum average energy of the precipitating electrons and ions, respectively.	B2e Earthward edge of the main plasma sheet B2i Earthward edge of central plasma sheet
B1	B1e, B1i equatorward boundary in the auroral emission identified from electron and ion data, respectively.	The zero-energy particle drift orbit in the magnetosphere, often coinciding with the plasmapause

At slightly lower latitudes, covering a narrower range in local time between 10 - 13 MLT, is the cusp aurora (Newell et al., 1991b; Newell and Meng, 1992). The cusp particle population is assumed to have direct entry into the magnetosheath with very high fluxes but low average energies of $<$ 200 eV.

Below the cusp aurora, at lower latitudes, Newell et al. (1991b) identified the LLBL population. The LLBL particle population is similar to the cusp plasma population; however, the plasma particles tend to be slightly hotter. The average energy of the LLBL particles is generally $<$ 400 eV. The LLBL population is also associated with field lines which are convecting anti-sunward, however near the equatorward edge of the LLBL aurora, the convection often decreases to zero or becomes erratic and potentially corresponds to a stagnation region where the sunward and anti-sunward flows act opposite to each other, effectively cancelling out any significant flow in this region.

The lower latitude emission between $\sim 60 - 80^{\circ}$ has been labelled the boundary plasma sheet (BPS) and central plasma sheet (CPS) emission by Newell and Meng (1992). The particles precipitating in these regions resemble nightside auroral precipitation and are thought to originate from magnetospheric sources in the magnetotail which drift around on sunward convecting magnetic field lines.

2.8 Summary

As discussed in this chapter, the dynamics of the auroral oval are driven by both the interaction with the upstream solar wind at the magnetopause and the internal substorm process. As previously mentioned, the trigger mechanism for the onset of the substorm expansion phase is not well understood and as such substorm onsets cannot yet be predicted in advance by auroral forecast models. The research presented in Chapter 6 of this thesis evaluates the performance of an auroral forecast model which is only driven by the solar wind and does not account for substorm activity.

Substorms are a crucial process with widespread impacts in all regions of the magnetosphere. One of the biggest impacts of substorms is the modulation of the

open flux content in the magnetosphere. Chapter 7 presents a detailed statistical analysis on the closure of flux during substorms and how the poleward boundary of the nightside auroral oval responds to the changes in the open flux content.

The charged particles which produce the aurora are known to precipitate into the ionosphere along closed magnetic field lines, however the auroral oval has a relatively sharp equatorward auroral boundary, below which there is very little to no auroral emission. Morphologically, the equatorward auroral boundary is expected to map to the plasmapause. The research presented in Chapter 8 uses a magnetospheric mapping model to compare the ionospheric projection of the observed plasmapause against the observed equatorward boundary of the auroral oval to determine whether the two boundaries are co-located, on average.

A better understanding of the auroral boundaries in the structure of the global magnetosphere and the auroral dynamics during active periods, such as substorms will help to improve future generations of auroral forecast models.

Chapter 3

Literature Review

The aurora is a manifestation of space weather which poses a threat to the aviation sector and ground-based infrastructure at Earth. This section describes the real-world impact of the energetic particles in the upper atmosphere and the ground-induced currents associated with enhanced auroral emission. Given the space weather risk, there is a large international effort to forecast the occurrence of aurora. A version of the OVATION-Prime 2013 auroral forecast model is used operationally in world-leading space weather forecast centres. The development and underlying data used in this model are discussed in this chapter and the performance of this model is then evaluated in Chapter 6 against global auroral image observations obtained from satellite data.

Understanding the externally and internally driven processes that control the auroral oval location in the context of the wider magnetosphere may provide a pathway to improvements in future generations of auroral forecasting models and potentially new uses of auroral data. The research presented in Chapters 7 and 8 explores the physical significance and dynamics of the poleward and equatorward auroral boundaries.

As discussed in Chapter 2, the poleward boundary of the auroral oval is closely associated with the open-closed field line boundary (OCB). The dynamics of the OCB and the poleward auroral boundary are highly dependent on the amount of open flux stored in the magnetosphere and the net rate at which open flux is being added by dayside reconnection, at the subsolar point, or closed by reconnection in

the magnetotail. Substorms play a significant role in the sudden closure of a large amount of open flux in the magnetosphere. The research in Chapter 7 presents a statistical analysis of the motion of the poleward auroral boundary, as a proxy for the OCB, to study the detailed changes in the flux content in each nightside local time sector during substorms. The content of this Chapter presents a brief overview of the auroral boundary data and discusses the results and discrepancies in previous studies which have analysed the dynamics of the OCB during substorms.

As suggested in Chapter 2, it is expected that morphologically, the equatorward boundary of the auroral oval maps to the plasmapause in the inner magnetosphere, at least in the nightside local time sectors. In this Chapter, the results from a number of studies which have used ground-based and in-situ data to show a strong association between the equatorward boundary of the auroral oval and the plasmapause are discussed. However, the data used in these studies have been limited in local time coverage and under limited geomagnetic conditions. The research presented in Chapter 8 presents a statistical analysis comparing the locations of the ionospheric projection of the plasmapause to the equatorward boundary of the auroral oval to evaluate whether the two boundaries are co-located on average and under what geomagnetic conditions the two boundaries correspond well with each other.

3.1 Forecasting the Aurora

3.1.1 The Aurora as a Space Weather Risk

The aurora poses a significant space weather risk to communication networks and ground-based infrastructure. High and ultra-high frequency (HF/UHF) radio communications used by aircraft for long-range communication and tracking are degraded by the free electrons and excited molecules in the ionosphere (Moore, 1951; Harang and Stroffregen, 1940; Jones et al., 2017; Cannon et al., 2013). The degradation in radio communication results from the absorption of HF radio signals in the ionosphere due to the increased electron precipitation (Greenberg and LaBelle, 2002; Jones et al., 2017). The societal impact of radio degradation due to high energy particles in the ionosphere was highlighted during the Earth-directed solar

storms and subsequent geomagnetic storms which occurred in September 2017 and coincided with the hurricane season, during which four hurricanes hit the Caribbean Islands (Redmon et al., 2018). During the space weather events, disruption to HF radio links were reported by the Caribbean emergency communication system operators. French Civil Aviation authorities also reported a loss of HF radio communication for 90 minutes (Redmon et al., 2018). While the HF radio disruption experienced in lower latitude regions such as the Caribbean was due to solar energetic particle events associated with coronal mass ejections and solar flares, similar impacts occur due to precipitating auroral particles in the high latitude polar regions. The degradation or loss of HF communications can lead to the diversion of polar flights which results in significant costs for the aviation sector (Schrijver et al., 2015).

In addition to the degradation of HF radio communications, the increased scattering of radio waves in the ionosphere also results in broadband noise in radio receivers (Benson and Desch, 1991; Jones et al., 2017) and spurious echoes in radar systems, known as radar clutter (Elkins, 1980; Jones et al., 2017) which can impact the defense and military sectors. This ionospheric scattering of HF and radar signals is a well known property of the ionosphere and can also be used to study space plasmas with large-scale radar observatories such as the Super Dual Auroral Radar Network (SuperDARN) (Greenwald et al., 1995).

The aurora is associated with enhanced ionospheric currents which can generate geomagnetically induced currents (GICs) (e.g. Erinmez et al., 2002; Cannon et al., 2013; Freeman et al., 2019; Smith et al., 2019). GICs are hazardous to ground-based infrastructure and can damage electricity supply networks by damaging infrastructure such as transformers and introducing voltage instabilities which can lead to power outages (Cannon et al., 2013; Eastwood et al., 2017) as during the space weather event on 13 March 1989 which caused widespread power outages in Québec, Canada (Boteler, 2019). GICs can also change the pipe-to-soil voltage along oil and gas pipelines which can lead to enhanced pipeline corrosion over time (Viljanen et al., 2006; Eastwood et al., 2017).

Given the risk of potentially severe damage and disruption to daily services caused by enhanced particle precipitation and currents, accurate forecasting of the occurrence and location of the aurora is necessary. Accurately forecasting the location of the aurora provides stakeholder industries with advanced warning of potentially hazardous space weather events, giving them time to take action to mitigate the risk of damage.

3.1.2 The OVATION-Prime 2013 Model

A number of empirical models have been developed to estimate the location of the aurora. Hardy et al. (1985) presented a statistical model of auroral particle precipitation under different levels of geomagnetic activity, defined by Kp. Similarly, Carbary (2005) developed a statistical model of the auroral boundaries with Kp, determined from averaged ultra-violet (UV) satellite observations of the auroral oval from the Polar spacecraft. More recently McGranaghan et al. (2021) have developed a new generation electron precipitation model using machine learning methods. However, currently both the UK Met Office and the US National Oceanic and Atmospheric Administration (NOAA) Space Weather Prediction Center (SWPC) use a version of the OVATION-Prime model (Newell et al., 2009).

The original Oval Variation, Assessment, Tracking, Intensity and Online Nowcasting (OVATION) auroral model was developed by Newell et al. (2002) and was based on auroral boundaries defined by Newell et al. (1996), observed in near real time from in-situ DMSP particle precipitation measurements. On the nightside, the B6 boundary was used as the poleward auroral boundary and to estimate the location of the open-closed field line boundary. The B1e boundary was generally used as the equatorward auroral boundary although sometimes the B2i boundary was used instead. The location of the dayside equatorward auroral boundary is determined where DMSP crosses into a region of auroral precipitation from a lower latitude region which is void of auroral precipitation. The precipitating auroral particles are thought to have originated from the nightside plasmasheet and drifted to the dayside (Newell et al., 1991b; Newell and Meng, 1992), illustrated in Figure 2.12. The poleward dayside auroral boundary was identified where DMSP crossed into a region

of open magnetic field lines identified from cusp, mantle or polar rain precipitation, as in Figure 2.12. The poleward and equatorward boundary shapes were taken from average boundary shapes determined from 12 years of DMSP data (Sotirelis and Newell, 2000). The observed DMSP auroral boundaries were then combined with various other datasets where available, including Polar UVI observations and meridian scanning photometer data from the University of Alaska. Optional model precipitation intensities could also be included from Sotirelis and Newell (2000). The OVATION model was designed to provide an instantaneous nowcast of the auroral oval location and prediction of the intensity of the auroral precipitation.

The OVATION-Prime (OP-2010, Newell et al., 2009) and the upgraded version, OVATION-Prime 2013 (OP-2013 Newell et al., 2014) models are solar wind driven auroral precipitation models developed to estimate the location and intensity of the auroral precipitation in near real time and to provide some level of forecasting capability of the aurora.

Newell et al. (2009) created averaged particle precipitation maps of the auroral oval collected by DMSP over a 21 year period between 1984-2005 to create global particle precipitation maps of the auroral oval and categorised the DMSP particle precipitation energy spectra into four categories of aurora: mono-energetic electron aurora, broadband electron aurora, diffuse electron aurora and ion aurora, as previously discussed in Section 2.6. These averaged global particle precipitation maps form the basis of the OP-2010 and OP-2013 auroral forecast models.

The OP-2010 and OP-2013 generations of the model are driven by an empirically derived solar wind - magnetosphere coupling function which estimates the solar wind driving of the magnetosphere based on the upstream solar wind conditions (Newell et al., 2007). A linear relationship between the solar wind driving and the precipitating auroral flux is assumed in each individual model bin, such that the auroral flux estimated in each model grid point increases linearly with increased driving of the magnetosphere by the solar wind as described by the coupling function.

The original OP-2010 and OP-2013 model code has been adapted for oper-

ational use by space weather forecast centres such as the UK Met Office Space Weather Operations Centre (MOSWOC) and the US National Oceanic and Atmospheric Administration (NOAA) Space Weather Prediction Center (SWPC). The research in this thesis uses a version of the OP-2013 auroral forecast model that was used operationally in daily space weather forecasts at the UK Met Office Space Weather Operations Centre until December 2020. This version of the model includes a conversion of the predicted auroral flux to probability of aurora occurring. A full and detailed description of the OP-2013 model is presented in Chapter 4. The conversion to probability is not fully documented in the literature and so it will be discussed in Chapter 4.

Newell et al. (2010b) explored the seasonal difference in the auroral precipitation. The largest seasonal difference was found to occur in the diffuse electron aurora in the nightside local time sectors which was found to be 30% higher in the winter hemisphere than in summer. Newell et al. (2010b) noted that the number fluxes of the particles which are responsible for producing the nightside diffuse electron aurora also increased in winter, however the enhancement in the number flux was smaller than the enhancement in the energy flux, implying that the average energy of the precipitating particles increases during winter. Newell et al. (2010b) suggested that local energisation processes occurring above the ionosphere which energise the particles more in winter may be responsible for the seasonal variations in the nightside diffuse electron aurora. On the dayside, the auroral fluxes were found to be higher in the summer hemisphere which is in part due to the tilt of the cusp, allowing ions more direct entry to precipitate into the ionosphere, and also due to the fact that the R1 currents are stronger on the dayside during summer (Fujii and Iijima, 1987), thus requiring greater auroral acceleration. Although there is some seasonal variation in the auroral precipitation, the variations in the auroral precipitation are dominated by the level of solar wind driving. The seasonal variations in each type of auroral precipitation were implemented in the OP-2013 model by calculating the predicted auroral flux as a function of season. Additional improvements to the model made in the upgrade from OP-2010 to OP-2013 include further

noise reduction and a smoother data interpolation in the post-midnight local time sectors (Newell et al., 2014). Figure 3.1 shows a comparison between the output from OP-2010 and OP-2013 for low, medium and high solar wind driving which illustrates upgrades made to the OP-2013 version including improved noise reduction and smoother interpolation in the local time sectors near midnight.

Using the upstream solar wind conditions as input to the auroral model means that the OP-2013 model can predict the location and intensity of the auroral oval with some forecast lead time, enabling its use in a space weather nowcasting or forecasting capacity. The forecast lead time depends on the propagation time of the solar wind between the L1 point where it is measured upstream and the arrival of the solar wind at the dayside of the magnetosphere. The propagation time depends on the velocity of the solar wind. As the OP-2013 model is externally driven by the upstream solar wind, the model is unable to resolve auroral dynamics which are driven by internal magnetospheric processes such as substorms.

To capture the contribution of precipitating particles from internal dynamics such as substorms, the OVATION-SuperMag (OVATION-SM) model was developed (Mitchell et al., 2013) which includes ground magnetometer data from the SuperMag stations. OVATION-SM uses the SuperMag Electrojet (SME) index and the substorm onset times determined from the SuperMag electrojet data in conjunction with DMSP particle precipitation data to calculate the auroral energy flux, using the time since the last substorm onset and the time until the next substorm onset as input parameters but does not use any upstream solar wind parameters as input data. The OVATION-SM model is able to capture the large-scale auroral morphology, including substorm onsets and auroral brightening and dimming events. The model also describes 70% of the nightside variance in the aurora when compared to global UV images obtained from satellites; however, the model did not accurately capture the dayside auroral dynamics. This suggests that the dayside auroral oval is well organised by the upstream solar wind conditions and solar wind driving of the magnetosphere, whereas the nightside dynamics are better described by the internal magnetospheric dynamics, such as substorms, highlighting the importance of

including both internal and external drivers in auroral forecast models. Given the dependence of the model on substorm onset times, the OVATION-SM model cannot currently be used in operational space weather forecasting until substorm onsets can be accurately predicted.

The work in this thesis aims to evaluate how well the solar wind driven OP-2013 model can accurately forecast the aurora and to better understand the magnetospheric processes that may reduce the performance of the model.

Previous verification studies have evaluated the performance of the OP-2010 version of the model (Newell et al., 2010a; Machol et al., 2012; Lane et al., 2015). Newell et al. (2010a) and Machol et al. (2012) evaluated the auroral forecasts of OP-2010 against data from the ultraviolet instrument (UVI) onboard the Polar satellite which captured UV images of the auroral oval. Newell et al. (2010a) compared the instantaneous and hourly averaged predicted auroral power to the observed power estimated from Polar UVI data. The auroral power predicted by OP-2010 correlated with the observed auroral power from Polar UVI with a correlation coefficient $r^2 = 56\%$ for the instantaneous power forecast and an $r^2 = 58\%$ for the hourly averaged auroral power, demonstrating that just over half of the observed auroral power can be forecast by the OP-2010 model. The verification of the predicted auroral power against observations provides no indication of how well the model predicts the location of the aurora. Machol et al. (2012) used truth table analysis to evaluate the forecasts from OP-2010 and the suitability of the model as a tool for forecasting visible nightside aurora. Machol et al. (2012) compared the nightside auroral forecast to the boundaries derived from a fixed brightness threshold of the nightside auroral emission in the Polar UVI data. From the truth table analysis, Machol et al. (2012) calculated a number of verification statistics which are commonly used in weather forecast evaluation. The truth table verification methodology and verification statistics are discussed in greater detail in Chapter 4. The result of this verification study found that the OP-2010 had a hit rate of 0.58 (the proportion of correct positive forecasts out of the total positive observations of aurora), a false alarm ratio of 0.14 (the proportion of aurora forecasts which were not observed) and an overall

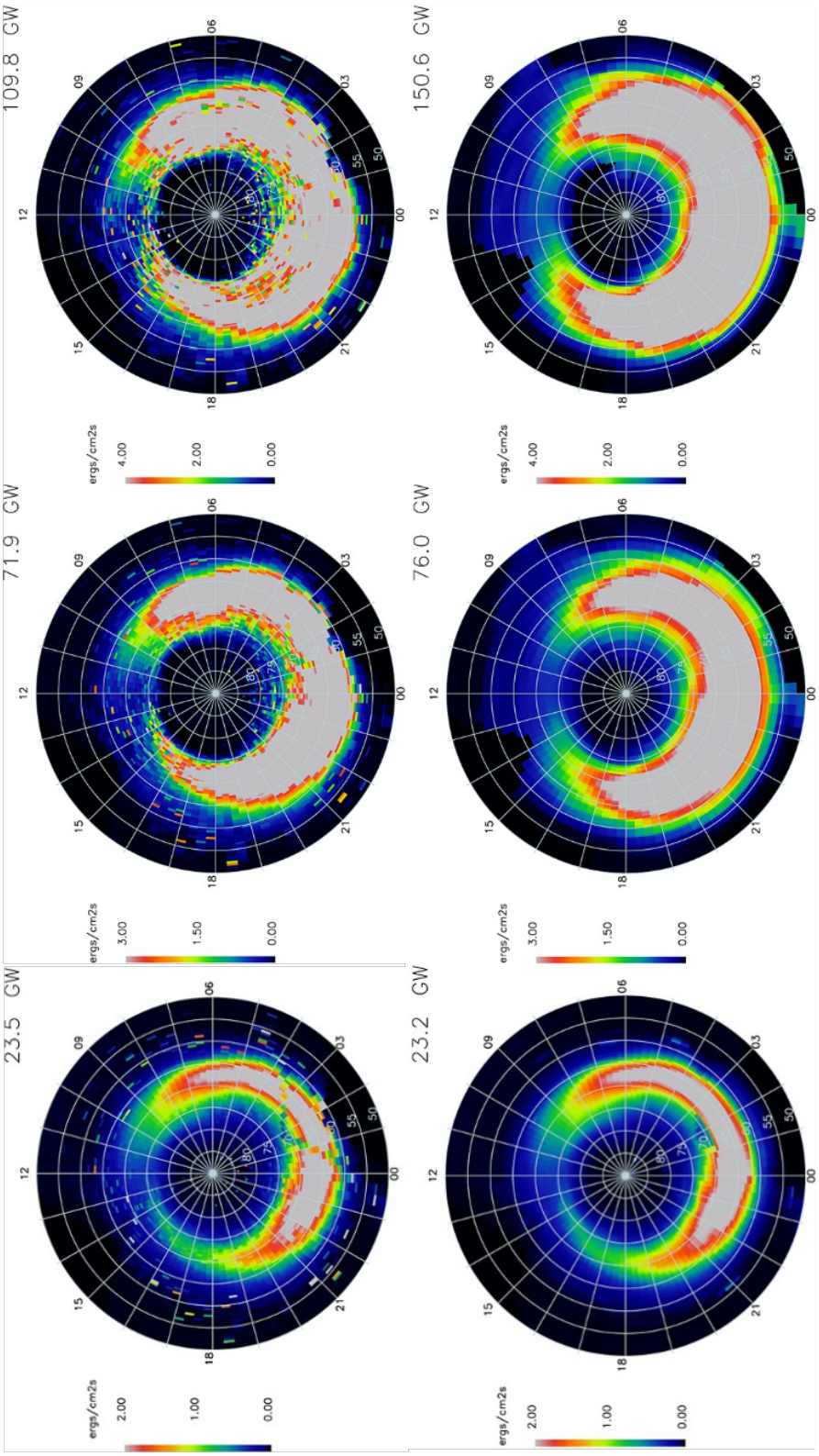

Figure 3.1: A comparison of the auroral forecasts produced by OP-2010 in the top row and OP-2013 in the lower row for low, medium and high solar wind driving from left to right, adapted from Newell et al. (2014).

accuracy of 0.86 (the proportion of correct positive and negative forecasts over the total number of forecasts). The verification analysis by Machol et al. (2012) shows that the model performs reasonably well compared to the observed aurora with a higher proportion of correct positive forecasts (hit rate) than the proportion of false positive forecasts (false alarm ratio). The overall accuracy of 0.86 is also reasonably high, with a maximum score of 1, however the accuracy statistic can be dominated by the number of correct negative forecasts in low latitude regions (i.e. forecasting that aurora will not occur and it does not occur). Lane et al. (2015) performed a comparison study of predicted location of the equatorward auroral boundary from 3 different models: OP-2010, the Kp-based auroral forecast model by Hardy et al. (1991), and a ring current model from the Space Weather Modeling Framework (Fok et al., 2001; Tóth et al., 2005) against the equatorward auroral boundary determined from particle precipitation measurements from the DMSP satellites. Similar to Machol et al. (2012), Lane et al. (2015) also used fixed energy flux thresholds to define the equatorward auroral boundary from each model and the observational DMSP data. The location of the predicted equatorward auroral boundary from the OP-2010 model is then compared against the observed auroral boundary location. The results of the comparison are presented in terms of the prediction efficiency, which is the model's ability to describe the percentage variance in the observed data set. The prediction efficiencies of OP-2010 were found to be 0.55 and 0.58 for the threshold values of 0.4 erg cm^{-2} s^{-1} and 0.6 erg cm^{-2} s^{-1}, respectively, showing that only 55 - 58% of the variance in the location of the observed equatorward boundary of the auroral oval can be reproduced by the model.

Although the studies of Newell et al. (2010a), Machol et al. (2012) and Lane et al. (2015) have evaluated the performance of the OP-2010 version of the model to some extent, the verification studies are limited. The study by Newell et al. (2010a) compares the forecast and observed auroral power which is a derived product of the observations and models. While this has been used by Newell et al. (2010a) to compare the results from 4 different models, the prediction of the hemispheric auroral power is not of significant interest to end users of the auroral forecast model.

End users of the model need to know how well the model predicts the location and occurrence of the aurora. The analysis of Machol et al. (2012) and Lane et al. (2015) moves towards answering these questions in evaluating how well the OP-2010 model predicts the location of the aurora but did not consider where or when the model performs well (i.e. in what latitudes and local time sectors) and under what conditions of geomagnetic activity the model performs well. In the research presented in Chapter 6, an evaluation of the performance of the operational implementation of a version of the OP-2013 model at the Met Office Space Weather Operations Centre is presented which aims to provide a more detailed analysis of how well the model predicts the location and occurrence of the aurora, where and under what geomagnetic activity the model performs well and the limitations of a solar wind driven auroral forecast model.

3.2 The Auroral Boundaries

Auroral boundary data determined from global images of the aurora obtained from satellite images are used in Chapter 6 to evaluate the performance of the OP-2013 auroral forecast model. The same auroral boundary data are also used in Chapters 7 and 8 to study the dynamics of the poleward auroral boundary during substorms and to compare the locations of the ionospheric projection of the plasmapause and the equatorward auroral boundary. This section contains a brief introduction to the auroral boundary data which is discussed in further detail in Chapter 4. The discussion then progresses to previous studies that have used the poleward boundary of the auroral oval as a proxy for the open-closed field line boundary location and the results from using the open-closed field line proxy to study changes in the open flux content during substorms in Section 3.2.2. Finally, Section 3.2.3 presents a review of the evidence from many studies which support the assumption that the equatorward auroral boundary maps to the plasmapause and discusses the limitations of these studies.

While the auroral boundaries can be identified from both ground and space based observations, this work focuses on the use of auroral boundary data identified

from spacecraft measurements. The boundaries of the auroral oval can be identified from spectrograms measured by in-situ particle precipitation instruments onboard spacecraft such as DMSP, similar to those shown in Figure 2.10 and as previously discussed in Section 2.7.1. While particle precipitation measurements from satellites such as DMSP provide the most accurate determination of the precipitation boundaries, the measurements can only be made in the orbital path of the satellite therefore they are spatially and temporally limited.

The auroral boundaries can also be identified from global auroral image data. The satellites carrying global auroral imagers onboard such as the NASA Imager for Magnetopause-to-Aurora Global Exploration (IMAGE) satellite are in highly elliptical polar orbits, allowing them to image the entire auroral oval. The IMAGE satellite and the onboard auroral imagers will be discussed in more detail in Chapter 4. Global auroral imagers provide the only dataset from which the location of the auroral boundaries can be identified simultaneously in all local time sectors. However, data from the auroral imagers can be limited by reflected solar ultraviolet emission which can saturate the auroral images on the dayside and by the resolution of the imaging camera.

The auroral boundaries determined from in-situ particle precipitation measurements and global auroral imagers are not always exactly co-located, due to limitations in the sensitivity of global auroral imagers. By definition, at the boundaries of the auroral oval, the particle energy flux decreases to a background level. However, a certain level of energy flux is required to produce auroral emission that is bright enough for the auroral imagers to detect above the background emission. It is estimated that an auroral brightness of between $110 - 1000$ R is produced per unit electron energy flux in erg cm^{-2} s^{-1} (Germany et al., 1990; Sotirelis et al., 2013). The minimum brightness threshold of aurora required to be detected by auroral imagers varies depending on the instrument. Particle precipitation data can measure lower energy flux levels and thus may be slightly offset from the auroral boundaries determined from auroral imagers. The auroral boundaries determined from global auroral image data are central to the research presented in this thesis.

3.2.1 The Poleward Auroral Boundary

As discussed previously in Chapter 2, the poleward boundary of the auroral oval encircles the polar cap and is closely associated with, although not directly equivalent to, the open-closed field line boundary (OCB) (e.g. Baker et al., 2000; Hubert et al., 2006; Kauristie et al., 1999; Rae et al., 2004). For a small number of events, Milan et al. (2003) found excellent correspondence between the location of the poleward auroral boundary from individual, global observations of the auroral oval and the OCB location determined from in-situ particle precipitation measurements. By comparing the average locations of the poleward auroral boundary identified from global auroral images relative to the open-closed field-line boundary from particle precipitation observations, average local-time dependent corrections to the auroral boundary can be determined to provide the location of the OCB from global auroral images (Boakes et al., 2008; Carbary et al., 2003; Longden et al., 2010). Discrepancies between the boundary identifications from auroral image data and in-situ particle data occur from limitations in the techniques used to identify the boundary locations from each dataset. As discussed previously, to identify the auroral boundary from the background emission in auroral imagers, the energy flux of the auroral emission must be sufficiently high. Generally, the auroral imagers would be expected to identify the poleward boundary at slightly lower latitudes than the in-situ particle precipitation measurements. If the poleward auroral boundary determined from the auroral imager is at a higher latitude than the boundary determined from in-situ data, it may suggest a limitation in the criteria used to determine the boundary in either or both datasets. The in-situ particle precipitation data should provide a better determination of the poleward boundary of the auroral oval and the OCB location compared to auroral imager data, although it may depend on how the OCB has been determined from the particle precipitation data. For example, both the B5 and B6 boundaries determined from DMSP data, discussed in Section 2.7.1, have been used as the poleward boundary of the auroral oval to compare against the OCB determined from global auroral images by Carbary et al. (2003), Hubert et al. (2006) and Boakes et al. (2008). The location of the poleward auroral boundary

identified from global auroral images and the OCB identified from particle precipitation measurements have been shown to agree within $\sim$ 2.5°, on average in all local time sectors (Longden et al., 2010).

Due to the close association between the poleward boundary of the auroral oval and the OCB, the poleward auroral boundary can be used as a proxy to estimate the open flux content of the polar cap (F_{PC}), as illustrated in Equation 3.1, by integrating the internal magnetic field strength B_I over the area of the polar cap in spherical coordinates (θ, ϕ).

$$\mathbf{F_{PC}} = \iint_A \mathbf{B_I}(\theta, \phi)\, d\theta\, d\phi \tag{3.1}$$

However, this calculation can be simplified by approximating a constant magnetic field strength in the ionosphere, $B_I \sim 5 \times 10^4$ nT, threading the polar cap area A_{PC} bound by the OCB, as shown in Equation 3.2 (Milan et al., 2003).

$$\mathbf{F_{PC}} = \mathbf{B_I} A_{PC} \tag{3.2}$$

Milan et al. (2009b) used the proton auroral oval captured by the SI12 instrument onboard the IMAGE spacecraft to estimate the open flux content from global auroral images. The proton auroral oval was used because the IMAGE data of the proton aurora is less affected by dayglow contamination. To estimate the open flux content from a large number of the auroral images, Milan et al. (2009b) approximated the auroral oval as a circle offset from the magnetic pole by $\sim$ 5° towards the nightside and $\sim$ 2° towards dusk. Circles with radii of between 8 $-$ 35° were then tested to find the best fit circle radius against the auroral brightness. The method of Milan et al. (2009b) allows the polar cap flux content to be estimated for lower quality IMAGE observations where only a partial auroral oval is observed due to poor data, a dim auroral oval or due to dayglow emission encroaching on the dayside auroral oval and saturating the auroral imager. Figure 3.2 from Milan et al. (2009b) shows three examples of the circle fitting technique when the auroral oval is contracted, more expanded and also when the auroral oval is only partially ob-

served. While this method of estimating the open flux content of the polar cap is robust in terms of estimating the flux content from poorer quality data, the underlying assumption of a circular polar cap breaks down during more dynamic periods such as substorms and may over-estimate the open flux content (Milan et al., 2021).

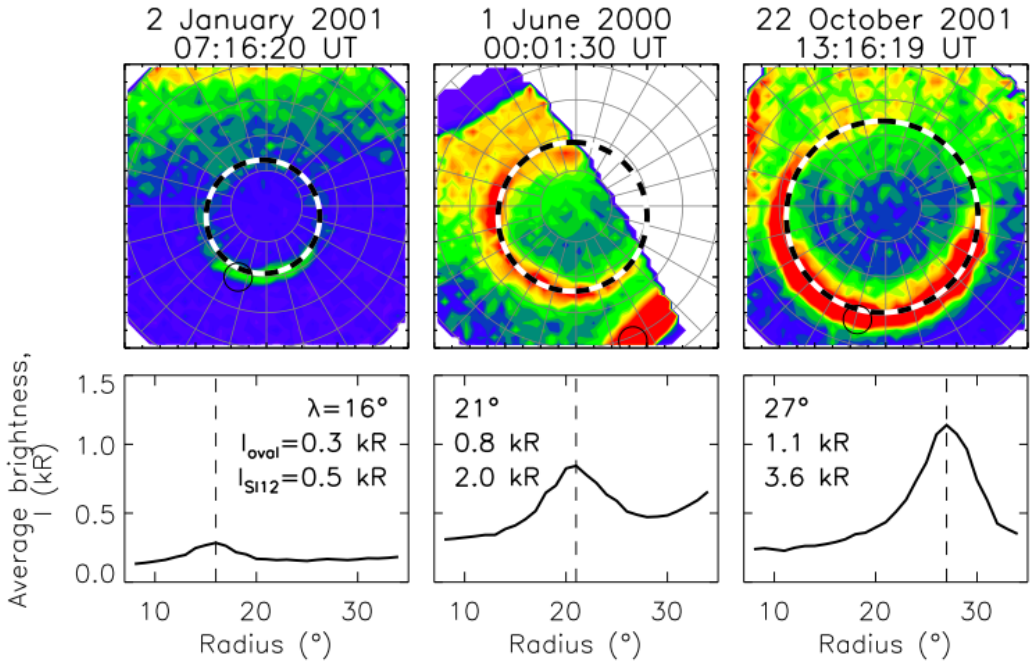

Figure 3.2: Figure from Milan et al. (2009b). 'Three example SI12 auroral images, demonstrating the fitting technique employed to determine the radius of the auroral oval. Lower panels show the variation of integrated brightness as a function of radius. The best-fit oval is shown by a black and white dashed circle in each panel. The peak of the nightside brightness is shown by small circles.'

Studies by Clausen et al. (2012, 2013) and Coxon et al. (2014) have used a similar technique to Milan et al. (2009b) fitting a circle to the location of the Region 1 (R1) field aligned currents as a proxy for the OCB, instead of the poleward auroral boundary from global images. The R1 currents are thought to flow into and out of the ionosphere in the boundary layer between open and closed magnetic flux. As a result, the location of the R1 current also moves poleward and equatorward with the changes in the open magnetic flux content of the polar cap. Clausen et al. (2012, 2013) and Coxon et al. (2014) followed a similar method to Milan et al. (2009b) by fitting an oval, displaced from the magnetic pole, to the maximum intensity of the R1 current.

Hubert et al. (2006) also determined the OCB from global images of the proton auroral oval obtained by the SI12 FUV instrument onboard IMAGE. In each image, Hubert et al. (2006) identified the poleward boundary of the auroral oval, where the auroral emission dropped to the level of the background UV emission. The poleward boundary of the auroral oval is then fitted with a Fourier series of five harmonics to provide full local time coverage. Using Fourier analysis to identify the boundary location allows the extrapolation of the boundary location in regions where the proton aurora is not bright enough to be detected by the auroral imager. By comparing the poleward boundary determined from the SI12 data against the OCB and poleward auroral boundaries determined from DMSP measurements, Hubert et al. (2006) applied a correction of $\sim 0.55^{\circ}$ poleward to their OCB identification in all local time sectors, except in one local sector centred on noon to account for cusp emission which generally occurs on open field lines.

The methods employed by Hubert et al. (2006), Milan et al. (2009b), Clausen et al. (2012) and Coxon et al. (2014) to determine the location of the OCB provide a reasonable estimate of the open flux content of the polar caps under quiet geomagnetic activity. However, the methods used are based on an assertion that pre-determines the shape of the auroral oval, (Milan et al., 2009b; Clausen et al., 2012; Coxon et al., 2014) or at least constrains the shape of the auroral oval (Hubert et al., 2006) which may over-estimate the open flux content and importantly, breaks down during dynamic periods.

An alternative fitting method to estimate the open flux content of the polar cap from global auroral image data was presented by Longden et al. (2010). In this method, Longden et al. (2010) identified the poleward and equatorward boundaries of the auroral luminosity in each local time sector. The exact details of this method will be discussed in more detail in Chapter 4. Using the OCB identified from DMSP data, Longden et al. (2010) calculated the statistical offset between the location of the poleward auroral luminosity boundary and the OCB in each local time sector, such that an average correction could be applied to the poleward auroral boundaries in each local time sector, from each global auroral image, to identify the location of

the OCB. By identifying the poleward auroral boundary in each local time sector, this method does not assume a pre-determined shape of the auroral oval and captures more detail of the auroral oval dynamics during active periods, such as substorms. As such, this method provides a more accurate proxy OCB location and thus a more accurate estimation of the open flux content than the methods previously discussed. While the method of Longden et al. (2010) does not assume a predetermined shape for the auroral boundaries, it does assume a latitudinal emission profile in each local time sector and models the auroral emission as either a single or double peaked Gaussian function with a quadratic component to model the background emission. This assumption may breakdown under certain conditions when the latitudinal auroral emission profile is more complex and the identification of the auroral boundaries could be less accurate.

The poleward and equatorward auroral boundaries and the proxy OCB location identified by Longden et al. (2010) are used extensively in the research presented in this thesis and will be discussed in more detail in Chapter 4.

3.2.2 Dynamics of the Poleward Auroral Boundary

As previously discussed in Chapter 2, substorms are an important process in the magnetosphere and in the modulation of the open flux content of the polar cap. The dynamics of the polar cap in response to changes in the open magnetic flux content can be described by the expanding and contracting polar cap (ECPC) model (Cowley and Lockwood, 1992). A diagram of the ECPC model is shown in Figures 3.3 and 3.4. During the substorm growth phase, magnetic field lines are opened via enhanced dayside reconnection faster than they are being closed in the nightside through reconnection in the magnetotail, forming a bulge of newly opened magnetic flux in the polar cap boundary, as shown in Figure 3.3b. Ionospheric convection transports the newly opened flux across the polar cap to the nightside, circulating the newly opened flux around the entire polar cap, as illustrated in Figure 3.3c. This redistribution of open magnetic flux causes an increase in the area of the polar cap and the OCB expands to lower latitudes, indicated by the dot-dashed line in Figure 3.3b. At substorm onset, the rate of nightside reconnection is expected to

immediately exceed the rate of dayside reconnection, resulting in the net closure of open magnetic flux. After the onset of nightside reconnection, the newly closed field lines form a bite out of the polar cap boundary, as illustrated in Figure 3.4b. This bite out is observed in the auroral oval as the formation of the auroral bulge. Again, the newly closed flux is eventually redistributed around the polar cap by ionospheric convection flows, which circularise the OCB, resulting in the global contraction of the polar cap and the poleward contraction of the OCB, as illustrated in Figures 3.4c and 3.4d.

From a statistical study of the ionospheric flows during 67 substorms using SuperDARN data, Provan et al. (2004) showed that, during substorms, the ionospheric convection was enhanced; however, at substorm onset there is a suppressed flow region in the substorm onset sectors which could indicate the auroral bulge. The reduction in flow is associated with high conductivities in the substorm onset sector (Morelli et al., 1995). After substorm onset, the low-latitude ionospheric return flow velocities begin to increase until 8 minutes after substorm onset, with the flow across the polar cap reaching a maximum at 12 - 14 minutes after susbtorm onset. In a larger statistical analysis of ionospheric flows during substorms, Grocott et al. (2009) divided the substorms by onset latitude, as lower latitude onset substorms are generally more intense due to the larger amount of open flux stored in the magnetotail. Grocott et al. (2009) found that for lower onset latitude substorms $< 64^{\circ}$, the localised reduction in flow at substorm onset observed in the onset sector was more pronounced compared to substorms with higher onset latitudes. The results from Provan et al. (2004) and Grocott et al. (2009) could suggest that there is a slight delay in the newly closed flux being redistributed around the polar cap by the localised reduction in convection immediately at substorm onset, in the substorm onset sector, in line with the schematic in Figure 3.3 from Cowley and Lockwood (1992).

Using the technique of Hubert et al. (2006) to identify the OCB from the proton auroral boundary, Coumans et al. (2007) performed a statistical analysis of the open flux content during 33 substorms. Coumans et al. (2007) found that the to-

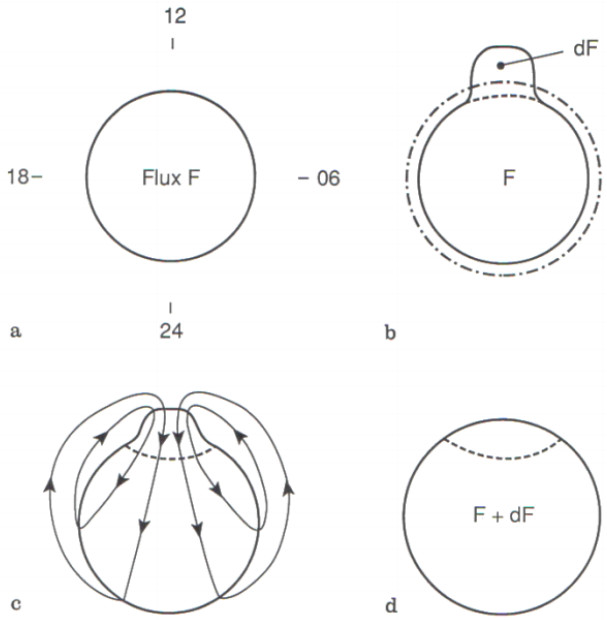

Figure 3.3: Figure from Cowley and Lockwood (1992) showing the expansion of the polar cap area due to an increase of dF the open flux content as a result of dayside reconnection.

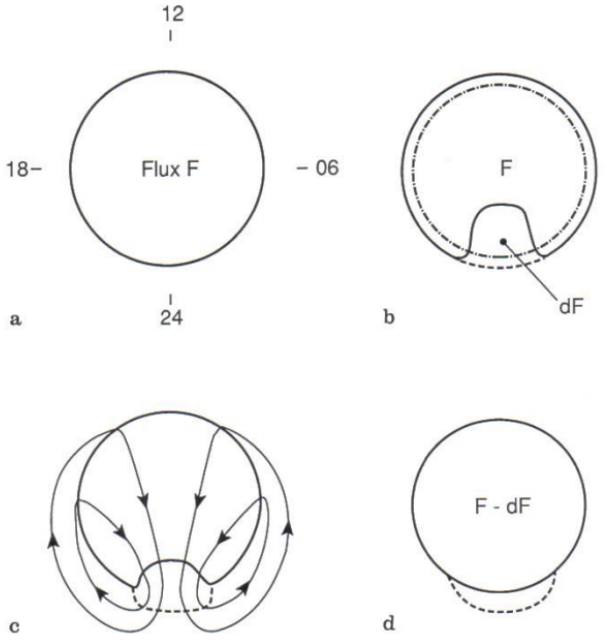

Figure 3.4: Figure from Cowley and Lockwood (1992) showing the contraction of the polar cap area due to an decrease of dF in the open flux content as a result of nightside reconnection.

tal open flux content of the polar cap did not immediately decrease during the 20 minutes after substorm onset. Instead on average, the open flux content remained approximately constant. In at least 5 out of the 33 substorms, the open flux content continued to increase in the 20 minutes following substorm onset. Similar results were also observed by Milan et al. (2009a), Clausen et al. (2013) and Coxon et al. (2014). This is consistent with a delay between the onset of reconnection on closed field lines and its progression to open field lines at the polar cap boundary. Alternatively, Coumans et al. (2007) suggested that there was a delay of 15 - 20 minutes before the rate of nightside reconnection superceded the rate of ongoing dayside reconnection. Under favourable IMF conditions, dayside reconnection might continue to increase the open flux content of the polar cap and exceed the closure of flux by nightside reconnection. However, the suppression followed by the gradual increase in the ionospheric convection flows for up to 8 minutes after substorm onset suggests that it may take some time for the newly closed magnetic flux to be circulated in the polar cap. Alternatively, the continued increase in the open flux content after substorm onset could be a result of the assumption and fitting of a circular OCB that underpins the estimation of the open flux content in each of these studies, which would break down during substorms.

As discussed, a modest interval of constant or increasing open flux content after substorm onset is consistent with the standard substorm model (e.g. Baker et al., 1996; Angelopoulos et al., 2008). The research presented in Chapter 7 uses the OCB determined by Longden et al. (2010) from global auroral image data to determine whether the approximately 20 minute continued increase in the open flux content reported by Coumans et al. (2007), Milan et al. (2009a), Clausen et al. (2013) and Coxon et al. (2014) might have been due to the breakdown of the OCB fitting methods used in these studies. The research presented in Chapter 7 analyses, in detail, the closure of open flux after substorm onset in each nightside local time sector and examines how the closure of flux propagates around the polar cap to understand the detailed motion of the OCB and the poleward auroral boundary in response to substorms.

3.2.3 The Equatorward Auroral Boundary

The relationship between the poleward auroral boundary and the OCB is well established, however the physical significance of the equatorward auroral boundary in the context of the wider magnetosphere is poorly understood.

As discussed previously, the particles precipitating into the ionosphere forming the main auroral oval precipitate on closed magnetic field lines. Most of the particles precipitating into the main auroral oval in the nightside ionosphere are thought to originate from the nightside plasma sheet (Feldstein and Galperin, 1985; Newell et al., 1996). Similarly, a significant portion of the lower latitude dayside auroral emission is thought to be due to nightside plasma sheet particles that have convected sunward and precipitate into the dayside ionosphere (Newell and Meng, 1992). The precipitating particles which result in the diffuse aurora at the equatorward edge of the auroral oval originate from the inner, Earthward edge of the nightside plasma sheet, while particles precipitating at higher, poleward latitudes in the ionosphere originate from further down tail. In the dipolar-like magnetic field which dominates the inner magnetosphere, the magnetic field lines which lie equatorward of the open-closed field line boundary are closed field lines which map between the north and south poles. However, auroral emission from particles precipitating on closed field lines is not observed at all latitudes. Instead, the auroral emission has a relatively sharp equatorward boundary at approximately $63-64^{\circ}$, on average determined from in-situ DMSP data (Niu et al., 2015). Jaggi and Wolf (1973) suggested that the abrupt equatorward auroral boundary was due to the zero energy Alfvén layer in the magnetosphere that coincided with the inner edge of the nightside plasma sheet, which acts to shield the inner magnetosphere from the externally induced convection electric field. The Alfvén layer is a separatrix between particles on closed and open drift paths. For the zero energy Alfvén layer, particles Earthward of this boundary are on closed, co-rotation dominated orbits while particles orbiting at larger radii than this boundary are convection dominated on open particle trajectories. Alternatively, Thorne et al. (1973) proposed that the cold plasmaspheric population of the plasmasphere limits the extent of the Earthward edge

of the plasma sheet into the inner magnetosphere through wave particle interactions, mainly hiss waves, which scatter energetic particles into the loss cone, resulting in the precipitation of energetic particles into the ionosphere.

The equatorward boundaries of the diffuse ion and electron aurora are closely associated with the zero energy convection boundary (Newell et al., 1996). The particles precipitating into the equatorward edge of the main auroral emission originate in a region of the magnetosphere where the particles have such low energies that their motion is only determined by the $\mathbf{E} \times \mathbf{B}$ convective drift motion. Theoretically, the zero energy convection boundary, where the particle motions are only governed by convection but have no gradient or curvature drift motions, would coincide with the plasmapause, where particle motions transition from being convection dominated to co-rotation dominated (Nishida, 1966) and the Alfvén layer of zero energy particles, under steady state convection conditions where magnetospheric convection has been relatively constant for a sufficient amount of time to allow particles to respond and establish relatively constant particle trajectories. The magnetosphere is rarely in a steady-state configuration, however there is significant evidence linking the source region of the equatorward diffuse aurora to regions in the magnetosphere near the plasmapause in some local time sectors and under certain levels of geomagnetic activity.

Simultaneous, ground-based observations of the equatorward edge of the diffuse aurora and the plasmapause, identified by the *knee* in the magnetospheric density profile in whistler wave data (Gringauz et al., 1961; Carpenter, 1963; Linscott and Scourfield, 1976) showed that the plasmapause and the equatorward auroral boundary were co-located to within approximately 0.25 R_E. These observations were made in the evening magnetic local time sectors (MLT 17 - 19) during an interval of disturbed but quietening geomagnetic activity with Kp decreasing from Kp 5 to 4. Similarly, in-situ observations comparing the location of the plasmapause and the inner edge of the plasma sheet, thought to be the source region of the particles precipitating to the equatorward edge of the auroral oval, found that the two were approximately co-located, within 0.1 - 0.2 L, in the midnight to noon sectors (Frank,

1971; Horwitz et al., 1982; Fairfield and Viñas, 1984), in the pre-midnight sectors during a substorm and during the main phase of a geomagnetic storm (Frank, 1971). Fairfield and Viñas (1984) proposed that during periods of disturbed geomagnetic activity, the cross-tail convection electric field moves the inner edge of the nightside plasma sheet closer to Earth, reducing the separation between the inner edge of the plasma sheet and the plasmapause.

Equally, there are observations which found the Earthward edge of the plasma sheet and the plasmapause to be significantly separated by between 1 - 5 R_E in the near midnight sectors (Schield and Frank, 1970) and between 1 - 3 R_E in the pre-midnight sectors (Frank, 1971), with an electron trough region observed in the separation region between the two plasma populations, filled with low energy electrons ($\sim$ 100 eV) with densities of $\sim$ 1 cm^{-3} (Schield and Frank, 1970). The differing results between some of these studies as to whether the inner edge of the plasma sheet is co-located with the plasmapause may be due to the different methods or definitions used to identify the plasmapause or plasma sheet boundaries. But the results of these studies also suggest that whether the two boundaries are co-located or not varies in local time and with the level of geomagnetic activity.

Further evidence of a link between the source region of the equatorward auroral emission and the plasmapause are in auroral features which are observed on or near the equatorward edge of the main auroral emission, such as undulations and pulsating aurora. Undulations on the equatorward boundary of the diffuse auroral emission are auroral structures with wavelengths typically between 200 - 900 km with amplitudes of 40 - 400 km that are most commonly observed to occur in the dusk local time sectors, during geomagnetically active periods and persist for around 30 minutes to 3.5 hours (Lui et al., 1982; Motoba et al., 2015; Forsyth et al., 2020a). The generation mechanism for undulations is unclear, however many of the proposed and observed mechanisms suggest activity at or near the plasmapause boundary, including a Kelvin-Helmholtz velocity shear flow instability at the plasmapause (Lui et al., 1982), intense sub-auroral polarisation stream (SAPS) flows (Henderson et al., 2010, 2018) and plasmapause surface waves (He et al., 2020; Horvath and

Lovell, 2021).

SAPS are sunward flows which occur in the duskside auroral region, at mid-latitudes below the equatorward edge of the auroral oval during periods of strong magnetospheric convection. Under these conditions, the ion plasma sheet population can be convected significantly further Earthward than the electron plasma sheet. The plasma flows in the ion plasma sheet are predominantly sunward while the flows in the co-rotating plasmasphere are directed anti-sunward in the dusk sectors. The oppositely directed flows create a velocity shear close to the plasmapause which results in large undulations along the plasmapause. It is thought that these undulations at or near the plasmapause map to auroral undulations observed in the dusk sector auroral ovals (Henderson et al., 2010, 2018). The first direct observation of coincident plasmapause surface waves and undulations in the equatorward edge of the dusk sector auroral oval was presented by He et al. (2020). The plasmapause surface wave was detected from in-situ data collected by the two Van Allen Radiation Belt Probes (A and B) and the Exploration of energisation and Radiation in Geospace (ERG, also called Arase) spacecraft. The in-situ data showed multiple plasmapause crossings by the spacecraft, suggesting a sawtooth-shaped plasmapause undulation. Figure 3.5 from He et al. (2020) shows a model of the plasmapause with the surface wave along the duskward edge, with the spacecraft trajectories shown in panel (a) and the in-situ measurements made by each spacecraft in panels (d) - (i). Panels (b) and (c) show the auroral observation from the DMSP satellite in the northern and southern hemispheres respectively, showing the coincident auroral undulations in the same dusk local time sectors as the plasmapause surface wave. He et al. (2020) suggested that the plasmapause surface wave could be excited by fast storm time injections, resulting in a sudden enhancement in the duskside ring current or plasma sheet.

Similarly, patches of diffuse aurora which exhibit quasi-periodic variations in luminosity, known as pulsating aurora, have been shown to have a strong correlation with chorus waves (Tsuruda et al., 1981; Ozaki et al., 2012, 2015; Hosokawa et al., 2020), which are typically observed outside the plasmasphere (e.g. Lauben

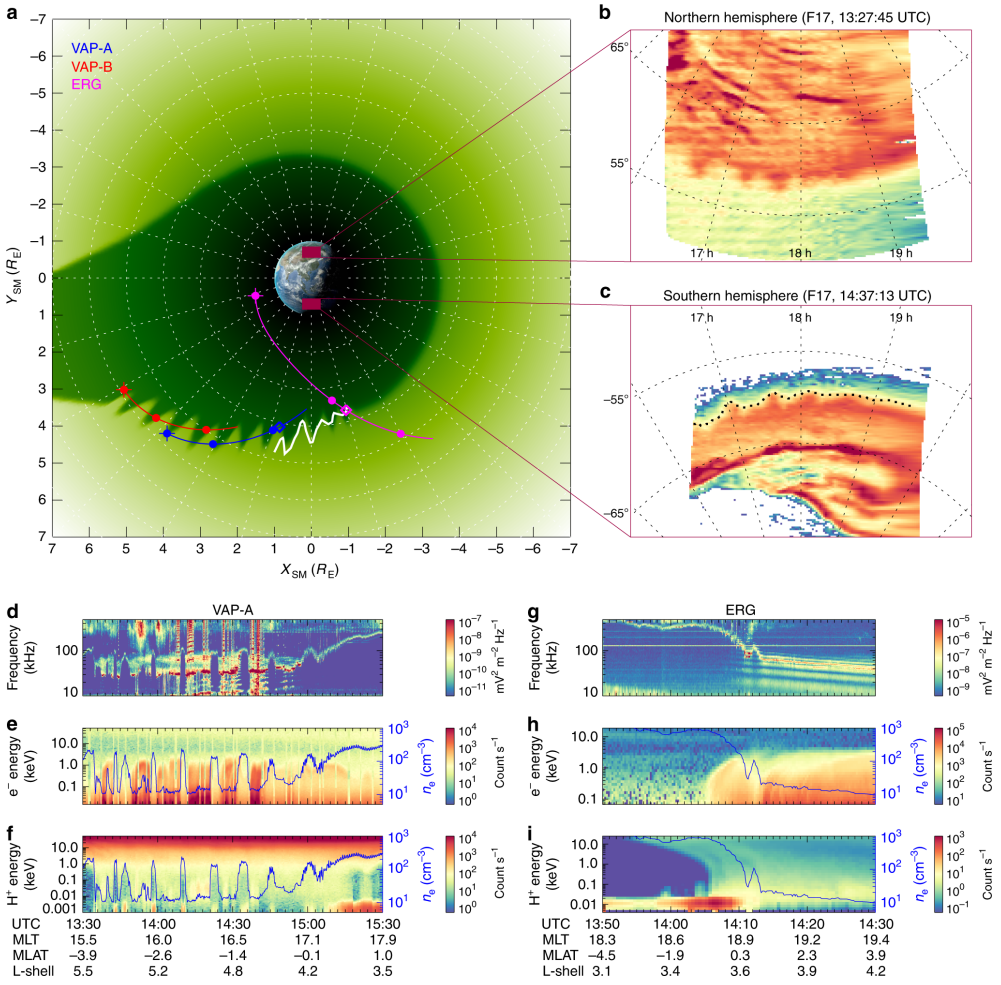

Figure 3.5: Figure from He et al. (2020). Panel a shows a model of the plasmapause shape illustrating the plasmapause surface wave and the tracks of the in-situ data from the two Van Allen Probes A/B shown in red/blue and the Arase spacecraft, shown in pink. Panels b and c show the auroral images captured by DMSP with the coincident undulation of the equatorward edge of the diffuse aurora observed in both hemispheres. Panels d - f and g - i show the in-situ data from the Van Allen Probe A and Arase, respectively.

et al., 2002). The pulsating aurora is generally observed in the equatorward part of the main auroral oval (Hosokawa et al., 2015; Ozaki et al., 2015), in the morning local time sectors, between midnight and dawn, during the substorm recovery phase (Hosokawa et al., 2015). The drift speed of the auroral patches corresponds to the $\mathbf{E} \times \mathbf{B}$ drift velocity, suggesting a link between the pulsating aurora and cold magnetospheric particle populations, such as the plasmasphere (Nakamura and Oguti, 1987). The coincident chorus waves observed at or near the plasmapause in the equatorial region scatter electrons into the loss cone which then precipitate into the

ionosphere, modulated by the frequencies of the chorus waves.

In summary, the poleward boundary of the auroral oval is reasonably well understood in the context of the wider magnetosphere and is strongly associated with the open-closed field line boundary. There is significant evidence that the equatorward boundary of the auroral oval maps to the plasmapause boundary; however, previous studies have been limited in local time and geomagnetic activity by data coverage. The final study in this thesis presents a statistical analysis which compares the average locations of the equatorward auroral boundary against the ionospheric projection of the plasmapause to identify whether the two boundaries are co-located and under what geomagnetic conditions the two boundaries are co-located, on average. This could provide an indication of the plasma configuration in the magnetosphere, potentially increasing the usefulness of auroral forecasts.

3.3 Open Questions

From this thorough review of recent literature, a number of open questions remain. The OVATION-Prime 2010 and 2013 auroral forecast models are used world-wide in space weather forecasting centres but, how well can an empirical solar wind driven model accurately predict the aurora, particularly in different local time sectors and under different levels of geomagnetic activity? The observation and analysis of the poleward and equatorward auroral boundaries contain a considerable amount of information about the global scale structure and dynamics of the magnetosphere. It is well understood that the poleward boundary of the auroral oval is closely associated with the open-closed field line boundary and that substorms play a significant role in modulating the open flux content of the magnetosphere. How do the details of the auroral dynamics fit into the wider understanding of the closure of flux in the magnetosphere, particularly during substorms? And, what does the equatorward auroral boundary translate to in the inner magnetosphere in all local time sectors? Understanding the physical significance of the auroral boundaries, their dynamics and controlling factors will help to improve future generations of space weather forecast models.

Chapter 4

Instrumentation and Data

4.1 The IMAGE Spacecraft

The NASA Imager for Magnetopause-to-Aurora Global Exploration (IMAGE) satellite was a medium-class explorer (MIDEX) mission that was developed as part of NASA's Sun-Earth Connection program. The IMAGE mission studied the global magnetospheric response to the interaction with the solar wind and carried a suite of instruments which were largely focused on global imaging of magnetospheric plasma regimes including the aurora, the plasmasphere and the neutral Hydrogen plasma in the geocorona. The observations of the IMAGE satellite could be used in conjunction with in-situ plasma measurements, such as those from within the magnetosphere observed by the ESA Cluster satellites and the upstream solar wind in-situ measurements from the NASA Advanced Composition Explorer (ACE) satellite to provide the context of the in-situ data and the global configuration of the magnetosphere. The IMAGE mission carried 3 suites of imaging instruments including neutral atom geocorona imagers (NAI), far ultraviolet global auroral imagers (FUV) and an extreme ultraviolet plasmapshere imager (EUV). In addition the IMAGE mission also had a radio plasma instrument to measure in-situ plasma resonance frequencies which consisted of two 10 m boom antennae and four 250 m wire antennae. The main science objectives of the IMAGE mission were to determine the dominant mechanisms for plasma injections into the magnetosphere on magnetospheric storm and substorm timescales, to observe the response of the

magnetosphere to changes in the solar wind driving and to identify the locations and processes in the magnetosphere where plasma is energised, transported and lost during magnetospheric storms and substorms. Figures 4.1 and 4.2 show diagrams of the IMAGE satellite and the layout of the IMAGE instrument plate.

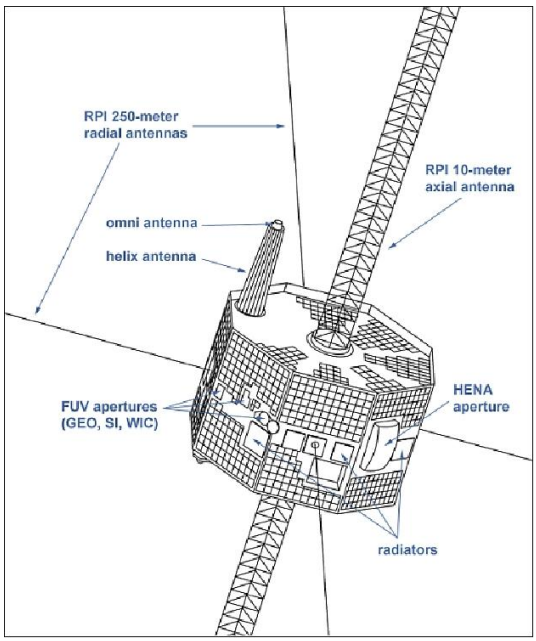

Figure 4.1: A schematic diagram of the IMAGE satellite, created by the Southwest Research Institute, with a number of key features labelled including the RPI antennae and the location of the FUV apertures.

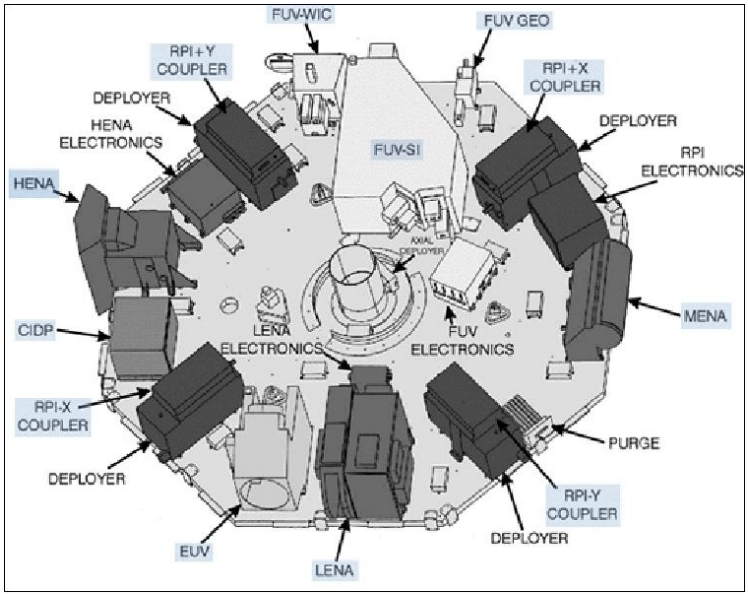

Figure 4.2: A diagram, created by the Southwest Research Institute, showing the layout of the instrument plate on the IMAGE satellite illustrating the location of the FUV and EUV instruments.

The IMAGE satellite was operational between 2000 and 2005 in a precessing polar orbit with a perigee of 1,000 km and an apogee of 44,000 km (~ 7 R_E) (Mende et al., 2000b). The IMAGE satellite was spin-stabilised, rotating about its axis once every 2 minutes. Over the first 2 years of nominal operations between 2000 and 2002, the orbital apogee was situated over the northern hemisphere and the inclination of the orbit precessed from 40° to 90°, directly over the pole and returned to 40°. Figure 4.3 shows a plot of the IMAGE satellite orbits from the same day in July 2000, 2001 and 2002. The mission duration was extended past the 2 years of nominal operations and the orbit precessed so that the apogee was situated over the south pole. In October 2000, September 2001, August 2002 and September 2004, the IMAGE satellite suffered repeated damage to the Radio Plasma Instrument (RPI) antenna (Frey, 2010) which affected the satellite pointing and resulted in an increased uncertainty in spacecraft pointing.

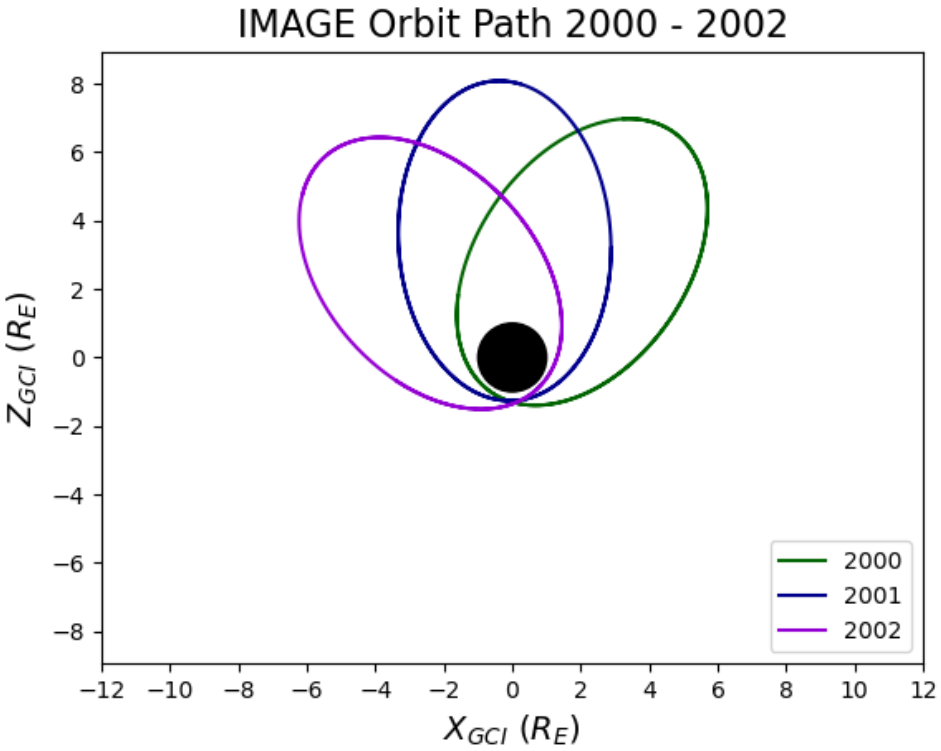

Figure 4.3: A figure showing the IMAGE precessing orbit plotted using data from 15 July 2000, 2001 and 2002.

The spin-stabilisation of the satellite presented unique design challenges for the imaging instruments on IMAGE to capture high, science quality images. The details of how the spin of the spacecraft was overcome for the FUV auroral and EUV plasmaspheric imagers is discussed in more detail in the following sections, however the damage sustained to the RPI antenna and the subsequent uncertainty in spacecraft pointing had a significant impact on the image quality, particularly of the FUV data, from August 2002 onwards.

The IMAGE mission ended in 2005 due to a communications failure with the satellite which likely resulted from an instantanous failure of the transponder power supply (IMAGE Failure Review Board, 2006). The IMAGE satellite was rediscovered by an amateur astronomer in 2018, however, communications with the satellite could not be reestablished. Overall, the IMAGE mission was considered highly successful in achieving its scientific objectives and providing the most extensive coverage of global magnetospheric images to date.

4.1.1 Imaging the Far-Ultraviolet Auroral Oval

The IMAGE satellite carried three far-ultraviolet (FUV) instruments to image the FUV auroral emission; a wideband imaging camera (WIC) and two spectral imagers (SI12 and SI13) (Mende et al., 2000b). Observation images were taken by each FUV instrument approximately every 2 minutes determined by the spin period of the IMAGE satellite (Burch, 2000). The FUV images were processed using Time Delay Integration. When the Earth was in view of the FUV instruements as the IMAGE satellite rotated, the FUV cameras captured the instantaneous field of view of the auroral emission. Subsequent FUV images were then superimposed with a time delay to account for the rotation of the spacecraft. The wider field of view of the WIC instrument meant that the WIC observations were made over a 10 second period, while the SI observations were made over a 5 second period. The full, raw FUV images were then corrected for the rotation and distortion by the onboard image processing system.

The WIC instrument was sensitive to emission in the 140 – 190 nm wavelength range dominated by the N_2-Lyman-Birge-Hopfield band system (Mende

et al., 2000a) while the two narrower passband spectral imaging cameras, SI12 and SI13, were centered on 121.8 and 135.6 nm, respectively (Mende et al., 2000c).

The SI12 passband detected the Doppler-shifted Lyman-α emission while rejecting the geocoronal Lyman-α and the nearby intense emission of Nitrogen at 120 nm. The Lyman-α emission detected by the SI12 instrument can be generated by charge exchange between the neutral Hydrogen atmospheric particles and high energy protons precipitating into the upper atmosphere, thus the SI12 observations capture the auroral emission associated with precipitating protons. The narrow passband and rejection of the geocoronal Lyman-α emission of the SI12 instrument meant that the SI12 observations were less affected by dayglow emission, compared to the WIC and SI13 instruments, although as demonstrated by Figure 4.6, the SI12 observations are sometimes still inferior for boundary determination due to the generally weaker emission. The SI13 instrument was sensitive to 135.6 nm Oxygen emission which is a bright, discrete auroral emission line associated with electron precipitation (Mende et al., 2000c).

The WIC instrument was higher resolution and had a slightly larger field of view of $17^\circ \times 17^\circ$, containing 256×256 pixels compared to a field of view of $15^\circ \times 15^\circ$, containing 128×128 pixels for the SI instruments. Each of the three instruments were designed to be able to resolve auroral features on the order of 100 km at apogee.

4.1.2 Imaging the Plasmasphere in the Extreme Ultraviolet

A second instrument onboard the IMAGE satellite was the Extreme Ultraviolet (EUV) imager which was designed to observe the plasmasphere (Burch, 2000; Sandel et al., 2000). Figure 4.4 shows an example image of the plasmasphere taken by the EUV imager from Sandel et al. (2003), highlighting the main features of the plasmasphere. As discussed in Chapter 2, He^+ ions are the second most abundant element in the plasmasphere. The He^+ ions resonantly scatter solar radiation at 30.4 nm wavelengths which was observed by the EUV imager (Meier and Weller, 1972; Sandel et al., 2000). The 30.4 nm emission observed from the He^+ ions is used because the most abundant ion H^+ has no optical emission (Sandel et al., 2000).

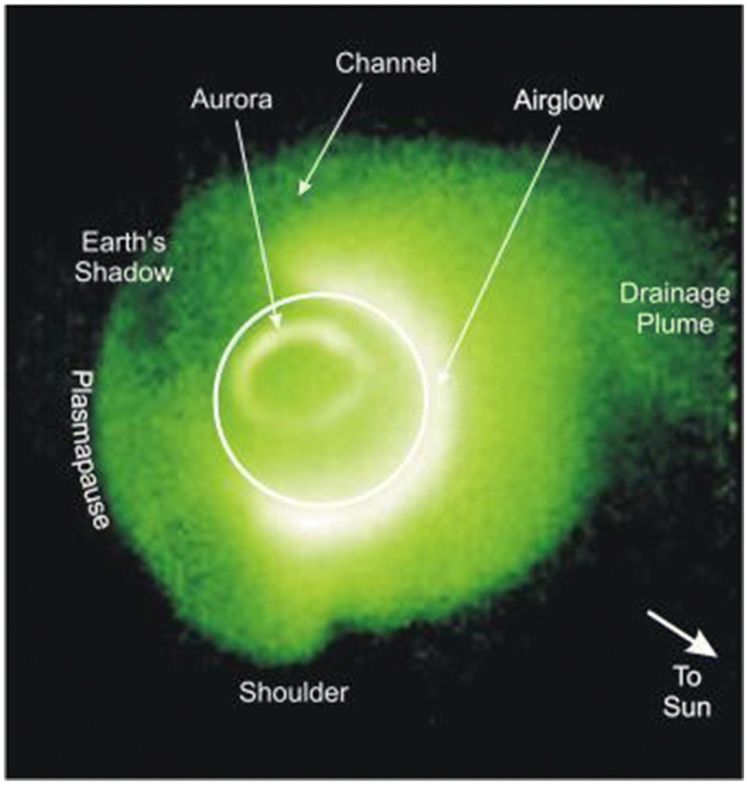

Figure 4.4: An image of the plasmasphere captured by the IMAGE EUV instrument at 07:34 UT on 24 May 2000 from Sandel et al. (2003). The main features of the plasmasphere are labelled and the white circle shows the approximate location and size of the Earth.

The EUV imager consisted of three identical sensors, each with a 30° field of view. The three sensors were tilted relative to each other to form a fan shape which results in an $84° \times 30°$ instantaneous field of view (Sandel et al., 2000). As the IMAGE spacecraft spins, the three EUV sensors sweep an $84° \times 360°$ field of view (Sandel et al., 2000). The EUV images are integrated over 5 spacecraft spins, providing one EUV image every 10 minutes, with a spatial resolution of 630 km (~ 0.1 R_E) (Sandel et al., 2000). The lower sensitivity threshold of the EUV emission at the edge of the plasmasphere was estimated to be $\sim 40 \pm 10$ ions cm^{-3} from comparisons with in-situ RPI data (Goldstein et al., 2003).

The underlying assumptions of the EUV imager are that the spatial distribution of He^+ ions is representative of the whole plasmaspheric distribution (Sandel et al., 2000) and that the 30.4 nm emission is optically thin i.e. that the 30.4 nm photons can pass through the plasmasphere without being absorbed (Meier and Weller,

1972; Sandel et al., 2000). As a result, the intensity of emission observed by the EUV imager is directly proportional to the line-of-sight integrated column density of He^+ ions (Sandel et al., 2000).

4.2 Auroral Boundary Identifications from the FUV Dataset

Between 2000 - 2002, the apogee of IMAGE was situated over the northern hemisphere, thus the satellite was in an optimal position to capture images of the northern hemisphere polar cap and auroral oval.

Using the FUV data from this period, Longden et al. (2010) identified the poleward and equatorward auroral boundary for each of the three FUV datasets (WIC, SI12 and SI13) between May 2000 - October 2002 inclusive. The auroral boundaries were determined by dividing the auroral images of the northern polar cap into 24 local time sectors and creating a latitudinal intensity profile of the UV emission for each sector. Each intensity profile was fitted with two model functions: a single Gaussian plus a quadratic component modeling a continuous auroral oval with no bifurcation or splitting, or a double Gaussian plus a quadratic component which better models a bifurcated auroral oval. The quadratic component modelled the background emission while the Gaussian functions modelled the auroral emission. The equations for both the single and double Gaussian plus quadratic fitting models are shown in Equations 4.1 and 4.2, respectively where λ is the magnetic latitude, A, μ and σ are the peak amplitude, peak latitude, and width of the Gaussian, respectively, and B, C, D, E, F and G are the coefficients of the quadratic background of the function.

$$f_s(\lambda) = A_0 exp\left[-\frac{(\lambda-\mu_0)^2}{2\sigma_0^2} \right] + B + C\lambda + D\lambda^2 \tag{4.1}$$

$$f_d(\lambda) = A_e exp\left[-\frac{(\lambda-\mu_e)^2}{2\sigma_e^2} \right] + A_p exp\left[-\frac{(\lambda-\mu_p)^2}{2\sigma_p^2} \right] + E + F\lambda + G\lambda^2 \tag{4.2}$$

In Equation 4.2, the coefficients with subscripts e are the coefficients for the most equatorward Gaussian function, while coefficients with subscripts p are the coefficients for the most poleward Gaussian function.

The Levenberg-Marquardt non-linear least squares fitting method was used to fit the Gaussian plus quadratic background models to the latitudinal intensity profiles of the auroral emission. Initial values for the functional fitting were estimated from the latitudinal intensity profile. The fitting was then iterated up to a maximum number of 200 times, until the model fits converged. The goodness of fit of the two model functions was evaluated in each local time sector using the reduced χ^2 statistic. Improvements in the model fit were considered negligible when the decrease in the reduced χ^2 statistic between subsequent iterations was less than 0.01. The parameters from the final iteration were then used to estimate the poleward and eqautorward luminosity boundary locations of the auroral oval. If the double Gaussian model function was a better fit, the poleward/equatorward auroral boundary was identified to be at the poleward/equatorward full width half maximum of the most poleward/equatorward Gaussian peak, offset from the centre of the peak, as shown in Equations 4.3 and 4.4. If the single Gaussian model function provided a better fit, the auroral boundaries were identified as the poleward and equatorward full width half maximum of the Gaussian peak offset from the centre of the peak, as shown in Equations 4.3 and 4.4 with $\mu_e = \mu_p = \mu_0$ and $\sigma_e = \sigma_p = \sigma_0$ for the single Gaussian function.

$$\lambda_e = \mu_e - 2\sqrt{2ln(2)}\sigma_e \tag{4.3}$$

$$\lambda_p = \mu_p + 2\sqrt{2ln(2)}\sigma_p \tag{4.4}$$

Figure 4.5 from Longden et al. (2010) shows an example of fitting the Guassian plus quadratic background models to the latitudinal intensity profiles of the auroral emission in two local time sectors and the identification of the poleward auroral boundary location from both the single and double Gaussian model. Figure 4.6

shows an example of the auroral boundaries determined by Longden et al. (2010) over-plotted on simultaneous WIC, SI12 and SI13 observations from 3 December 2000. The figure demonstrates the lower resolution of the SI12 and SI13 data compared to the WIC observations and also that the auroral boundaries determined by Longden et al. (2010) were not always able to be identified in all local time sectors.

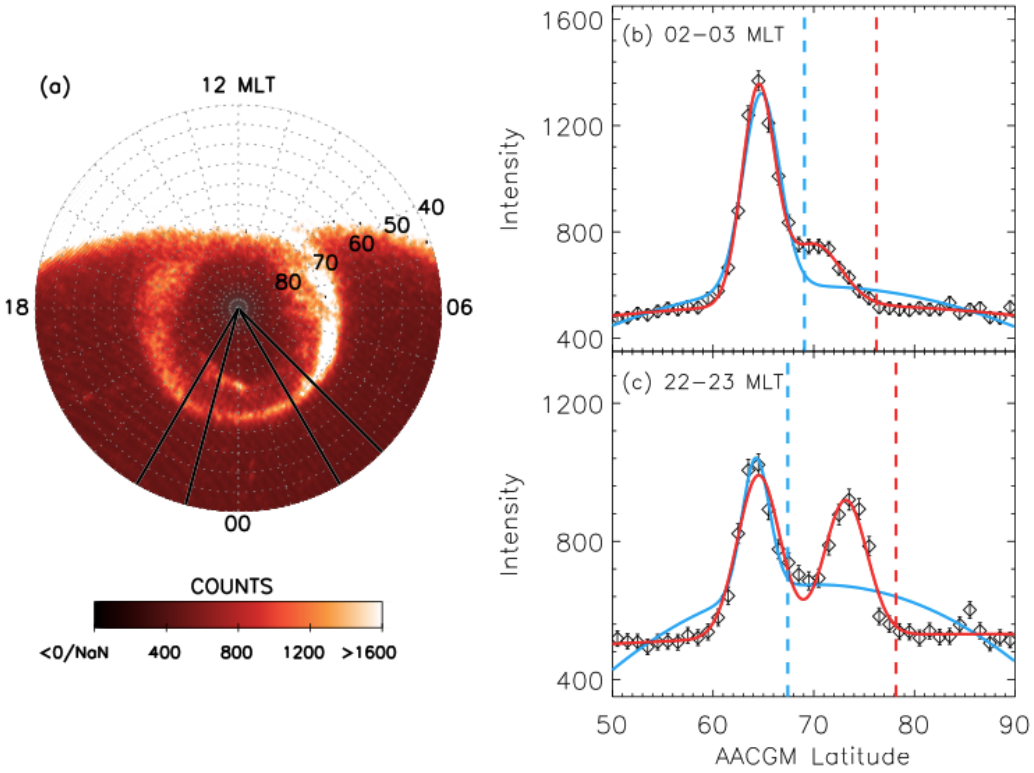

Figure 4.5: Figure from Longden et al. (2010). Panel (a) shows an auroral observation from the IMAGE WIC instrument at 00:10 UT 1 February 2001 in Altitude-Adjusted Corrected Geomagnetic (AACGM) coordinates in which all count values $>$ 1600 have been saturated. The solid black lines highlight the 0200 - 0300 and 2200 - 2300 local time sectors. Panel (b) shows two examples fitting the model functions to the latitudinal intensity profile in the 0200 - 0300 and 2200 - 2300 local time sectors. The mean count values and the associated standard error of the observed latitudinal intensity profile are shown by the black diamonds and error bars. The blue/red curves show the result of the single/double Gaussian functions plus quadratic background models fit to the observational data. The blue and red dashed lines show the location of the poleward auroral luminosity boundary in each of the two local time sectors identified using the single and double Gaussian models, respectively.

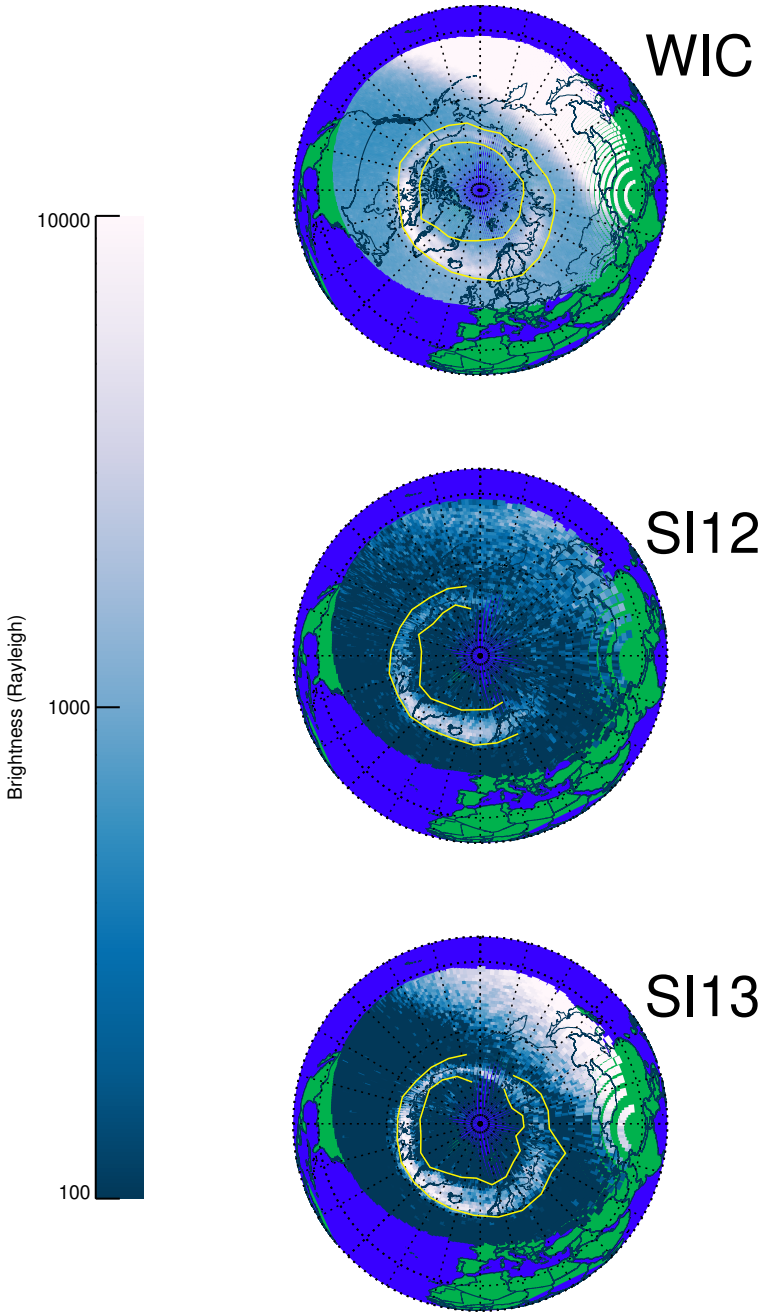

Figure 4.6: An example of the auroral boundary locations identified by Longden et al. (2010) plotted on the WIC, SI12 and SI13 auroral observations from 07:05:22 on 3 December 2000. Figure provided by Colin Forsyth.

The method follows a similar approach to the techniques of Carbary et al. (2003) and Boakes et al. (2008), which both fitted single Gaussian functions to the luminosity profiles, and the method of Mende et al. (2003), which used a double Gaussian profile to account for bifurcation or splitting of the auroral oval. Fitting both Gaussian functions allows for automation without prior knowledge of the level of bifurcation, or splitting, in the auroral oval in different MLT sectors (Longden et al., 2010). The latitudinal profile of auroral emissions is assumed to be well described by either a single or double Gaussian and does not account for more complex auroral emission profiles.

4.2.1 The Poleward Auroral Boundary as a Proxy for the Open-Closed Field Line Boundary

Using the location of the poleward auroral luminosity boundary (PALB), Longden et al. (2010) determined the statistical offset between this boundary and the OCB location identified from particle precipitation measurements from DMSP to provide a correction factor from which the OCB location can be calculated.

Statistical studies have shown that the true location of the OCB determined from precipitating particle fluxes measured by low-Earth orbiting spacecraft can be offset from the auroral boundary by several degrees (Kauristie et al., 1999; Carbary et al., 2003; Boakes et al., 2008). These precipitating particle fluxes are usually only available four times per spacecraft orbit and provide a local determination of the OCB location. In contrast, auroral imagers such as the FUV cameras provide a global snapshot of the location of the aurora, thus the poleward boundary of the UV oval provides a useful global proxy for the OCB. Boakes et al. (2008) characterised the difference between the DMSP particle precipitation data and the UV poleward auroral oval boundary for each of the IMAGE FUV instrument data sets (WIC, SI12, and SI13) in each local time sector. Longden et al. (2010) extended the work of Boakes et al. (2008) to determine the average correction factors in each local time sector and for each of the FUV cameras for their poleward auroral boundaries. Similar to Boakes et al. (2008), Longden et al. (2010) found that for all FUV data sets, statistically, the PALBs near noon and midnight were found

to lie poleward of the OCB location determined from DMSP particle precipitation measurements. In the dawn sectors, SI12 PALBs were also found to lie poleward of the particle precipitation OCB, while the WIC and SI13 PALBs required little correction in this region. In the dusk sectors, the SI12 PALBs were located slightly equatorward, while the SI13 and WIC PALBs were poleward of the OCB location determined from DMSP particle precipitation measurements. All the corrections in the OCB location are within $\pm 4^{\circ}$, with the majority of the corrections between $\pm 2^{\circ}$. The statistical corrections for the OCB location determined for the WIC, SI12 and SI13 datasets in all local time sectors are shown in Figure 4.7. The statistical offset between the OCB determined from the particle precipitation boundaries and the poleward auroral boundary identified by Longden et al. (2010) may be due to the definition of the boundary location by Longden et al. (2010) as the full width half maximum, offset from the centre of the peak of the Gaussian function. This definition of the poleward boundary location may identify the poleward boundary at slightly higher latitudes than the location of the poleward particle precipitation boundary. The poleward offset could also be due to the spreading of the auroral emission captured in the IMAGE FUV data resulting in a diffuse edge of the latitudinal emission profiles. The full description of the method can be found in Longden et al. (2010).

The poleward and equatorward luminosity boundaries and the determination of the OCB location from Longden et al. (2010) are used extensively in the research presented in this thesis.

4.3 EUV Plasmapause Identifications

There are a number of methods that can be used to identify the plasmapause boundary, including ground-based or in-situ observations, which have been discussed briefly in Chapter 3. Similar to the auroral boundaries, identifying the plasmapause boundary using in-situ data provides the most accurate measurement of the plasmapause boundary, however, in-situ data is spatially and temporally limited.

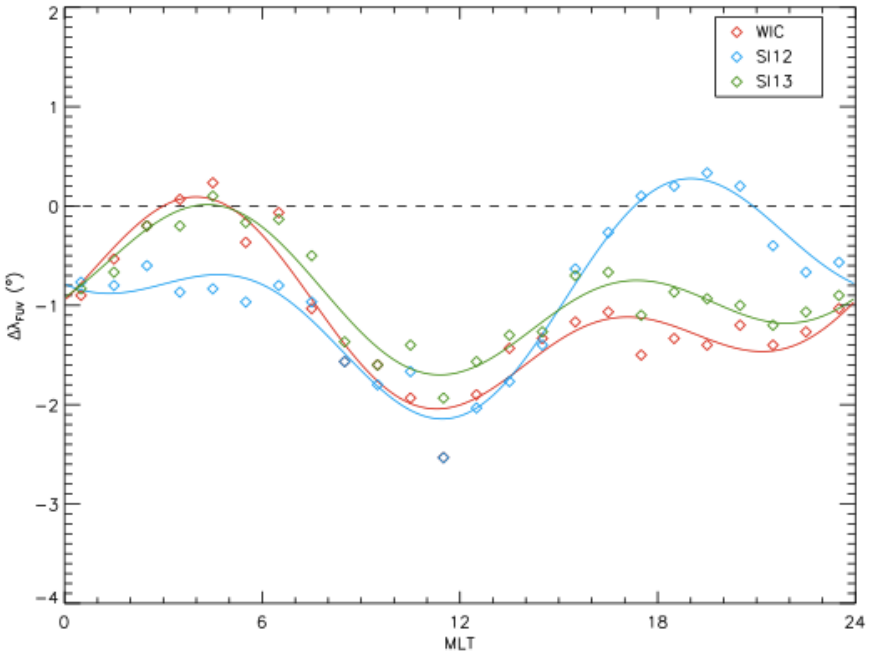

Figure 4.7: The statistical offset between the poleward luminosity auroral boundary location identified by Longden et al. (2010) and the OCB determined from particle precipitation measurements obtained by DMSP for each magnetic local time sector (MLT). A positive/negative correction ($\Delta\lambda_{FUV}$) indicates that the OCB is located at higher/lower latitudes than the poleward auroral luminosity boundary. Figure from Longden et al. (2010).

Goldstein et al. (2003) identified the global plasmapause from IMAGE EUV observations by eye, as the sharp edge of the He^+ emission observed in the EUV images, and showed that the extracted plasmapause identifications corresponded well with in-situ measurements of the plasmapause location identified from IMAGE RPI data. The plasmapause locations were then mapped to the equatorial plane, assuming a dipolar magnetic field model. The dipolar field line model was used to calculate the magnetic field line with minimum distance away from Earth in the equatorial plane, known as the L value, providing a corresponding coordinate for the plasmapause location in the equatorial plane in magnetic local time and L value (in Earth radii). Figure 4.8 shows an example plasmapause from Goldstein et al. (2004b) determined from the IMAGE EUV data. The uncertainty in the plasmapause locations identified by eye was estimated to be between 0.2 - 0.8 R_E, depending on the sharpness of the He^+ emission edge (Goldstein et al., 2003).

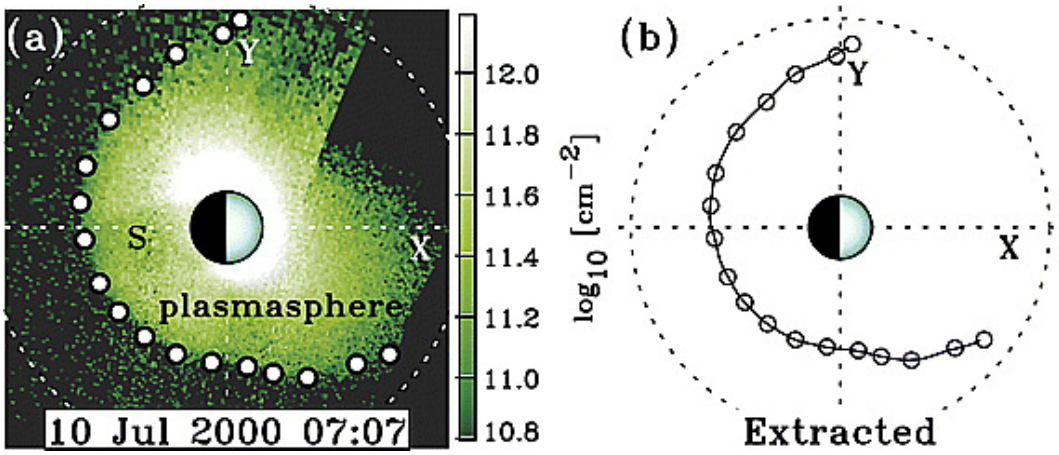

Figure 4.8: Figure from Goldstein et al. (2004b). 'Example of extraction of plasmapause curve from IMAGE EUV, 10 July 2000, 7:07 UT. (a) EUV image, mapped to the magnetic equator (Earth at center; Sun to the right). Dotted lines are X- and Y-axes; dotted circle is geosynchronous orbit. The colour bar gives line-of-sight integrated He+ column abundance. Black region in upper right is sunlight contamination. Filled white circles are manually-extracted ('click') points along the plasmapause. (b) Fourier expansion of the click points (circles) is plotted as the solid curve.'

For 47 orbits in June 2001, Goldstein et al. (2003) compared the plasmapause identifications from the EUV data with in-situ measurements of the plasmapause location identified using the Radio Plasma Instrument (RPI) data. The plasmapause location was identified in the RPI data by a sharp gradient in the electron density data. Comparing the L values of 47 plasmapause locations identified from the EUV image that was observed closest in time to the RPI data crossing the plasmapause, Goldstein et al. (2003) showed that 77% of the plasmapause locations agreed within 0.5 L. Goldstein et al. (2003) also found a reasonable correlation between the L values of the plasmapause locations identified using the in-situ versus the remote sensing data of $r = 0.83$ ($r^2 = 0.69$).

To account for the time difference between the EUV observations and the RPI in-situ measurement, Goldstein et al. (2003) assumed that the evolution of the plasmapause was dominated by co-rotation only and the RPI measurements were rotated, either forwards or backwards, in local time to align with the EUV observations. This assumption may break down in some local time sectors, particularly in the dusk sectors, where convection is known to play a significant role in the

plasmapause dynamics especially in the formation and evolution of the drainage plume during geomagnetically active periods. No duskside data were included in the comparison between the EUV and RPI plasmapause locations. The time difference between the EUV and RPI observations is expected to be the largest source of error and the main reason for observed differences in the plasmapause location identified from each dataset as the convection rate or rates of filling or depletion of the plasmasphere, which affect the radial extent of the plasmapause, are difficult to account for.

The reasonably good correlation between the plasmapause location identified by eye from the EUV data mapped to the equatorial plane and the assumed *true* plasmapause location measured from in-situ RPI data indicates that the plasmapause location extracted from the EUV images gives a reasonable estimation of the plasmapause location.

Goldstein et al. applied the technique of identifying the plasmapause location from the He^+ edge of the EUV data by eye and mapping the extracted plasmapause to the equatorial plane to to a larger set of 3143 EUV images between 2000 - 2004. The plasmapause identifications in L value and magnetic local time are available at `https://enarc.space.swri.edu/EUV/`. The plasmapause locations from this database determined by Goldstein et al. are used in the research presented in Chapter 8 of this thesis, which is referred to as the Goldstein plasmapause database.

The Goldstein plasmapause database does not have complete coverage of the plasmapause location for the full period between 2000 - 2004. This may be due to the time intensive nature of extracting the plasmapause locations by eye from the EUV images or it could be due to limitations in the EUV data such as a limited number of observations where the plasmasphere is bright enough to easily detect the He^+ edge. Alternatively, Goldstein et al. may have taken a more targeted approach and only determined the plasmapause location during specific periods of interest, such as geomagnetically active periods e.g. Goldstein et al. (2004a). However, the Goldstein plasmapause database identifies multiple plasmapause locations in each magnetic local time sector and also identifies the inner (Earthward) and outer

boundaries of features such as the plasmaspheric drainage plume.

Alternative databases of plasmapause locations extracted from the He^+ edge of the EUV observations are available, for example, Katus et al. (2015) and Zhang et al. (2017) which use automated techniques to identify the plasmapause location from the EUV data. The database of plasmapause locations identified from EUV data by Zhang et al. (2017) were explored as an alternative database to the Goldstein plasmapause database that was used in this thesis. However, Figure 4.9 shows the distribution of the differences in the radius of the plasmapause locations identified from both the Goldstein et al. and Zhang et al. (2017) databases and illustrates that while the majority of the plasmapause identifications agree with those of Goldstein et al. within ± 1 R_E, some of the Zhang et al. (2017) plasmapause locations lie up to approximately ± 4 R_E away from the Goldstein et al. locations. Such large differences in the location of the plasmapause will have a significant impact on the magnetic field line tracing used to map the plasmapause location to ionospheric altitudes. The reason for the large differences in the plasmapause location from both data sets is unknown but may be due to the different methods used to identify the plasmapause, with Goldstein et al. identifying the plasmapause by eye in each EUV image and the automated technique applied by (Zhang et al., 2017). It may be that the different methods identify the plasmapause at different brightness thresholds or that the automated method occasionally picks out an erroneous plasmapause due to poor or inconsistent EUV data.

Due to the large difference in the plasmapause locations between the two databases, the decision was taken to use the Goldstein et al. database as these plasmapause identifications were individually extracted by eye and so each EUV image and subsequent plasmapause identification was carefully checked. Future work could involve an investigation into the use of different plasmapause databases and identification methods.

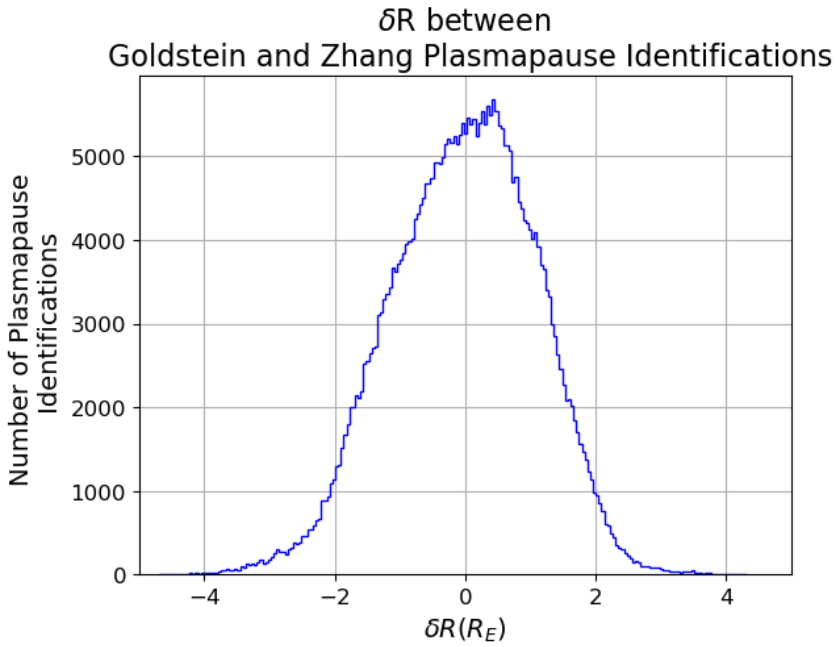

Figure 4.9: Figure showing a histogram of the radial difference in plasmapause locations identified by Goldstein et al. and by Zhang et al. (2017).

4.4 Forecasting the Auroral Oval: The OVATION-Prime 2013 Model

The OVATION-Prime 2013 (OP-2013, Newell et al., 2014) auroral forecast model predicts the precipitating electron and proton auroral flux based on upstream solar wind conditions, measured at the Lagrange 1 (L1) point. Particle precipitation measurements collected by the Special Sensor J (SSJ) instruments onboard the DMSP satellites are used as the underlying model data, with additional UV auroral data from the Global Ultraviolet Imager (GUVI) instrument onboard the Thermosphere Ionosphere Mesosphere Energetics and Dynamics (TIMED) satellite which was added to improve the performance of the model at higher values of Kp, between Kp = 5 to Kp = 8 (Newell et al., 2014).

The OP-2013 model grid covers 50° - 90° magnetic latitude (MLAT) and all magnetic local time sectors with a grid resolution of 0.5° MLAT and 0.25h MLT (Newell et al., 2010b, 2014). In each model grid point, the auroral power is predicted from a linear scaling of the upstream solar wind conditions in the form of Equation 4.5, where, $\frac{d\phi_{MP}}{dt}$ is the solar wind-magnetosphere coupling function, given

by Equation 4.6 (Newell et al., 2007) and a and b are constants. The auroral power in each grid point is calculated for each of the four types of diffuse, monoenergetic, broadband and ion aurora, as discussed in Section 2.6 and Chapter 3, as a function of season.

$$Auroral\ Power(MLAT,\ MLT,\ season,\ auroral\ type) = a + b\frac{d\phi_{MP}}{dt} \tag{4.5}$$

The solar wind driving of the magnetosphere is calculated from the empirically derived solar wind coupling function (Newell et al., 2007) in Equation 4.6, where the B_z and B_y are components of the interplanetary magnetic field, B_T is the total magnetic field strength, v_{sw} is the solar wind velocity and θ_c is the IMF clock angle.

$$\frac{d\phi_{MP}}{dt} = v_{sw}^{4/3} B_T^{2/3} sin^{8/3}\left(\frac{\theta_c}{2}\right) \tag{4.6}$$

The resultant maps of linear scaling coefficients are then used to predict the precipitating electron and proton fluxes under all upstream conditions. Full details of the OP-2010 and OP-2013 models can be found in (Newell et al., 2007, 2009, 2010b, 2014).

4.4.1 Met Office Implementation of OVATION-Prime 2013

A version of the OP-2013 auroral model was used operationally in daily space weather forecasts at the UK Met Office Space Weather Operations Centre until December 2020. The operational implementation of the OP-2013 model at the Met Office takes the previous 4 hours of solar wind data as input to produce an auroral forecast that predicts the occurrence of aurora in 30 minutes time, i.e. 30 minutes after the most recent solar wind observations. A weighted average is applied to the solar wind parameters which gives the highest weighting to the most recent solar wind data. Using 4 hours of solar wind data makes the operational auroral forecast less vulnerable to solar wind data outages and also incorporates some time history of the solar wind conditions which might result in a slightly different magnetospheric response. In this thesis, archived solar wind data provided by the U.S. National

Oceanic Atmospheric Administration (NOAA) were used to reproduce the auroral *hindcasts* between 2000 - 2002. Auroral forecasts that were produced in near real time by Met Office space weather forecasters were not evaluated in this thesis. The auroral hindcast dataset produced from the Met Office operational implementation of the Ovation-Prime 2013 nowcast model that was used in this study was provided by the Met Office and is available at: http://doi.org/10.5281/zenodo.4653288 (Marsh and Mooney, 2021).

In the operational implementation of the model, the combined precipitating particle flux from all types of aurora at each grid point is linearly scaled into an estimated probability of aurora occurring which is interpreted as the probability of an observer seeing the visible aurora. In the version of OP-2013 that was used operationally at the Met Office, the predicted auroral fluxes are converted into a probability of aurora occurring. The linear conversion applied to convert the auroral flux to a probability of aurora in each grid point is $probability = 8 \times auroral\ flux + 10$, where the auroral flux is the combined precipitating particle flux from all four types of aurora in each grid cell in erg cm^{-2} s^{-1}. A further scaling is then applied to the probability of aurora occurring nowcast in each grid cell: $probability = 1.8 \times probability$, with a maximum probability of 100%. The conversion of auroral flux to probability implemented in this version of OP-2013 at the Met Office is as originally developed by the U.S. NOAA Space Weather Prediction Center (SWPC) and could be further refined. The forecast probabilities were tuned by SWPC in response to citizen science observations under the assumption that the forecast probabilities of aurora occurring were mainly used by members of the public and may under-predict the probability of aurora occurring (Rodney Viereck, private communications).

An example output of the Met office implementation of the version of the OP-2013 model is shown in Figure 4.10. The figure was reproduced using archived solar wind data from 16 July 2000 during the Bastille Day geoeffective solar storms. In this version of the model, the forecast location of the auroral oval is plotted over a geographical map with the colours showing the probability of aurora occurring in

30 minutes time.

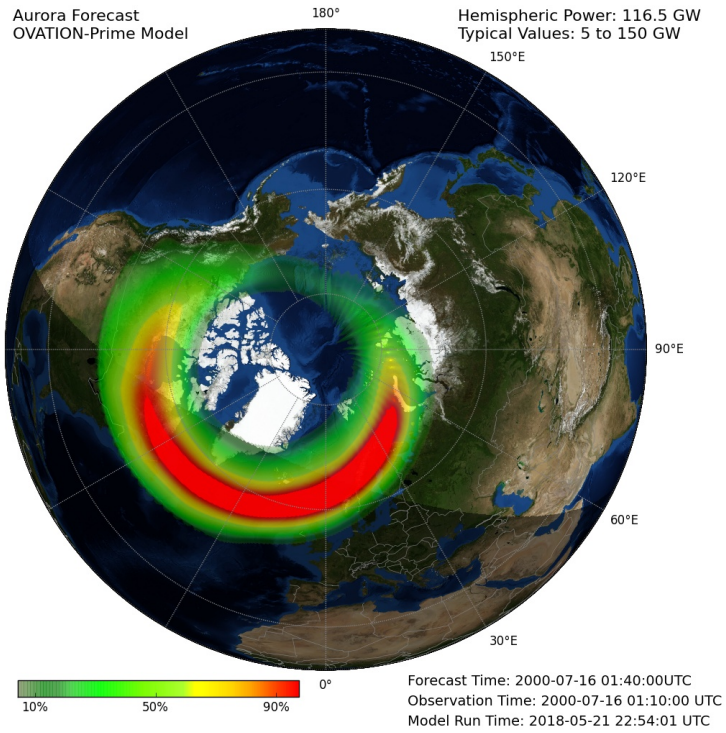

Figure 4.10: An example auroral forecast output from the operational implementation of the version of the OP-2013 model at the Met Office Space Weather Operations Centre. This example was produced using archived solar wind data from 16 July 2000 during the Bastille Day storm. The map shows the forecast location of the auroral oval in 30 minutes time with the colour bar showing the forecast probability of aurora occurring, where green/red indicates a lower/higher probability of aurora.

A version of the OP-2013 auroral forecast model has been implemented in leading space weather forecasting centres including the SWPC, the U.S. Department of Defense, Space Weather Operations Centre (Jones et al., 2017) as well as the UK Met Office. The OP-2013 model was originally supplied to the Met Office by SWPC, however the operational implementations at the Met Office and SWPC have since diverged. In 2016, the Met Office converted the code to Python and returned the Python version of OP-2013 to SWPC. In October 2020, SWPC implemented an upgraded version of OVATION termed *OVATION 2020* which differs from the Met Office implementation. OVATION 2020 uses an improved geomag-

netic field model to provide a more accurate auroral location. In addition, OVATION 2020 provides the modelled energy flux in erg cm^{-2} s^{-1} as well as the scaled probability of seeing the aurora. SWPC have also implemented an estimate of the solar wind driving based on Kp data to use as an alternative to run the model when upstream solar wind data is unavailable. Details of the SWPC auroral forecast using OVATION 2020 can be found on the SWPC website.

In the operational version of OP-2013 implemented at the Met Office and used in this thesis, a fixed solar wind propagation time of 30-minutes is assumed such that the model produces a forecast of the aurora 30-minutes ahead. This corresponds to a fast solar wind speed of $\sim$ 700 km/s. The Met Office also run a version of OP-2013 which produces auroral forecasts up to 3 days ahead, and which is driven by Kp index forecasts instead of solar wind data. This Kp-driven version of OP-2013 was developed at the Met Office independently of the SWPC Kp-driven model. In this thesis, the 30-minute auroral forecast is referred to as a 'nowcast' to distinguish it from the alternative 3-day auroral forecast.

4.5 Additional Data Sources

A number of additional data sources have been used in this thesis including Van Allen Probe, solar wind and geomagnetic activity index data which are described in the following sections.

4.5.1 Van Allen Probes

The Van Allen Probes were a set of 2 identical spinning spacecraft launched in 2012 to explore the characteristics and behaviour of Earths radiation belts. The Van Allen Probes were placed into elliptical Earth orbits in the inner magnetosphere with a perigee of 0.1 R_E and an apogee of 4.7 R_E.

The Van Allen satellites carried a number of radiation hardened instruments which could withstand the high energy particle regime of the radiation belts, including Energetic Particle Composition and Thermal Plasma Suite (ECT), the Electric and Magnetic Field Instrument Suite (EMFISIS), the RBSP Proton Spectrometer (RPS), the Electric Field and Waves Instrument (EFW) and the RBSP Ion Compo-

sition Experiment (RBSPICE).

In this thesis, plasma wave data from the EMFISIS instruments have been used to determine the plasma density in observations of the inner magnetosphere as per Equation 2.3 in Chapter 2. In addition, data from the ECT Helium Oxygen Proton Electron (HOPE) instrument which measures particles with energies in the range $\leq$ 20 eV - 45 keV have been used to observe the distribution of particle populations in the inner magnetosphere.

4.5.2 Kp Index

The Kp index is a 3 hourly index which quantifies the intensity of geomagnetic activity on a planet-wide scale and is considered a proxy for the level of solar wind driving of the magnetosphere (Bartels et al., 1940; Bartels, 1949; Matzka et al., 2021a,b). The Kp index is determined from disturbances in the horizontal component of the Earth's magnetic field measured by 13 geomagnetic observatories at subauroral latitudes (between $44 - 60^{\circ}$) in both the northern and souther hemispheres. The Kp index is determined from the weighted mean of the measurements from the 13 observatories to average out local time and seasonal variations in the observed geomagnetic disturbance. The weighted-mean deflection is then converted to the Kp index scale, which is a quasi-logarithmic scale with 28 possible values of $0o, 0+, 1-, 1o, 1+, 2-, ..., 8+, 9-, 9o$, using conversion tables originally developed by Bartels et al. (1939).

The Kp index is used in many magnetospheric and space weather applications including, for example, the parameterisation of empirical magnetospheric magnetic field models (Tsyganenko, 1989) and global patterns of auroral precipitation (Hardy et al., 1985). It is also used by NOAA SWPC and the Met Office to categorise geomagnetic storms, ranging from a minor storm for Kp = 5 to an extreme storm for Kp = 9.

The Kp data used in this thesis were provided by International Service of Geomagnetic Indices (ISGI) German Research Centre (GFZ) Potsdam and are publicly available.

4.5.3 Solar Wind Data

4.5.3.1 ACE Solar Wind Data

The Advanced Composition Explorer (ACE) spacecraft is located along the Sun-Earth line and makes in-situ measurements of the incoming solar wind and interplanetary magnetic field (IMF) upstream of the Earth. The ACE satellite orbits around the Lagrangian 1 (L1) point which is an equilibrium point where the gravitational force of the Sun and the Earth are balanced.

The upstream solar wind data are used extensively in solar wind - magnetospheric coupling research and often provide the input data for many magnetospheric and space weather models, including the OP-2013 auroral forecast model.

Historical ACE data from 2000 - 2002, provided by NOAA, were used in this thesis to produce the auroral hindcasts using the Met Office operational nowcast version of OP-2013.

4.5.3.2 OMNIWeb Data

The OMNIWeb dataset is a large dataset which combines near-Earth solar wind plasma and IMF data from several spacecraft in geocentric or L1 orbits, including ACE. The OMNIWeb data are available in low and high resolution (1-minute, 5-minute and hourly averaged) and span from 1963 to present day. The OMNI2 dataset also includes geomagnetic activity indices such as Kp.

OMNIWeb data are used in this thesis as input to the Tsyganenko 1996 magnetospheric model (Tsyganenko and Stern, 1996). OMNIWeb data are provided by the NASA Goddard Space Flight Center, Space Physics Data Facility and publicly available at `https://omniweb.gsfc.nasa.gov/html/ow_data.html`.

Chapter 5

Verification Methodology

5.1 Auroral Forecast Verification; An Application of Auroral Boundary Data

Forecast evaluation is an important step in both the implementation and development of space weather forecast models. Model verification assesses the quality of the forecast by comparing the output to an appropriate, independent and unbiased set of observational data. Verification can provide information on the skill, accuracy and reliability of models and provides quantitative benchmarks to compare different forecast models. A variety of forecasting methods and metrics exist. The research presented in this thesis focuses on three main forecast verification methodologies; truth tables, relative operating characteristic analysis and reliability analysis.

5.1.1 Evaluating Deterministic Forecasts

The output of a forecast model generally falls into two categories: those that either return a discrete prediction out of a finite set of possible values; or those that return a continuous, probabilistic prediction, that provide an estimate of the likeliehood of an outcome. Forecast models that provide discrete forecasts are termed *deterministic forecasts* and forecasts that predict the likelihood of a certain outcome occurring are termed *probabilistic forecasts*. The verification methods and metrics applied to a given forecast model depend on whether the model provides a deterministic or a probabilistic forecast.

The verification study presented in this thesis evaluates the operational implementation of the OP-2013 model at the Met Office against the observed auroral boundaries determined by Longden et al. (2010). The OP-2013 model is a probabilistic model as it outputs a predicted probability of aurora occurring in each grid cell. However, it can also be assessed as a deterministic forecast by discretising the forecasts into two outcomes such that:

- **Outcome 1** the aurora are predicted to occur, defined by a forecast probability of aurora occurring greater than a specified value.
- **Outcome 2** the model predicts that the aurora will not occur when the probability of aurora occurring is less than the specified value.

The auroral boundaries provide a poleward and equatorward limit on where the auroral emission was observed in each magnetic local time sector, providing a band of observed auroral emission in magnetic latitude. Between these two boundaries, the observational outcome is that the aurora was observed to occur, outside of these boundaries (i.e. at higher latitudes of the poleward boundary or at lower latitudes than the equatorward boundary), the aurora did not occur. The forecasts can then be evaluated where observational data are available.

5.1.1.1 Truth Tables

Truth tables are a method of model verification that is often applied to deterministic forecasts to compare the predicted forecast against the observed outcome. Truth tables present the verification data in a $Y \times Z$ table, illustrating the $Y \times Z$ possible combinations of forecast and observation pairs. The simplest is a 2×2 truth table that compares discrete predictions (an event will or will not happen) to discrete occurrences (an event did or did not happen).

An example 2×2 truth table is shown in Table 5.1. For each forecast that has corresponding observational data, the predicted and observed outcomes are evaluated. The truth table is populated by increasing the value in the relevant table entry depending on the outcome of forecast-observation comparison. There are four possible outcomes of a 2×2 truth table.

- **True positive or hit:** the event is forecast to occur and was subsequently observed.
- **False positive or false alarm:** the event is forecast to occur but subsequently did not occur.
- **False negative or missed forecast:** the event is not forecast to occur but it subsequently did occur.
- **True negative or correct rejection:** the event is not predicted to occur and is not subsequently observed.

Table 5.1: An example 2×2 truth table.

	Observed		
Forecast		Yes	No
	Yes	A = True Positives	B = False Positives
	No	C = False Negatives	D = True Negatives

A number of useful verification statistics can be derived from truth tables. These include the Hit Rate (Equation 5.1) which is the number of true positives divided by the total number of *yes* observations and the False Alarm Rate (Equation 5.2) is the number of false positives divided by the total number of *no* observations. The False Alarm Ratio, defined by Equation 5.3, is the fraction of *yes* forecasts that are false positives. The proportion of True Positives, defined by Equation 5.4, is the fraction of *yes* forecasts that were true positives. The proportion of False Negatives, defined by Equation 5.5, is the fraction of *no* forecasts which were false negatives. The accuracy, defined by Equation 5.6, is the proportion of correct forecasts (either true positives or true negatives) out of all the data in the truth table. In Equations 5.1 - 5.6, A, B, C and D are as defined in Table 5.1. The definitions of these equations have been taken from Wilks (2006). Each verification metric on its own provides a limited summary of the forecast performance, particularly as most of the metrics, with the exception of accuracy, are calculated using only two values from the truth table. Although the accuracy is calculated using all the coefficients in the truth table, it can be dominated by the number of correct rejections which may give a

misleadingly high value and hides the false alarms and missed forecasts. Verification analysis is often reported using a combination of metrics which provide a more complete description of the model performance.

$$\text{Hit Rate} = \frac{A}{(A+C)} \tag{5.1}$$

$$\text{False Alarm Rate} = \frac{B}{(B+D)} \tag{5.2}$$

$$\text{False Alarm Ratio} = \frac{B}{(A+B)} \tag{5.3}$$

$$\text{Proportion of True Positives} = \frac{A}{(A+B)} \tag{5.4}$$

$$\text{Proportion of False Negatives} = \frac{C}{(C+D)} \tag{5.5}$$

$$\text{Accuracy} = \frac{A+D}{(A+B+C+D)} \tag{5.6}$$

5.1.1.2 Relative Operating Characteristic (ROC) Analysis

ROC analysis (Swets et al., 1955; Swets, 1988; Mason, 1982) can also be used to assess deterministic forecasts by evaluating how well a forecast model correctly predicts a binary event, in this case, whether the aurora occurs or not. ROC curves evaluate the model's ability to distinguish between the observed occurrence and non occurrence of an event, known as the model discrimination. ROC curves are obtained by plotting the Hit Rate against the False Alarm Rate, calculated from the truth table. An example ROC curve is shown in Figure 5.1, produced from a single value for the Hit Rate and False Alarm Rate calculated from a truth table which forms the *knee* of the ROC curve. A good forecast model which exhibits high discrimination in distinguishing between events and non events will have a high Hit Rate and a low False Alarm Rate such that the knee of the ROC curve

tends towards the top left hand corner of the plot, maximising the area under the curve. As described previously, for a probabilistic forecast, a minimum threshold probability can be set so that only forecasts with a value greater than the threshold value are considered to be a positive forecast that the event will occur. The threshold can be increased incrementally between 0 - 100% to produce a truth table for each probability threshold. This allows the verification statistics, such as the Hit Rate and False Alarm Rate to be determined for each probability threshold. In the analysis presented in this thesis, 10% probability increments have been used. Calculating the verification statistics from a series of truth tables for different forecast thresholds provides a higher number of data points for the ROC curve and can inform the user at what probability threshold the model performs best as a deterministic model.

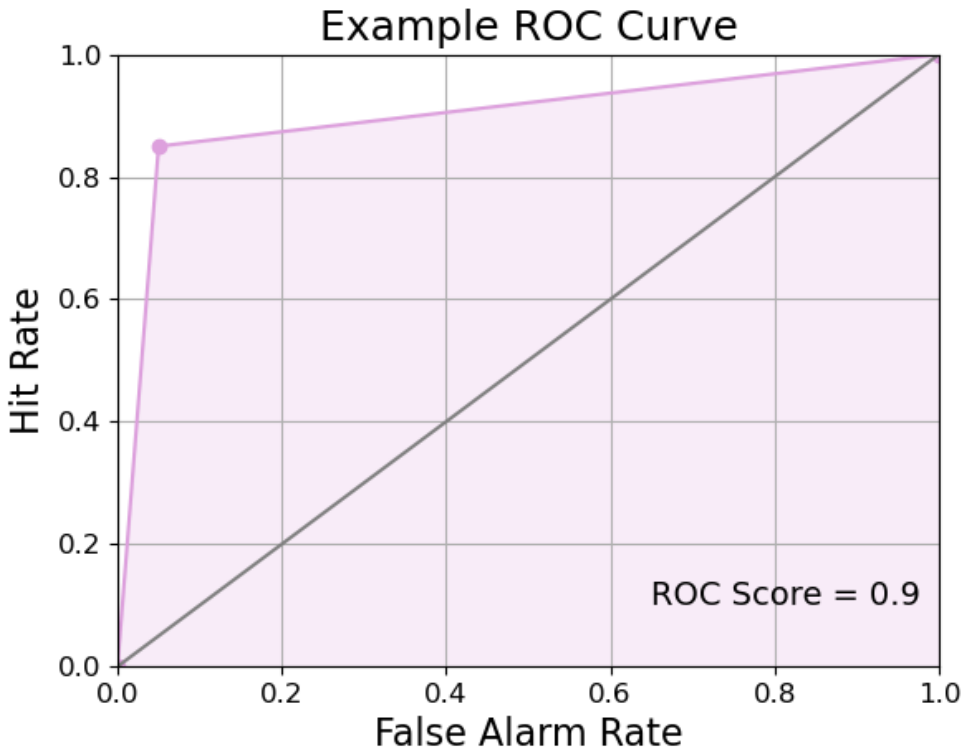

Figure 5.1: A figure of an example ROC curve. The ROC curve is shown in pink. The shaded area under the ROC curve is the area used to calculate the ROC score, shown in the lower right corner. The grey line indicates the y = x line of no skill.

A ROC score provides a quantitative summary of the model discrimination indicated by the ROC plot and a quantitative measure to fairly compare different models and monitor upgrades made to models. The ROC score is defined as the proportional area under the ROC curve and ranges between 0 - 1. A ROC score of 1 indicates that the model always correctly discriminates events from non-events. A ROC score of 0 means that the model always incorrectly discriminates events from non-events, i.e. the observations are always the opposite to what is forecast. A ROC score of 0.5 indicates that the forecast model has no skill at discriminating events from non-events. In this case, the model is no more skillful than a 50:50 chance prediction. A ROC score above 0.5 indicates that the Hit Rate exceeds the False Alarm Rate for the majority of forecasts. If the model has a perfect ROC score of 1.0, the Hit Rate tends towards 1.0 for all non-zero values of the False Alarm Rate and 0.0 when the False Alarm Rate is zero. All forecast models that have a ROC score greater than 0.5 have some skill and ability to discriminate events from non-events.

5.1.2 Evaluating Probabilistic Forecasts

5.1.2.1 Reliability Analysis

Reliability or attribute diagrams (Jolliffe and Stephenson, 2012; Wilks, 2006) assess the reliability of the probabilities that are forecast by a model by plotting the observed occurrence rate (or observed frequency) of an event determined from the observational data, within different probability bands.

To produce a reliability curve, the forecast probabilities are divided into probability bins. In this thesis, 10% probability intervals have been used. To calculate the observed occurrence rate (or observed frequency) for a single probability bin, for each forecast in the probability bin, the number of times that the corresponding observation is that the event occurred (i.e. that the aurora was observed) is counted. This value is then divided by the total number of observations for this forecast probability. The occurrence rate is essentially the fraction of times that the event was actually observed to occur when a forecast probability of the event occurring between X - Y% was predicted. For example, for a probability bin of 10 - 20%, say

there are 100 times that the forecast probabilities lie within this range with corresponding observations. If in 25 out of these 100 forecast-observation pairs the event was observed, the occurrence rate for this forecast bin would be 25%.

If the model is perfectly reliable, there will be a one-to-one correspondence between the forecast probability and the observed occurrence rate of aurora occurring in each forecast probability bin. The resulting reliability curve would form a diagonal line from (0,0) to (1,1). For example, for a perfectly reliable forecast, a probability bin centred on a forecast probability of p% will have an observed occurrence rate of p%. Reliability curves can be used to determine whether the forecast probabilities in each probability bin are being under-forecast or over-forecast by comparing the reliability curve to the diagonal, perfect reliability curve. If the points on the reliability curve lie above the diagonal, the probability values in that bin are being under-forecast i.e. the aurora occurs more frequently than the model predicts. Similarly, if the points on the reliability curve lie below the diagonal, the probability values in that bin are being over-forecast i.e. the aurora occurs less frequently than the model predicts. Reliability diagrams can therefore be used as a calibration curve to improve the forecast probabilities of the event occurring, predicted by the model by correcting the probabilities with which events are forecast. ROC curves and reliability diagrams provide complementary information and are often presented together in verification studies. Reliability analysis can only be applied to a series of model forecasts and observations to assess trends in whether the model is under-forecasting or over-forecasting the probability of an event occurring. It cannot be applied to a single forecast and observation pair.

Additional information can be added to a reliability diagram such as histograms showing the distribution of the forecast probabilities, the average within-sample climatology and the line of no skill. The average within-sample climatology is calculated from the observational dataset and is the proportion of observations in which the event is observed to occur out of the total available observation data. The line of no skill is calculated as the halfway between the perfect reliability diagonal line and the within-sample climatology. Reliability diagrams with the inclusion

of this additional information are known as attribute diagrams (Hsu and Murphy, 1986). An example attributes diagram is shown in Figure 5.2.

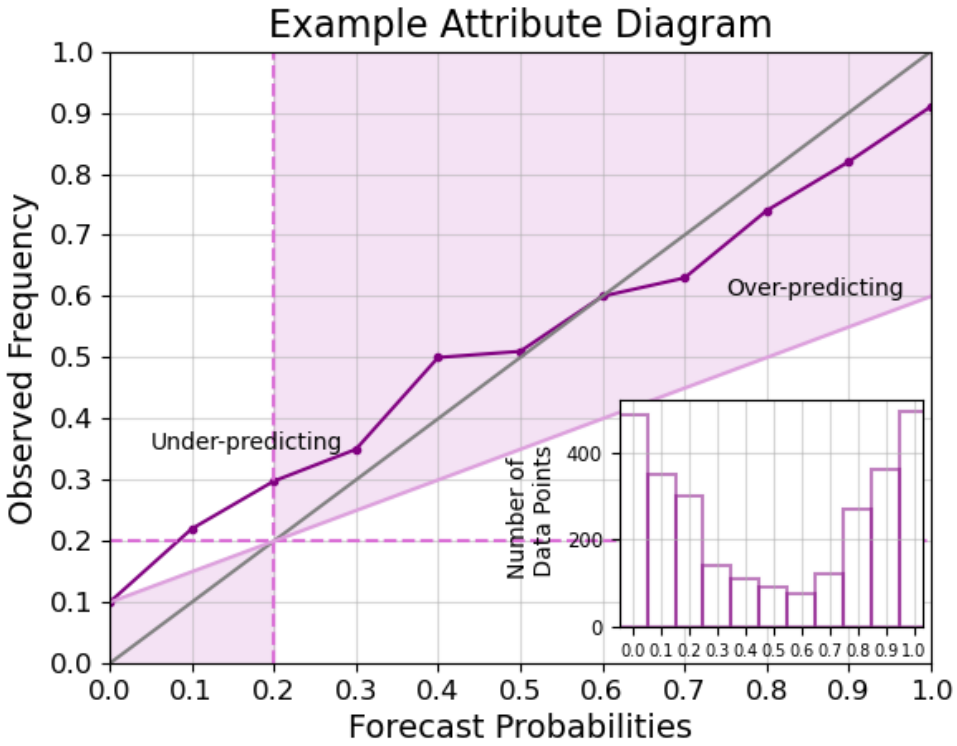

Figure 5.2: An example attributes diagram. The reliability curve is shown in solid purple. The grey line shows the y = x line of perfect reliability. If the reliability curve lies above/below the perfect reliability, the model is under-predicting/over-predicting the probability of occurrence. The dashed vertical and horizontal lines indicate the average within-sample observed climatology. The solid pink diagonal line indicates the line of no skill. Points on the reliability line which lie in the shaded region contribute positively to the Brier Skill Score. The histogram in the corner shows the distribution of the forecast probabilities.

5.1.3 Brier Skill Score

The Brier Score is the mean squared error between the forecast probability values (y_i) and the corresponding binary observations (o_i), where an observation value of $o_i = 1$ represents an observation where the event occurred and an observation value of $o_i = 0$ represents an observation where the event did not occur. The squared errors are then summed over n numbers of forecasts and divided by n to give the mean square error as shown in Equation 5.7.

$$Brier\ Score = \frac{1}{n}\sum_{i=1}^{n}(y_i - o_i)^2 \tag{5.7}$$

By comparing the reliability curve with a reference forecast, a quantitative measure known as the Brier Skill Score (Brier, 1950; Murphy, 1973) can be determined from the reliability analysis. The Brier skill score evaluates how well the forecast probabilities from the model compare with those forecast by a reference model. Points on the reliability curve which lie within the shaded region in Figure 5.2 delimited by the line of no skill and the vertical climatology line contribute positively to the Brier Skill Score. The within-sample observed climatology (mean occurrence of the event determined from observations) is a commonly used reference forecast and is used in the analysis presented in this thesis. To calculate the Brier Score of the reference climatology, all forecast probabilities (y_i) were set to the within-sample climatology value. However, the reference model could also be a previous generation of the same model, for example, to quantitatively assess improvements and upgrades made to the model which may be expected to improve the probabilities forecast by a model.

The equation to calculate the Brier Skill Score is shown in Equation 5.8, where the Brier Score in the numerator refers to the Brier Score of the forecast model and $Brier\,Score_{ref}$ refers to the Brier Score of the reference forecast model.

$$Brier\ Skill\ Score = 1 - \frac{Brier\ Score}{Brier\ Score_{ref}} \tag{5.8}$$

Brier skill scores range from $-\infty$ to +1 with positive scores indicating that the forecast model being tested is more skilled than the reference model and negative scores indicating the opposite. A Brier skill score of zero indicates that the model provides no improvement on the reference model. If the observed climatology is being used as the reference model, a Brier Skill Score of zero suggests that the probabilities predicted by the forecast model provide no improvement on forecasting the average, climatological probability of aurora occurring.

In summary, forecast verification assesses the performance of forecast models

by comparing the model output against a suitable observational dataset. ROC and reliability analysis are standard methods used in forecast verification by the weather community (for example, Dube et al., 2017) and they are being adopted by the space weather community. They have been used to evaluate flare forecasts from the Met Office Space Weather Operations Centre in studies by Murray et al. (2017) and Sharpe and Murray (2017), to evaluate the performance of a new radiation belt forecast model (Forsyth et al., 2020b) and to assess a sudden storm commencement probabilistic forecast model (Smith et al., 2020). ROC scores and Brier Skill Scores provide quantitative summary values of the model performance.

Chapter 6

Evaluating OVATION-Prime 2013 Auroral Forecasts Against Observed Auroral Boundaries

The aurora is a readily visible phenomenon of interest to many members of the public and has become more accessible via auroral alert systems such as AuroraWatch UK and Aurorasaurus (Case et al., 2017; MacDonald et al., 2015). The aurora and associated phenomena can significantly impact communication networks and ground-based infrastructure. Forecasting the location of the auroral oval is therefore a key component of space weather forecast operations. A version of the solar wind driven OVATION-Prime 2013 (OP-2013) auroral precipitation model (Newell et al., 2014) is currently used by the UK Met Office Space Weather Operations Centre (MOSWOC). The operational implementation of the version of the OP-2013 model at the UK Met Office evaluated in this study delivers a 30-minute forecast of the location of the auroral oval and the probability of observing the aurora, derived from the predicted particle fluxes.

This chapter presents an evaluation of the performance of auroral forecasts from the 30-minute forecast version of OP-2013 that was being used operationally at the Met Office until December 2020. The model's ability to predict the location and probability of the aurora occurring is assessed by comparing the forecasts with observed auroral boundaries determined by Longden et al. (2010) from global

FUV images of the auroral oval obtained by the IMAGE satellite between 2000 and 2002, using weather forecast evaluation techniques as described in Chapter 5. The analysis assesses the model performance in predicting the location of the auroral oval using truth tables and the results are presented using Relative Operating Characteristic (ROC) curves. The probabilities of aurora occurring output by the model are also assessed using reliability curves. The performance of the MOSWOC implementation of the OP-2013 model is evaluated by season, in magnetic local time sector and under different levels of geomagnetic activity, defined by Kp level and substorm phase.

A selection of the results presented in this chapter have been published in *Space Weather* with the citation: Mooney, M. K., Marsh, M. S., Forsyth, C., Sharpe, M., Hughes, T., Bingham, S., Jackson, D. R., Rae, I. J. and Chisham, G (2021) Evaluating auroral forecasts against satellite observations, *Space Weather*, https://doi.org/10.1029/2020SW002688.

6.1 Introduction

Forecasting the location and intensity of the aurora is of interest to many stakeholder industries such as the aviation, defense and energy sectors (Cannon et al., 2013). The free electrons and excited molecules in the upper atmosphere are known to degrade long-range radio communications in high to ultra-high frequency (HF/UHF) wavebands used by aircraft (Moore, 1951; Harang and Stroffregen, 1940; Jones et al., 2017; Cannon et al., 2013). Radio wave scattering can cause radar backscatter, resulting in radar clutter (Elkins, 1980; Jones et al., 2017), and can also result in broadband noise in radio receivers (Benson and Desch, 1991; Jones et al., 2017). Increased electron precipitation in the upper atmosphere can also cause increased absorption of radio signals in the ionosphere (Greenberg and LaBelle, 2002; Jones et al., 2017). Ionospheric currents associated with enhanced auroral activity can induce currents in the ground which can damage ground-based infrastructure such as electricity supply networks e.g. (Erinmez et al., 2002; Cannon et al., 2013; Freeman et al., 2019; Smith et al., 2019). In addition, forecasting the occurrence of

visible aurora is of importance for auroral tourism and is a key tool in promoting public awareness and engagement with space weather, through projects such as Aurorasaurus (MacDonald et al., 2015) and AuroraWatch UK (Case et al., 2017).

The OVATION-Prime 2013 (OP-2013) auroral forecast model (Newell et al., 2014) is an empirical model which predicts the location of the auroral oval based on the upstream solar wind conditions. The model uses average particle precipitation maps obtained from Defense Meteorological Space Program (DMSP) satellites (Hardy et al., 1984, 1985) spanning 21 years between 1 January 1984 to 31 December 2005, UV auroral data from the Global Ultraviolet Imager onboard the TIMED satellite and real time solar wind conditions measured at the L1 point to produce maps of the predicted auroral flux. A full description of the OP-2013 model and the Met Office operational implementation of the model at MOSWOC has been provided in Chapter 4.

In this chapter, the 30-minute auroral forecast is referred to as the *nowcast* version to distinguish it from an alternative 3-day Kp driven version of the OP-2013 model developed at the Met Office. The Kp driven version of OP-2013 is not assessed. In this study, hindcasts of the output from the 30-minute nowcast version of OP-2013 used at the Met Office were produced using historical solar wind data for the period between May 2000 to October 2002, not auroral forecasts that were issued in near real time by the Met Office.

Figure 6.1 shows an example hindcast for the northern hemisphere from 25 September 2000 produced using the Met Office 30 minute nowcast version of the OP-2013. The model output was produced using historical Advanced Composition Explorer (ACE) solar wind data, provided by NOAA. The auroral oval is plotted on geographic coordinates with the colour scale showing the forecast probability of aurora occurring. The operational implementation of the model assumes a fixed 30 minute propagation time for the solar wind measured at the L1 point to arrive at Earth, providing an auroral forecast for both the northern and southern hemispheres 30 minutes ahead of the current time.

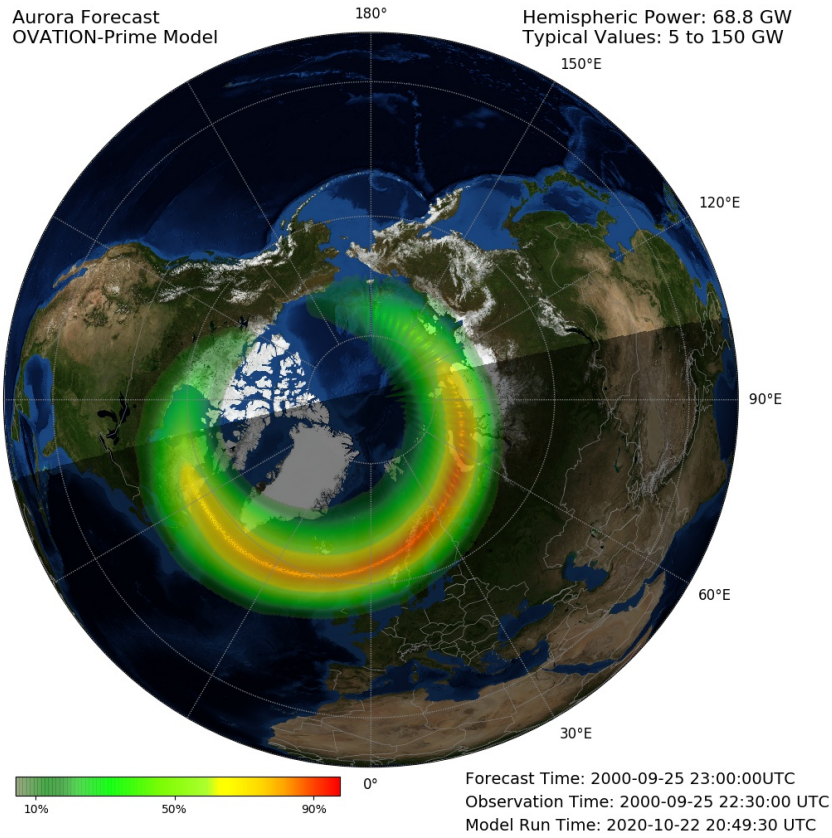

Figure 6.1: An example output forecast from the Met Office operational implementation of the OP-2013 nowcast model showing the northern hemisphere auroral forecast 30 minutes ahead for 23:00 on the 25 September 2000, in geographic coordinates. The central meridian is centred on 2300 local time. The colour scale shows the probability of aurora occurring with green/red showing lower/higher probabilities. The day/night terminator is indicated on the map as the line separating the dark and light faces of Earth and the estimated total hemispheric auroral power is shown in the top right hand corner.

6.1.1 Observational Auroral Boundary Data

In this study, the poleward and equatorward auroral luminosity boundaries determined from the IMAGE WIC data by Longden et al. (2010) are used as a *ground truth* observational data set to compare with the auroral hindcast probability maps. A full description of the auroral boundary identification was presented in Chapter 4. The auroral boundaries from the WIC dataset are used as the WIC instrument is sensitive over the largest wavelength range of auroral emission and thus is most

comparable to the auroral emission predicted by the model, compared to the SI12 and SI13 datasets. Generally, the precipitating electrons contribute a higher proportion of the number flux, energy flux and hemispheric power of the aurora than the precipitating ions, particularly for higher levels of geomagnetic activity (Hubert et al., 2002; Newell et al., 2009). In addition, the WIC instrument also had a higher resolution than the SI12 and SI13 imagers. The auroral boundary data available for the northern auroral oval spanned 30 months from May 2000 to October 2002 (Chisham, 2017).

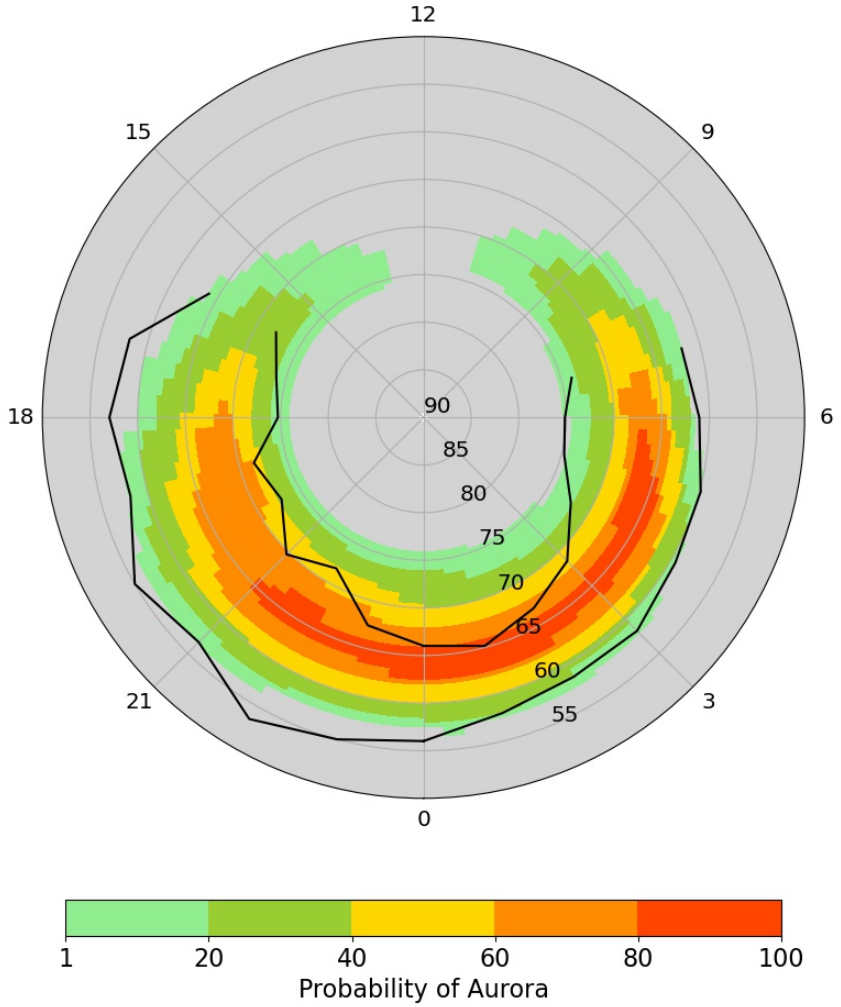

Figure 6.2: The OP-2013 forecast (colour shading) for the same date and time as in Figure 6.1 but plotted in AACGM magnetic coordinates (magnetic latitude by magnetic local time). The black lines show the equatorial and poleward boundaries of the aurora from Longden et al. (2010) for the forecast date and time. The central meridian is centred on 0000 local time and so the contours are effectively rotated by 1 MLT sector, compared to Figure 6.1.

Figure 6.2 shows a comparison of the probability nowcast maps from the Met Office operational version of OP-2013 with the poleward and equatorward auroral boundaries determined by Longden et al. (2010) in magnetic local time (MLT) and magnetic latitude coordinates. The colours show the 30 minute hindcast of the probability of aurora occurring as output from OP-2013. Grey regions indicate a forecast probability of aurora occurring of less than 1%. The black lines show the corresponding observed boundaries. In this example, there is a lack of observed auroral boundaries in some dayside local time sectors. While the method of Longden et al. (2010) aims to identify the poleward and equatorward auroral luminosity boundaries in each local time sector, the number of successful boundary identifications in dayside sectors is lower than on the nightside. The dayside aurora tends to be dimmer and thinner (Holzworth and Meng, 1975; Carbary, 2005) and is more contaminated with dayglow making it more difficult to identify the dayside auroral boundaries. In this study, the model is only evaluated where there are corresponding observational auroral boundaries.

6.2 Forecast Verification

For this analysis, the OP-2013 auroral hindcasts were produced spanning the period of May 2000 - October 2002, coinciding with the available observational auroral boundary data from Longden et al. (2010), using historical solar wind data measured by the ACE satellite, provided by the National Oceanic Atmospheric Administration (NOAA). In particular, and in contrast to Machol et al. (2012), Newell et al. (2010a) and Lane et al. (2015), this study examines the output auroral probabilities from the operational auroral hindcasts, rather than the physical quantities (the predicted auroral power, energy or auroral flux) provided by the underlying OP-2013 model. In the 30-minute nowcast version of the model, each hindcast requires four hours of input solar wind data, thus in order to ensure that the hindcasts were independent of one another, the hindcast dataset was down-sampled to a four hour resolution. To match the model hindcast and the observational ground truth auroral boundaries, the auroral boundaries that are closest in time and within ± 2.5 minutes of the 4 hour

separated forecast time were used. This resulted in 3360 corresponding hindcast and observation pairs. The model performance in predicting the location of the auroral oval is assessed using truth tables and the results are presented in ROC curves. The hindcast probabilities of aurora occurring output by the model are also assessed using reliability curves. A detailed description of truth tables, ROC and reliability analysis is presented in Chapter 5.

Truth tables evaluate how well the OP-2013 model discriminates between auroral and non-auroral regions, compared to the Longden et al. (2010) auroral boundaries and thus evaluates how well the model performs as a deterministic forecast for predicting the location of the auroral oval. Since OP-2013 provides a continuous probability output between 0 - 100%, rather than a binary output, the truth table analysis is performed by setting a threshold probability value, above which the deterministic forecast is that aurora will occur. The threshold probability levels are increased between 0 - 100% in 10% increments. For each forecast probability threshold, in each grid point with available hindcast and observation data where the hindcast probability is greater than the probability threshold, the hindcast and observational data are compared to determine the input value to the truth table from each individual grid point. This test is repeated for each probability threshold to build up truth tables for different forecast probability levels. From the truth tables for each level, the hit rate and false alarm rate can be calculated. These hit rates and false alarm rates are combined and presented on ROC curves (Swets et al., 1955; Swets, 1988; Mason, 1982). The model performance is summarised by a ROC score which is calculated from the area under the ROC curve.

Secondly, the validity of the forecast probabilities against the observed occurrence of the aurora is assessed using reliability (or attribute) diagrams (Wilks, 2006; Jolliffe and Stephenson, 2012). The forecast model would be completely reliable if, over all the occasions during the assessment period when the forecast probability was p, the aurora was observed $p\%$ of the time. However, if the forecast probabilities and observed frequencies of occurrence do not have a one-to-one correspondence, the reliability diagram provides information on whether the model

is under-forecasting or over-forecasting the probabilities. This information can be used to re-calibrate the forecast probabilities by rescaling the probability of aurora occurring against the observed occurrence of aurora.

The spherical geometry of the auroral forecasts means that the area of each grid cell is not uniform. This can influence how well the forecast is judged to perform. For example, near the pole, where aurora are not generally expected to occur, there is a greater concentration of grid cells than at 60°, where there is a greater likelihood of auroral activity. To account for this, the inputs into our ROC and reliability analysis were weighted by the cosine of the latitude of each grid cell (e.g. Young, 2010).

6.3 Model Evaluation Results

6.3.1 Overall Model Performance

Figure 6.3 shows the ROC curve from the comparison of all hindcast and observational pairs between May 2000 and October 2002 in all local time sectors. The ROC curve shows that at each 10% probability increment the model hit rate is higher than the false alarm rate. The probability bin centred on 10% has the largest difference between the hit rate and the false alarm rate, also referred to as the Peirce Score (Peirce, 1884). This shows that a probability of between 5 - 15% is the threshold at which the OP-2013 model performs the best at discriminating between regions of aurora and no aurora, compared to the observed auroral boundaries. Over the 2.5 year verification period, the model has a ROC score of 0.83, showing that the model performs well at predicting the location of the auroral oval. The overall ROC score compares well with that of other space weather forecast models. For example, Murray et al. (2017) evaluated M-class solar flare forecasts issued by the Met Office and found ROC scores of 0.71 - 0.82.

The uncertainty in the ROC score was evaluated using a bootstrap sampling method by randomly selecting 1000 forecast and observation pairs to calculate 1000 ROC scores. Although a range of ROC scores were determined (0.72 - 0.91), the 95% confidence level was 0.825 ± 0.05, in line with the overall result.

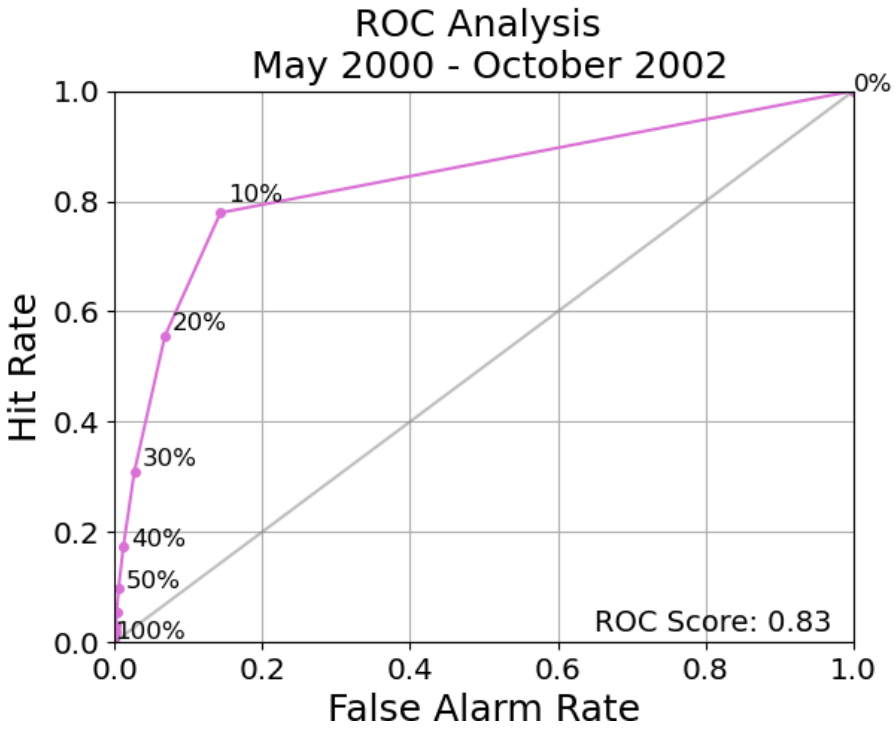

Figure 6.3: The result of the ROC analysis from the 2.5 years of model and observation comparisons. Each point on the ROC curve corresponds to the hit rate vs false alarm rate in each 10% threshold bin. The high ROC score of 0.82, defined by the fractional area under the ROC curve, shows that the model performs well as a deterministic forecast at predicting the location of the auroral oval.

Figure 6.4 shows the reliability diagram for the full $\sim$ 2.5 year verification period, plotting the occurrence rate of auroral observations for given forecast probability ranges. Figure 6.4 shows that the model largely under-predicted the occurrence of aurora, with the occurrence frequencies greater than the forecast probabilities for probabilities up to 80%. The lowest non-zero probabilities of 10% and 20% are under-predicted by a factor of $\sim$ 6 while the 80% probabilities are only under-predicted by a few percent. The 90% and 100% probability bins slightly over-predicted the probability of aurora occurring with the highest probability value of 100% over-predicting the occurrence by $\sim$ 20%, a factor of 1.25.

The dotted horizontal and vertical lines indicate the observed climatological frequency of occurrence of aurora is 0.30, calculated as the fraction of positive auroral observations that the aurora did occur out of the total number of auroral observations. The histogram in Figure 6.4 shows the number of data points in each

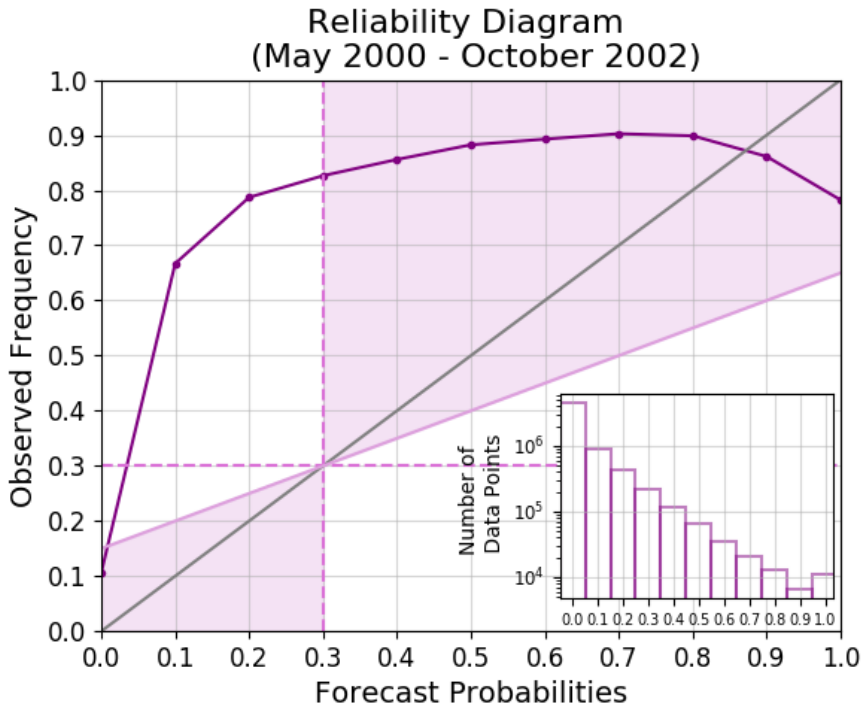

Figure 6.4: The result of the reliability analysis on the forecast probabilities of aurora occurring from the 2.5 years of model and observation comparisons, plotting the observed frequency of aurora against the forecast probability of aurora occurring. The histogram shows the distribution of the forecast probabilities over the 2.5 year period. The grey diagonal line indicates the perfect reliability line of 1:1 correspondence between the forecast probabilities and the observed aurora. Regions where the pink reliability line lies above/below the grey diagonal line indicate that the model is underforecasting/overforecasting the occurrence of aurora. The vertical and horizontal dashed lines show the observed climatology. The solid pink diagonal line of no skill delineating the shaded region, lies mid-way between the diagonal line of perfect reliability and the horizontal climatology line. Data points within the shaded region contribute positively to the Brier skill score.

forecast probability bin. The histogram shows that the probabilities forecast by the OP-2013 model are distributed across all probability bins and are not clustered around the climatology value. The lowest forecast probability bin contains all forecasts issued with a probability of 5% and lower and has the largest number of data points. This bin is dominated by the grid points where the main auroral oval is rarely or never predicted to occur, for example at low and high magnetic latitudes. The large number of forecasts with a low probability of aurora occurring in this bin correspond to a large number of observations where the aurora was not observed

to occur which reduces the overall observed climatology (mean occurrence). The solid pink diagonal line of no skill lies mid-way between the diagonal line of perfect reliability and the horizontal climatology line. Points on the reliability curve which lie above/below the line of no skill, contribute positively/negatively to the Brier skill score. Pink shading indicates the region where the forecast is skilful compared with the in-sample climatology. The majority of points on the reliability line lie in the shaded skill region except for probabilities of 10% and 20% which appear to be extremely under-predicted by the model. The Brier skill score of -0.03 indicates that overall, the model is not more skilful at predicting the probability that the aurora will occur than simply always forecasting the within-sample climatology of 0.30. While the Brier skill score indicates that the model provides no additional forecast skill compared to using a simple climatological forecast, the attributes diagram shows that the majority of forecast probabilities are skillful. The discrepancy in the conclusions drawn from these two analyses metrics highlights the increased understanding of the model performance that can be gained from using the full attributes diagram rather than only using the value of the Brier skill score.

6.3.2 Model Performance with Season

The seasonal variation in the precipitating particle number and energy flux density was examined by Newell et al. (2010b), as previously discussed in Chapter 3, and implemented in the OP-2013 model by calculating the predicted auroral flux as a function of season. Here, the seasonal variability in the model performance is evaluated. For the seasonal analysis, data and forecasts from 5 February 2001 into 4 February 2002 are used as this is the only complete year of WIC observational data including all seasons. The seasons were defined similarly to those used by Newell et al. (2010b) as being 90 days centred on the equinoxes and solstices. The start and end dates of each season were then adjusted slightly to include the six uncategorised days that fall between the seasons by this definition. The seasonal dates used in the analysis are as follows: spring is between 5 February to 6 May; summer is between 7 May to 8 August; autumn is between 9 August and 6 November; winter is between 7 November and 4 February.

Figure 6.5 shows the ROC curves for each season in 2001 - 2002. There is some seasonal variation in the ROC scores, with ROC scores ranging from 0.79 - 0.86; however, these scores are within the bootstrapping range and indicate that the model performs well in identifying the auroral oval in all seasons. The results of the ROC scores for each full season between May 2000 - October 2002 are summarised in Table 6.1. On average, the spring and winter ROC scores are consistently highest, with spring and winter seasons having mean ROC scores of 0.86, while the summer ROC scores were the lowest, with a mean of 0.77 across the three summer periods.

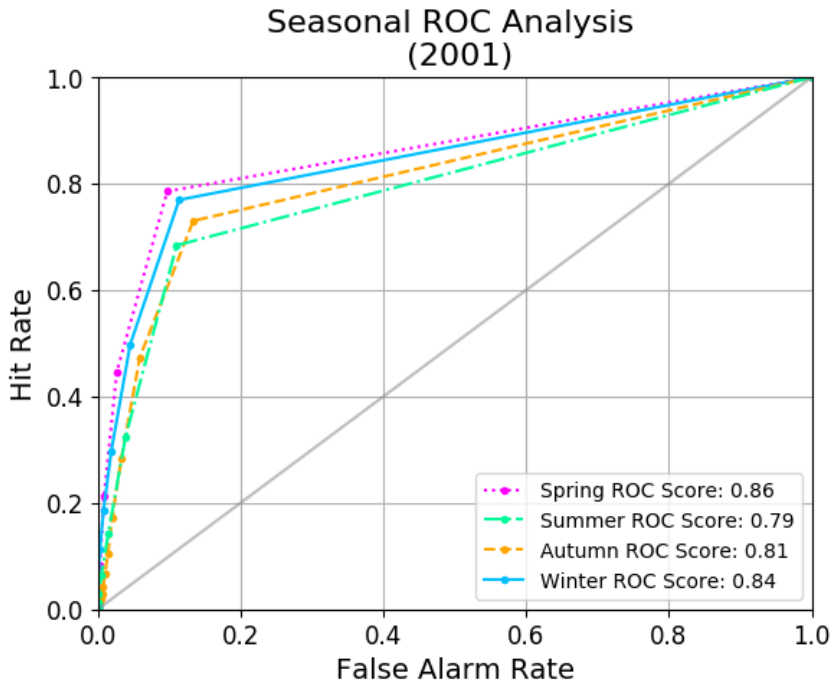

Figure 6.5: (a) The results of the ROC analysis for each season in 2001. The high ROC scores for each season demonstrate that the OP-2013 model performs well all year round.

The seasonal variation in the ROC score may be indicative of the model performance but it may also be due to the seasonal variations in the identification of the auroral boundaries. Figure 6.6 shows the number of successful auroral boundary identifications in all local time sectors, in each season. The exact values for each season are also shown in Table 6.1. The winter seasons consistently contain the highest number of successful boundary identifications, with winter 2000 and 2001 containing approximately 3 times the number of successful boundary identi-

fications in summer 2000 and 2001. During the summer months, the increased UV contamination from reflected sunlight reduces the number of successfully identified auroral boundaries in the WIC data. The ROC scores and the number of successful boundary identifications in summer and autumn 2002 are reduced compared to the same season in previous years. In summer 2002, the IMAGE satellite suffered damage to the boom which affected the satellite pointing and resulting in an increased uncertainty in spacecraft pointing (Frey, 2010) and thus increased uncertainty in the location of the auroral boundaries.

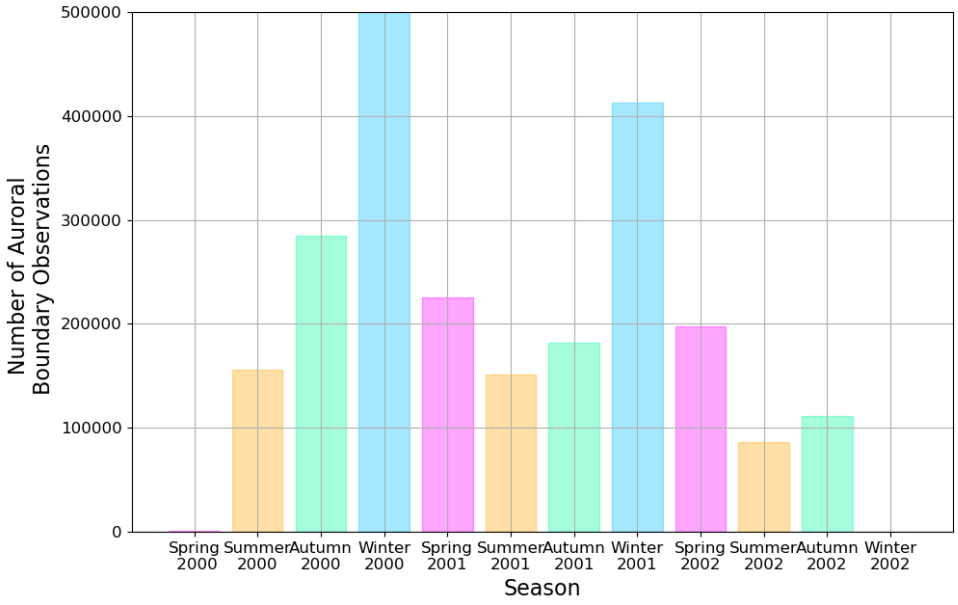

Figure 6.6: A histogram showing the total number of successful auroral boundary identifications in all local time sectors, in each season determined by Longden et al. (2010).

Newell et al. (2010b) identified seasonal variability in the number and energy density of the precipitating particles which would impact the performance of the conversion of the auroral flux to probability. Figure 6.7 shows the reliability diagram for each of the seasons in 2001. The seasonal reliability is consistent with the overall reliability shown in Figure 6.4. In all seasons, the occurrence frequency increases rapidly with probability, thus there is an under-prediction of the auroral occurrence. For autumn and spring forecasts, the observed auroral occurrence

Table 6.1: ROC scores and number of auroral boundary identifications for all seasons between summer 2000 - autumn 2002.

Season	Year	ROC Score	Number of Auroral Boundary Observations
Summer	2000	0.78	155911
Summer	2001	0.79	151498
Summer	2002	0.74	86641
Autumn	2000	0.84	284914
Autumn	2001	0.81	181704
Autumn	2002	0.80	111276
Winter	2000	0.85	499954
Winter	2001	0.84	412769
Spring	2001	0.86	225738
Spring	2002	0.84	197712

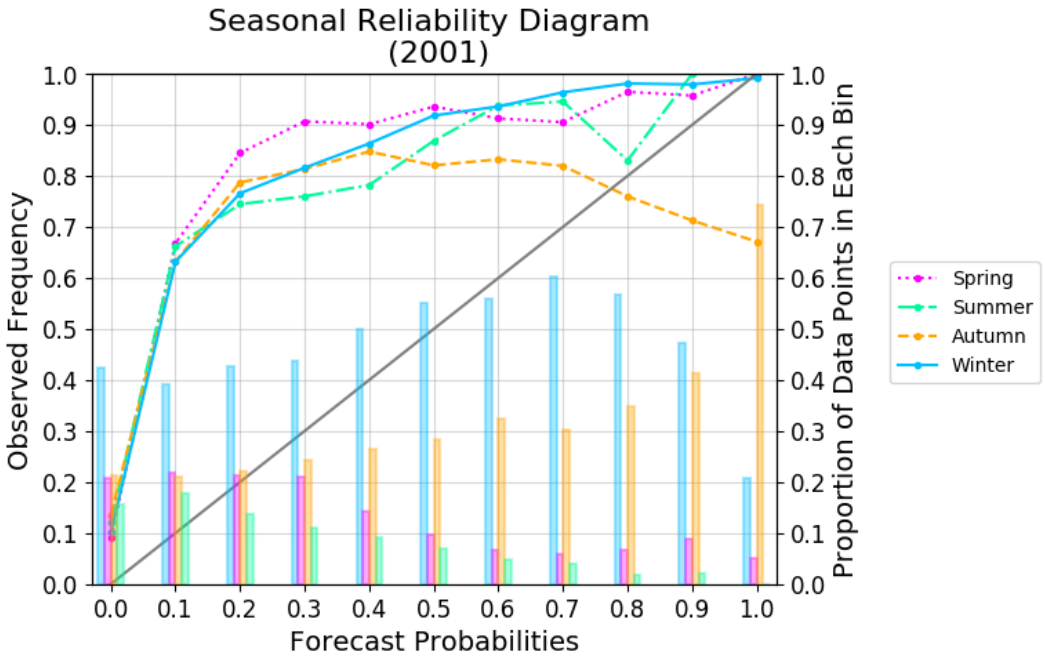

Figure 6.7: The results of the reliability analysis for each season in 2001. The reliability results for spring, summer, autumn and winter are shown by dotted pink, dot-dash green, dashed orange and solid blue lines, respectively. The histogram shows the proportion of data in each season, for each probability bin. The histogram results for spring, summer, autumn and winter are shown in pink, green, orange and blue, respectively.

plateaus at ~ 0.8 and ~ 0.9 respectively for mid range forecast probabilities between $\sim 20-70\%$, whereas the occurrence rate in summer and winter increases steadily with probability above a forecast probability of 20%. Only the autumn forecasts are over-predicted at the higher probability values of 80-100%, indicating that the over-prediction at these probability levels observed in the overall results in Section 6.3.1 are dominated by the over-prediction during the autumn period. There was no significant difference in the solar or geomagnetic activity between the seasons in 2001 however, there were a number of large geomagnetic storms and at least one Earth-directed halo CME (Jing et al., 2004) in late October 2001 which may have resulted in the over-prediction of high forecast probabilities of aurora occurring in Autumn 2001.

6.3.3 Magnetic Local Time Dependence

The shape of the auroral oval varies with local time sector. Typically, the dayside auroral oval tends to be thinner and dimmer (e.g. Holzworth and Meng, 1975; Carbary, 2005) while the nightside aurora generally extends over a wider magnetic latitude range and is more variable with enhanced auroral precipitation linked to magnetospheric activity such as substorms. Here, the model performance is evaluated in the noon, dawn, dusk and midnight regions. Each region is defined as three hours of MLT centred on MLT sectors 00, 12, 06 and 18. Three hour local time segments were chosen to ensure there were a sufficient number of forecast and observational pairs to produce the ROC curves while also not covering too large a range of local times that may average out the MLT dependence in the model performance. A single local time sector, particularly MLT 12, may not have had sufficient data coverage to produce a full ROC curve whereas using five or six hours of MLT centred on MLT sectors 00, 12, 06 and 18 might have averaged out the results. The ROC curves of each 3-hour MLT sector are shown in Figure 6.8 and show that the model performs well in the dawn, dusk and midnight sectors, with ROC scores of between 0.78-0.86. However, the ROC score from the noon region is considerably lower, at 0.59 showing that the forecast model does not perform as well in this region. Using a probability threshold of 10% to indicate the presence of aurora only

gives a hit rate of ∼0.2, much lower than the hit rates of 0.6-0.85 observed in the other local time sectors. The results in the truth table for the noon analysis are dominated by false negative (or missed) forecasts and true negative forecasts (or correct rejections) where the aurora is not forecast by the model. The lack of forecast aurora in this region may be because of a data gap in the underlying DMSP particle precipitation data, due to the dawn-dusk orbit of the spacecraft. The midnight data gap was interpolated over in the upgrades between OP-2010 and OP-2013 (Newell et al., 2010b) to improve the coverage of the forecast aurora in the near-midnight local time sectors, however there are no details on whether the corresponding dayside data gap around the noon local time sector was interpolated.

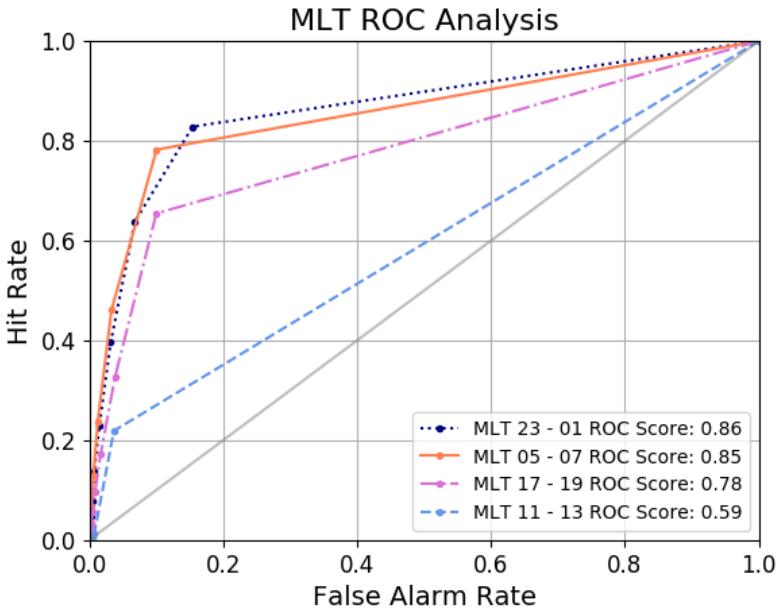

Figure 6.8: A ROC analysis for 4 MLT regions of the auroral oval. The MLT sectors for midnight (23 - 01), dawn (05 - 07), dusk (17 - 19) and noon (11-13) and are shown by dotted navy, solid orange, dot-dashed pink and dashed light blue respectively.

Figure 6.9 shows a map of the ROC score calculated for each grid cell using all forecast-observation pairs. The grey dashed lines in Figure 6.9 show the average location of all the observed poleward and equatorward auroral boundaries determined by Longden et al. (2010), between May 2000 - October 2002. In the nightside local time sectors, there is a band of grid cells between $\sim 55 - 68^{\circ}$ which have high ROC scores between 0.51 - 0.8. This band of reasonably high ROC scores extends into

most dayside sectors, except around noon, and extends poleward to about 70° and reflects the average location of the observed auroral oval. In the dayside sectors, there is an additional band of high ROC scores, generally between 0.6 - 0.8 at high latitudes between 75 - 80°. In the nightside sectors between $\sim$ 67 - 75°, there is a band of ROC scores which are less than 0.5, suggesting that in this region, the model forecasts often predict the opposite to what is observed, corresponding to a high number of missed forecasts or false alarms in the truth table. In the very low and very high latitudes regions, less than 55° on the nightside, below $\sim$ 60 - 65° on the dayside and above $\sim$ 75 - 80°, the ROC scores tend towards 0.5 as the aurora is rarely predicted or observed to occur at these latitudes. The high ROC scores at the lowest latitudes between $\sim 55-65°$ in the nightside to post-dawn (e.g. MLT 18 - 09) local time sectors, indicate that the model performs well at predicting the location of the auroral oval near the equatorward edge in these regions. The low ROC scores of < 0.5 in the high latitudes regions between $\sim 65-75°$ in the nightside local time sectors, between MLT 18 - 06 indicates that the model does not perform well at predicting the location of the poleward auroral boundary and instead often results in false alarm or missed forecasts in this region.

Figure 6.10 shows the reliability diagrams for each three hour MLT region. The reliability curves for the dawn, dusk and midnight sectors are similar to those of the 2.5 year verification shown in Figure 6.4 with forecast probabilities below 70 - 80% being largely under-predicted and greater than 80% being over-predicted. The reliability curve for the noon MLT sectors is quite different to the other MLT sectors, showing that the model tends to under-predict when forecasting aurora with probabilities less than 30% and over-predict when forecasting aurora with probabilities between 30% and 60%; whereas, aurora was not forecast with probabilities $>$70%.

6.3.4 Model Performance during Substorms

The nightside auroral oval is typically more dynamic than the dayside, particularly on timescales of $\sim$ 30 minutes. The nightside auroral dynamics are primarily driven by internal processes, such as substorms which cause a rapid expansion and bright-

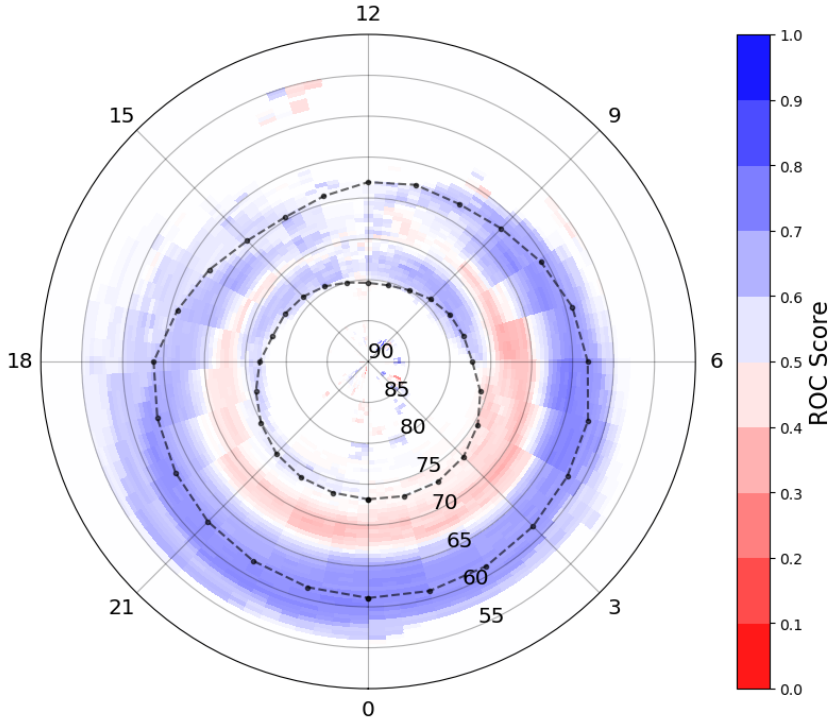

Figure 6.9: A map of the ROC score in each grid cell in the MLT x Mlat grid. Blue/red regions indicate grid cells which have a ROC score above/below 0.5. White regions indicate a ROC score of 0.5. The grey dashed lines show the average latitude of all the observed poleward and equatorward auroral boundaries determined by Longden et al. (2010), between May 2000 - October 2002.

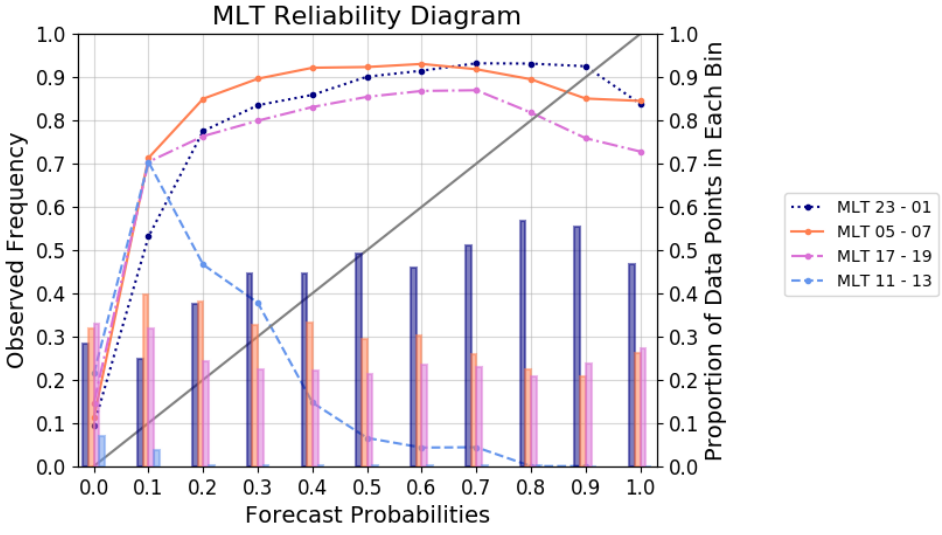

Figure 6.10: The results of the reliability analysis for 4 MLT regions of the auroral oval, each spanning 3 hours of MLT. The MLT sectors for midnight (23 - 01), dawn (05 - 07), dusk (17 - 19) and noon (11-13) are shown by dotted navy, solid orange, dot-dashed pink and dashed light blue, respectively. The same colours are used in the corresponding histograms.

ening of the auroral oval. The assumed linear relationship between the upstream solar wind conditions and the predicted auroral flux cannot forecast substorm activity and the 30-minute resolution of the operational forecasts cannot explicitly capture substorm dynamics. In this section, the impact of substorms on the performance of the model is tested.

The forecast and observation pairs were divided by substorm phase using the SOPHIE substorm phase list (Forsyth et al., 2015) which determines start and end times of substorm expansion and recovery phases and identifies possible growth phases from the SML index determined from SuperMAG ground magnetometer data between 1996 - 2014. Only model and observation pairs from isolated substorms and not enhanced convection events, as identified in the SOPHIE list, have been used in this analysis. Isolated substorms have a distinct growth, expansion and recovery phase. Growth phase forecast and observation pairs were selected if they occurred within 10 minutes before the beginning of the expansion phase. Expansion phases pairs were selected at 10 minutes before the beginning of the recovery phase and recovery phase pairs were selected at 10 minutes before the end of the recovery phase, when the system either returned to another growth or expansion phase. The forecast and observation pairs were selected 10 minutes before the end of each phase to give the auroral oval time to react to the substorm phase and capture the maximum dynamics in each phase.

Figure 6.11 shows the results for the ROC analysis for each of the three substorm phases. The results show that during the growth phase, the model performs well at predicting the location of the auroral oval, with a high ROC score of 0.84. During the expansion and recovery phases, the ROC scores decrease to 0.60 and 0.68, respectively, indicating a significant decrease in the model performance. During the substorm growth phase, dayside reconnection at the magnetopause dominates over nightside reconnection resulting in the accumulation of open flux. Perhaps the OP-2013 model performs well during this phase because it is driven in real time by the upstream solar wind conditions and so it performs well during the growth phase when the magnetosphere is predominantly being externally driven by

the solar wind, whereas the expansion and recovery phases are dominated by internal driving.

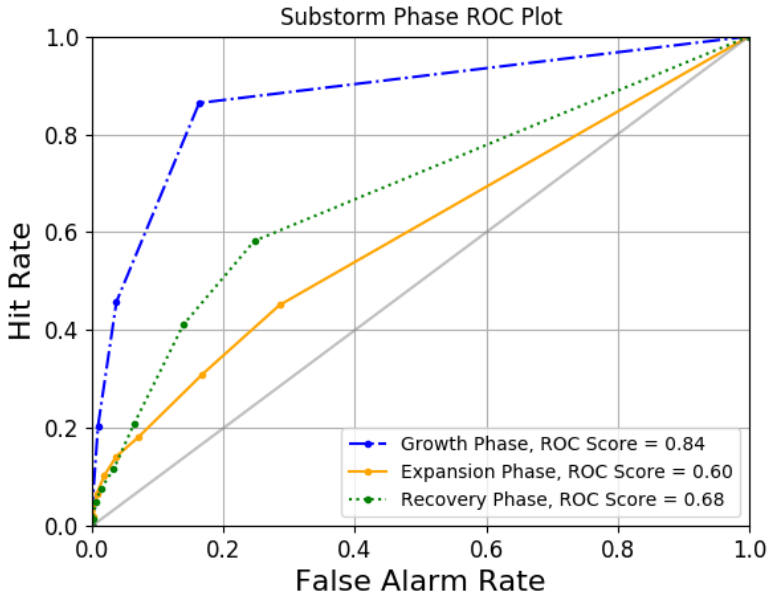

Figure 6.11: A ROC analysis for the model during substorm phases. The ROC curves for the substorm growth, expansion and recovery phases are shown by the dot-dashed blue, the solid orange and the dotted green, respectively.

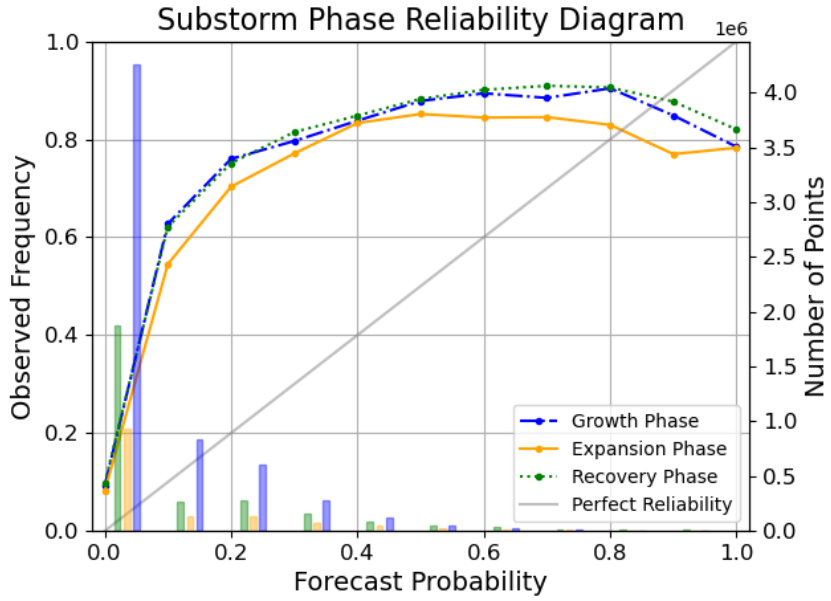

Figure 6.12: A reliability diagram for the model during substorm phases. The ROC curves for the substorm growth, expansion and recovery phases are shown by the dot-dashed blue, the solid orange and the dotted green, respectively.

The reliability diagram in Figure 6.12 shows a similar performance to the overall reliability analysis in Section 6.3.1, with forecast probabilities of less than 80% being under-predicted and forecast probabilities of 90% and above slightly over-predicted. Interestingly, the reliability curve from the substorm expansion phase lies slightly closer to the perfect reliability line from probabilities of 80% or less, compared to the reliability curves for the growth and recovery phases. The slightly improved reliability curve could suggest the linear relationship converting auroral brightness to probability in the operational version of the OP-2013 model performs better during the expansion phase when the nightside aurora may be brighter.

6.3.5 Model Performance with Kp

In the following section, the model performance under different levels of geomagnetic activity is evaluated. The level of geomagnetic activity is defined by Kp level. In a space weather context, Kp levels of 5 and above are generally considered to be geomagnetically active periods and so it is important to evaluate the performance of the OP-2013 model during these levels of geomagnetic activity which can have a real impact on daily services at Earth. The OP-2010 model was known to break down at higher levels of geomagnetic activity of Kp $\geq$ 5 (Newell et al., 2014). This led to the inclusion of additional GUVI data at higher Kp levels (Kp 5 - 8) as part of the upgrade to the OP-2013 generation.

All corresponding forecast and observation pairs between May 2000 and October 2002 were divided into subsets based on the level of Kp measured at the time. The results of the ROC analysis, including all the ROC scores for each Kp level, are shown in Figure 6.13. The ROC scores generally decrease for increasing levels of Kp, with Kp = 1 having a ROC score of 0.83 and Kp = 8 having a ROC score of 0.55. The ROC scores for Kp = 1 - 6 are within 0.05 of each other, implying that the model performs relatively well at discriminating between auroral and non-auroral regions at these levels of activity. However, at the highest activity levels of Kp = 7 and Kp = 8, the ROC score drops to 0.7 and 0.55 respectively. While these ROC scores indicate that the forecast has some skill in identifying where the aurora will be, these forecasts are less skillful than at lower activity levels. The results

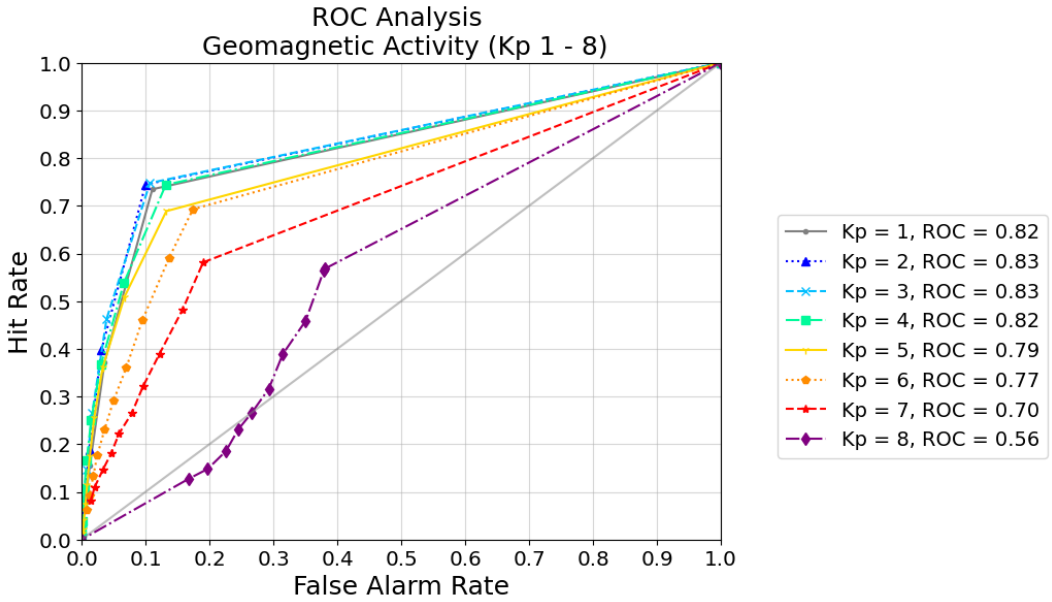

Figure 6.13: A ROC analysis for the model during different levels of geomagnetic activity spanning Kp = 1 - 8.

for Kp = 8 show that the hit rates are lower and the false alarm rates are higher compared to the results for lower Kp levels, indicating that the model is predicting that aurora will occur but not always in the correct locations, compared to the observed auroral boundaries. It is not uncommon for models which perform well within a nominal range of average conditions to perform less well during extreme events. Despite the improvements made to the OP-2013 model using GUVI data during higher levels of Kp, these observations are likely limited due to the rarity of periods of extremely high Kp. It would be informative to repeat this analysis with the predecessor OP-2010 model to quantify the improvement made by including the GUVI data at high levels of Kp.

Figure 6.14 and 6.15 show the reliability diagrams for Kp levels of 1-8. The reliability curves for Kp levels 1-5 plateau at an observed frequency of $\sim$0.8 - 0.9 for forecast probabilities of 30% and above. The reliability curves for Kp levels 6-7 plateau at a lower observed frequency of aurora of $\sim$ 0.7 - 0.8 for forecast probabilities of 10% and above. Kp = 8 shows the reliability curve dropping with increasing probability such that the observed occurrence of high probabilities is much lower than the forecast probability indicating a more concerning over-prediction. From

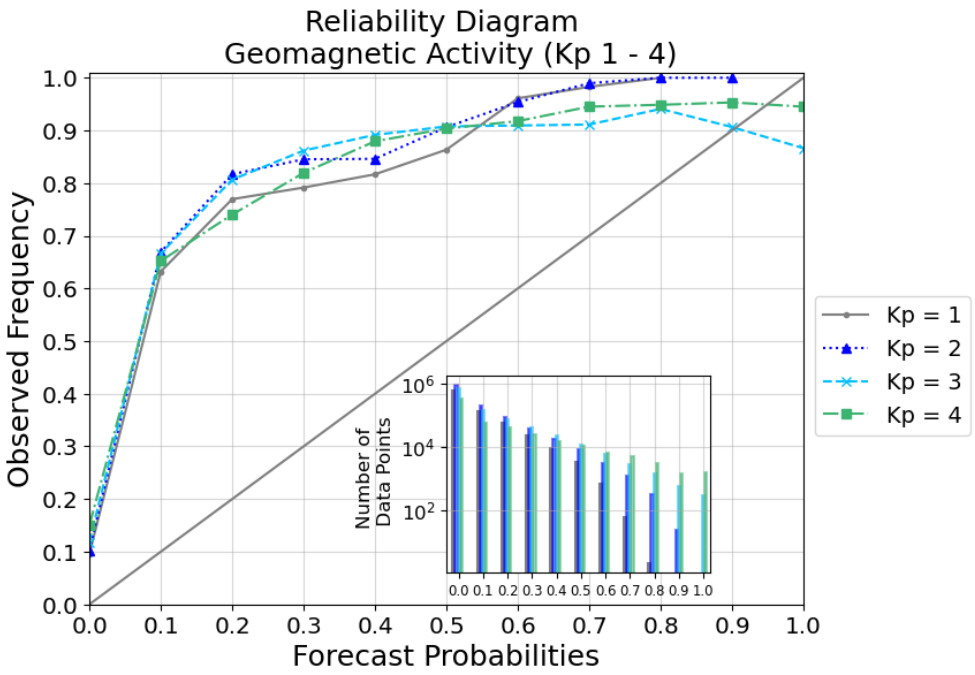

Figure 6.14: A reliability diagram for the model during different levels of geomagnetic activity spanning Kp = 1 - 4.

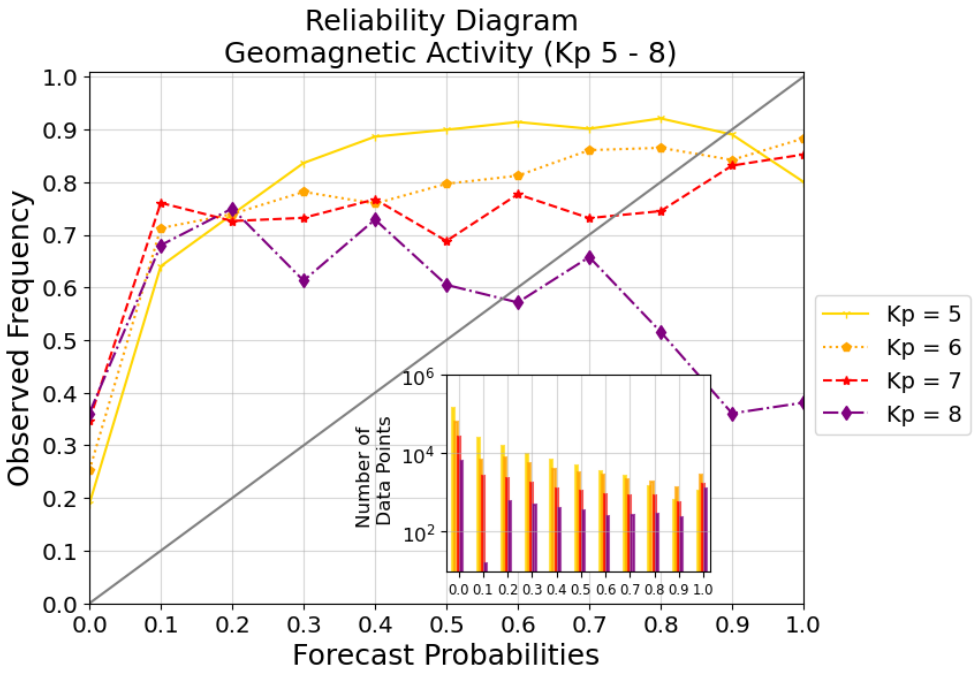

Figure 6.15: A reliability diagram for the model during different levels of geomagnetic activity spanning Kp = 5 - 8.

the histogram, note that Kp levels between 1-3 are the most common, with the highest number of points in these categories representing low geomagnetic activity. Kp levels of 7 and 8 are statistically much more rare events and have the lowest number of data points in the ROC and reliability analysis. There are 18 forecast and observation pairs for Kp = 7 and only 5 forecast and observation pairs for Kp = 8, compared to Kp = 2 which has 640, the highest number of forecast and observation pairs for any Kp level. The inclusion of more data in the analysis for this level of high geomagnetic activity would help to confirm this evaluation of the OP-2013 model during these high Kp levels.

6.4 Discussion

This study has evaluated the performance of the version of OP-2013 that was used operationally by the Met Office in daily space weather forecasts by comparing the forecast outputs with the FUV auroral boundaries identified from the IMAGE WIC observations by Longden et al. (2010). Forecast evaluation techniques which are routinely used in weather forecast verification have been used to assess both the deterministic and probabilistic nature of the auroral forecast model. Overall, as a deterministic model, the OP-2013 model performed well at predicting the location of the auroral oval, with ROC scores of between 0.6 - 0.8 in most local time sectors, although the forecast skill was lower around noon sectors (ROC score of 0.59). The overall ROC scores are similar to the ROC scores of M-class solar flare predictions issued by the Met Office (ROC scores = 0.71 - 0.82) (Murray et al., 2017). In the high latitude region of the nightside auroral oval, between 65 - 75°, the ROC scores were generally below 0.5, indicating that in these regions there are a high number of missed forecasts or false alarms. The OP-2013 model predicts the location of the auroral oval reasonably well under most geomagnetic conditions of Kp $\leq$ 7 (ROC scores $\geq$ 0.7) and during all substorm phases (ROC scores $\geq$ 0.6).

As a probabilistic model, the forecast probabilities tended to under-predict the occurrence of the aurora, with the observation frequency of the aurora typically being $\sim$0.8 for forecast probabilities exceeding 20%. This means that 80% of the

time the model output a forecast probability of aurora occurring greater than 20%, the aurora occurred in the observational data. For a perfectly reliable forecast, the forecast probability and the observed occurrence would have a 1:1 correspondence, for example, 20% of the time that the aurora is predicted to occur with a probability of 20%, the aurora should occur in the observational data.

6.4.1 Deterministic Auroral Forecasts

The results of the ROC analysis shows that the model performs well at discriminating between regions of aurora and no aurora. In the seasonal analysis, the summer ROC scores were consistently the lowest while the ROC scores during spring and winter were generally the highest. While there is some seasonal variability in ROC scores, all ROC scores are greater than 0.74, indicating that the model performs well year-round. This suggests that seasonal statistical variations in the location of the aurora are well captured by the model. The impact of seasonal dependence in the model could be evaluated by reproducing the auroral hindcasts with the seasonal dependence in the model turned off and repeating the ROC analysis. The difference in the ROC scores for hindcasts produced with and without the model seasonal dependence would quantify the value added by the seasonal dependence in the model and in which seasons the auroral forecasts are improved the most by including the seasonal dependence.

In the evaluation of the auroral hindcasts by local time sector, the model had a lower ROC score in the dayside local time sectors centred on the noon MLT (11-13 MLT). The noon MLT sectors had a ROC score of 0.59 compared to the dusk (17-19 MLT), dawn (05-07 MLT) and midnight (23-01 MLT) sectors which had ROC scores between 0.78 - 0.86. The higher ROC scores in the nightside local time sectors indicate that the model performs better at predicting the location of the aurora in these regions.

The further break down of the model performance by ROC score in each grid cell showed that the model performed well at predicting the average location of the auroral oval in most local time sectors with ROC scores generally between 0.6 - 0.8, except the noon MLT sectors where the ROC score tended towards 0.5. In the

high latitude nightside local time sectors, the ROC scores decreased to less than 0.5, indicating that these grid cells are dominated by missed forecasts or false alarms. The lower ROC scores near the nightside poleward auroral boundary could be due to an offset in the location of poleward edge of the auroral boundary identified from global FUV image data compared to particle precipitation measurements, such as those from DMSP (Kauristie et al., 1999), or due to substorm activity. In the evaluation of the model performance during substorms, the model performed well during the growth phase with a high ROC score of 0.84 however the ROC scores dropped significantly to 0.60 and 0.68 during the expansion and recovery phases, respectively. The location of the auroral oval, particularly at the poleward edge, is much more variable during the expansion and recovery phases in response to the rapid closure of flux. The solar wind driven OP-2013 model is unable to forecast substorm activity and the 30 minute resolution of the operational forecasts cannot capture substorm dynamics, which may result in a higher number of missed forecasts or false alarms in the poleward edge of the auroral emission. Further investigations into the detailed dynamics and timescale over which the poleward auroral boundary contracts in response to substorm onset and the motion of the boundary during the recovery phase could lead to improvements in the performance of OP-2013 and other auroral forecast models.

The model performed well in predicting the location of the equatorward boundary with ROC scores above 0.5, suggesting that the linear relationship between the upstream solar wind conditions and the predicted auroral flux and the 30-minute resolution of the operational forecasts capture the location and dynamics of the equatorward edge reasonably well. This raises interesting questions regarding what controls the dynamics of the equatorward edge of the auroral boundary and the response timescales of the equatorward boundary to driving processes that are either external or internal to the magnetosphere.

In the evaluation of OP-2013 under different geomagnetic conditions, the geomagnetic index, Kp, was used to define the level of geomagnetic activity. In a space weather context, Kp levels of 5 and above are generally considered to be ge-

omagnetically active periods, with Kp = 7 and Kp = 8 classed as strong to severe geomagnetic storms which reflect the possible impact on daily services at Earth. The results showed that the ROC scores decreased with increasing Kp levels from 0.83 to 0.55 for Kp = 1 and Kp = 8, respectively. All ROC scores for Kp 1 - 7 are greater than 0.70. For higher Kp levels, the hit rates are lower while the false alarm rates are higher, indicating that the model is predicting that the aurora will occur but not in the correct locations, compared to the observed UV auroral boundaries. The results show that the model generally performs reasonably well at forecasting the location of the auroral oval during most levels of geomagnetic activity. However, the model performance is significantly lower during severe geomagnetic storm periods which have the potential to have a significant impact on global, daily services. The inclusion of GUVI data in the upgrade to the OP-2013 model was hoped to improve the performance of the model for higher levels of geomagnetic disturbance, for Kp levels between 5 - 8 (Newell et al., 2014). The relatively high ROC scores above 0.70 for geomagnetic activity up to Kp = 7 may indicate that the additional GUVI data may be having a positive effect on the performance of OP-2013 at disturbance levels between Kp 5 - 7, however a similar study evaluating the performance of OP-2010 during periods of Kp 5 - 7 would be required to confirm this.

The higher Kp levels occur less frequently as shown by the histogram of Figure 6.15 and so there are fewer forecast and observation pairs at higher Kp levels and thus the model is less well constrained. This could suggest that the linear scaling of auroral flux with solar wind driving used by Newell et al. (2007) to construct the OP-2010 and OP-2013 models breaks down during more extreme and statistically more rare events of Kp $\geq$ 7.

6.4.2 Evaluating the Forecast Auroral Probabilities

The reliability diagrams show that the forecast probabilities of aurora occurring tend to be under-predicted, that is that the aurora occurs more frequently than the model predicts, particularly for lower probability values of less than 80%. At the highest forecast probability values, greater than 80%, the model tends towards a slight over-prediction of the probability of aurora occurring. This is observed in

most cases from the seasonal, MLT sector and geomagnetic activity analysis.

The observed frequency of aurora does not increase linearly with the forecast probabilities but instead is relatively constant between 0.7 - 0.9 for all the forecast-observation pairs for forecast probabilities of 20% and above. This means that the lower forecast probabilities of 20% are under-predicted by a factor of $\sim$6. As the forecast probability of aurora occurring tends towards the observed frequency of aurora, the difference between the forecast probability and the observed frequency decreases and so the factor of how much the aurora is under or over-predicted also decreases.

The results of the reliability analysis show that the conversion from auroral flux to probability of aurora occurring is not particularly robust, however, this conversion is a non-trivial task. As previously mentioned in Chapter 4, the conversion of auroral flux to probability was tuned by SWPC to reduce the number of false alarm forecasts for the benefit of members of the public using the auroral forecasts to try to observe the aurora (Rodney Viereck, private communications). It is therefore unsurprising that the forecasts generally under-predict the occurrence of aurora. Using the results of the reliability analysis, a correction to re-calibrate the probabilities forecast by the model could be developed to improve the reliability of OP-2013 auroral forecasts against the observed FUV auroral boundaries. The probabilities forecast by the OP-2013 model vary with season, MLT sector and geomagnetic activity (Kp level) which would need to be accounted for if a correction were to be developed. However, the results of the reliability analysis showed that for forecast probabilities above 20 - 30%, the observed occurrence of aurora is approximately constant at around 0.7-0.9, which would make it difficult to linearly re-scale the forecast probabilities. All forecast probabilities of $\sim$ 20% or above would be re-scaled to an $\sim$ 80% probability of aurora occurring, effectively producing a deterministic forecast.

The relatively constant observed frequency of aurora between 0.7 - 0.9 reflects the fact that the occurrence of the aurora is binary. Once a certain flux threshold of precipitating particles is exceeded (i.e. some threshold at which the aurora is

detectable either by eye or from global FUV images), the aurora is observed. Below this threshold, the aurora is not detectable and thus is classed as not occurring. For the aurora to be visible to the naked eye, the auroral brightness must exceed $\sim$ 1 kR (Kivelson and Russell, 1995) which corresponds to a precipitating electron energy flux of $\sim$ 1 erg cm^{-2} s^{-1} (Germany et al., 1990; Sotirelis et al., 2013). If the flux of precipitating particles increases, the observed aurora may be brighter but it is not more likely to occur. The OP-2013 model is an empirical statistical model that provides a single value of predicted flux with no estimation of the uncertainty in the flux. Without a range or uncertainty in the predicted flux, a true probability of aurora occurring cannot be predicted.

Rather than scaling the predicted flux into a probability of aurora occurring it may be preferable to develop a flux threshold system. For example, in regions where the predicted auroral flux is greater than zero indicates that there may be some auroral effects. In regions where the auroral flux exceeds a certain brightness threshold (e.g. 1 erg cm^{-2} s^{-1}) would indicate that the aurora should be visible with the naked eye and the brightest aurora would be predicted in the regions of maximum auroral flux.

6.4.3 Comparisons with Previous Auroral Forecast Evaluation Studies

Newell et al. (2010a); Machol et al. (2012) and Lane et al. (2015) evaluated the auroral forecasts from OP-2010. From these three studies, the truth tables methods applied by Machol et al. (2012) are the most comparable to the analysis applied in this study. Machol et al. (2012) evaluated the use of the OP-2010 model as an operational forecast model for visible aurora by assessing the deterministic ability of the model to forecast the location of the aurora compared to Polar UVI observations. This study has similarly examined how well the OP-2013 model performs as a deterministic forecast of the location of the aurora, although IMAGE FUV data have been used as the ground truth dataset and ROC curves and scores have been used to examine the performance of the model. Extending this, this study has also examined the validity of the forecast probabilities of aurora occurring as well as

examining the performance of the model with season, local time and geomagnetic activity.

The most notable difference between the analysis presented in this study and the analysis of Machol et al. (2012), other than the updated model in this study, is the determination of the ground truth data. Machol et al. (2012) compared the locations of model predictions of electron fluxes exceeding 1 erg cm^{-2} s^{-1} and auroral luminosities from Polar UVI exceeding 0.25 kR whereas this study used auroral luminosity boundaries determined from IMAGE WIC data by Longden et al. (2010). As such, a direct comparison between the results cannot be used to infer any change in performance between the OP-2010 and OP-2013 models, but may still be informative.

Table 6.2 shows the verification statistics calculated from the 10%, 50% and 80% truth tables in this study with the results of Machol et al. (2012). In the study by Machol et al. (2012), the results were presented in terms of the false alarm ratio (as defined by Wilks (2006)). The False Alarm Rate is the number of false positives divided by the total number of negative observations in the truth table where aurora was not observed to occur ($False\ Alarm\ Rate = False\ Alarms/(False\ Alarms + True\ Negatives)$). The False Alarm Ratio is the fraction of positive forecasts that are false alarms ($False\ Alarm\ Ratio = False\ Alarms/(True\ Positives + False\ Alarms)$). In Table 6.2 the results are presented in terms of the false alarm rate and the false alarm ratio, for comparison with the results of Machol et al. (2012). The equations for all the verification statistics in Table 6.2 are provided in Chapter 5. Comparing the results of Machol et al. (2012) and the 10% bin from this analysis, all of the statistics are within 15%. Machol et al. (2012) found that by increasing the energy flux threshold used to define the location of the auroral boundaries, resulted in an increase in the number of false positives and a decrease in the number of false negatives in the truth table. In contrast, the truth tables calculated in this study show that as the probability threshold is increased, the number of false positives decreases and the number of false negatives increases.

Overall, the results of the verification statistics from both studies show a similar performance for both the OP-2010 and OP-2013 generations of the model. The results of these two studies cannot be directly compared to assess improvements made between the two generations of the model. Differences in the results between the two studies presented in Table 6.2 may reflect the upgrades made to the model between the OP-2010 and OP-2013 generations, however due to the differences in the observational datasets and the definition of the observed auroral boundaries between this study and the study by Machol et al. (2012), the comparison of the two sets of results cannot be used to quantify the upgrades implemented in the model.

Table 6.2: A comparison of the verification statistics derived from the results of the 10%, 50% and 80% probability thresholds from current OP-2013 evaluation study presented in this paper with those from the OP-2010 evaluation study carried out by Machol et al. (2012).

Verification Statistic	**Results from Machol et al. (2012) Analysis of OP-2010**	**Results from Present Analysis of OP-2013**		
		10%	**50%**	**80%**
Hit Rate	58%	73%	8%	2%
False Alarm Rate	–	11%	0%	0%
False Alarm Ratio	14%	25%	11%	14%
Proportion of True Positives	86%	75%	89%	86%
Proportion of False Negatives	26%	12%	30%	31%
Accuracy	77%	84%	71%	69%

Previous studies have discussed the suitability of using UV data from global auroral imagers as a ground truth data set for model verification (e.g. Machol et al., 2012). While particle precipitation measurements from satellites such as DMSP provide more accurate determinations of the location of the auroral oval, the measurements are spatially and temporally limited. Global auroral imagers are the only dataset which provide information about the location of the auroral oval boundaries in all MLT sectors at any one time. In addition, as the OP-2013 model uses averaged DMSP and TIMED GUVI data, for a forecast evaluation study, it is good practice to use an observational data set which is independent of the data used in the model to compare with the model output. The poleward boundary identifications from Longden et al. (2010) have been shown to be co-located with the poleward emission

boundary measured from DMSP within 3°on average in all MLT sectors, making the boundaries a suitable observational dataset to compare with the OP-2013 forecasts.

6.5 Conclusions

This study has evaluated the performance of the version of OP-2013 that was used operationally by the Met Office in daily space weather forecasts by comparing the forecast outputs with the location of the auroral oval identified from IMAGE FUV data by Longden et al. (2010). Forecast evaluation techniques which are routinely used in terrestrial weather forecast verification have been applied to assess both the deterministic and probabilistic nature of the auroral forecast model. Overall, the OP-2013 model performed well at predicting the location of the auroral oval, with ROC scores of between 0.70 to 0.86, although the forecast skill was notably lower around noon (ROC score of 0.59) and at higher Kp (ROC score of 0.55, for Kp = 8).

The OP-2013 model is solar-wind driven and is therefore unable to predict substorm activity and the 30-minute resolution of the operational forecasts cannot explicitly capture substorm dynamics. The model performed well during the substorm growth phase (ROC score = 0.94) when the external driving of the magnetosphere at the dayside dominates over nightside reconnection resulting in the accumulation of open flux within the magnetosphere. However, the performance of the model dropped significantly during the substorm expansion phase (ROC score = 0.60) which is internally driven by nightside reconnection. This result highlights the need to include external and internal drivers in future generations of auroral models. The ROC scores were also reduced near the poleward edge of the aurora in the nightside local time sectors which is likely due to substorm activity when the polar cap expands and contracts with the changes in the open flux content. In contrast, ROC scores were higher near the equatorward auroral boundary, which may suggest that the dynamics of this boundary are well organised by the external driving of the magnetosphere. These results underline the research questions set out in this thesis of how do the details of the auroral dynamics fit into the wider understanding of

the closure of flux in the magnetosphere, particularly during substorms? And, what does the equatorward auroral boundary translate to in the inner magnetosphere in all local time sectors? These questions will be address in Chapters 7 and 8.

The reliability analysis showed that the observed frequency of aurora is approximately constant at 80 - 90% for forecast probabilities of $\sim$ 20% and above and does not scale linearly with increasing forecast probability. This results in the lower forecast probabilities of 20% being significantly under-predicted, by a factor of 6 (i.e. the aurora occurs 6 times more frequently than the model predicts for a forecast probability of 20%). The highest forecast probabilities of $\sim$ 90-100% are over-predicted by up to approximately 20%; that is the aurora occurs up to 20% less frequently than the model predicts for these high forecast probability values. The results of the reliability analysis from this study suggest that the conversion of auroral flux to probability is not robust and that an alternative, threshold based alert system might be more appropriate for end users of auroral forecasts.

The ROC and reliability analysis presented in this study show a robust methodology that is widely used in terrestrial weather forecast verification that can also be applied to a wide range of space weather forecast models which have an appropriate set of observations to use in the analysis. These methods can be used to fairly compare forecasts from similar models or to quantify improvements made to space weather models during model development. The results presented in this analysis provide a performance benchmark against which upgrades to the OP-2013 auroral forecast model or alternative auroral forecast models can be fairly and quantitatively tested.

Chapter 7

Examining Local Time Variations in the Nightside Open Magnetic Flux Content during Substorms

The analysis in Chapter 6 showed that the OP-2013 auroral forecast model performed well at predicting the location of the main auroral emission, however the performance of the model was reduced in the high latitude region, particularly in the nightside local time sectors and during geomagnetically active times. The poleward boundary of the auroral oval is closely associated with the open-closed field line boundary, which expands and contracts in response to the changing open flux content of the magnetosphere. While this flux may be constantly changing due to the interaction between the solar wind and the magnetosphere, some of the largest and most rapid changes are observed as a result of substorm activity. This chapter examines in detail the motion of the nightside poleward auroral boundary in response to substorm activity. The results of the analysis show that after the onset of nightside reconnection during the substorm expansion phase, the poleward auroral boundary does not contract uniformly in all nightside local time sectors. Close to the substorm onset sector, the poleward auroral boundary contracts immediately following substorm onset; however, the poleward auroral boundary in more dawnward and duskward local time sectors continues to expand equatorward for up to 30 - 40 minutes after substorm onset. The poleward auroral boundary is then used

as a proxy for the open-closed field line boundary (OCB) to examine the change in the open magnetic flux content in individual nightside local time sectors during substorm growth, expansion, and recovery phases.

The results show that in the hour prior to substorm onset, the total nightside open flux content increases by up to 0.12 GWb on average, resulting in an equatorward expansion of the OCB, as expected during the growth phase. Following substorm onset, the open flux content of the substorm onset sector decreases immediately while the open flux content of sectors up to $\pm$6 hours of local time from the substorm onset sector continues to increase for up to 20 - 40 minutes after substorm onset. Despite the continued increase in the open flux content of these sectors after substorm onset, the total nightside open flux content begins to decrease immediately at substorm onset, eventually reducing by up to 0.14 GWb on average. This indicates that the net nightside reconnection rate exceeds the dayside rate immediately following substorm onset.

The results presented in this chapter have previously been published in the *Journal of Geophysical Research* with the citation: Mooney, M. K., Forsyth, C., Rae, I. J., Chisham, G., Coxon, J. C., Marsh, M. S., Jackson, D. R., Bingham, S. and Hubert, B. (2020). Examining local time variations in the gains and losses of open magnetic flux during substorms. *Journal of Geophysical Research: Space Physics*, 125, e2019JA027369. https://doi.org/10.1029/2019JA027369.

7.1 Introduction

Many studies have used the poleward edge of the auroral oval from UV images as a proxy for the OCB location to estimate the open flux content of the polar caps (Boakes et al., 2008, 2009; Coumans et al., 2007; Hubert et al., 2006; Longden et al., 2010; Milan et al., 2009a,b). Using the technique of Hubert et al. (2006) to fit a Fourier series of five harmonics to the poleward auroral boundary from global images of the proton auroral oval as a proxy for the OCB location, Coumans et al. (2007) performed a statistical analysis of 55 substorms and found that on average, the open flux content remained constant or continued to increase within the first 20

minutes of substorm onset. Similarly, a superposed epoch analysis of UV auroral intensity during substorms by Milan et al. (2009b) found that the latitude of the maximum intensity continues to move equatorward after substorm onset, particularly in the dawn and dusk regions of the auroral oval, while in the midnight sector, the location of the maximum intensity moves toward the pole immediately at substorm onset. Clausen et al. (2012) showed that the location of the Region 1 (R1) Birkeland current system could also be used as a proxy for the OCB. By calculating the area of a circle fitted to the latitude of the R1 current in each local time sector Clausen et al. (2013) and Coxon et al. (2014) presented two superposed epoch analyses of substorms using the R1 OCB proxy location to observe changes in the open magnetic flux content of the northern hemisphere polar cap during substorms. The results from these studies indicated that the open flux content continues to increase for up to 15–20 minutes after substorm onset, particularly in the dusk sector (Clausen et al., 2013). Clausen et al. (2013) and Coxon et al. (2014) suggested that the results were indicative of dayside reconnection continuing to dominate over nightside reconnection in the first 15 – 20 minutes after substorm onset in certain sectors, in agreement with Coumans et al. (2007).

The findings presented in these studies are somewhat unexpected in the context of the standard substorm model (e.g. Baker et al., 1996; Angelopoulos et al., 2008), given that Baker et al. (1996) specify a 5 - 15 minute delay between substorm onset and the reduction in the open flux content of the polar cap and the poleward contraction of the OCB due to nightside reconnection dominating over dayside reconnection. A delay of up to 20 minutes presents an open question as to whether other factors are at play. The underlying assumption in the fitting methods used by Coumans et al. (2007); Milan et al. (2009b); Clausen et al. (2013) and Coxon et al. (2014) is that the poleward auroral boundary and, by proxy the OCB, retain a circular shape as they expand and contract uniformly in all local time sectors in response to the opening and closure of flux. This study examines, in detail, the expansion and contraction of the OCB in individual nightside local time sectors, during the substorm growth and expansion phases to reconcile the recent findings

with the substorm model. Understanding the detailed motion of the OCB and poleward auroral boundary in response to nightside reconnection and during substorm expansion and recovery phases could result in improved auroral forecasting models that are able to capture substorm auroral dynamics.

7.2 Data and Method

In this work, a superposed epoch analysis was performed on the OCB locations determined from the poleward auroral boundary identified from each of the three IMAGE FUV instruments by Longden et al. (2010) during substorms identified by Frey et al. (2004). It is noted that the location of the OCB estimated from each of the three datasets (WIC, SI12 and SI13) may differ, however they are three estimates of one single OCB location and not three different OCBs.

Milan et al. (2009a) performed a superposed epoch analysis of substorm auroral brightness for a list of substorms identified in the IMAGE FUV data by Frey et al. (2004). In that study, Milan et al. (2009a) subdivided the substorms into five categories based on their onset latitude, Λ_{onset}:

1. $\Lambda_{onset} < 62^{\circ}$
2. $62^{\circ} \leq \Lambda_{onset} < 64^{\circ}$
3. $64^{\circ} \leq \Lambda_{onset} < 66^{\circ}$
4. $66^{\circ} \leq \Lambda_{onset} < 68^{\circ}$
5. $\Lambda_{onset} \geq 68^{\circ}$

Using these onset latitude categories, Milan et al. (2009a) found that lower onset latitude substorms resulted in larger expansions of the auroral oval in the midnight magnetic local time (MLT) sector. In order to ensure the statistical results presented in this study are not unduly influenced by these larger events and to aid comparisons with other studies, the analysis was similarly subdivided by substorm onset latitude. Milan et al. (2009a) showed the distribution of substorm onset in local time and latitude from substorms identified in the Frey et al. (2004) list between

May 2000 and April 2002. The analysis performed by Milan et al. (2009a) indicated that the majority of substorm onsets occurred in the premidnight local time sectors between MLT 21 and MLT 00 and had onset latitudes between 66° and 68°. In this study, there is no significant difference in the substorm onset local time distributions in each substorm onset latitude category.

In this study, a superposed epoch analysis of the OCB latitude determined from the IMAGE WIC, SI12, and SI13 FUV instruments keyed to substorm onset was performed, covering the hour prior to substorm onset and 2 hours after substorm onset. Given that substorm onset does not always occur in the same local time sector, variations in the OCB are examined in sectors relative to the onset sector, effectively rotating each OCB so that the substorm onset sectors were colocated, as previously done by e.g. Coxon et al. (2017) and Provan et al. (2004). As the poleward contraction of the OCB after substorm onset in each nightside local time sector is of particular interest in this study, this rotation acts to minimize the spreading of the results of the superposed epoch analysis over a range of sectors.

Due to the spin of the spacecraft, there is an interval of just over 2 minutes between the images collected by the IMAGE FUV instruments and hence between the OCB identifications. Prior to the superposed epoch analysis, the time series of OCB latitudes in each local time sector was linearly interpolated to a regular 2 minute cadence. There is no requirement in the superposed epoch analysis that the proxy OCB location had to be identified in all sectors at all times.

The analysis showed distinctly different results for the highest latitude substorms (greater than 68°). Further investigation of these showed that the Longden et al. (2010) technique was occasionally fitting the poleward auroral boundary to bright, low-latitude artifacts in the FUV data, particularly data from the SI12 camera, prior to substorm onset when the auroral oval was dimmer. This effect was limited to the high-latitude category; hence, the results are presented for substorms with onsets latitudes up to 68° only.

7.3 Results

In the following, the results of the superposed epoch analysis of the OCB location for substorms with onset latitudes between 64° and 66° are focused on, however the results for all substorm onset latitudes are also included for completeness. The $64 - 66°$ substorm onset latitude category contains 581 substorms and is in the middle of the substorm onset latitude categories in this study and as such contains the midsized substorms. Morphologically, the results of this substorm onset latitude category are generally representative of the other substorm onset latitude categories.

The superposed epoch analysis of the OCB location was performed on each data set obtained from the three FUV instruments onboard IMAGE (WIC, SI12, and SI13). The results of each instrument are presented separately for comparison.

7.3.1 Successful Boundary Identifications in Each Local Time Sector

In the list of substorm onsets identified by Frey et al. (2004), 581 substorm onsets were identified by brightenings in the auroral oval at a latitude between $64° - 66°$. If there was a data gap in the OCB data of 10 minutes or more in the hour before or 2 hours following onset, the event was not included in the analysis. In the superposed epoch analysis, 451 substorms were included in the SI13 data, 469 in the WIC data, and 449 in the SI12 data. The OCB location did not have to be identified in all local time sectors to be included in the analysis.

Figure 7.1 shows the number of successful OCB identifications in each local time sector for the hour before and 2 hours following substorm onset for substorm onset latitudes between $64° - 66°$. The results are shown for each of the three FUV instruments, SI12 in Figure 7.1a, WIC in Figure 7.1b, and SI13 in Figure 7.1c. In Figures 7.1–7.6, the substorm onset sector is defined to be $MLT = 0$, negative MLT sectors are duskward of the onset sector, and positive MLT sectors are dawnward of the onset sector. On the y-axis, time is defined from substorm onset at $t = 0$, where the onset time is as defined by Frey et al. (2004). Similar figures for substorm onset latitudes $< 62°$, $62 - 64°$ and $66 - 68°$ are shown in Figure 7.2.

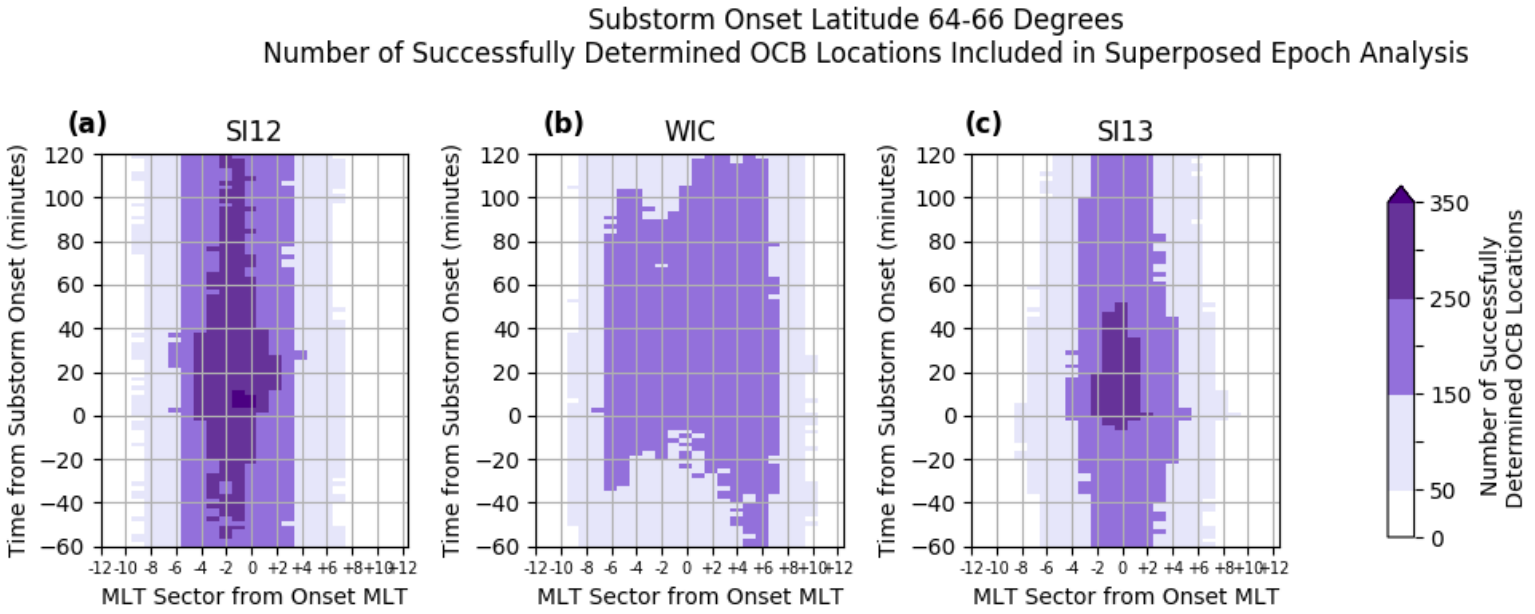

Figure 7.1: Plots showing the number of successfully fitted OCB locations in each local time sector at each time step during the 3 hours superposed epoch analysis. The color bar shows five discrete levels to highlight times and local time sectors which contain a particularly high or low number of successful OCB identifications. The steps with less than 50 data points, indicated in white, have been excluded from the analysis. Panels (a)–(c) show the number of successfully determined OCB locations from SI12, WIC, and SI13 data, respectively.

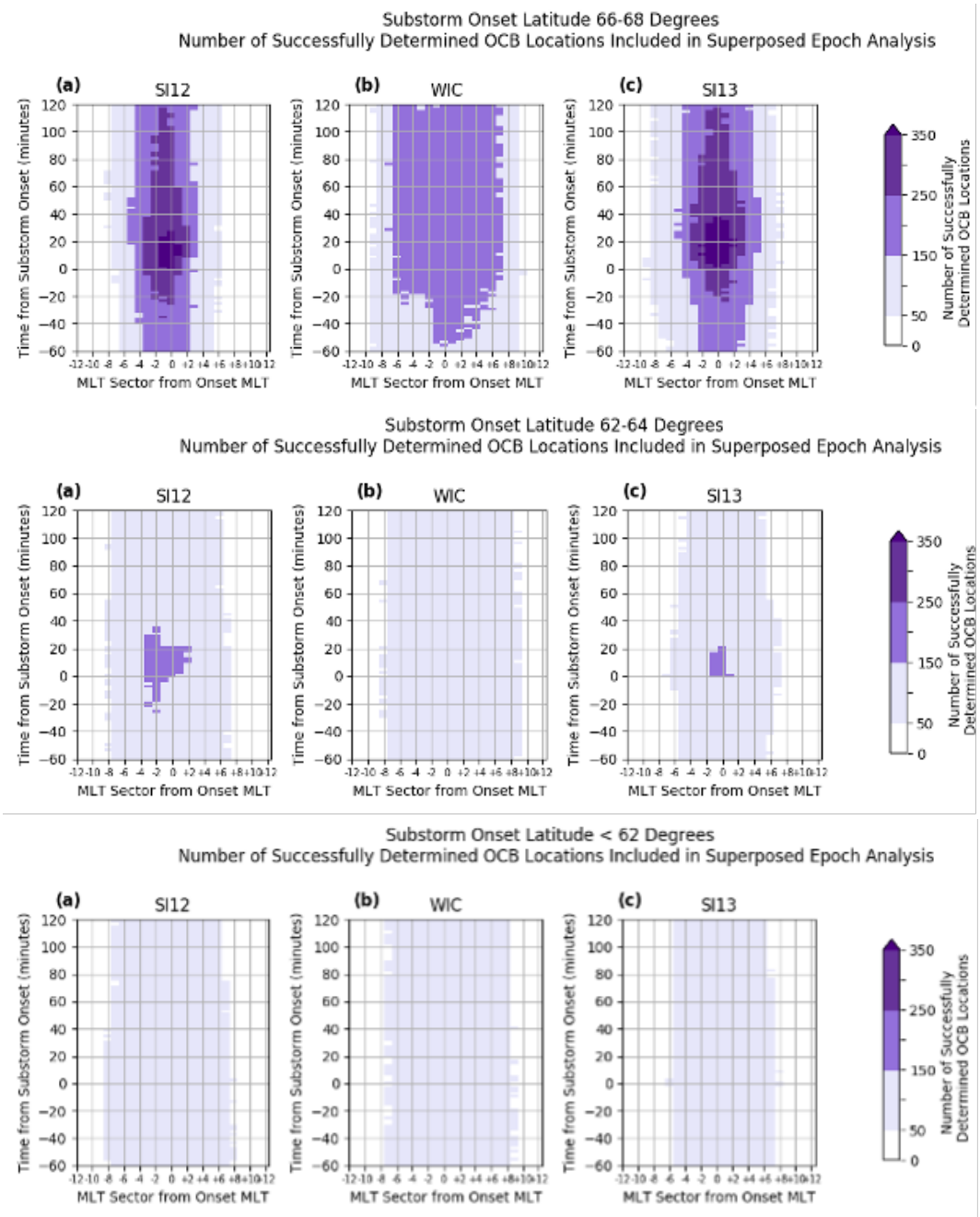

Figure 7.2: Plots showing the number of successfully fitted OCB locations in each local time sector at each time step during the 3 hours superposed epoch analysis, for all substorm onset latitudes. The highest substorm onset latitude of $66 - 68^{\circ}$ in the top row, with substorm onset latitude decreasing down to the lowest onset latitude category of $< 62^{\circ}$ in the lowest row. The color bar shows five discrete levels to highlight times and local time sectors which contain a particularly high or low number of successful OCB identifications. The steps with less than 50 data points, indicated in white, have been excluded from the analysis. In each row, panels (a)–(c) show the number of successfully determined OCB locations from SI12, WIC, and SI13 data, respectively.

Figure 7.1 shows that successful boundary identifications varied with imager and with time. The highest number of successful boundary identifications in the WIC data at any 2 minute time interval is around 180, compared to more than 300 and 350 for SI13 and SI12, respectively. The numbers of the successful identifications in the WIC and SI13 data were relatively symmetric about the onset sector, with at least 50 identifications in each local time sector between −8 and +8 for WIC and between −6 and +6 for SI13. In contrast, there were more boundary identifications duskward of the onset sector for SI12, with at least 50 identifications in each local time sector between −8 and +6. Despite the lower overall numbers of successfully fitted OCB locations from the WIC data compared to the SI12 and SI13 data, the number of successfully fitted OCB identifications in the WIC data is higher across a wider range of local time, particularly in the dawnward sectors.

In all instruments, for all substorm onset latitude categories, the boundaries are more successfully fitted in the nightside local time sectors between MLT −6 and MLT +6 with far fewer (less than 50) fitted in the dayside sectors. One reason for this is that the auroral emission in dayside sectors is generally dimmer than that of the nightside sectors, especially following substorm onset, making it more difficult to fit Gaussian functions to the latitudinal intensity profiles of the dayside sectors. Furthermore, models generally show the auroral oval to be thinner on the dayside (e.g. Carbary, 2005; Holzworth and Meng, 1975), which may make a Gaussian fit more challenging. Given the low number of fits on the dayside, the analysis focused on the nightside sectors between MLT −6 and MLT +6.

In Figure 7.1, both SI12 and SI13 show higher numbers of boundary identifications in the onset sector and close to the onset time, with at least 250 identifications within −10 to +50 minutes of onset. The higher number of successfully fitted boundaries for the spectral imaging cameras around substorm onset coincides with the rapid brightening of the auroral oval around the onset sector at substorm onset and into the expansion phase. When the auroral oval is brighter compared to the background emission, the poleward edge of the auroral oval and hence the OCB location may be more easily identified by the technique used by Longden et al.

(2010). The higher number of successfully fitted boundaries near the substorm onset sector prior to substorm onset may be due to pre-existing auroral emission in the onset sector, as previously observed by Milan et al. (2010). Similar results are also observed in Figure 7.2 in the $62 - 64^{\circ}$ and $66 - 68^{\circ}$ substorm onset latitude categories. However, for the lowest substorm onset latitude category of $< 62^{\circ}$, the number of successfully fitted boundaries is approximately the same, between 50 - 150, for all times during the 3 hour period.

7.3.2 Superposed Epoch Analysis of the OCB Location in Nightside Local Time Sectors During Substorms

Figure 7.3 shows the results of the superposed epoch analysis of the OCB location in the nightside local time sectors over a 3 hour period covering 1 hour prior to substorm onset and 2 hours after substorm onset. Substorm onset is defined at t = 0. The panels in Figure 7.3 show the results from (a) SI12, (b) WIC, and (c) SI13. The panels in Figure 7.3 have been limited to show only the local time sectors which contain 50 or more successfully fitted boundary identifications in each time step, as previously discussed in Section 7.3.1. Gray time steps indicate where there are fewer than 50 successful boundary identifications. In each local time sector, each time step shows the difference in the latitude of the OCB in that sector from the location of the OCB at substorm onset. Blue indicates the boundary was located at a lower latitude (equatorward) with respect to the latitude at substorm onset, and red indicates that the boundary was at a higher latitude (poleward) than at substorm onset. White indicates that there was no change in the latitude of the boundary compared to substorm onset. The black dots and crosses in Figure 7.3 indicate the time at which the OCB reaches its most equatorward location in each local time sector i.e. the time after which the OCB began to contract poleward. This will be discussed in more detail in Section 7.3.3.

The results from all three instruments show that prior to substorm onset, the OCB was located poleward of its location at substorm onset, as shown by the red shading in each cell. This shows that, on average, the polar cap was expanding and the OCB moved equatorward in all nightside sectors in the hour prior to substorm

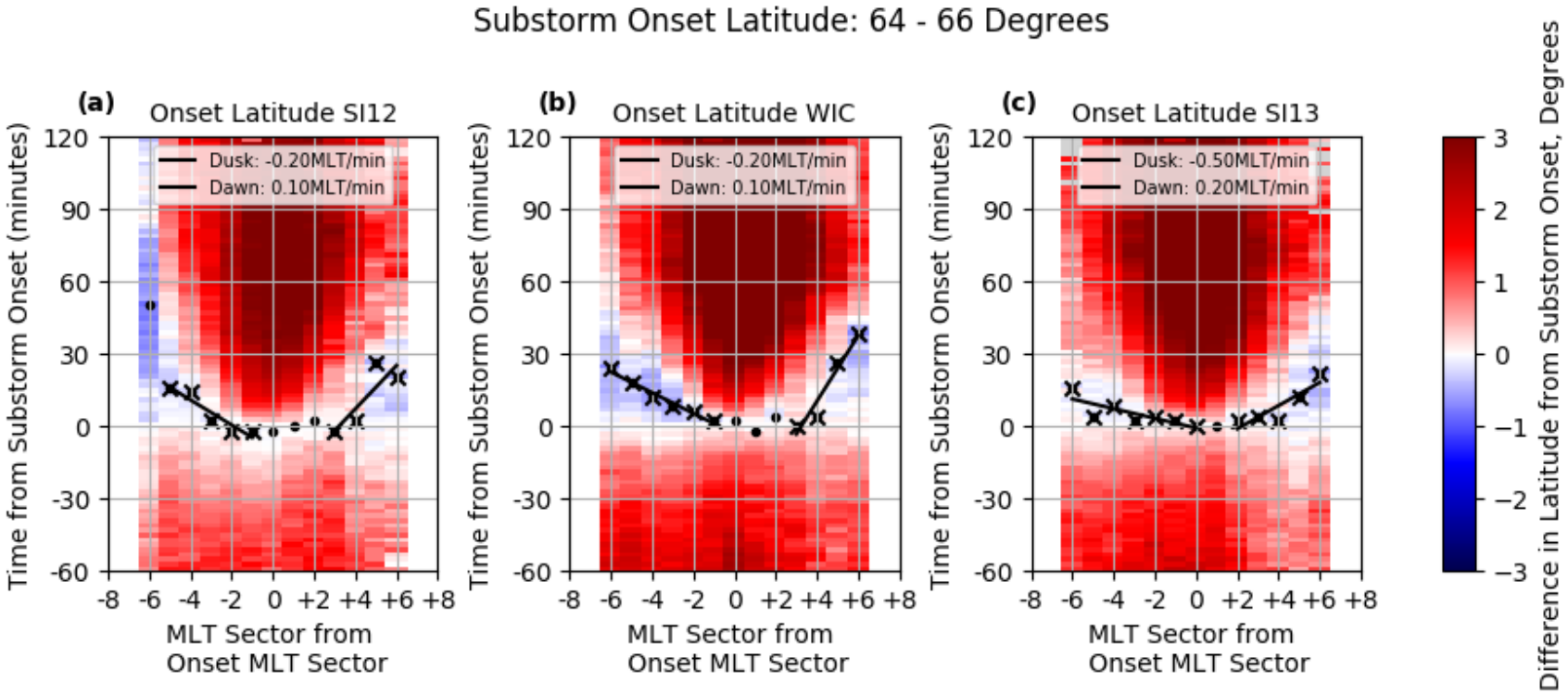

Figure 7.3: The results of the superposed epoch analysis of the OCB location from SI12, WIC, and SI13 ((a)–(c) respectively). The panels show the difference between the OCB location in each local time sector with its location at substorm onset and with respect to time for substorms with onset latitudes between $64^\circ - 66^\circ$. Red indicates that the OCB is located poleward of its location at onset; blue indicates the OCB is located equatorward of its location at onset. Gray indicates when there were less than 50 successfully identified OCB locations. The black dots and crosses indicate the time at which the OCB reaches its most equatorward location in each local time sector. Two lines of best fit are calculated using the dawnward and duskward data points marked with crosses. The slopes of these two lines are displayed in the legend in each panel. The slopes of the lines of best fit for all substorm onset latitudes are provided in Tables 7.1 and 7.2.

onset due to the accumulation of open flux during the substorm growth phase. At substorm onset, the OCB in the local time sectors around the onset sector immediately began to contract poleward as shown by the change in color from white to red. In the WIC data, the rapid poleward contraction of the OCB following onset occurs most quickly in the substorm onset sector, while the SI12 and SI13 boundaries show a shift in the most rapid contraction toward dusk and dawn, respectively. The immediate poleward contraction of the OCB at substorm onset near the substorm onset sector is indicative of the closure of flux in these sectors following substorm onset.

The local time sectors further from the onset sector, both duskward and dawnward, show an extended period of continued equatorward motion of the OCB after substorm onset, indicated by the extended white and blue regions after t = 0. The OCB location estimated from each of the three FUV imagers continued to expand equatorward for up to $\sim$ 20 minutes after substorm onset in the MLT −6 sector and for 20–40 minutes after substorm onset in the MLT +6 sector. The OCB in these furthest dawn and dusk sectors remained equatorward of their location at onset for some time but contracted poleward within an hour of substorm onset.

7.3.3 Rate of the Apparent Motion of the OCB Poleward Contraction

Figures 7.4 - 7.6 show the change in the latitude of the OCB for onsets at latitudes (a) $66 - 68^\circ$, (b) $64 - 66^\circ$, (c) $62 - 64^\circ$ and (d) $\leq 62^\circ$. The results for the WIC, SI12 and SI13 datasets are shown separately in Figures 7.4, 7.5 and 7.6 respectively. For brevity and clarity, only the results from WIC are discussed in detail as the results from SI12 and SI13 are morphologically similar. In Figures 7.3 - 7.6, the time of the most equatorward location of the OCB in each local time sector is indicated by a black cross or dot. For all onset latitude categories, the OCB reaches its most equatorward latitude within 30 minutes of substorm onset in the majority of local time sectors. The OCB in sectors further from the substorm onset sector contracts poleward at increasingly later times. This shows an apparent duskward and dawnward motion or expansion of the region of contracting OCB. Linear regression was

used to further quantify this motion towards the dawn and dusk sectors. The data points included in the analysis were varied by including or excluding the three data points from either end, that is, around the substorm onset sector and the far dawn and dusk sectors. The statistical R^2 value indicating the goodness of fit of the line was used to determine the line of best fit. In Figures 7.3 - 7.6, the crosses show the data points used to provide the best fit lines given in the figures. The results of the linear regression analysis are presented in Tables 7.1 and 7.2. The data presented in Tables 7.1 and 7.2 include the gradients of the best fit lines in the dawn and dusk directions from each FUV instrument and the average gradients across all the FUV data sets for each substorm onset latitude category.

In Tables 7.1 and 7.2, the R^2 values are higher than 0.5 with the exception of the dawnward gradients from WIC and generally higher than 0.7. These high R^2 values indicate that fitting a linear gradient is a reasonable assumption and generally provides a good fit to the data across all substorm onset latitude categories. In the mean gradients averaged across all three IMAGE FUV data sets, the apparent dawnward motion is slightly slower ($\sim |0.2|$ MLT hours/minute) than the duskward motion ($\sim |0.3|$ MLT hours/minute) corresponding to a speed of approximately 1.1 km/s at 65°. This may be indicative of the westward traveling surge; however, the difference of 0.1 MLT hours/minute is comparable to the level of uncertainty in this analysis.

There are some differences in the gradients derived from the three instrument data sets. The gradients derived from the WIC data are generally similar in both the dawnward and duskward directions and are consistent across all substorm onset categories. The dawnward gradients derived from the SI12 data and the duskward gradients derived from the SI13 data tend to be more varied, across the substorm onset latitude categories. The largest gradients in the duskward direction tend to be found in the SI13 data, particularly in the lowest onset latitude substorm categories of less than 62°. The largest gradients in the dawnward direction are found in the lower onset latitude categories in the SI12 data ($\leq 62°$) and in the WIC data ($62 - 64°$).

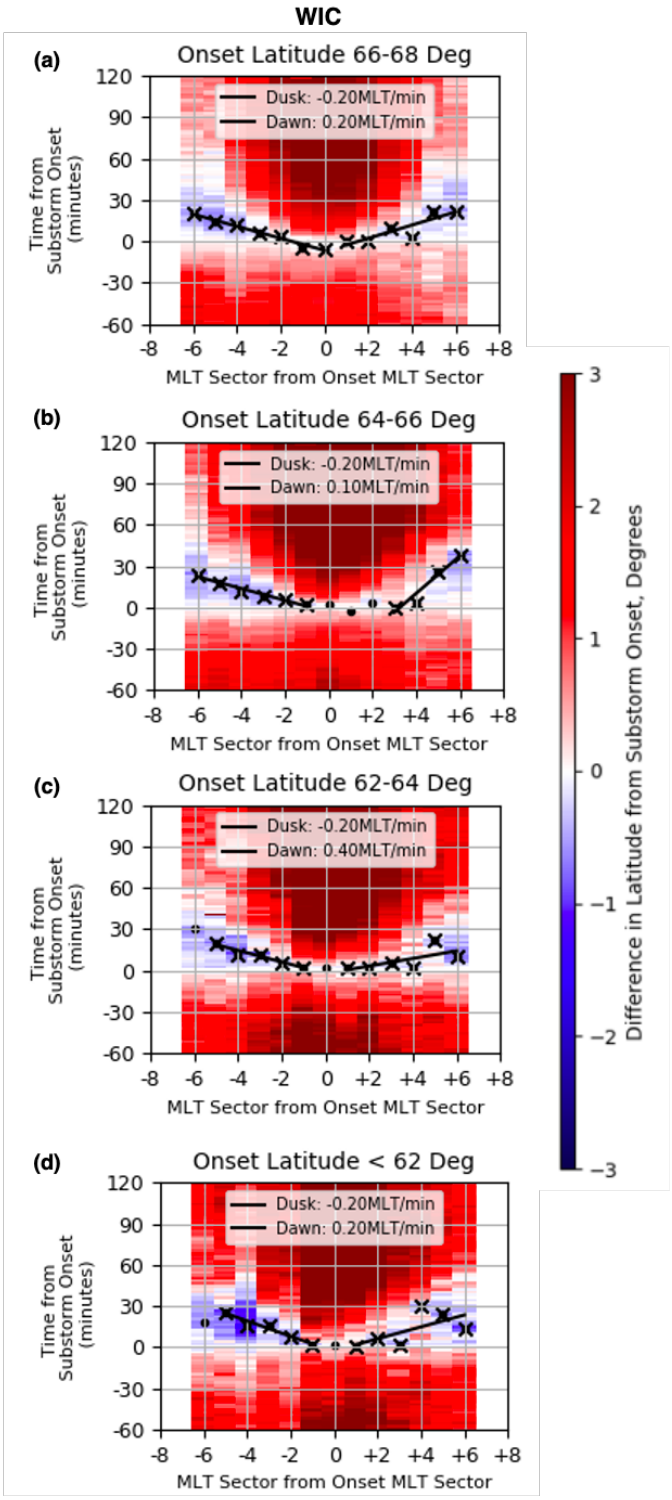

Figure 7.4: The results of the superposed epoch analysis using WIC data for substorms with onset latitudes in the ranges (a) $66 - 68°$, (b) $64 - 66°$, (c) $62 - 64°$ and (d) $\leq 62°$, presented as per Figure 7.3.

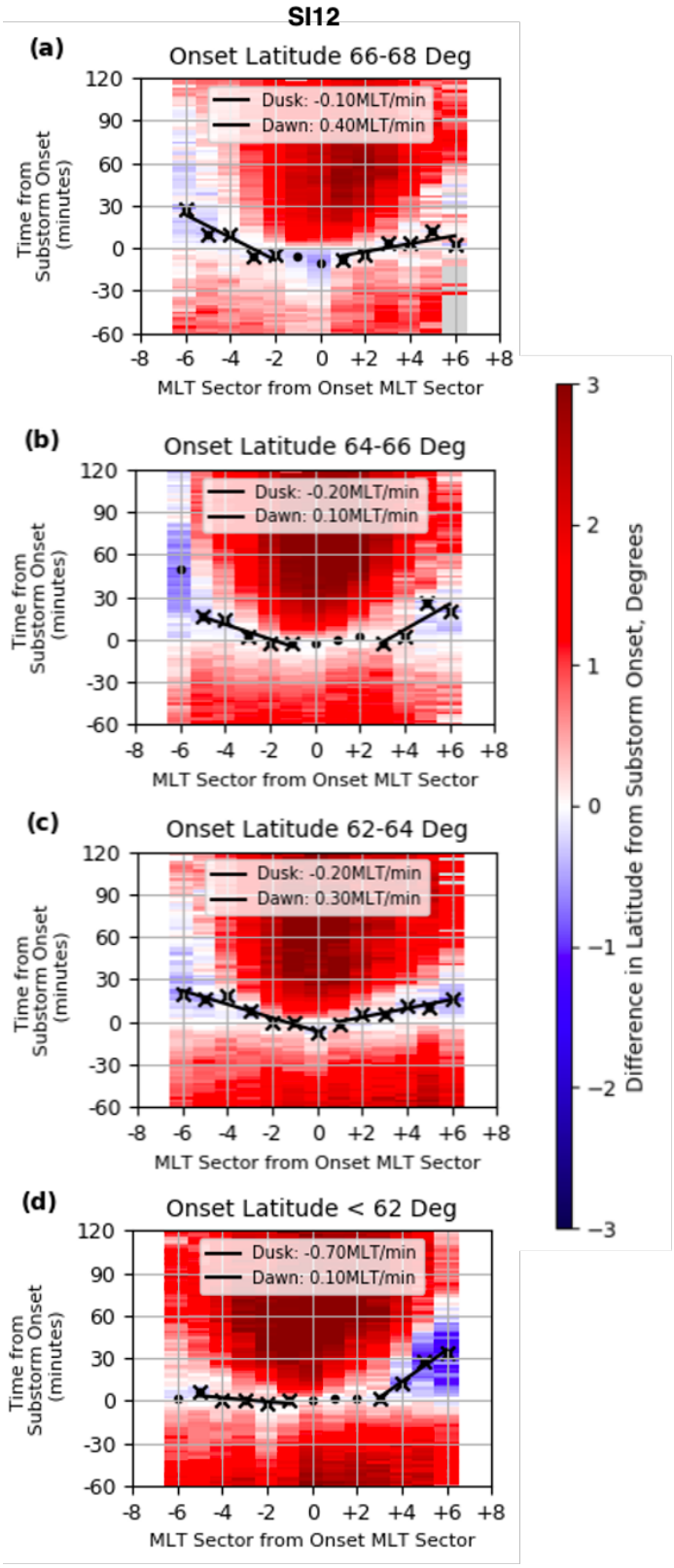

Figure 7.5: The results of the superposed epoch analysis using SI12 data for substorms with onset latitudes in the ranges (a) $66 - 68°$, (b) $64 - 66°$, (c) $62 - 64°$ and (d) $\leq 62°$, presented as per Figure 7.3.

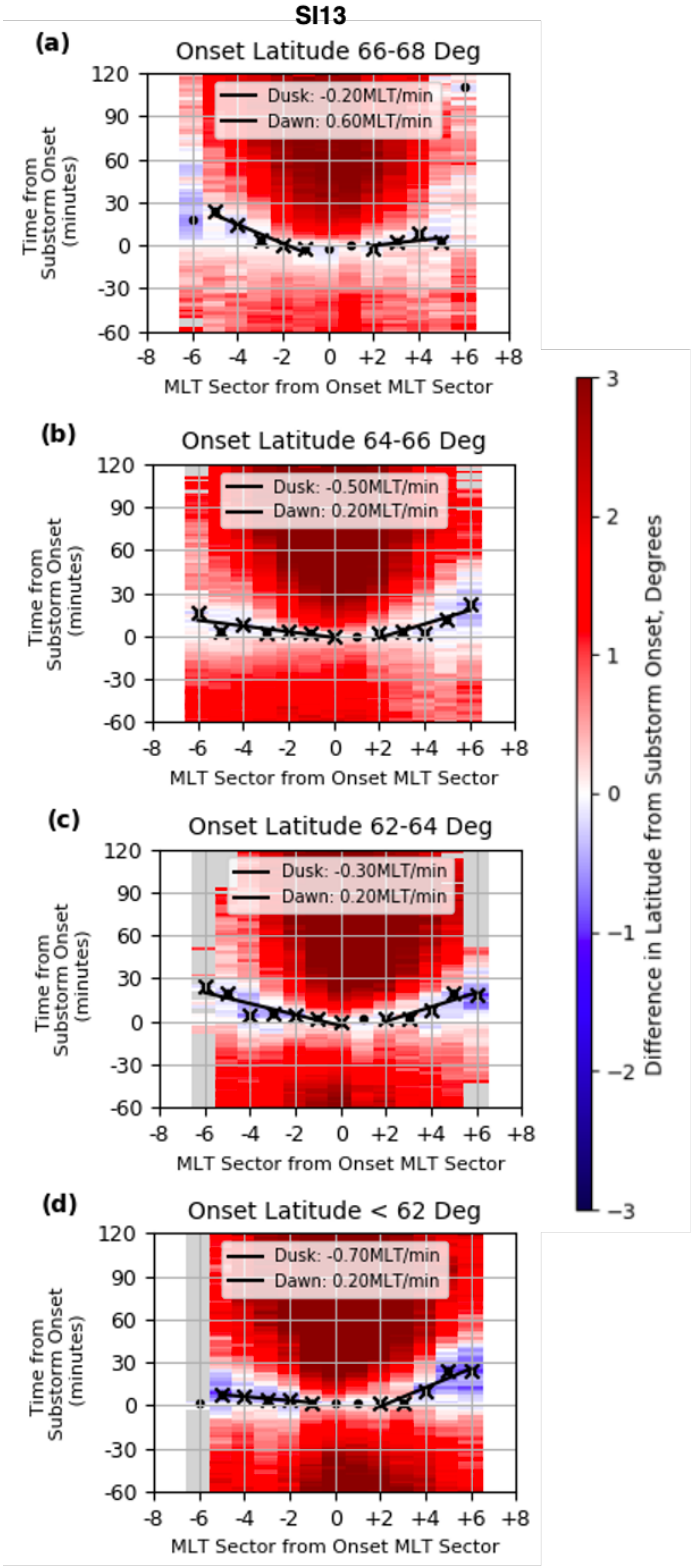

Figure 7.6: The results of the superposed epoch analysis using SI13 data for substorms with onset latitudes in the ranges (a) $66 - 68°$, (b) $64 - 66°$, (c) $62 - 64°$ and (d) $\leq 62°$, presented as per Figure 7.3.

Dawnward							
	SI12		**WIC**		**SI13**		**Mean**
Onset Latitude (°)	Gradient (MLT hours/ minute)	R^2	Gradient (MLT hours/ minute)	R^2	Gradient (MLT hours/ minute)	R^2	Gradient (MLT hours/ minute)
66 - 68	0.4	0.56	0.2	0.73	0.0	0.54	0.1
64 - 66	0.1	0.73	0.1	0.94	0.2	0.77	0.1
62 - 64	0.3	0.87	0.4	0.43	0.2	0.84	0.3
≤ 62	0.1	0.97	0.2	0.44	0.2	0.89	0.2

Table 7.1: The results of the linear regression analysis tracking the poleward contraction of the OCB towards the dawn sectors from each of the FUV instruments, illustrated in Figure 7.4.

Duskward							
	SI12		**WIC**		**SI13**		**Mean**
Onset Latitude (°)	Gradient (MLT hours/ minute)	R^2	Gradient (MLT hours/ minute)	R^2	Gradient (MLT hours/ minute)	R^2	Gradient (MLT hours/ minute)
66 - 68	- 0.1	0.86	- 0.2	0.98	- 0.1	0.97	- 0.1
64 - 66	- 0.2	0.88	- 0.2	0.97	- 0.5	0.69	- 0.3
62 - 64	- 0.2	0.93	- 0.2	0.94	- 0.1	0.82	- 0.2
≤ 62	- 0.7	0.53	- 0.2	0.95	- 0.7	0.94	- 0.5

Table 7.2: The results of the linear regression analysis tracking the poleward contraction of the OCB towards the dusk sectors from each of the FUV instruments, illustrated in Figure 7.4.

For the highest latitude onsets between $66-68^{\circ}$, the OCB in the sectors close to the onset sector reached its most equatorward position prior to substorm onset and the OCB does not expand as much prior to onset for these events. A smaller expansion of the OCB prior to substorm onset is consistent with higher onset latitude substorms accumulating less open flux before substorm onset and hence being associated with smaller substorms (Milan et al., 2009a). In addition, some of the brightenings in the higher latitude substorm onset categories identified by Frey et al. (2004) may be poleward boundary intensifications (PBIs de La Beaujardiere et al., 1994) or pseudobreakups rather than substorm onsets. PBIs are a repetitive brightening at the poleward boundary in the nightside auroral oval which are thought to be signatures of reconnection in the distant magnetotail (de La Beaujardiere et al., 1994). Pseudobreakups are another brightening of the auroral oval which have been associated with the reconnection in the magnetotail (Kullen et al., 2009). However, pseudobreakups tend to be short-lived (5 - 16 minutes Kullen and Karlsson, 2004), compared to substorms and do not lead to a global expansion of the bright auroral region and the closure of a significant amount of open flux as observed during the substorm expansion phase. PBIs and pseudobreakups can occur during each substorm phase (Kullen and Karlsson, 2004) and are difficult to distinguish from substorms onset, particularly from observing auroral brightenings in isolation of other geomagnetic indices. The main difference between substorm onsets, PBIs and pseudobreakups are that PBIs and pseudobreakups are more localised auroral events which may close a smaller amount of open flux compared to a substorm occurring at a similar onset latitude and there is not necessarily an increase in the open flux content prior to the observed brightenings, as would be the case in the substorm growth phase. The inclusion of PBIs and pseudobreakups in the statistical analysis presented this study may bias the results by reducing the amount of flux opened/closed before/after substorm onset, particularly in the higher onset latitude categories.

7.3.4 Nightside Open Flux Content

The location of the OCB in each nightside local time sector is used to estimate the open flux content in each sector, using Equation 7.1 where A is the area of the local time sector and **B** is the strength of the magnetic field threading the sector, as previously discussed in Chapter 3. In this analysis, **B** was assumed to have a constant magnetic field strength in the ionosphere with a fixed value of $B_I \sim 5 \times 10^4$ nT threading the polar cap area (Milan et al., 2003). The summation of the flux from all local time sectors then provides an estimate of the total nightside flux content. The flux is calculated for the −6 to +6 MLT sectors for all three FUV instruments.

$$\phi = A \cdot \mathbf{B} \tag{7.1}$$

Figure 7.7 shows the results of the superposed epoch analysis of the nightside flux profiles during the 1 hour before and after substorm onset for each substorm onset latitude category and for all three FUV data sets. For all substorm onset latitudes, the total nightside flux content increases prior to substorm onset, consistent with the accumulation of open flux during the substorm growth phase. After onset, the open flux decreases immediately, indicating that nightside reconnection becomes dominant over dayside reconnection at substorm onset. This is observed across all FUV imagers. The continued decrease in the total nightside flux content during the hour after substorm onset indicates that open flux continues to be closed even after the end of substorm expansion phase, typically 20–30 minutes after onset (e.g. Forsyth et al., 2015), and well into the recovery phase.

While the overall trends in open flux are similar for each imager and all onset latitudes, there are subtle differences in the flux profiles. The nightside flux from WIC is consistently ∼0.05 GWb lower than that calculated from SI12 and SI13, which are approximately equal for all but the lowest onset events (Figure 7.7d). This corresponds to a 7–10% difference in the nightside open flux content at onset and shows no apparent dependence on onset latitude. The flux profile from WIC for the lowest latitude events shows a plateau in the total nightside flux content for

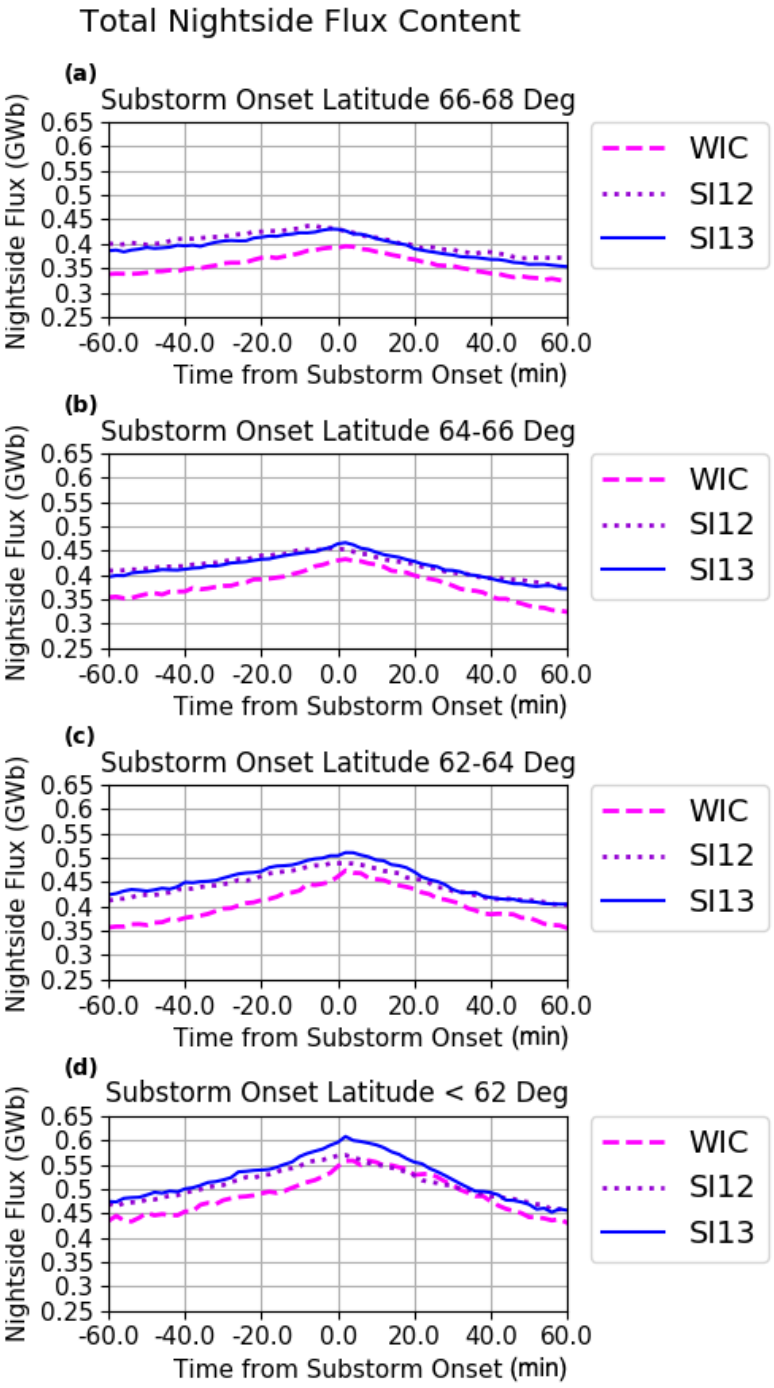

Figure 7.7: Results of superposed epoch analysis of the total nightside flux content calculated between the MLT sectors −6 and MLT +6 for each of the three FUV instruments in the 1 hours before and after substorm onset. WIC data are shown in pink, SI12 data are shown in purple, and SI13 data are shown in blue. (a) shows the total nightside flux content for the highest substorm onset latitude category with the substorm onset latitudes decreasing in (b)–(d).

10 minutes after substorm onset. This result is not replicated in the results of any other substorm onset category or in the SI12 or SI13 data for the same substorm onset latitude category. By linearly fitting the rate of change in the total nightside flux content during the 30 minutes before and after substorm onset, the net difference in the dayside and nightside reconnection rates can be calculated in terms of a difference in reconnection voltage. The results of the rate of change of total flux are presented in Table 7.3. The change in flux content during both the periods before and after onset is greatest for the lowest latitude events and decreases with increasing substorm onset latitude, in keeping with previous results (e.g. Milan et al., 2009a). The rates of change of flux are 1.7–3.4 times greater for the substorms with onsets of $< 62^{\circ}$ compared to onsets in the 66 – 68° range. The results in Table 7.3 also highlight that the loss of open flux occurs more quickly than the increase in flux prior to onset. For the highest onset latitude events, flux is closed 1.3–2.1 times faster than it was opened, whereas for the lowest latitude events, flux is only closed 1.0–1.2 times faster than it was opened.

	Growth Phase (kV)			**Expansion Phase (kV)**		
Substorm Onset Latitude (°)	**SI12**	**SI13**	**WIC**	**SI12**	**SI13**	**WIC**
66 - 68	8.0	12.2	15.1	-16.6	-21.3	-19.3
64 - 66	12.5	18.8	21.0	-20.4	-25.7	-29.4
62 - 64	21.4	22.3	29.0	-23.8	-27.6	-29.3
≤ 62	27.3	33.7	31.0	-30.3	-38.8	-32.0

Table 7.3: The estimated net difference between dayside and nightside reconnection rates, calculated from the rate of change in the total nightside flux content in Figure 7.7.

During both the substorm growth and expansion phases, in all substorm onset latitude categories, the rate of change of flux estimated from the SI12 data is consistently the smallest out of the three FUV data sets. In the growth phase, the rate of increase of flux estimated from the WIC data is generally the largest for all substorm onset latitude categories, except the lowest onset latitude category ($\leq 62^{\circ}$). During the 30 minutes following substorm onset, the percentage difference in the total nightside flux closure estimated from the three FUV instruments is between 5% and

36%. The largest percentage difference is between the WIC and SI12 instruments for substorms with onset latitudes between $64 - 66^{\circ}$.

Figures 7.8, 7.9 and 7.10 show the contribution to the total nightside flux content estimated from the WIC, SI12 and SI13 data, respectively, for five representative local time sectors during the hour before and after substorm onset. The flux contribution from the substorm onset sector (MLT 0) is shown in solid black, a pre-onset sector (MLT −3) in solid blue, a dusk sector (MLT −6) in dashed blue, a post-onset sector (MLT +3) in solid red, and a dawn sector (MLT +6) in dashed red.

The results from each of the FUV datasets shown in Figures 7.8 - 7.10 are similar. The substorm onset sector, MLT 0, contains the largest contribution to the total nightside open flux content, approximately 10% for all substorm onset latitude categories. The pre-onset and post-onset sectors (MLT −3 and MLT +3, respectively) contribute approximately equal amounts of flux to the total nightside open flux content throughout the 2 hours period encompassing onset, each containing $\sim$8% of the total nightside flux content at substorm onset. The dawn and dusk sectors (MLT +6 and MLT −6) contain the smallest amount of flux in the nightside local time sectors, each contributing approximately 5–6% to the total nightside open flux content, in all substorm onset latitude categories. At substorm onset, the open flux in the onset sector begins to decrease within 2 - 4 minutes of substorm onset for onsets at all latitudes and then continues to gradually decrease throughout the hour after substorm onset. One hour after substorm onset, the open flux content of the onset sector is slightly lower compared to the open flux content 1 hour prior to substorm onset. The open flux in the pre-onset and post-onset (MLT −3 and MLT +3) sectors changes more gradually, plateauing at substorm onset before starting to decrease within 10–20 minutes of substorm onset in keeping with the continued equatorward expansion of the OCB in Figures 7.3 and 7.4. In the dawn and dusk sectors (MLT +6 and MLT −6), there is a much smaller change in the flux content over the 2 hour period; however, the flux content of these local time sectors is observed to increase prior to substorm onset and continue to increase for up to 10–30 minutes after onset. Approximately 30–40 minutes after substorm onset, a slight decrease in the

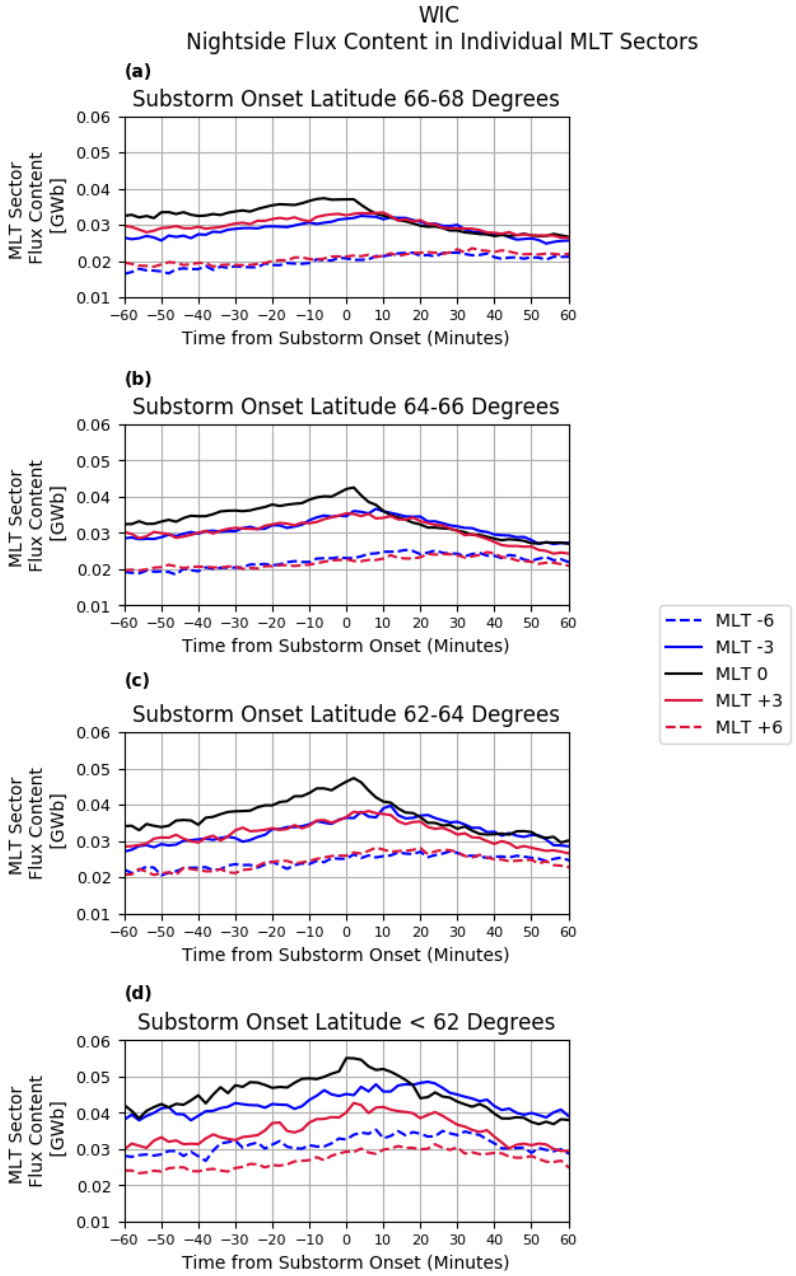

Figure 7.8: Superposed epoch analysis results of the open flux calculated from WIC from five 1 hour local time sectors including the substorm onset sector (MLT 0), a pre-onset sector (MLT -3), a post-onset sector (MLT +3), and a dawn (MLT +6) and dusk sector (MLT -6). For clarity, only a selection of local time sectors are shown. The highest substorm onset latitude of $66 - 68^{\circ}$ is shown in (a), with substorm onset latitude decreasing in panels (b) – (d), to the lowest onset latitude category of less than 62° in (d).

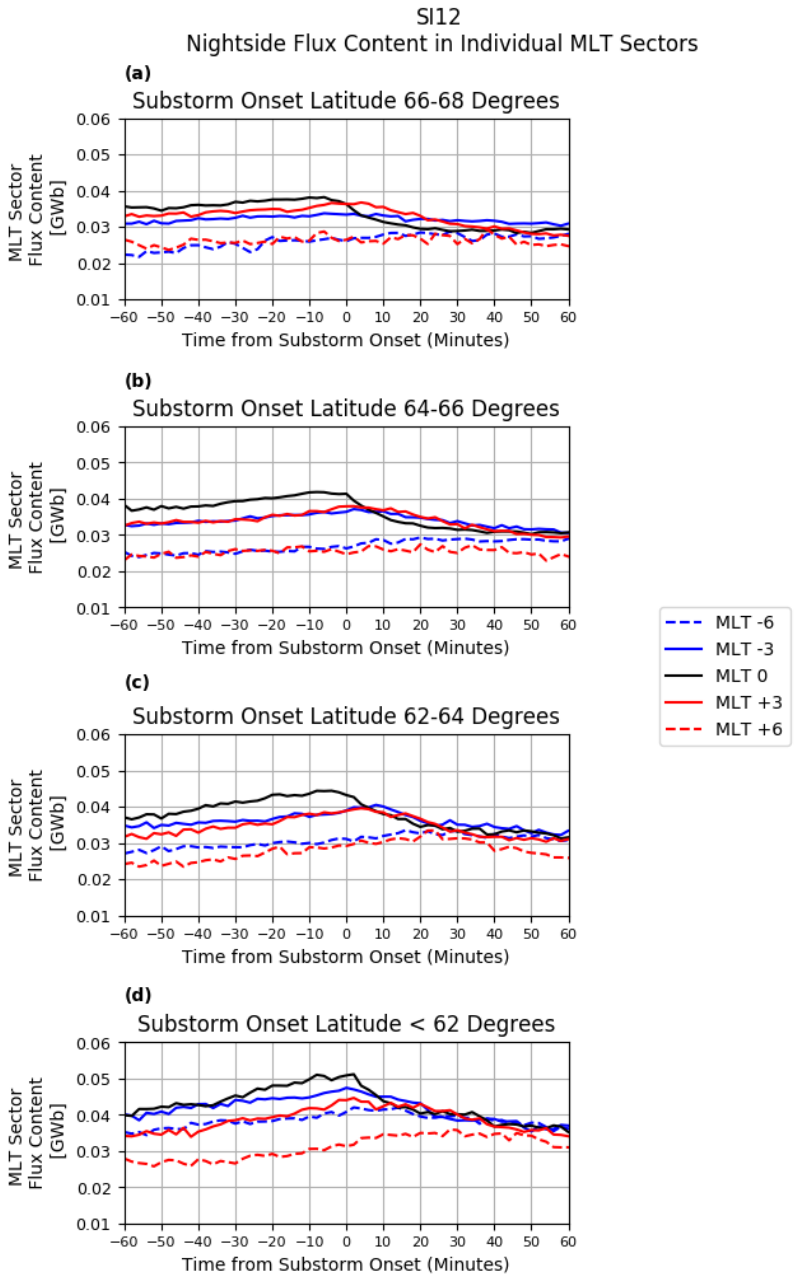

Figure 7.9: Superposed epoch analysis results of the open flux calculated from SI12 from five 1 hour local time sectors including the substorm onset sector (MLT 0), a pre-onset sector (MLT -3), a post-onset sector (MLT +3), and a dawn (MLT +6) and dusk sector (MLT -6). For clarity, only a selection of local time sectors are shown. The highest substorm onset latitude of 66 – 68° is shown in (a), with substorm onset latitude decreasing in panels (b) – (d), to the lowest onset latitude category of less than 62° in (d).

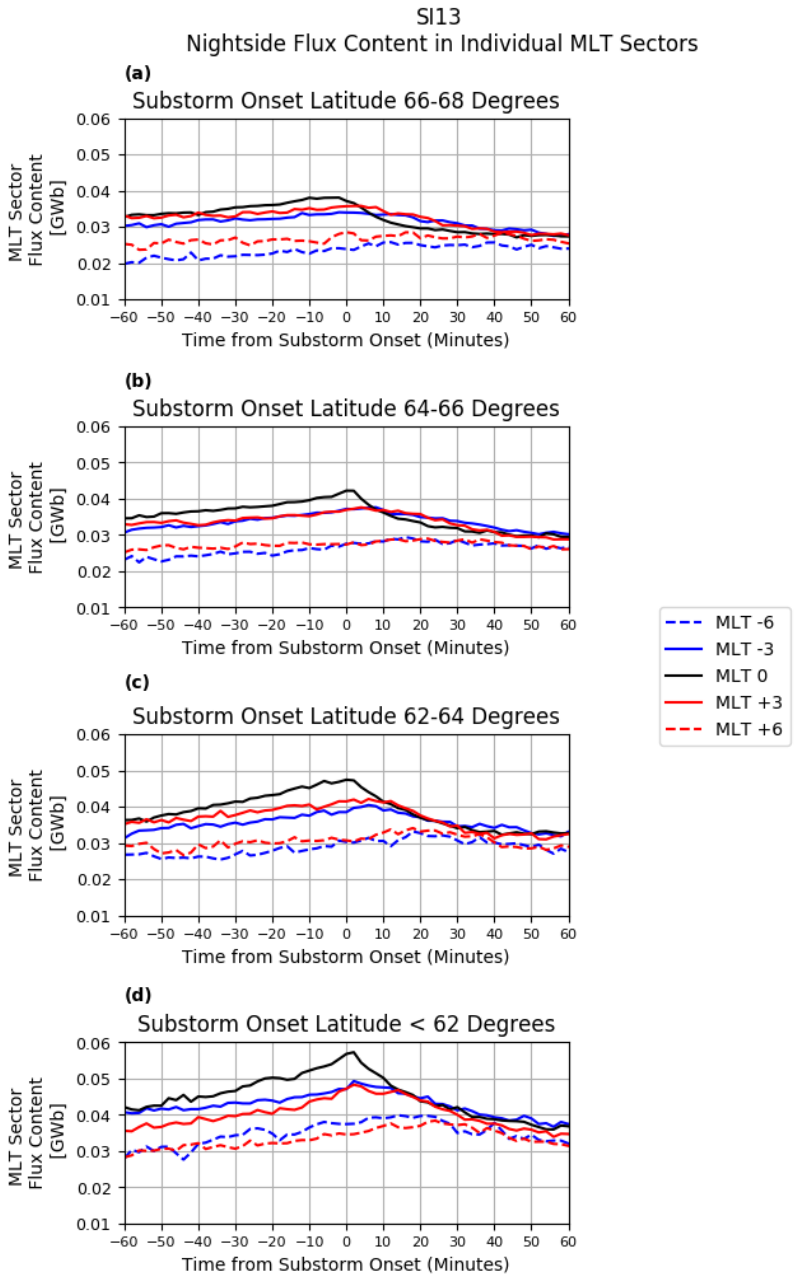

Figure 7.10: Superposed epoch analysis results of the open flux calculated from SI13 from five 1 hour local time sectors including the substorm onset sector (MLT 0), a pre-onset sector (MLT -3), a post-onset sector (MLT +3), and a dawn (MLT +6) and dusk sector (MLT -6). For clarity, only a selection of local time sectors are shown. The highest substorm onset latitude of 66 – 68° is shown in (a), with substorm onset latitude decreasing in panels (b) – (d), to the lowest onset latitude category of less than 62° in (d).

flux content is observed in these local time sectors for the lower substorm onset latitudes in panels c and d. In the highest substorm onset latitudes shown in panels a and b, the flux content of these local time sectors remains approximately constant during the 40–60 minutes after substorm onset, with no significant change in flux observed.

For onsets above 62°, the pre-onset and post-onset sectors (MLT −3 and MLT +3) and the dawn and dusk sectors (MLT +6 and MLT −6) contain equal amounts of flux throughout the 2 hours period. In the lowest substorm onset latitude category, the flux content of the pre-onset and dusk sectors is significantly higher than the flux content of the corresponding post-onset and dawn sectors. In the highest substorm onset latitude category ($66 - 68^{\circ}$), the opposite is observed in that the flux content of the post-onset sectors is marginally higher than that of the pre-onset sectors. This may suggest an asymmetry in the opening and closure of flux in the pre-onset versus the post-onset sectors in the highest and lowest substorm onset latitude categories.

7.4 Discussion

This study has examined the detailed motion of the OCB, based on auroral boundary observations, with respect to substorm onset time and with respect to the substorm onset sector and the effect this has on the calculation of open magnetic flux in the polar cap. The results of the superposed epoch analysis of the OCB latitude showed the OCB does not contract poleward uniformly in all local time sectors immediately after substorm onset but continues to expand equatorward for 20–40 minutes after onset at 6 hours of local time away from the onset sector, with the region of contracting OCB expanding dawnward and duskward at 0.2–0.3 MLT hours/minute, on average. Similarly, using auroral image data from WIC and SI12 Walach et al. (2017) found that the brightening of the electron auroral oval also expanded toward the dawn and dusk sectors 10–40 minutes after substorm onset. Despite the continued equatorward expansion of the OCB in the dawn and dusk sectors, the total open nightside flux content of the polar cap begins to decrease at substorm onset, dominated by the change in OCB location close to the onset sector.

Figure 6.9 in Chapter 6 showed that the poleward edge of the nightside auroral oval is poorly defined by the solar wind driven OP-2013 auroral forecast model. In this region, ROC scores of less than 0.5 indicated that the model forecasts often predict the opposite to what is observed, resulting in a high number of missed forecasts or false alarms in the truth table. The results of the superposed epoch analysis presented in this chapter show the detailed motion of the nightside poleward auroral boundary and OCB in response to substorms. Incorporating the response of the auroral oval to magnetotail-driven activity in auroral models could lead to significant improvements in the next generation of auroral forecast models. However, this would require the inclusion of an input dataset that captures substorm onsets in real time in auroral forecast models.

7.4.1 Suitability of the Proxy OCB Determined from FUV Auroral Images

The OCB used in this study was identified by Longden et al. (2010) from the poleward auroral luminosity boundary (PALB) derived from global FUV images of the auroral oval from the IMAGE satellite. In each local time sector, a latitudinal correction was applied to the PALBs derived from (Longden et al., 2010) to account for the average statistical offset between PALBs derived from auroral FUV images and the location of the OCB inferred from particle precipitation measurements, which provide a more accurate proxy of the OCB location (Boakes et al., 2008; Carbary et al., 2003; Longden et al., 2010). In the noon and midnight sectors, all PALBs were found to lie poleward of the particle precipitation boundary. The advantage of using the PALBs from global auroral image data as an OCB proxy is that the OCB is defined in all local time sectors around the auroral oval. While particle precipitation measurements from satellites such as DMSP provide the most accurate determination of the OCB location, these measurements are spatially and temporally limited. A superposed epoch analysis of the OCB location during substorms, would not be possible without using the corrected PALBs as a proxy for the OCB. However, the correction determined by Longden et al. (2010) and used in this study is a statistical average and may not be correct in any given case.

The results show that there are subtle differences between the OCBs calculated from the WIC, SI12, and SI13 FUV imagers on IMAGE. Overall, the open flux content estimated from SI12 and SI13 are similar, while the open flux content estimated from WIC is ∼10% smaller, despite the corrections applied to the PALBs. This may be the result of the different resolution of the three imagers. For SI12 and SI13, each pixel covered a minimum of 0.94° when looking straight down at the Earth's surface, while each WIC pixel covered a minimum of 0.48°, with this difference in resolution increasing away from the nadir. Note that a 10% difference in flux can be accounted for by approximately a 5% difference in the latitude of the OCB. Comparing the nightside open flux content estimated from each of the three instruments provides an assessment of the uncertainty in the open flux calculation. Alternatively, these results may indicate that the corrections to the PALB have some dependence on geomagnetic activity that is not currently accounted for. It is unclear from the results of this study which of the OCB identifications from each of the three FUV instruments provide the closest boundary identification to the true OCB location or whether the boundaries from any of the instruments consistently over or under estimate the total flux content of the polar cap. The consistently lower estimation of the total nightside flux content from the WIC data is relevant for future upcoming missions, such as SMILE. The SMILE mission will host the ultraviolet imager (UVI) onboard for science monitoring of the northern hemisphere aurora (Branduardi-Raymont et al., 2018). The proposed UVI will have a wide passband sensitive to Lyman-Birge-Hopfield emission which is similar to the passband of the WIC instrument of 140–190 nm. Future estimations of the polar cap flux content using data from the SMILE UVI may slightly under-estimate or over-estimate the total flux content of the polar cap and, by extension, the net difference in dayside and nightside reconnection rates.

7.4.2 Expansion of the Contracting OCB Region towards the Dawn and Dusk Sectors

The formation of an *auroral bulge* and its rapid duskward expansion in a *westward traveling surge* were some of the first reported features of the auroral phenomenol-

ogy of substorms (Akasofu, 1964), with the westward traveling surge moving at speeds of up to 0.4–2.2 km/s (Craven et al., 1989; Marklund et al., 1998; Gjerloev et al., 2007). The results of the superposed epoch analysis presented in this chapter found that the average rate of expansion of the region of contracting OCB toward the dawn and dusk directions was $|0.2|$ and $|0.3|$ MLT hours/minute, respectively, corresponding to approximately 1.1 km/s at 65° latitude, in agreement with these earlier studies of the expansion of the auroral brightness and westward and eastward moving surges. Gjerloev et al. (2007) found that, on average, the eastward propagation of the auroral bulge toward the dawn was marginally faster than toward dusk. In contrast, by applying directed network analysis to ground magnetometer data, Orr et al. (2019) found that magnetic perturbations associated with substorm activity and loosely linked to the auroral bulge expanded westward toward the dusk local time sectors after substorm onset before expanding dawnward at a later time. The results of the analysis presented here suggest that the propagation of the poleward contraction of the OCB in the dusk direction is slightly faster than the propagation in the dawn direction, however the difference of 0.1 MLT hour/minute is comparable to the level of uncertainty in the analysis.

Cowley and Lockwood (1992) argued that a localized decrease in the open flux content of the polar cap from nightside reconnection would form a bulge in the OCB that would be redistributed around the polar cap by excited plasma flows. The plasma flows direct the closed flux away from the near-midnight local time sectors, where nightside reconnection is occurring downtail, toward the dawn and dusk sectors. The results presented in this study are in keeping with this ECPC framework, showing that the nightside OCB does not contract poleward uniformly in response to the sudden onset of unbalanced nightside reconnection at substorm onset, but rather, there is a localized contraction which spreads duskward and dawnward for up to 20 - 40 minutes after onset. Furthermore, the OCB in local times further from the substorm onset sector continues to move equatorward until the contracting "bulge" expands into those sectors.

Provan et al. (2004) found that the overall ionospheric convection is enhanced for all substorms to some degree, but there is a localized reduction in the ionospheric return flow in the auroral region close to substorm onset. Grocott et al. (2009) found that the localized reduction in the flow is more pronounced in low onset latitude substorms ($< 64^{\circ}$) but is less apparent for higher latitude onsets. The continued expansion of the OCB after substorm onset and particularly in sectors further from the substorm onset sector shown in this study have been interpreted as ionospheric flows redistributing closed flux around the polar cap. Based on the results of previous studies by Provan et al. (2004) and Grocott et al. (2009), it may be expected that the lower onset latitude substorms in this study would show a slower redistribution of flux compared to higher onset latitude substorms. However instead, to the limits of what this study has been able to resolve, the results show that the poleward contraction of the OCB away from the onset sector was faster for lower onset latitude substorms, particularly in the duskward direction as estimated from the SI12 and SI13 data. This could hint that in addition to the ionospheric flows redistributing newly closed flux, there may be other processes influencing the results, such as an expansion of the reconnection region in the magnetotail or the excitation of the westward travelling surge which could decrease the open flux content in sectors away from the onset sector at a faster rate, particularly in the duskward direction, than ionospheric convection can redistribute the newly closed flux.

7.4.3 Variations in the Total Nightside Flux Content

Using the OCB location to estimate the total nightside flux content calculated over 12 hours of local time shows that, on average, the total nightside flux content increases before and decreases immediately after substorm onsets identified by Frey et al. (2004) consistent with dayside reconnection being dominant before onset and nightside reconnection being dominant after onset. These results were consistent across each of the IMAGE FUV instruments and across all substorm onset latitude categories. However, the exact timing of substorm onset and hence the ordering of events with respect to onset remain a contentious issue within substorm research.

Frey et al. (2004) identified onsets as local brightenings that spread azimuthally in local time for at least 20 minutes, from low spatial resolution FUV images. These have an inherent timing uncertainty of ±2 minutes due to observational cadence of the FUV imagers. In addition, small-scale auroral brightenings known as auroral beads (e.g. Kalmoni et al., 2015, 2017) and exponential growth in ultralow frequency (ULF) wave activity (e.g. Rae et al., 2010), which are reported as the first signatures of substorm activity, can be seen 6–10 minutes before the large-scale auroral enhancements reported by Frey et al. (2004) (Murphy et al., 2009). As such, the results presented in this chapter show that, on average, nightside reconnection becomes dominant, and there is a net closure of flux following the large-scale brightening of the aurora; however, other physical processes associated with substorm activity may occur before this. The definition of substorm onset is highly dependent on the onset signature used (e.g. auroral beads, ULF wave activity or local brightenings in the auroral oval) and how the signature relates to the activity in the magnetotail and the relative timing of the onset signature with respect to the exact onset of reconnection in the magnetotail which cannot be directly observed. It may be that the large scale auroral brightenings identified by Frey et al. (2004) and interpreted as substorm onsets in this study occur after the onset of reconnection in the magnetotail, which may explain why the results of this study show the closure of open flux in the substorm onset sector within a few minutes of onset. However, the study by Coumans et al. (2007) also used the substorm onset list from Frey et al. (2004) and observed a continued increase in the open flux content for up to 20 minutes after onset in some cases. In contrast, the study by Coxon et al. (2014) used the AL magnetometer index to define substorm onset. It may be that the substorm onset identified from the AL index occurs before the onset identified by large-scale auroral brightenings which is why Coxon et al. (2014) observed that the open flux content continued to increase for up to 15 minutes after substorm onset. However, this does not explain the difference in the results presented in this study with those of Coumans et al. (2007).

The total nightside open flux content at substorm onset ranged from approx-

imately 0.40 – 0.60 GWb for high to low substorm onset latitudes, respectively. Previous studies have shown the total open flux content at substorm onset to be between 0.53 and 1.01 GWb (Boakes et al., 2011; Coumans et al., 2007; Hubert et al., 2006, 2017); thus, the nightside flux calculated in this chapter accounts for between 60% and 80% of the total flux. This is a natural consequence of the offset of the center of the auroral oval from the magnetic pole, with the OCB in the midnight sector typically approximately 6 – 12° further from the pole than in the noon sector (Carbary, 2005; Holzworth and Meng, 1975). Over the hour before onset, the nightside flux increased by 0.05–0.135 GWb or 10–22% of the flux at onset. Boakes et al. (2011) reported that the total flux increased over 5 hours before onset by 22% relative to the flux at the start of the interval. Estimating from the figures of Boakes et al. (2011) shows that, over an hour before onset the total open flux increased by 0.1 GWb or 15% of the flux at onset. Correcting for the fact that the observations from this chapter are of the nightside only but that the majority of the auroral oval is on the nightside, this implies that the majority of the variation in the location of the OCB in the hour before and after substorm onset is on the nightside.

The rate of change of flux estimated from the three FUV instrument data sets during the growth and expansion phases showed slightly different results. The rate of change of flux estimated from the SI12 data was consistently smaller than the rates estimated from the WIC and SI13 data during both the growth and expansion phases for all substorm onset latitude categories. In general, the rate of change of flux estimated from the WIC data during both the growth and expansion phases were the largest for all substorm onset latitude categories except lowest onset latitude ($< 62°$) category where the rates estimated from the SI13 data were largest for both the growth and expansion phases. Although this analysis is based on the Frey et al. (2004) substorm onset list, the data selection criteria mean that the analysis of the WIC, SI12, and SI13 derived OCBs used different numbers of events (Figure 7.1). The analysis presented in this chapter was repeated using only a subset of substorms for which there were successful OCB locations derived from all three FUV instruments but found that this had no impact on the presented results.

Examining the contribution to the total nightside flux content of five individual nightside local time sectors (onset MLT 0, pre-onset MLT −3, post-onset MLT +3, dawn MLT +6, and dusk MLT −6) showed that the substorm onset sector consistently contained the highest flux content throughout the 2 hour period and decreased sharply at substorm onset, while the post-onset and pre-onset sectors had a more rounded peak in the flux profile. The dawn sector flux profiles were observed to plateau or continue to increase in the hour after substorm onset. A dawn-dusk asymmetry in the opening and closure of flux during the highest and lowest substorm onset latitude categories was also observed. In the lowest substorm onset latitude category ($< 62^{\circ}$), the flux contribution from the duskward local time sectors was significantly higher than the dawnward local time sectors, while in the highest latitude substorm onset category (66 – 68°), the flux contribution from the dawnward sector MLT +3 was marginally larger than the contribution from the duskward sector MLT −3 prior to substorm onset.

The continued equatorward motion of the OCB after substorm has previously been observed in the R1 and R2 currents (Clausen et al., 2012, 2013; Coxon et al., 2014; Milan et al., 2009b, 2021). From these studies, it has been suggested that the total open flux content continues to increase after substorm onset (Clausen et al., 2012, 2013; Coumans et al., 2007; Coxon et al., 2014). Clausen et al. (2012, 2013) and Coxon et al. (2014) use the R1 Birkeland current as a proxy for the OCB location and found that an oval fitted to the boundary of the R1 current (and by proxy, the OCB) continued to expand equatorward for up to 15–20 minutes after substorm onset before contracting poleward. Clausen et al. (2013) showed that the continued expansion in the OCB after substorm onset is particularly notable in the dawn sectors, which is also shown in the results presented in this study. Clausen et al. (2013) and Coxon et al. (2014) suggested that the continued expansion after substorm onset may be due to dayside reconnection initially dominating over nightside reconnection in the dawn and dusk sectors after substorm onset. Milan et al. (2021) observed that the dayside driving rate remained high after substorm onset in many substorms which resulted in the open flux content continuing to increase for up to 20

minutes after substorm onset. Coxon et al. (2018) observed a 20 minute plateau in the magnetic energy density of the magnetotail lobes around substorm onset. The authors suggested that this may be due to a 15 minutes uncertainty in the timing of the substorm onset which may also provide an alternative explanation for the delayed poleward contraction of the OCB observed by Coxon et al. (2014). The results presented here show that the OCB continues to move equatorward after onset in those local time sectors far from the onset sector and may indicate a movement of open flux propagating toward dawn and dusk sectors before the closure of flux from nightside reconnection propagates round from the substorm onset sector. The contraction of the OCB close to the onset sector is greater than the continued expansion, and thus, there is a net decrease in open flux after substorm onset. The apparent discrepancy between the results presented in this study, showing a net closure of flux after onset, and the results of Clausen et al. (2012, 2013); Coxon et al. (2014) and Milan et al. (2021), showing a continued increase in open flux after onset, may be explained by dayside reconnection continuing to add more flux than is removed by nightside reconnection immediately after substorm onset, as has been suggested by these studies. It may be that it is not until a later time after substorm onset when the closure of flux as a result of nightside reconnection spreads toward dawnward and duskward local time sectors that the flux closure begins to dominate and the total flux content decreases. However, if this were the case, one would expect to observe a similar result in this study. The discrepancy between these findings may instead be due to the timing uncertainty between different substorm onset lists using different signatures of global auroral brightenings and magnetometer data to define substorm onset. Alternatively, it may be that the results from the oval-fitting methods are dominated by more sectors showing the equatorward motion of the OCB than the number of sectors showing a poleward contraction of the OCB initially after substorm onset. The results from the analysis presented in this study show that the localised deformation in the OCB can result in an immediate reduction in the nightside flux content. As such, the circular fitting techniques may not be suitable for investigating dynamics during substorms but may be applicable for analysis of

the auroral oval and the open flux content before and after substorms.

This study has only been able to examine the change in the flux content of the nightside local time sectors during substorms and infer the rates of nightside reconnection, but has not been able to include the changes in the flux content of the dayside local time sectors or reconnection rates. It would be interesting to repeat the analysis presented in this study with the substorms sub-divided by low and high dayside driving after substorm onset. However, the results of this study have highlighted that the distorted shape of the OCB is key to understanding the changes in open flux during substorms.

7.5 Conclusions

This study has examined the detailed motion of the poleward auroral boundary as a proxy for the open-closed field line boundary during substorms in all nightside local time sectors. The results of the analysis have shown that the OCB does not expand and contract uniformly in all local time sectors. During substorms, the OCB is observed to expand toward the equator during the growth phase in all nightside local time sectors indicative of open magnetic flux accumulating in the polar cap. At substorm onset, the OCB in local time sectors around the substorm onset sector immediately contracts poleward, while in the dawn and dusk regions the OCB continues to expand toward the equator. After substorm onset, the poleward contraction of the OCB appears to propagate away from the substorm onset sectors round toward the dawn and dusk regions. This results in the OCB in local time sectors furthest from the onset sector continuing to expand toward the equator for longer after substorm onset, causing the OCB to become distorted during the substorm expansion phase as the newly closed flux is circulated around the polar cap. The apparent motion of the flux closure away from the substorm onset sectors was found to be slightly faster in the duskward direction, indicating that the OCB in the dusk sectors begins to contract poleward slightly earlier while the OCB in the dawn sectors continues to expand equatorward.

After substorm onset and into the expansion phase, the magnetic flux content of

the dusk and dawn sectors (MLT −6 and MLT +6) continues to increase, as indicated by the continued equatorward expansion. However, the total nightside flux content decreases immediately at substorm onset. The decrease in the flux content of the onset sector is shown to dominate the overall decrease in the total nightside flux content, despite the continued increase in the flux content observed in the far dusk and dawn sectors.

The total nightside flux content estimated from each of the three FUV instrument datasets differed by up to 10% at substorm onset. The WIC dataset consistently estimated the lowest nightside flux content at substorm onset compared to the SI12 and SI13 datasets. The lower nightside flux content estimated from WIC data is relevant for scientific analysis of the polar cap flux content from future missions which will host a wideband UV instrument similar to WIC, such as the upcoming SMILE mission.

The non-uniform shape of the nightside poleward auroral boundary during substorms may explain the poor ROC scores of < 0.5 in this region in the verification analysis of the OP-2013 auroral forecast model presented in Chapter 6. The solar wind driven OP-2013 model is unable to capture the detailed motion of the auroral boundaries during substorms which are driven by internal activity in the magnetotail. The inclusion of the detailed motion of the poleward boundary of the auroral oval and OCB in response to substorms in the nightside local time sectors will have a significant impact on the performance of the next generation of auroral forecast models. This would require an additional input dataset in future auroral forecast models that captures substorm onsets in real time.

Chapter 8

Exploring the relationship between the equatorward auroral boundary and the Plasmapause

The analysis in Chapter 7 examined the statistical motion of the poleward auroral boundary in response to substorms. The poleward auroral boundary can be used as a proxy for the location of the OCB. Magnetic field lines at higher latitudes above the OCB are considered to be *open* and connect to the IMF while magnetic field lines at lower latitudes are closed with both foot points connected to the Earth. The particles which contribute to the main auroral emission are hence from these closed magnetic field lines and precipitate down to the ionosphere. The results of Chapter 6 also showed that, on average, the FUV aurora extends down to approximately between $60 - 70^{\circ}$ latitude. Below this latitude, the magnetic field lines remain closed and yet no auroral emission is observed. Since the poleward auroral boundary is associated with the open-closed field line boundary and the auroral oval doesn't extend down to the equator, this raises the question; what is the physical significance of the equatorward auroral boundary in the magnetosphere? Some studies (e.g. Linscott and Scourfield, 1976; He et al., 2020) have found observational evidence that implies a link between the equatorward auroral boundary and the plasmapause, the outer boundary of the plasmasphere. However, the observational evidence linking these two boundaries is limited and has so far only been presented in a few case

studies. It thus remains an open question as to whether this link holds more broadly in all local time sectors and under different levels of geomagnetic activity.

This chapter presents a statistical analysis of the ionospheric footpoint of the plasmapause location to compare against the equatorward boundary of the auroral oval determined from FUV images of the auroral oval. This chapter aims to explore why the auroral emission does not extend to lower latitudes and whether the cold plasmaspheric population plays a role in preventing particles precipitating into the ionosphere at lower latitudes. In addition, this study also evaluates whether the equatorward boundary of the auroral oval determined from global FUV images could be used to model or predict the location of the plasmapause.

8.1 Introduction

A number of previous studies have provided observational evidence identifying a close relationship between the plasmapause and the equatorward boundary of the auroral oval. Ground-based observations of whistler-mode waves and in-situ observations in the dusk local time sectors have identified times when the equatorward edge of the diffuse aurora coincided with the plasmapause location to within $\sim 0.1-0.25$ L (Linscott and Scourfield, 1976; Horwitz et al., 1982), with the ground based whistler observations made during disturbed, but quietening, geomagnetic conditions, when Kp decreased from 5 to 4 (Linscott and Scourfield, 1976). Case studies have also shown a direct link between whistler-mode chorus waves, which are typically observed outside the plasmasphere (e.g. Lauben et al., 2002), and pulsating aurora (Tsuruda et al., 1981; Ozaki et al., 2012, 2015; Hosokawa et al., 2015). Recent studies have identified giant undulations and waves in the equatorward auroral boundary in dusk local time sectors from auroral images that have been linked to waves, instabilities and plasma injections at the plasmapause (Motoba et al., 2015; Henderson et al., 2010, 2018; Forsyth et al., 2020b; He et al., 2020; Horvath and Lovell, 2021), providing further evidence that the equatorward auroral boundary may be closely associated with the plasmapause location in dusk local time sectors. Conversely, in another case study under quiet geomagnetic activity, Schield

and Frank (1970) found that the inner edge of the plasma sheet, which is thought to be the source region of the auroral particles precipitating to the lowest latitudes of the auroral oval in the ionosphere, and the plasmapause were separated by between 1 - 5 R_E in the midnight local time sectors. Between the inner, Earthward edge of the plasmasheet and the plasmapause, Schield and Frank (1970) observed a warm plasma population with electron energies in the range of $\leq$ 100 eV with an electron density on the order of $\sim$ 1 cm^{-3}.

The location of the plasmapause is relevant for radiation belt models and larger scale magnetospheric models. The plasmasphere impacts the radiation belt dynamics and inner magnetospheric particle populations, such as the ring current, through wave-particle interactions (Thorne, 2010) which can either act as an energisation mechanism and accelerate particles in the radiation belt or, as a loss mechanism by pitch angle scattering radiation belt particles, resulting in particles being lost to the ionosphere. Despite the importance of the plasmasphere to radiation belt and magnetospheric dynamics, there is currently no global monitoring of the plasmasphere or plasmapause location. Several empirical models of the plasmasphere and plasmapause location have been derived from in-situ plasma density observations (e.g. Binsack, 1967; Carpenter and Anderson, 1992; Moldwin et al., 2002; O'Brien and Moldwin, 2003) and medium-scale field aligned currents (Heilig and Lühr, 2013), parameterised by geomagnetic indices including Kp, AE and Dst. Another model of the plasmapause has been developed from plasmapause identifications from global EUV images and parameterised by upstream solar wind parameters such as the IMF B_Z component, the IMF clock angle and the estimated dayside reconnection rate by Larsen et al. (2007), resulting in a predictive model of the plasmapause location. However, if the equatorward boundary of the auroral oval is linked to the plasmapause, monitoring of the auroral boundary would provide a useful, alternative and more direct way of determining the plasmapause location from observations.

This study analyses the statistical location of the plasmapause mapped to the ionosphere compared to the equatorward boundary of the auroral oval and evaluates whether the equatorward auroral boundary determined from global FUV images

could be used to model or predict the location of the plasmapause.

8.2 Data and Magnetospheric Mapping

Goldstein et al. identified the plasmapause location in 3143 images of the plasmasphere taken by the EUV instrument onboard the IMAGE spacecraft in the period between 2000 - 2004. Between 2000 - 2002, when the FUV auroral boundaries determined by Longden et al. (2010) are also available, the plasmapause was identified in 2993 EUV images. The plasmapause identifications span all local time sectors, although the plasmapause is not identified in all local time sectors in every EUV image. The plasmapause locations also identify features such as plasmaspheric drainage plumes in the dusk local time sectors. This database of plasmapause identifications was previously discussed in Chapter 4 and will be referred to as the Goldstein et al. plasmapause database. The plasmapause identifications are publicly available at `https://enarc.space.swri.edu/EUV/`. Figure 8.1a shows a histogram of the plasmapause radius from all the Goldstein identifications in all local time sectors. The plasmapause radius is generally found between $2-6$ R_E in agreement with e.g. O'Brien and Moldwin (2003), with a mean radius of 3.7 R_E. The distribution has an extended tail to further radii, with a maximum radius of 8.0 R_E. The furthest plasmapause identifications are likely from plume features in the dusk and dayside sectors where the plasmasphere extends radially outwards. The distribution of plasmapause locations at lower radii is steeper and does not generally extend closer to Earth than ~ 2 R_E.

In this study, the plasmapause identifications determined from IMAGE EUV data by Goldstein et al. were traced down into the ionosphere using magnetic field mapping models. The magnetic field mapping of the plasmapause identifications to the ionosphere is crucial in this study, as such the results of three magnetospheric mapping models were tested; the International Geomagnetic Reference Field (IGRF) model and the Tsyganenko 1989 (Tsyganenko, 1989) and Tsyganenko 1996 models (Tsyganenko and Stern, 1996). From this point, the Tsyganenko 1989 and 1996 models will be referred to as T89 and T96, respectively. The IGRF is a

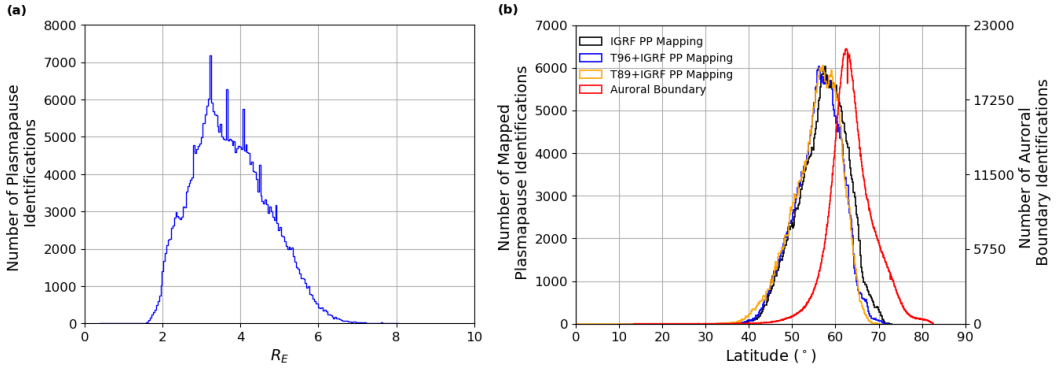

Figure 8.1: (a) The distribution of plasmapause identifications in all local time sectors, from the Goldstein plasmapause database between 2000 - 2002. (b) The distribution of the mapped plasmapause locations using the IGRF only (black), T89+IGRF (orange) and T96+IGRF (blue) and the distribution of the equatorward boundary of the auroral oval determined from FUV data by Longden et al. (2010) between 2000 - 2002 (red).

model of the Earth's internal magnetic field and provides a more realistic internal magnetic field model than assuming a simple dipole. The T89 and T96 models provide larger scale models of the Earth's magnetic field and account for the interaction between the geomagnetic field and the IMF and solar wind. In this study, the T89 and T96 mappings both used the IGRF model as the internal geomagnetic field, rather than a dipole internal field. The inner magnetosphere is largely dominated by the internal geomagnetic field, however testing the results of mapping from the IGRF, T89 and T96 models provides an indication of the potential uncertainty in the mapping.

The average location of the plasmapause identifications mapped to the ionosphere can then be compared to the average location of the equatorward auroral boundary in each local time sector, using auroral boundary identifications from Longden et al. (2010). The auroral boundary identifications used in this study were determined from the WIC FUV instrument onboard the IMAGE spacecraft which captures the wideband auroral emission spectrum from precipitating electrons, as previously discussed in Chapter 4.

Figure 8.1b shows the mapped plasmapause latitudes using the IGRF, T89 and T96 in black, orange and blue, respectively. There are some subtle differences in the distribution of mapped latitudes for all three mapping models. The peaks of the

distribution are slightly offset and there are some differences in the high and low latitude tails of the distributions. There is a greater difference between the IGRF only mapping and the Tsyganenko models for higher latitudes, with the IGRF model mapping to slightly higher latitudes. Overall, there is very little difference between the T89 and T96 distributions and there is good agreement between all three distributions for lower latitudes below the peak values. The means of the distributions are between $55.8 - 57.2^{\circ}$ indicating that the distributions are relatively similar. This suggests that the mapping using the T96 and T89 models are dominated by the internal IGRF model in the inner magnetosphere, rather than the externally driven component. However, based on the fact that there is some impact of the external field model, in the remainder of this study the T96 model has been used to map the plasmapause identifications to the ionosphere. The red histogram in Figure 8.1b shows the latitudinal distribution of the equatorward auroral boundaries identified from the FUV data by Longden et al. (2010). There is some overlap between the FUV boundary distribution and the mapped plasmapause distributions; however, the peak auroral boundary distribution is poleward of the plasmapause with the mean value approximately 10° poleward at 63.7°, suggesting an overall lack of agreement between the plasmapause and equatorward auroral boundary. Given the evidence from previous studies, it is pertinent to assess any agreements between the two boundaries in any local time sectors or under any geomagnetic conditions.

8.3 Results

8.3.1 Case Study: Comparing the Locations of the Plasmapause Mapped to the Ionosphere and the Auroral Boundary

In the following section, two examples are presented comparing the plasmapause identification mapped to the ionosphere against the location of the equatorward auroral boundary under different levels of geomagnetic activity. These examples have been chosen as they have good coverage of both the plasmapause identifications and the equatorward auroral boundary data.

The first example, presented in Figure 8.2 panels (a) and (b) from 10:33 -

10:43 UT on 10 June 2001, has been taken during the recovery phase of a relatively small geomagnetic storm when geomagnetic activity is disturbed but quietening. The peak of the storm occurred shortly before 02:00 UT when the geomagnetic disturbance reached a minimum level of $SYM-H = -44$ nT and Kp = 5. The geomagnetic activity had been constant with Kp = 3 since 03:00 UT. At 10:38 UT when the data for this example were taken, the geomagnetic activity level was Kp = 3 and was decreasing. The plasmaspheric dynamics on the 10 June 2001 have been studied in greater detail by Spasojević et al. (2003) and Pierrard and Cabrera (2005).

The second example, presented in panels (c) and (d), is from 05:32 - 05:42 UT on 18 June 2001 and was taken during the main phase of a geomagnetic storm when the level of geomagnetic activity was increasing. The storm sudden commencement occurred around 03:00 UT and the geomagnetic activity reached a minimum of $SYM-H \approx -80$ nT around 08:00 UT. The level of geomagnetic activity during this example was higher with Kp = 4+ between 03:00 - 06:00 UT and increasing to Kp = 5 between 06:00 - 15:00 UT. The plasmaspheric dynamics on the 18 June 2001 have been studied in greater detail by Goldstein and Sandel (2005).

The purpose of these two case studies is to show to what extent the plasmapause identification mapped to the ionosphere aligns with the location of the equatorward auroral boundary under conditions where geomagnetic activity is quietening in Case Study 1 and where geomagnetic activity is increasing in Case Study 2. The exact details of the events are peripheral to the discussion.

Panels (a) and (c) in Figure 8.2 show the plasmapause identifications from the Goldstein et al. database. Panels (b) and (d) in Figure 8.2 show the result of the plasmapause location mapped to the ionosphere using the T96+IGRF magnetospheric mapping model in blue and the equatorward auroral boundary identification from Longden et al. (2010) in red. Due to the difference in the cadence between the frequency of the FUV auroral images (one image per 2 minutes) and the EUV plasmasphere images (one image per 10 minutes), the auroral boundary data have been averaged across 10 minutes ($\pm$ 5 minutes of the EUV image time). This also

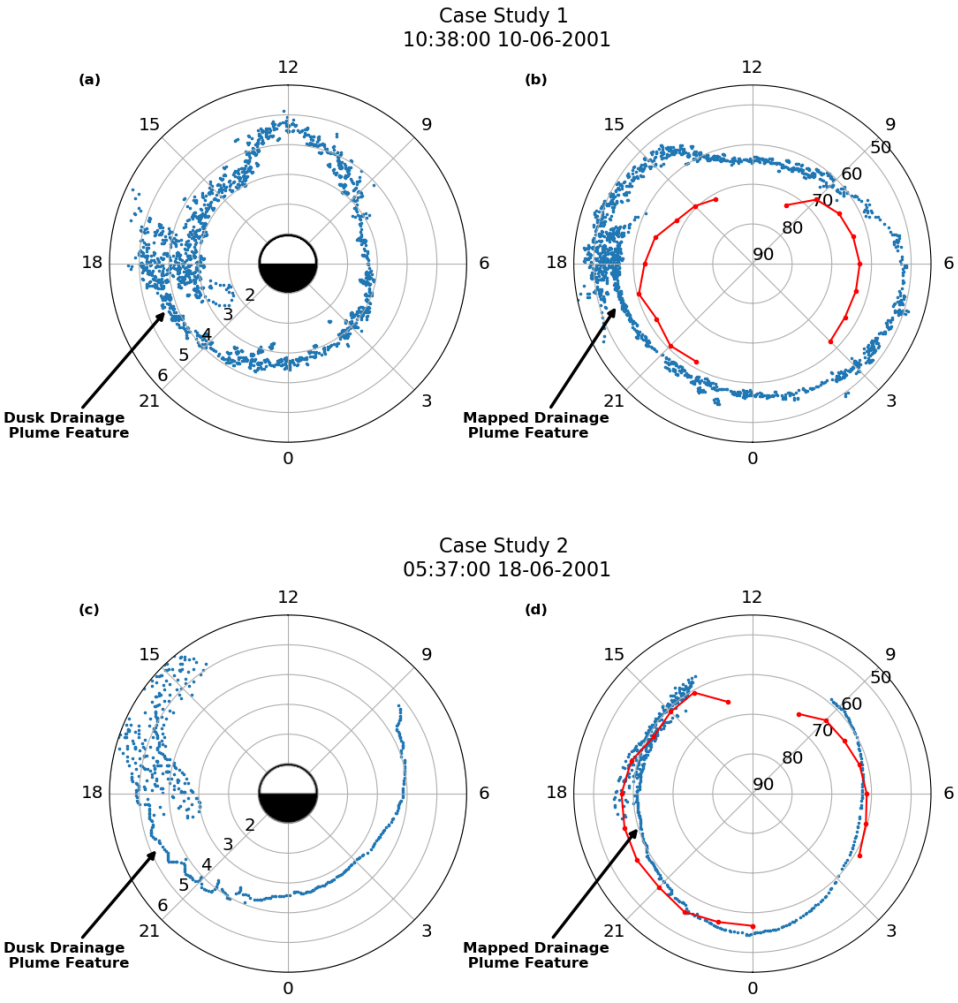

Figure 8.2: Panels (a) and (c) show the plasmapause location identified by Goldstein et al. for 10:38 10 June 2001 and 05:37 18 June 2001, respectively. Panels (b) and (d) show the mapped plasmapause location using the T96+IGRF (blue) and the 10-minute averaged equatorward auroral boundary location (red) identified by Longden et al. (2010).

improves the coverage of the auroral boundary data in local time in these example comparisons.

8.3.1.1 Case Study 1 - Quietening Geomagnetic Activity

The plasmapause identification in Figure 8.2a shows the outline of a drainage plume in the dusk local time sectors and a possible dayside plume extending outwards centred on noon. In the post-noon, post-midnight and dawn sectors, the plasmapause extends to approximately 3 R_E and in the dusk and noon sectors near the plumes the plasmapause extends out to $\sim 4-5$ R_E. Figure 8.2b illustrates that the more contracted regions of the plasmapause that had a radial extent of ~ 3 R_E in the post-noon, post-midnight and dawn local time sectors map to lower latitudes, as low as 50° in the ionosphere while the extended plume regions map to higher latitudes. The result of Figure 8.2b shows that the equatorward auroral boundary lies at higher latitudes than the plasmapause identifications mapped to the ionosphere, in all local time sectors where there is available auroral boundary data.

8.3.1.2 Case Study 2 - Increasing Geomagnetic Activity

Panel (c) shows a more expanded plasmapause, located between $4-6$ R_E with a plume feature also in the dusk local time sectors, stretching into the late afternoon sectors. In this example, the plasmapause identifications mapped to the ionosphere in panel (d) agree well with the FUV equatorward auroral boundary in all local time sectors with available data. One interesting feature in panel (d) is that the plasmaspheric drainage plume feature mapped to the ionosphere, indicated by the black arrow, lies inside the auroral oval. This suggests that the magnetic field lines in the plasmaspheric drainage plume must be auroral field lines and that the hot precipitating plasma that causes the auroral emission is superimposed on a cold plasma population which may result in interesting dynamics.

The results of these two case studies show one event where the plasmapause identification mapped to the ionosphere and the equatorward boundary of the auroral oval are broadly in agreement during increasing levels of geomagnetic activity and one event where the plasmapause identification mapped to the ionosphere lies at significantly lower latitudes than the auroral boundary, during disturbed but qui-

etening levels of geomagnetic activity. In addition, Figure 8.1 showed that while there was some overlap between the distributions of the plasmapause identifications mapped to the ionosphere and the equatorward auroral boundary, overall they were quite different, with the distribution of the plasmapause identifications mapped to the ionosphere largely located equatorward of the auroral boundary. This suggests that the close association between the plasmapause and the equatorward auroral boundary found in previous studies by Linscott and Scourfield (1976); He et al. (2020) and others, may not consistently occur. The following sections analyse the statistical mean locations of the plasmapause identifications mapped to the ionosphere and the equatorward auroral boundary.

8.3.2 Mean Boundary Locations

The results presented in this section show the mean latitude of all the FUV auroral boundary identifications and mean latitude of all the mapped EUV plasmapause identifications, using the T96+IGRF magnetospheric model. There are only 1682 times out of the 2993 that have both Goldstein et al. plasmapause and FUV auroral boundary identifications in at least one local time sector. As such, there are an insufficient number of events to present meaningful mean latitudes for only times where both boundaries are available, particularly when the analysis is then further subdivided by local time. For example, in the noon local time sector (MLT 12) there were a total number of 5112 plasmapause identifications and 18817 equatorward auroral boundary identifications. Limiting the data to times when there is both a plasmapause identification and a corresponding equatorward auroral boundary identification reduces the dataset to 395 in the noon local time sector, which corresponds to approximately 8% and 2% of the total plasmapause and auroral boundary datasets for MLT 12, respectively. This is further reduced when the data was subdivided by geomagnetic activity. The low data coverage when using only times where there is both a plasmapause and auroral boundary identification caused significant variability in the distributions in many local time sectors. In contrast, using the full datasets provides a greater number of events, increasing confidence in the results. In the following sections, the 2-minute cadence FUV auroral boundary data

were used to calculate the mean auroral boundary location, unlike in the case study presented in Figure 8.2 where the equatorward auroral boundaries determined from approximately 5 FUV images were averaged over a 10 minute period.

Figure 8.3 shows the mean latitudes of all FUV equatorward auroral boundary identifications in red and all plasmapause identifications mapped to the ionosphere in blue in each local time sector. The error bars show the standard deviation of the boundaries in each local time sector. On average, the mapped plasmapause lies equatorward of the auroral boundary at $\sim 55^{\circ}$ in all local time sectors. In contrast, the latitude of the equatorward auroral boundary varies from $\sim 60^{\circ}$ in 02 MLT to $\sim 70^{\circ}$ at 14 MLT. In the nightside sectors, between 21 - 03 MLT, the mean latitudes of the two boundaries are aligned to within one standard deviation of each other. In the dayside sectors, the auroral boundary is located further poleward, on average, such that the two boundaries are much further separated, by up to $\sim 15^{\circ}$.

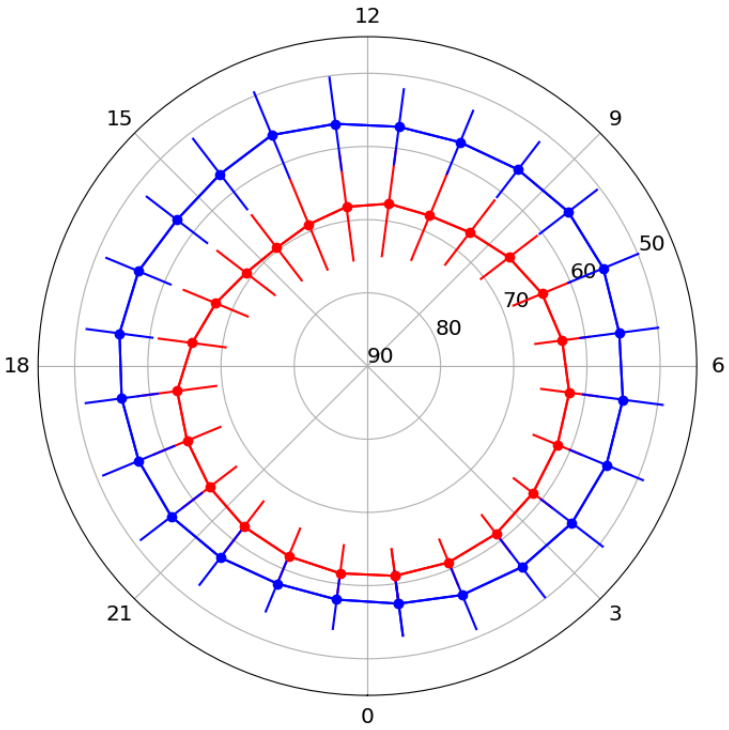

Figure 8.3: The average location of the mapped plasmapause boundary (blue) and the equatorward auroral boundary (red), in all local time sectors, under all geomagnetic conditions for boundary data available between 2000 - 2002. The error bars show the standard deviation of the distribution in each local time sector.

Figure 8.4 shows the latitude distributions of the mapped plasmapause and auroral boundaries in all local time sectors. The auroral boundary distributions appear approximately Gaussian in most sectors, with peak latitudes between 61.5° in the post-midnight sectors to 73° in the noon sector. The histograms in MLT sectors 11 - 13 suggest multiple distributions, with an additional smaller peak at lower latitude just below 60°. The distributions in some local time sectors, such as the pre-noon sectors (MLT 9) and the afternoon to dusk sectors (MLT 14, 15 and 18), have a slightly extended tail in the distribution to lower latitudes. The mapped plasmapause boundary distributions are much more complex than the auroral distributions and have multiple peaks indicative of multiple underlying distributions. This could be as a result of a selection bias in the more limited database of plasmapause identifications. The Goldstein et al. plasmapause database does not have a full coverage of plasmapause identifications for all times when the IMAGE spacecraft was operational. This could be due to limited data coverage from the EUV instrument or a limited number of high quality observations from which the plasmapause location can be well identified. As a result, the Goldstein et al. database of plasmapause identifications may be biased by containing high densities of plasmapause identifications in certain periods of time which had good EUV data coverage or, under certain geomagnetic conditions when the plasmapause can be clearly identified. In the dusk to dayside local time sectors, peaks in the distributions at high latitudes could be due to radially extended plume features. As also observed in Figure 8.2, the mean mapped plasmapause location is approximately constant in all local time sectors between $\sim 54 - 57°$ while the latitude of the largest peak in each distribution varies between 53° in the post-midnight sector (MLT 3) to 64° in the noon sector.

The mean and peak latitudes of the mapped plasmapause and auroral boundary distributions are summarised in Table 8.1. The results in Table 8.1 show that the mean latitude of the two boundaries is offset in all local time sectors, with the mean auroral boundary generally at higher latitudes than the mean latitude of the plasmapause identifications mapped to the ionosphere. The largest differences between the mean latitudes of the boundaries are in the dayside local time sectors (MLT 06 -

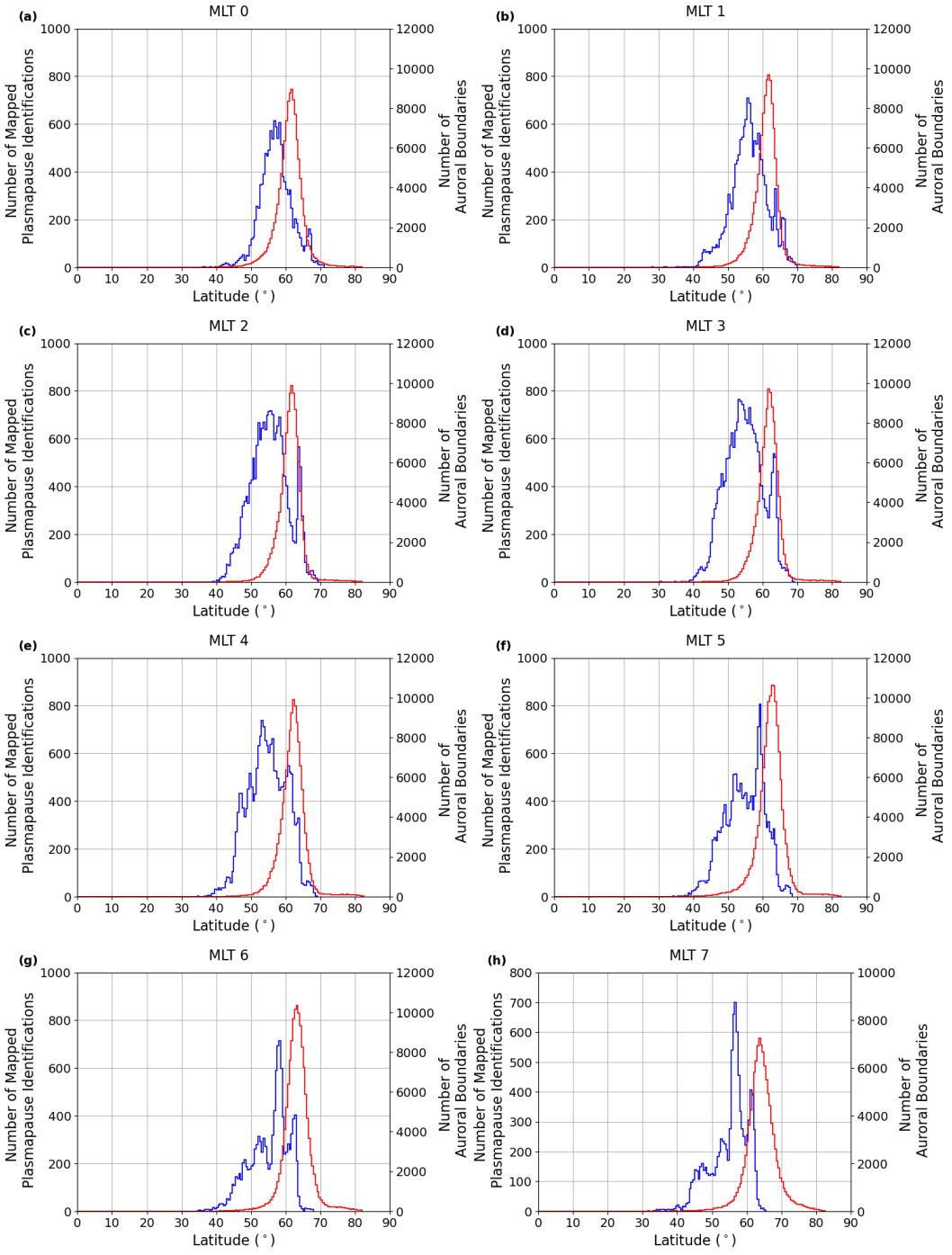

Figure 8.4: The latitude distribution of the mapped plasmapause locations (blue) and auroral boundary identifications (red) in all local time sectors from MLT0 to MLT 23 in panels (a) - (x).

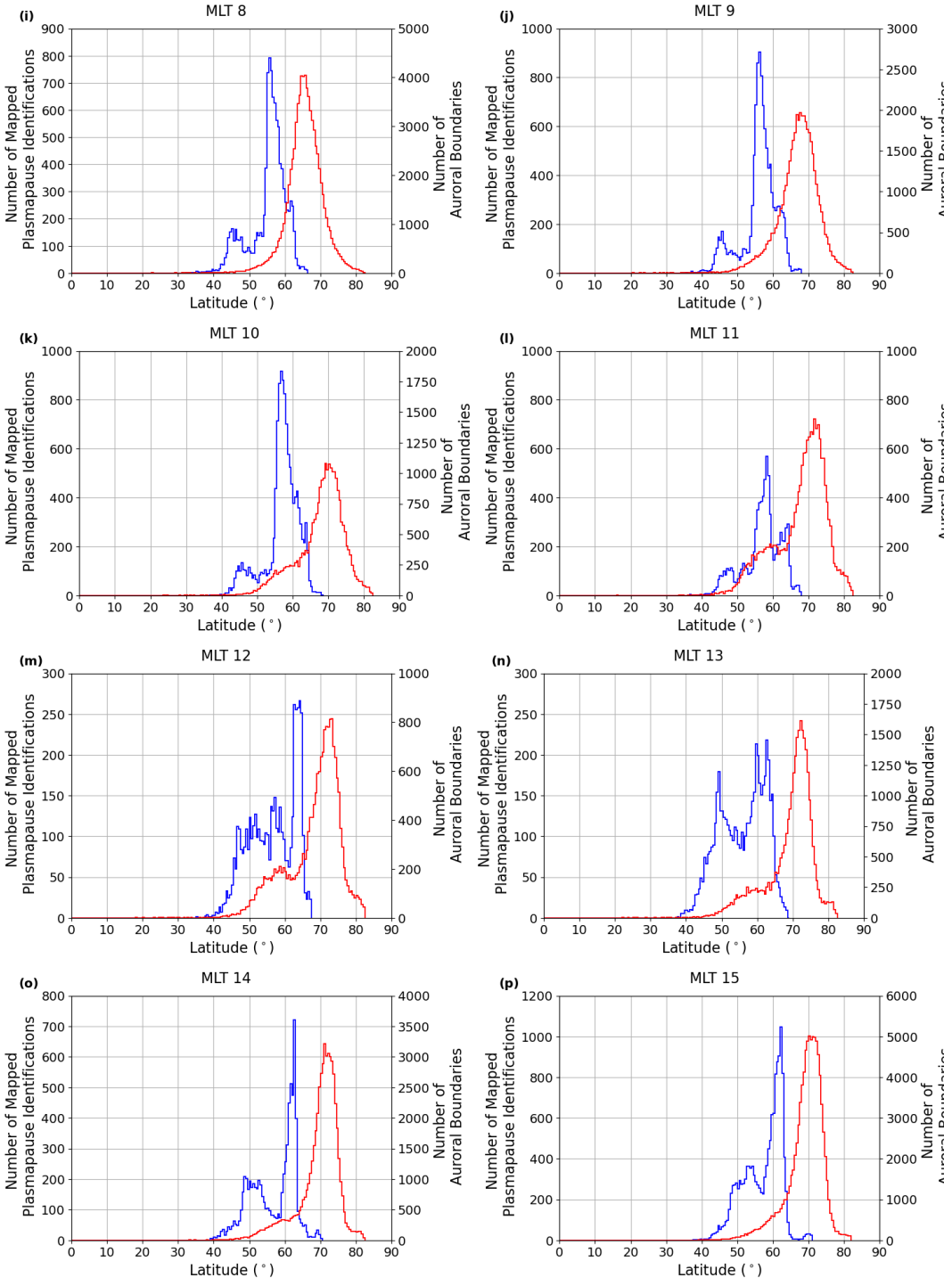

Figure 8.4: The latitude distribution of the mapped plasmapause locations (blue) and auroral boundary identifications (red) in all local time sectors from MLT0 to MLT 23 in panels (a) - (x).

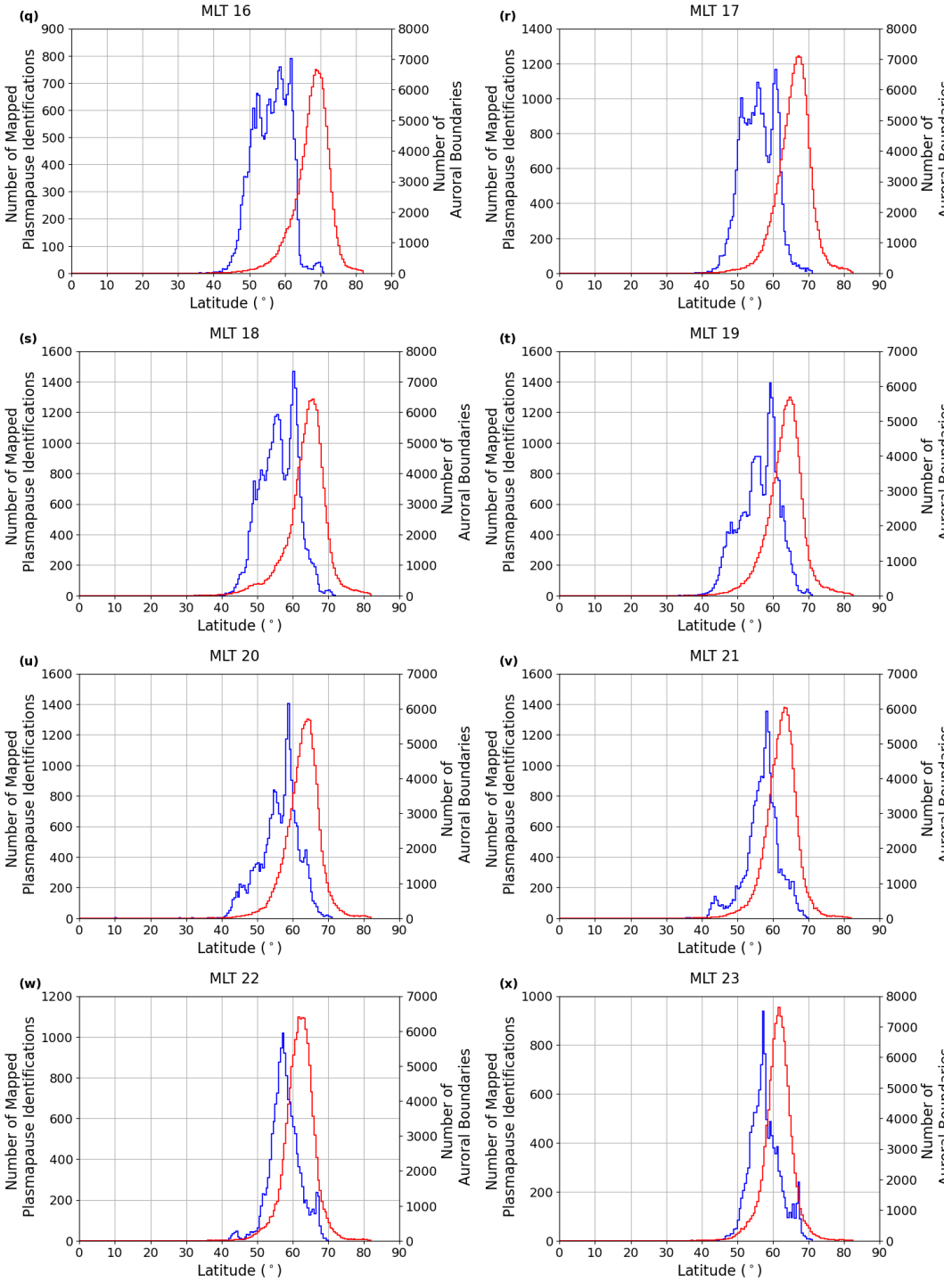

Figure 8.4: The latitude distribution of the mapped plasmapause locations (blue) and auroral boundary identifications (red) in all local time sectors from MLT0 to MLT 23 in panels (a) - (x).

17), separated by 7.9° in MLT 06 and 13.3° in MLT 13, while the mean latitudes in the nightside local time sectors (MLT 18 - 06) are much closer, separated by 3.6° in MLT 23 to 7.7° in MLT 18. In the near midnight sectors between MLT 21 - 02, the difference in latitudes of the largest peaks in the distributions is between $4.5 - 6°$. The peak latitudes for both boundaries are also offset by between $3.5 - 13.5°$ in all local time sectors.

Table 8.1: The mean and peak latitude in the mapped plasmapause and auroral boundary distributions in each local time sector.

MLT	Mapped Plasmapause Latitude (°)		Mean Auroral Boundary Latitude (°)	
	Mean	**Peak**	**Mean**	**Peak**
0	57.3	56.5	61.1	61.5
1	56.1	55.5	61.0	61.5
2	55.4	55.5	61.1	61.5
3	54.8	53.0	61.5	61.5
4	54.7	53.0	61.9	62.0
5	54.8	59.0	62.2	62.5
6	55.3	58.0	63.2	63.0
7	55.1	56.5	64.2	63.5
8	55.4	55.5	65.6	65.5
9	56.2	56.0	67.0	67.5
10	56.9	56.5	67.8	69.0
11	57.0	58.0	67.6	71.5
12	56.6	64.0	68.1	73.0
13	55.8	62.5	69.1	72.0
14	56.9	62.5	69.6	71.0
15	57.2	62.0	69.1	70.0
16	56.1	61.5	67.6	68.5
17	55.8	60.5	65.9	67.0
18	56.1	60.0	63.8	65.5
19	56.2	59.0	63.3	64.5
20	56.2	58.5	62.8	64.0
21	57.0	58.0	62.3	63.0
22	57.8	57.0	61.9	61.5
23	57.8	57.0	61.4	61.5

8.3.3 The Effect of Geomagnetic Activity

The results presented in Section 8.3.2 show that, on average, under all levels of geomagnetic activity combined, there is an offset between the mean latitudes of the

plasmapause identifications mapped to the ionosphere and the equatorward auroral boundary distributions in all local time sectors. However, there is significant overlap between the distributions, particularly in the nightside local time sectors. In the case studies presented in Section 8.3.1, Figure 8.2d showed an example when the two boundaries show good agreement, during disturbed and increasingly active geomagnetic activity. This section examines the effect of geomagnetic activity, defined by Kp level, on the location of the two boundaries in each local time sector.

Figure 8.5 shows the mean latitude of all the auroral boundary identifications and plasmapause identifications mapped to the ionosphere separated by the level of geomagnetic activity, defined by Kp level. As in Figure 8.4, the auroral boundary generally lies poleward of the mapped plasmapause in all local times, however, the nightside boundaries start to coincide at higher levels of geomagnetic activity. For all Kp levels of $Kp \leq 6$ the mean location of the plasmapause boundary mapped to the ionosphere is fairly circular with a latitude of $\sim 55-60^{\circ}$ in all local time sectors. For low Kp levels, the plasmapause boundary mapped to the ionosphere has a bulge extending to lower latitudes in the late afternoon sectors between MLT 15 - 18. A lower, more equatorward mapped latitude signifies that the plasmapause lies at a closer radial distance in this region indicating a bite out feature in the plasmapause boundary. At very high levels of geomagnetic activity of Kp > 6, the plasmapause boundary mapped to the ionosphere globally expands to lower latitudes between $\sim 50-55^{\circ}$, on average. This signifies a contracted plasmapause which may be indicative of the loss of plasma from the plasmasphere via the drainage plume during high levels of geomagnetic activity (e.g. Carpenter, 1966; Carpenter et al., 1993). Under these conditions, plasma is drained from the plasmasphere faster than it can be refilled from the ionosphere.

The equatorward auroral boundary, shown in red in Figure 8.5 is approximately circular but offset from the geomagnetic pole towards the nightside, such that the boundary lies at lower, more equatorward latitudes in the nightside sectors and at slightly higher latitudes in the dayside sectors. For low Kp levels, the auroral boundary is located between $\sim 65-70^{\circ}$ in the dayside local time sectors and between

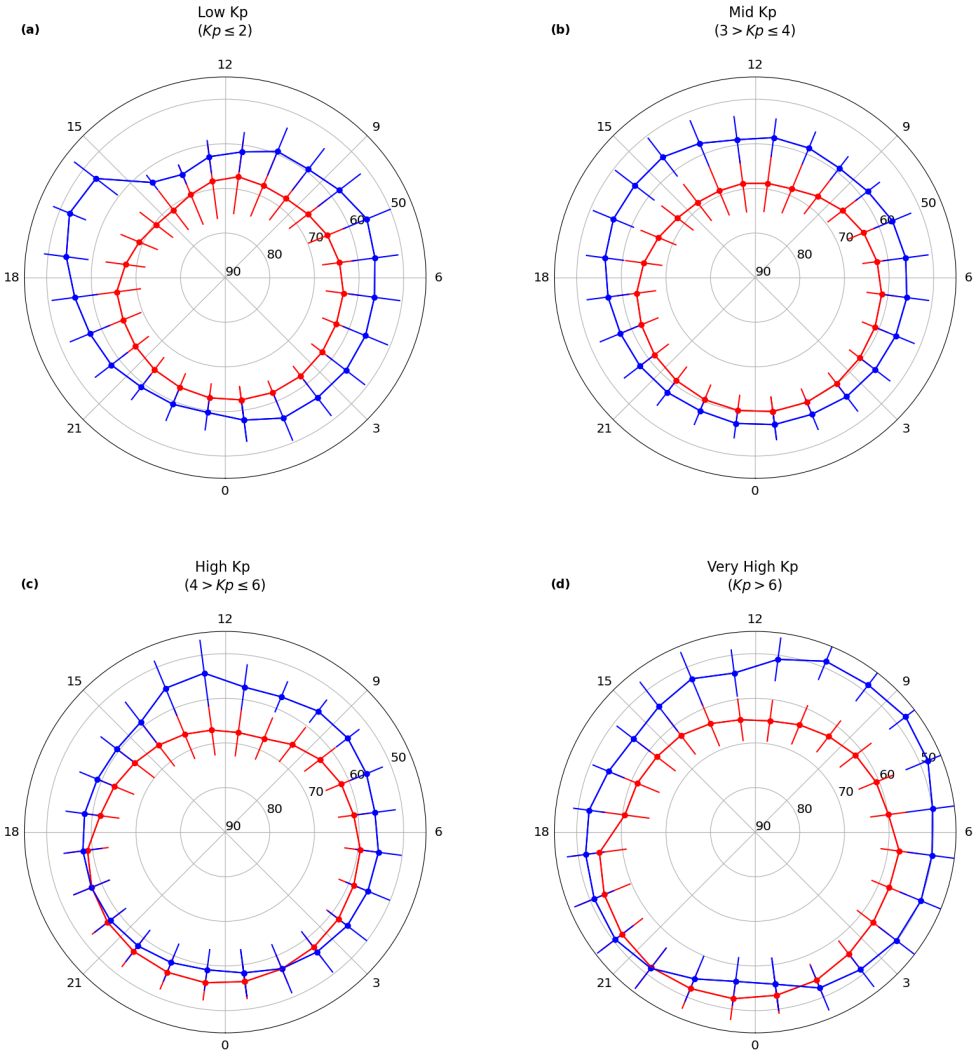

Figure 8.5: The average location of the mapped plasmapause boundary (blue) and the equatorward auroral boundary (red), in all local time sectors, under different levels of geomagnetic activity, defined by Kp, from low to very high in panels (a) - (d), respectively. The error bars show the standard deviation of the distribution in each local time sector.

$\sim 60 - 65^{\circ}$ in the nightside local time sectors. As geomagnetic activity increases, the auroral boundary is located at lower, more equatorward latitudes in all local time sectors. The auroral boundary does not move equatorward uniformly in all local time sectors with increasing Kp level. The largest change in the equatorward boundary location is observed in the dusk to pre-midnight sectors, with the mean boundary location in MLT 21 moving $\sim 12^{\circ}$ equatorward, on average, from $\sim 64^{\circ}$ during low Kp (Kp ≤ 2) to $\sim 52^{\circ}$ during very high levels (Kp > 6) of geomagnetic activity. In comparison, the boundary in the noon local time sector only moves $\sim 3.5^{\circ}$ equatorward, on average, from $\sim 68^{\circ}$ to $\sim 64.5^{\circ}$ during low and very high levels of geomagnetic activity, respectively.

At high levels of geomagnetic activity, Kp > 4, there is significant overlap between the plasmapause boundary mapped to the ionosphere and the equatorward auroral boundary, particularly in the dusk to post-midnight local times sectors (MLT 18 - 03). The improved agreement between the two boundaries under geomagnetically active periods was also observed in the second case study in Figure 8.2d.

Figure 8.6 shows the latitudinal distribution of both boundaries in 8 representative local time sectors (MLT 00, 03, 06, 09, 12, 15, 18 and 21) for each level of geomagnetic activity. In all local time sectors shown, the distribution of the auroral boundary generally lies poleward of the distribution of the plasmapause identifications mapped to the ionosphere, particularly for low levels of geomagnetic activity (Kp ≤ 2). As geomagnetic activity increases, the auroral boundary distribution moves equatorward to lower latitudes, particularly in the nightside local time sectors, which results in a greater overlap between the distributions of the two boundaries. While the auroral boundary distributions in the dayside local time sectors also shift equatorward with increasing levels of geomagnetic activity, there is still a distinct separation between the two boundary distributions in the noon (MLT 12) and pre-noon (MLT 09) sectors, even at very high levels of geomagnetic activity.

In summary, during low levels of geomagnetic activity, the equatorward auroral boundary and the plasmapause boundary mapped to the ionosphere are separated, with the auroral boundary generally located at higher, more poleward latitudes. Dur-

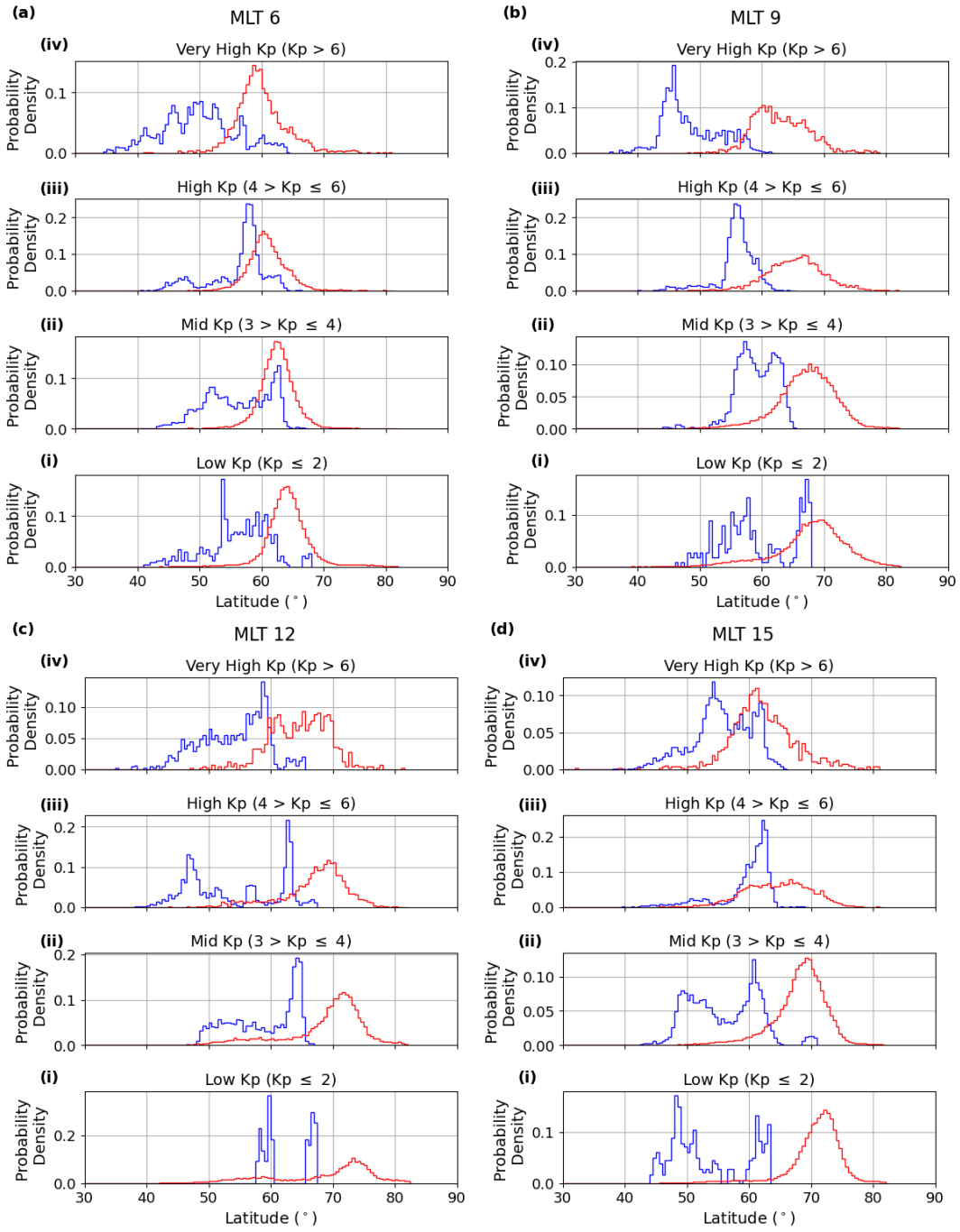

Figure 8.6: The latitude distribution of the mapped plasmapause locations (blue) and auroral boundary identifications (red) in 4 representative dayside local time sectors from MLT6 to MLT 15 in panels (a) - (d), under different levels of geomagnetic activity, defined by Kp, from low to very high in panels (i) - (iv), respectively.

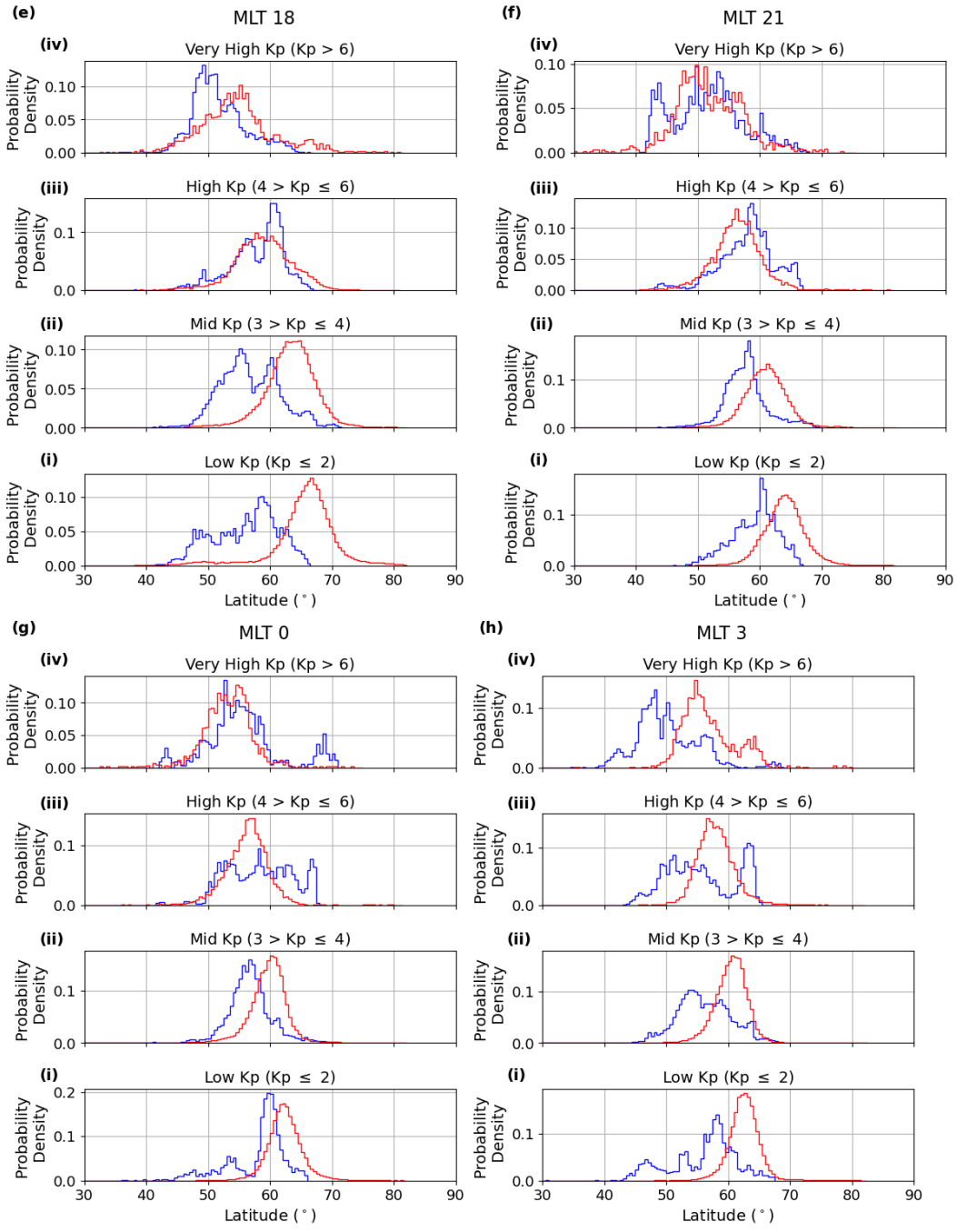

Figure 8.6: The latitude distribution of the mapped plasmapause locations (blue) and auroral boundary identifications (red) in 4 representative nightside local time sectors from MLT18 to MLT 03 in panels (e) - (h), under different levels of geomagnetic activity, defined by Kp, from low to very high in panels (i) - (iv), respectively.

ing periods of higher geomagnetic activity, the auroral boundary moves to lower, more equatorward latitudes, on average, with the largest equatorward expansion in the dusk to pre-midnight local time sectors. The plasmapause boundary mapped to the ionosphere remains at an approximately constant latitude between $\sim 55 - 60^{\circ}$ for Kp $\leq$ 6, although for very high levels of geomagnetic activity (Kp $>$ 6), the plasmapause boundary mapped to the ionosphere is located at lower latitudes. Due to the equatorward expansion of the auroral boundary, during more geomagnetically active periods (Kp $>$ 4) and very high levels of geomagnetic activity, there is a greater overlap between the two boundaries in the nightside sectors while the dayside sectors are still separated.

Additional tables have been included in the Appendix detailing the number of plasmapause and equatorward auroral boundary identifications that have been used in Sections 8.3.2 and 8.3.3. Table A.1 contains the total number of plasmapause identifications and the total number of equatorward auroral boundary identifications in each MLT sector from Section 8.3.2. Table A.2 contains the number of plasmapause identifications and the number of equatorward auroral boundary identifications in each MLT sector, in each Kp category, defined in Section 8.3.3.

8.3.4 In-situ Particle Measurements in the Inner Magnetosphere

Despite the close association between the two boundaries in the nightside sectors under high levels of geomagnetic activity, in the majority of local time sectors under most levels of geomagnetic activity, there is a gap between the ionospheric projection of the extent of the plasmaspheric cold particle population and the energetic precipitating particle population. This suggests that there is a separation in the inner magnetosphere between the cold plasmaspheric population and the precipitating thermal particles that result in the auroral emission. However, in the inner magnetosphere, the cold plasmaspheric population co-exists in the same region as the more energetic radiation belt and ring current particle populations, as described in Chapter 2.

Thorne et al. (1973) suggested that the cold plasmaspheric population limits the extent of the Earthward edge of the plasma sheet into the inner magnetosphere through wave particle interactions, mainly hiss waves, which would prevent auroral emission at lower latitudes. From the results presented in this study, the apparent spatial separation between the auroral and plasmaspheric particle populations may suggest that the cold plasmaspheric population does not limit the auroral precipitation occurring at lower latitudes.

In this section, two examples of in-situ data measurements are presented from the Van Allen Radiation Belt satellites to analyse the spatial distribution of the particle populations in the inner magnetosphere. The data presented were selected to show a spacecraft crossing in both the dayside and nightside local time sectors but otherwise the periods were randomly selected.

The data presented in Figures 8.7 and 8.8 show the in-situ observations crossing the inner magnetosphere in the nightside sectors and in the dayside sectors, respectively. In both figures, panel (a) shows the in-situ particle density, panel (b) shows the differential energy flux along the orbital path and panel (c) shows the path of the satellite orbit in L-shell against local time. In panel (a), the horizontal dotted line indicates the 40 cm^{-3} particle density threshold which is the estimated lower sensitivity limit of the EUV instrument (Goldstein et al., 2003). The vertical red solid lines are included as a guide in panels (b) and (c) to show where the plasma density is 40 cm^{-3}. The dashed line in panel (b) indicates the 200 eV energy level.

In the nightside crossing shown in Figure 8.7a, the location of the plasmapause can be identified in each orbit by the sharp gradient in the particle density. In this example, the sharp gradients largely agree with where the particle density in panel (a) crosses the 40 cm^{-3} threshold except in the first crossing where there is a slight offset. In Figure 8.7a, the satellite crossed the plasmapause out of the plasmasphere between 2100 - 2200 UT and again crossed the plasmapause, entering the plasmasphere, at approximately 0200 UT. Between the plasmapause crossings, inside the plasmasphere, the particle density is characteristically high ($>$ 1000 cm^{-3}). Inside the plasmasphere where the particle density is higher, the differential energy

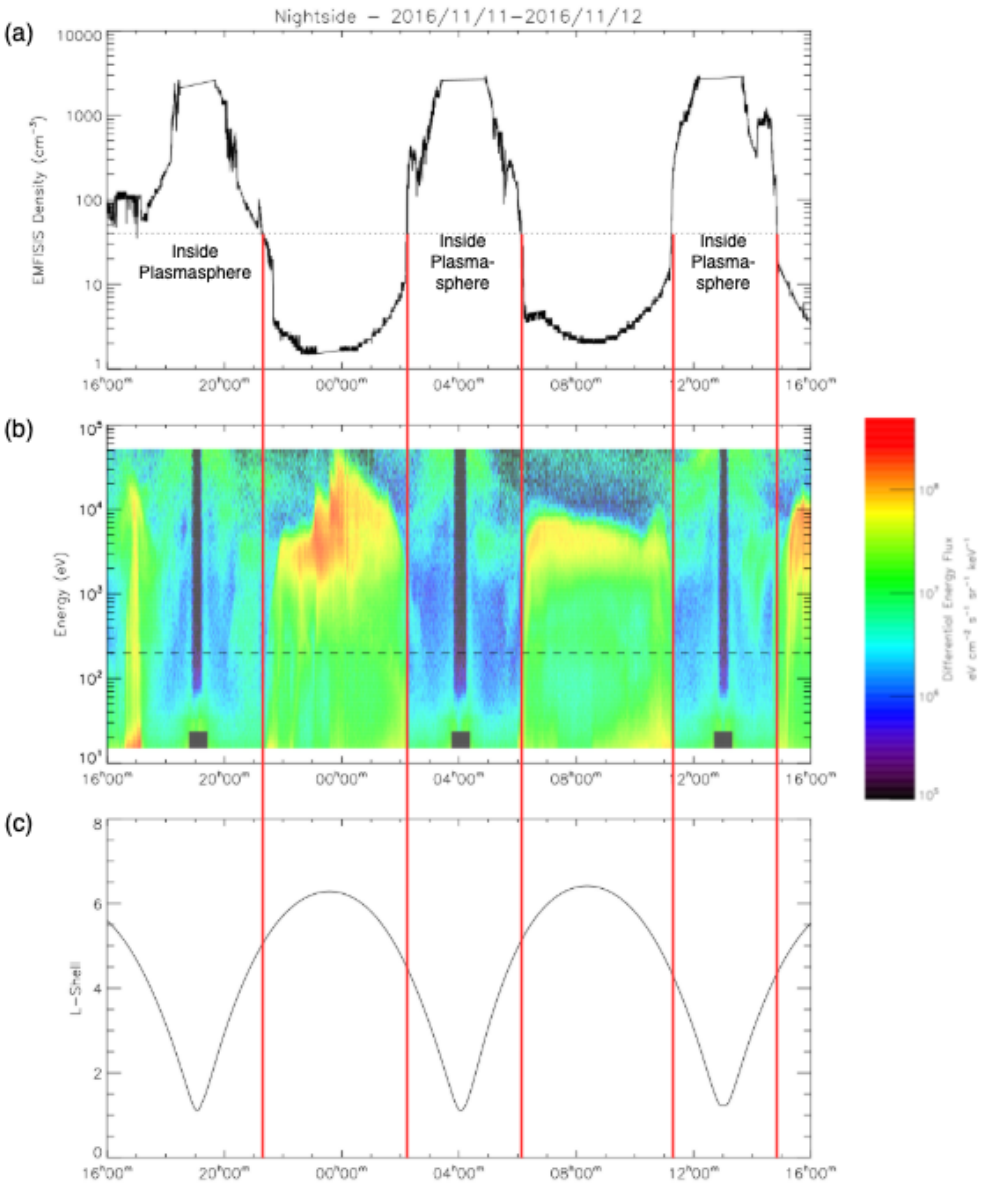

Figure 8.7: Data from the Van Allen Probe spacecraft crossing the inner magnetosphere in the nightside local time sectors. Panel (a) shows the in-situ particle density, panel (b) shows the differential energy flux along the orbital path and panel (c) shows the path of the satellite orbit in L-shell against local time. Figure provided by Colin Forsyth.

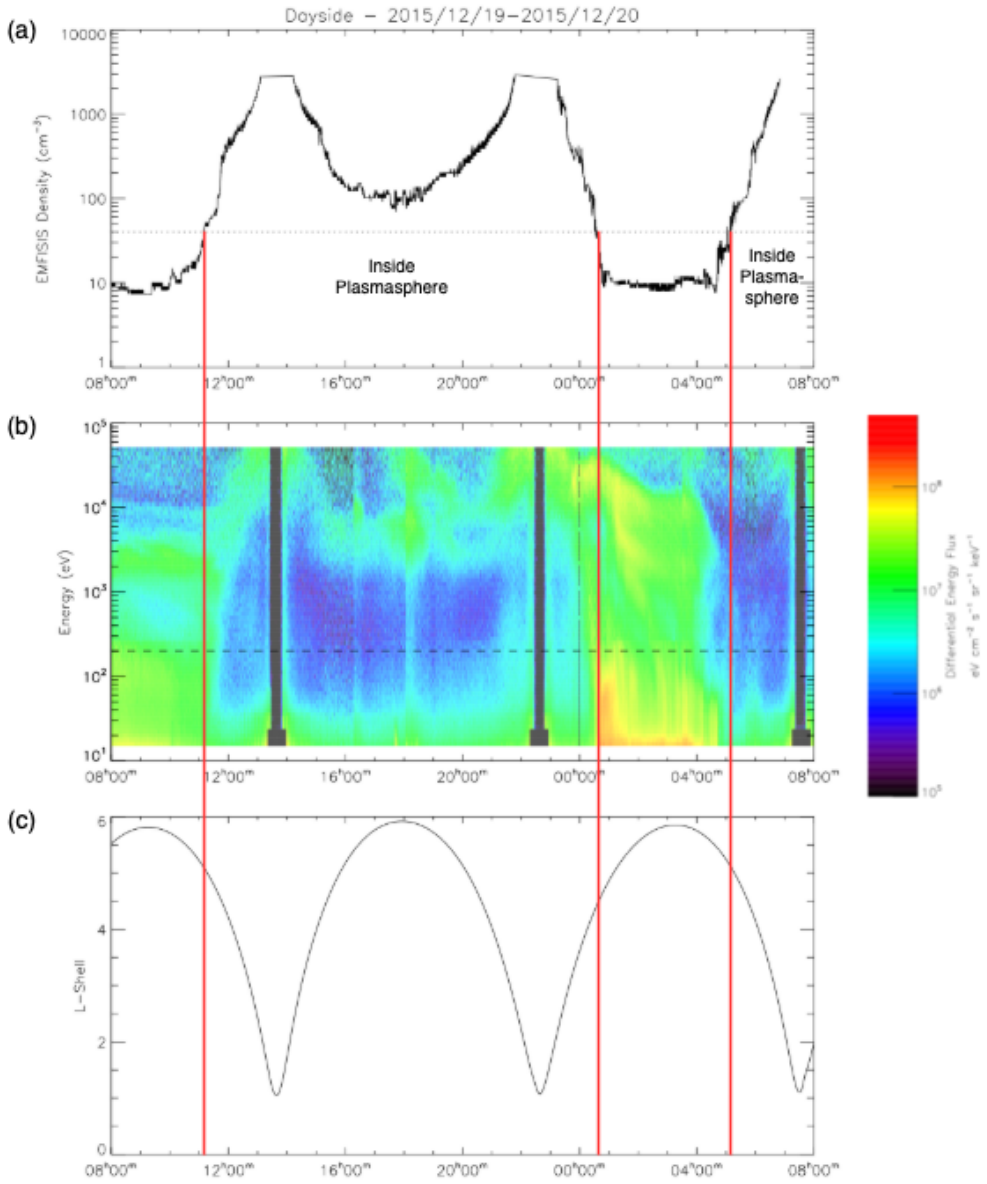

Figure 8.8: Data from the Van Allen Probe spacecraft crossing the inner magnetosphere in the nightside local time sectors. Panel (a) shows the in-situ particle density, panel (b) shows the differential energy flux along the orbital path and panel (c) shows the path of the satellite orbit in L-shell against local time. Figure provided by Colin Forsyth.

flux in panel (b) shows that there is a low energy flux of particles at most energies, indicated in blue; however, there is a slightly higher energy flux of particles with energies $<$ 100 eV and $>$ 10^4 eV, shown in green, which could indicate the low energy plasmaspheric population and the higher energy radiation belt or ring current populations, respectively, which are known to be approximately co-located in the inner magnetosphere. Outside the plasmasphere, where the particle density is lower, there is a higher energy flux of particles across all energies, shown in green, and and a particularly high energy flux of high energy particles $>$ 1 keV, shown in yellow and red.

In the dayside crossing in Figure 8.8, the spacecraft crosses the plasmapause, entering the plasmasphere between 1100-1200 UT and back out of the plasmasphere between 0000-0100 UT and finally crosses back into the plasmasphere around 0500 UT, as defined by the 40 cm^{-3} plasma density threshold. Similar particle distributions are observed inside and outside of the plasmapause in the dayside local time sectors as discussed in the nightside crossing. However, in the dayside data, there is an apparent offset between where the plasma density crosses the 40 cm^{-3} threshold and the change in the particle populations observed in panel (b). In the first crossing around 1200 UT, the offset may be due to the definition of the plasmapause as a steep density gradient is observed at a slightly later time, after the density crosses the 40 cm^{-3} threshold, which could be the true plasmapause location. However, in the final spacecraft crossing into the plasmasphere around 0500 UT, there is evidence that the high energy particle population drops away before the spacecraft crosses the plasmapause boundary and does not extend right up to the plasmapause boundary in this case.

The results from the nightside in-situ data show that a high energy thermal plasma population extends right up to the plasmapause and there is no spatial separation between the thermal and cold plasmaspheric populations in these observations. However, in the dayside in-situ data, there is some evidence of an observable separation between the high energy thermal plasma and the cold plasmaspheric populations, suggesting that the high energy thermal plasma population may not always

extend right up to the plasmapause boundary in some dayside sectors or under certain geomagnetic conditions.

The higher energy thermal particle population observed just outside the plasmapause could be the radiation belt or ring current plasma populations which are co-located with the plasmasphere in the inner magnetosphere. However, the differential energy flux of the thermal plasma population observed in the nightside crossings is $\sim 10^8$ eV cm^{-2} sr^{-1} keV^{-1} s^{-1} which is the same order of magnitude as the differential energy flux observed further downtail in the nightside plasma sheet by Walsh et al. (2011), suggesting that the observed hot thermal plasma population may be plasma sheet particles that extend into the inner magnetosphere, right up to the plasmapause boundary. The nightside plasmasheet population is considered to be the main plasma source for particles that precipitate into the ionosphere, causing the auroral emission on the nightside and the lower latitude dayside auroral emission. It would be expected that the plasmasheet particle population just outside the plasmapause boundary would also precipitate into the ionosphere and produce low latitude auroral emission. As a result, the plasmapause boundary mapped to the ionosphere would align with the equatorial boundary of the auroral emission. It may be the case that the plasmasheet particles just outside the plasmapause on the nightside and which drift around to the dayside sectors do precipitate but the resulting auroral emission is not sufficiently high above the background level to be detected by the IMAGE WIC instrument or that the equatorward auroral boundaries determined by Longden et al. (2010) are identified at a higher latitude than this faint emission, resulting in the observed separation between the two boundaries in the statistical analysis. However, during higher levels of geomagnetic activity the higher convection may cause more plasmasheet particles to be convected in to the inner magnetosphere near the plasmapause which precipitate and produce brighter, low latitude auroral emission, giving a better agreement between the location of the equatorward auroral boundary and the plasmapause boundary mapped to the ionosphere.

The two example in-situ observations are limited. Future work may include a statistical study of the particle populations inside and outside of the plasmapause to analyse the average distribution of the particle populations in the inner magnetosphere and to determine whether the two example observations are representative.

8.4 Discussion

This study has compared the average locations of the equatorward auroral boundary identified from FUV global image data and the ionospheric footpoint of the plasmapause identified from EUV images, mapped to the ionosphere using the T96 model. Case studies (e.g. He et al., 2020) have shown a link between activity observed on the the equatorward edge of the auroral oval and the plasmapause, particularly in the dusk local time sectors. However, the statistical analysis presented in this study suggests that this does not hold in all local time sectors or under all levels of geomagnetic activity. On average, the electron auroral boundary lies poleward of the mapped plasmapause in all local time sectors. In the nightside sectors, the two boundaries are located within $\sim 4-8^{\circ}$, with overlapping latitude distributions, while the dayside boundaries are separated by $\sim 8-11^{\circ}$ with distinctly separate distributions.

As Kp increases, the auroral boundary is observed to move gradually further equatorward, particularly in the nightside sectors. This could indicate that the source of the aurora moves Earthward towards the plasmapause with increasing geomagnetic activity. The increase in convection during more disturbed levels of geomagnetic activity may cause the inner boundary of the nightside plasmasheet to move Earthward and so the ionospheric projection of the plasmasheet, the equatorward auroral boundary, expands to lower latitudes (Thomsen, 2004; Thomas and Shepherd, 2018). The latitude of the mapped plasmapause is fairly constant, between $55-60^{\circ}$ in most local time sectors at all levels of geomagnetic activity of Kp = 6 or below. For very high levels of geomagnetic activity exceeding Kp = 6, the plasmapause moves equatorward to $\sim 50-55^{\circ}$ in most local time sectors. The equatorward motion of the plasmapause boundary could indicate plasmaspheric

erosion with plasma being lost via the drainage plume under high levels of geomagnetic activity. For higher levels of geomagnetic activity (Kp $\geq$ 4), the equatorward auroral boundary and the mapped plasmapause boundary are very closely aligned in the nightside local time sectors, particularly between MLT 18 - 03.

In the in-situ particle measurements from the Van Allen Radiation Belt Probes, in the nightside local time sectors, there was no observed separation between the cold plasmaspheric population and a higher energy thermal plasma population. The thermal particle population was observed immediately outside the plasmapause boundary and could precipitate into the ionosphere resulting in auroral emission. The observed thermal plasma population may include ring current particles or radiation belt particles which are known to be co-located with the cold plasmaspheric population in the inner magnetosphere. Or, they could also be plasmasheet particles which have been convected inwards to the inner magnetosphere. In contrast, in the dayside local time sectors, there was an observable separation between the higher energy particle population and the cold plasmaspheric population in the in-situ data, in at least one spacecraft crossing. This could suggest that in some local time sectors or under certain geomagnetic conditions/activity levels, the high energy thermal particle population does not extend right up to the plasmapause boundary.

It may be the case that during lower levels of geomagnetic activity, the auroral emission resulting from the precipitation of the higher energy thermal population just outside the plasmapause is not sufficiently above the background emission to be observed by the IMAGE WIC instrument or for the Longden et al. (2010) auroral boundary fitting technique, resulting in the observed gap between the equatorward auroral boundary and the plasmapause boundary mapped to the ionosphere. However, if a higher density of plasmasheet particles are convected inwards to the inner magnetosphere during higher levels of geomagnetic activity, this could produce brighter low latitude auroral emission, resulting in a better agreement between the two boundaries in the ionosphere.

The in-situ observations presented in this study are limited. A future statistical analysis of the in-situ particle data inside and outside the plasmapause boundary

could be informative to analyse the average distribution of the particle populations in the inner magnetosphere, under different geomagnetic conditions to determine whether the in-situ observations are representative.

It remains unclear what prevents the auroral oval from extending to lower latitudes. Jaggi and Wolf (1973) suggested that the abrupt equatorward auroral boundary was due to the zero energy Alfvén layer coincident with the inner edge of the nightside plasma sheet which separates particles on closed and open drift trajectories. An alternative theory by Thorne et al. (1973) proposed that the cold plasmaspheric population limits the extent of the Earthward edge of the plasma sheet into the inner magnetosphere through wave particle interactions, mainly hiss waves, which would prevent auroral emission at lower latitudes. The in-situ observations presented in this study support a higher energy plasma population extending right up to the plasmapause boundary which could then be scattered. However, the high energy radiation belt and ring current particle populations which co-exist in the same region of the inner magnetosphere as the cold plasmaspheric population could precipitate into the ionosphere and produce low latitude auroral emission.

It is also unclear where the equatorward auroral boundary maps to in the magnetosphere in all local time sectors and whether the boundary maps to the same location in the dayside and nightside local time sectors. Newell et al. (1996) suggested that the equatorward boundary of the auroral oval on the nightside maps to the inner edge of the nightside plasmasheet and that the dayside aurora is the result of nightside plasmasheet particles that drift around to the dayside sectors and then precipitate into the ionosphere. The results presented in this analysis show that the dayside auroral boundary is statistically located at higher latitudes than the nightside auroral boundary which could suggest that the dayside boundary maps further out, closer to the magnetopause. It could be that the lower latitude auroral emission on the dayside which results from drifting plasmasheet particles is very faint compared to the background emission and cannot be observed by the WIC instrument or identified as the equatorward auroral boundary by Longden et al. (2010).

8.4.1 Uncertainties and Limitations in the Analysis

There are a number of sources of uncertainty in this analysis from the identifications of both boundaries and the magnetospheric mapping of the plasmapause boundary inward to the ionosphere. In this study, the standard deviation of the distribution of each boundary in each MLT sector has been shown to quantify the spread of the distribution.

The database of plasmapause identifications by Goldstein et al. were visually extracted from the EUV images. There are only $\sim$ 3000 global plasmapause identifications from EUV images between 2000 - 2002, overlapping with the period of available auroral boundaries determined by Longden et al. (2010). Calculating the average location for each boundary using only simultaneous plasmapause and auroral boundaries was explored during this study but the data coverage was insufficient, as only 1682 out of the 2993 (56%) of the EUV observations with a successfully identified plasmapause had corresponding auroral boundary data in at least one local time sector. In addition, although Goldstein et al. (2003) found a good correspondence between the plasmapause identified from the sharp decrease in brightness in the EUV images and the in-situ measurements of the electron density gradients from the RPI, the global plasmaspheric images only see the high-density portion of the plasmapause with number densities of $>$ 40 cm^{-3} (Goldstein et al., 2003; Goldstein and Sandel, 2005; Moldwin et al., 2003). As a result, the visual identification of the plasmapause from global image data may under-estimate the radial extent of the plasmasphere. The accurate identification of the plasmapause location is also limited by the resoluation of the EUV data, which is estimated to be ($\sim$ 0.1 R_E) (Sandel et al., 2000). The plasmapause does not always form a sharp boundary, particularly during extended periods of low geomagnetic activity or when the plasmasphere is refilling after periods of high activity for example after a storm. A diffuse plasmapause boundary is more difficult to accurately determine by eye, particularly given the lower sensitivity threshold of $>$ 40 cm^{-3}. A relatively small uncertainty in the plasmapause identifications could result in a large uncertainty in the mapped ionospheric projection of the plasmapause.

The method of Zhang et al. (2017) uses an automated technique to identify the radial extent of the plasmapause from the IMAGE EUV observations. As both Zhang et al. (2017) and Goldstein et al. (2003) use the same EUV observational dataset, the plasmapause database from Zhang et al. (2017) is subject to many of the same constraints as the Goldstein et al. database, such as the resolution and sensitivity of the EUV instrument. The results of initial analysis showed that the plasmapause identifications from Zhang et al. (2017) were generally identified at larger radii with a range between 1.26 - 9.33 R_E compared to the range of the Goldstein et al. plasmapause database which was between 0.38 - 8.07 R_E. The larger radii plasmapause identifications from Zhang et al. (2017) would map to higher latitudes in the ionosphere which may show better agreement with the average equatorward auroral boundary location. However, due to the large difference in the plasmapause locations between the two databases, as shown in Chapter 4 Figure 4.9, the decision was taken to use the Goldstein et al. database as these plasmapause identifications were individually extracted by eye and so each EUV image and subsequent plasmapause identification was carefully checked. Further work in this study could provide a more in-depth evaluation to compare the two plasmapause databases.

The Tsyganenko magnetospheric mapping models have been continuously developed since the first model was published in 1989 (Tsyganenko, 1989). In this study, an early version of the model (T96) was used with the IGRF as the internal field model. There are more sophisticated versions of the Tsyganenko model available which account for more complex magnetospheric dynamics, however, the histograms of the mapped latitude using the IGRF only, the IGRF+T89 and IGRF+T96 models in Figure 8.1 show that in the inner magnetosphere, within the radius of the plasmapause identifications, the magnetospheric mapping is largely dominated by the internal IGRF model. Repeating the analysis using one of the more recently developed Tsyganenko models may change the results slightly but it is not expected to have a significant impact on the overall conclusions.

Part of the work in this study looked at the outward mapping of the equatorward auroral boundary to the magnetosphere to compare the location of the

mapped auroral boundary with plasmapause location. This was performed using both the IGRF+T89 and IGRF+T96 models however the distribution of mapped auroral boundaries had a long tail which extended to extremely large and unphysical radii of > 100 R_E and so the results have not been included in this chapter. The magnetic field diverges as the field lines are traced outwards from the ionosphere out to the inner magnetosphere which could result in large uncertainties in the location of the end points of the magnetic field line in the inner magnetosphere. As field lines are mapped inwards from the magnetosphere to the ionosphere, the magnetic field lines converge which reduces the uncertainty and provides a better mapping result.

If the auroral boundary from global auroral image data could be reliably mapped outward into the magnetosphere, it may be possible to use the mapped auroral boundary as a proxy for the plasmapause location and thus develop a statistical model of the plasmapause under different levels of geomagnetic activity. However, given that the two boundaries identified from plasmaspheric and auroral image data presented in this analysis show separated, more distinct distributions in the dayside local time sectors and during low levels of geomagnetic activity, a plasmapause model based on the outward mapping of the equatorward auroral boundary is not likely to provide a reliable plasmapause model that is an improvement on existing plasmapause models.

8.5 Conclusions

This study compared the location of the ionospheric projection of the plasmapause, identified from global EUV images against the location of the equatorward electron auroral boundary determined from global FUV auroral images between 2000 - 2002. Overall, in all local time sectors under all levels of geomagnetic activity, the mapped plasmapause was located 4–11° equatorward of the auroral boundary. As geomagnetic activity increases, the separation between the two boundaries decreases, with the two boundaries becoming approximately co-located in the dusk to post-midnight local time sectors (MLT 18 - 03) during periods of Kp > 4.

The statistical offset between the ionospheric footpoint of the two boundaries suggests that the cold plasmaspheric population does not play a significant role in preventing the auroral precipitation from extending to lower, equatorward latitudes. However, the in-situ observations showed a higher energy plasma population, possibly originating from the nightside plasmasheet, that extended right up to the plasmapause boundary in both nightside and dayside local time sectors, which could precipitate into the ionosphere and produce auroral emission. There was no observed spatial separation between the cold plasmaspheric and higher energy thermal particle populations.

Given the difficulties associated with effectively mapping the auroral boundary outward to the magnetosphere, using the mapped auroral boundary as a proxy for the plasmapause location would not provide a reliable plasmapause model. However, the results of this study highlight a number of outstanding questions including the processes which prevent the auroral oval from extending to lower latitudes, the magnetospheric source region of the particles precipitating into the equatorward edge of the auroral oval and why the plasmapause and auroral boundaries become co-located during periods of higher geomagnetic activity in the dusk and post-midnight sectors. Performing a statistical analysis of the spatial distribution of the particle populations in the inner magnetosphere inside and outside the plasmapause under different levels of geomagnetic activity could provide a better understanding of the particles which precipitate into the ionosphere and cause the low latitude auroral emission.

Chapter 9

General Conclusions

The auroral emission and associated current systems pose a risk for space and ground-based infrastructure. Space weather forecast models provide stakeholder industries with advanced warning of disruption and thus help to mitigate the risk of space weather impact. Auroral boundaries are a useful diagnostic tool which can be used to assess these forecasts and study the location and dynamics of the auroral oval, providing valuable information about the large scale structure and dynamic processes that dominate in the magnetosphere. Increased scientific understanding of the physical significance of the auroral boundaries, their dynamics and controlling factors will help to improve future generations of auroral and space weather forecast models.

In this thesis, the auroral boundaries determined from FUV images have been used to evaluate the performance of an operational auroral forecast model. This thesis has also explored the location and dynamics of the auroral boundaries in the context of the wider magnetosphere and the response of the auroral boundaries to large scale magnetospheric processes, such as substorms. The research presented in this thesis has addressed the following questions.

- How well does a solar wind driven auroral forecast model predict the aurora?
- How does the poleward auroral boundary (and by proxy, the open-closed field line boundary) respond to substorms?
- Where does the equatorward auroral boundary map to in the inner magnetosphere?

The performance of a version of the OVATION-Prime 2013 auroral forecast model that has been used operationally in the Met Office Space Weather Operations Centre was thoroughly assessed using a combination of verification techniques that are routinely applied to evaluate weather models. The analysis found that, as a deterministic forecast, the model performed well at predicting where aurora would or would not occur, with a reasonably high overall ROC score of 0.82 over 2.5 years of forecast and observation comparisons. The model performed well year-round, although the performance was reduced in the noon local time sectors and during more active periods of geomagnetic activity such as during the substorm expansion and recovery phases and for very high levels of Kp ($Kp = 8$). However, the results of this study also showed that the model performance was reduced at higher latitudes near the poleward edge of the auroral emission, particularly on the nightside. It was noted that the reduced performance of the model in this region may be due to auroral dynamics associated with substorm activity which the model is unable to capture, due to the model being driven only by the upstream solar wind conditions and the time resolution of the 30 minute forecast window.

The evaluation of the probabilistic forecasts from the model showed that the linear scaling from the predicted auroral flux to the probability of aurora occurring generally under-predicts occurrence of aurora. This may be because the linear scaling, originally developed by SWPC, has been tuned for use by citizen science observers to limit the false alarm forecasts when aurora was predicted with a reasonably high probability but not visible to observers on the ground. The results of the reliability analysis could be used to adjust the forecast probabilities to make them more robust and increase the reliability of the forecast probabilities against observations, however this may not be suitable for ground-based observers. An alternative approach to further develop auroral forecasts may be to design an alert system based on the predicted auroral flux output by the auroral forecast model.

The results of the verification analysis presented in this study provide a benchmark against which upgrades to the OVATION-Prime 2013 model and future generations of auroral forecast models can be compared against. However, this study

highlights some of the current difficulties in space weather forecasting in producing a probabilistic forecast model and the limitations with driving auroral models from upstream solar wind conditions, which provide a forecast lead time but which cannot account for internal magnetospheric processes such as substorms. Another common difficulty in space weather forecasting is the availability of a suitable observational dataset to compare the model output against. The model dataset must be independent from data used as input to the model. The auroral boundaries derived from IMAGE FUV data provide an excellent observational dataset to evaluate an auroral forecast or particle precipitation model, like OVATION-Prime 2013. Although the auroral boundary data coverage from IMAGE FUV is limited to only 2.5 years, the auroral boundaries determined from the upcoming SMILE UVI data will provide an additional dataset for the future evaluation of auroral models.

The location and dynamics of the poleward auroral oval and the open-closed field line boundary are driven by processes which are both internal and external to the magnetosphere. The expanding and contracting polar cap framework of Cowley and Lockwood (1992) describes how the area enclosed by the open-closed field line boundary expands and contracts depending on the competing rates of dayside and nightside reconnection. High rates of dayside reconnection with the southward oriented component of the interplanetary magnetic field increase the open flux content of the magnetosphere and the area of the polar cap. During substorms, a large amount of open flux is closed as a result of a rapid increase in the nightside reconnection rate in the magnetotail after substorm onset. The rapid closure of flux on the nightside causes the polar cap and open-closed field line boundary to contract. However, previous studies by, for example Coumans et al. (2007); Milan et al. (2009b); Clausen et al. (2012) and Coxon et al. (2014), found that the open-closed field line boundary continued to expand for up to $15-20$ minutes after substorm onset.

The research presented in Chapter 7 of this thesis performed a statistical analysis of the poleward boundary corrected to the open-closed field line boundary location to determine the detailed motion of the open-closed field line boundary and

associated change in the flux content in each magnetic local time sector during substorms. The results of this study showed that the open-closed field line boundary begins to contract poleward immediately at substorm onset, with onset defined by a brightening in the auroral oval observed by imaging spacecraft in the substorm onset sectors. This poleward contraction of the open-closed field line boundary is then observed to occur in local time sectors which are further from the substorm onset sector at gradually later times after substorm onset. In the furthest local time sectors from the substorm onset sector ($\pm$6 hours of local time), the open-closed field line boundary was found to continue to expand equatorward after substorm onset for up to $30-40$ minutes, until the flux closure in the magnetotail was circulated around to these local time sectors. In other words, the OCB does not contract poleward uniformly in all local time sectors after substorm onset. However, the estimated total nightside flux content was observed to decrease immediately at substorm onset, despite the continued increase in flux in the furthest local time sectors from the onset sector.

The results presented in this analysis suggest that the continued increase in the flux content observed by Coumans et al. (2007); Milan et al. (2009b); Clausen et al. (2012) and Coxon et al. (2014) may have been a result of the fitting method used to define the open-closed field line boundary in these studies which averaged out the motion of the OCB accross a wide range of local time sectors. Alternatively, the continued equatorward motion of the OCB observed in the furthest local time sectors $\pm$ 6 hours from the onset sector could be the result of dayside reconnection continuing to open larger amounts of flux than is being simultaneously closed by nightside reconnection in these sectors, immediately after substorm onset. Future analysis to determine whether this is the case could involve dividing the substorms into two categories based on the upstream B_Z component of the IMF after substorm onset. A negative IMF B_Z component after substorm onset would suggest that the magnetosphere remains in a driven state and that the rate of dayside reconnection may continue to dominate the open flux content of the polar cap, rather than the closure of flux by the substorm.

It is well understood that the poleward boundary of the auroral oval is associated with the open-closed field line boundary, however it remains less clear where the equatorward auroral boundary maps to in the inner magnetosphere. Jaggi and Wolf (1973) proposed that the equatorward auroral boundary was due to an Alfvén layer which coincides with the inner edge of the nightside plasmasheet and which shields the inner region of the magnetosphere from the solar wind driven induced convection. Thorne et al. (1973) suggested that the cold plasmaspheric population limits the extent of the inner edge of the nightside plasmasheet into the inner magnetosphere through wave-particle interactions, predominantly hiss waves. In the final research chapter, the physical significance of the equatorward auroral boundary was explored, specifically, the analysis examined whether the plasmapause boundary mapped to the equatorward auroral boundary in the ionosphere.

A number of studies have found a good agreement between the inner edge of the nightside plasmasheet, the expected source region of particles precipitating at the lower edge of the auroral oval, and the plasmapause with seprations between the two boundaries of 0 - 0.25 L from in-situ data covering a limited range of local time sectors and geomagnetic activity levels (Linscott and Scourfield, 1976; Frank, 1971; Horwitz et al., 1982). Fairfield and Viñas (1984) suggested that the higher cross-tail convection during periods of disturbed geomagnetic activity might move the inner edge of the nightside plasmasheet closer to Earth and closer to the plasmapause.

Additional evidence of a link between the equatorward auroral boundary and the plasmapause is from auroral activity such as undulations and pulsating aurora which may be driven by corresponding activity at or near the plasmapause including a Kelvin-Helmholtz velocity shear flow instability at the plasmapause, intense sub-auroral polarisation streams (SAPs) flows, chorus-mode waves and plasmapause surface waves (Tsuruda et al., 1981; Lui et al., 1982; Motoba et al., 2015; Henderson et al., 2010, 2018). The cumulative findings of these studies present compelling evidence that there may be a close association between the plasmapause and the equatorward auroral boundary.

The research in this thesis compared the statistical locations of the plasmapause

mapped to the ionosphere and the equatorward auroral boundary in all local time sectors and under different levels of geomagnetic activity. The results of the study found that, on average, the plasmapause mapped to the ionosphere was located between $4 - 11^{\circ}$ further equatorward than the auroral boundary, with the largest separations between the two boundaries observed in the dayside local time sectors. However, the separation between the two boundaries decreased with increasing levels of geomagnetic activity, in agreement with Fairfield and Viñas (1984). Given the statistical offset between the two boundaries, the results presented in this thesis suggest that the cold plasmaspheric population does not prevent the auroral emission at lower, equatorward latitudes. On the other hand, the results from two in-situ observations crossing the inner magneotsphere in both the dayside and nightside local time sectors showed a thermal particle population, similar to the nightside plasma sheet population, which extended right up to the plasmapause with no spatial separation between the thermal and cold plasmaspheric particle populations.

The results of this study highlight a number of outstanding questions regarding the equatorward auroral boundary, in particular regarding what the processes are that prevent auroral emission occurring at lower latitudes and what are the properties and source region of the magnetospheric particles precipitating into the equatorward edge of the auroral oval in all local time sectors? Future work to answer these questions could involve the statistical analysis of the plasma populations in the inner magnetosphere in all local time sectors using in-situ data, particularly to examine the plasma populations in the regions between the plasmapause and the magnetospheric source region of the equatorward auroral boundary in the dayside local time sectors.

Appendix A

Number of Plasmapause and Equatorward Auroral Boundary Identifications

This chapter contains tables showing number of plasmapause identifications in each magnetic local time (MLT) sector from the Goldstein et al. database, determined from the IMAGE EUV data and the number of equatorward auroral boundary identifications in each MLT sector identified by Longden et al. (2010) from the IMAGE FUV (WIC) data, used in Chapter 8. Table A.1 shows the total number of identifications in each MLT sector for both the plasmapause and auroral boundary datasets. Similarly, Table A.2 shows the number of identifications in each MLT sector for both the plasmapause and auroral boundary datasets, separated by the level of geomagnetic activity, defined by Kp.

Table A.1: The total number of plasmapause identifications in each MLT sector (N_{EUV}) and the total number of equatorward auroral boundary identifications in each MLT sector (N_{FUV}).

MLT	**N_{EUV}**	**N_{FUV}**
0	11487	120540
1	14529	119305
2	18893	118213
3	20543	119883
4	19353	127254
5	15464	145901
6	11295	141576
7	9832	112533
8	10543	77446
9	11290	44454
10	12274	25561
11	8314	18082
12	5112	18817
13	5512	29427
14	7617	54629
15	14519	92841
16	19247	128229
17	26423	139205
18	30924	129869
19	26480	112910
20	22372	109039
21	19825	110385
22	15448	115058
23	12297	118752

Table A.2: The number of plasmapause identifications (N_{EUV}) and the number of equatorward auroral boundary identifications (N_{FUV}) separated by the level of geomagnetic activity, defined by Kp.

	Kp $\leq$ 2		**2 >Kp$\leq$ 4**		**4 >Kp $\leq$ 6**		**Kp >6**	
MLT	$\mathbf{N_{EUV}}$	$\mathbf{N_{FUV}}$	$\mathbf{N_{EUV}}$	$\mathbf{N_{FUV}}$	$\mathbf{N_{EUV}}$	$\mathbf{N_{FUV}}$	$\mathbf{N_{EUV}}$	$\mathbf{N_{FUV}}$
0	1108	74709	6039	37653	3684	6966	656	1212
1	1705	72781	6551	38154	4415	7056	1858	1314
2	1773	70569	7989	38864	5807	7408	3324	1372
3	1822	69725	8635	40419	6157	8122	3929	1617
4	1695	70725	8002	45020	6156	9515	3500	1994
5	1041	77373	6482	54295	5655	11829	2286	2404
6	467	72308	4594	55282	4789	11878	1445	2108
7	260	52658	3982	46906	4266	10974	1324	1995
8	251	35872	4099	31923	4642	8062	1551	1589
9	228	21752	4327	16702	5288	4786	1447	1214
10	160	12462	4304	9142	6721	2977	1089	980
11	143	8545	3548	6331	3664	2326	959	880
12	89	9204	2610	6661	1427	2156	986	796
13	55	15680	2583	10438	1840	2525	1034	784
14	99	30626	2791	19349	3116	3786	1611	868
15	365	50872	4413	34547	5829	6275	3912	1147
16	678	66478	7442	50544	5632	9776	5495	1431
17	1239	70099	12418	56355	7351	11114	5415	1637
18	2054	64314	13946	51770	9460	11448	5464	2337
19	1886	58834	10533	42748	9055	9504	5006	1824
20	1644	60827	9237	38553	7356	8224	4135	1435
21	1475	65058	9235	36710	6517	7298	2598	1319
22	845	70251	7626	36440	5967	7086	1010	1281
23	758	73535	6580	37012	4407	6947	552	1258

Bibliography

S.-I. Akasofu. The development of the auroral substorm. *Planetary and Space Science*, 12:273–282, April 1964. doi: 10.1016/0032-0633(64)90151-5.

V. Angelopoulos, J. P. McFadden, D. Larson, C. W. Carlson, S. B. Mende, H. Frey, T. Phan, D. G. Sibeck, K-H. Glassmeier, U. Auster, E. Donovan, I. R. Mann, I. J. Rae, C. T. Russell, A. Runov, X-Z. Zhou, and L. Kepko. Tail Reconnection Triggering Substorm Onset. *Science*, 321(5891):931, August 2008. doi: 10.1126/science.1160495.

M. P. Aubry, C. T. Russell, and M. G. Kivelson. Inward motion of the magnetopause before a substorm. *Journal of Geophysical Research*, 75(34):7018, January 1970. doi: 10.1029/JA075i034p07018.

D. N. Baker, T. I. Pulkkinen, V. Angelopoulos, W. Baumjohann, and R. L. McPherron. Neutral line model of substorms: Past results and present view. *Journal of Geophysical Research*, 101(A6):12975–13010, June 1996. doi: 10.1029/95JA03753.

J. B. Baker, C. R. Clauer, A. J. Ridley, V. O. Papitashvili, M. J. Brittnacher, and P. T. Newell. The nightside poleward boundary of the auroral oval as seen by DMSP and the Ultraviolet Imager. *Journal of Geophysical Research*, 105(A9):21,267–21,280, September 2000. doi: 10.1029/1999JA000363.

J. Bartels. The standardized index, Ks, and the planetary index, Kp. *International Association of Geomagnetism and Aeronomy Bulletin*, 12b(3):97–120, 1949.

J. Bartels, N. H. Heck, and H. F. Johnston. The three-hour-range index measuring geomagnetic activity. *Terrestrial Magnetism and Atmospheric Electricity (Journal of Geophysical Research)*, 44(4):411, January 1939. doi: 10.1029/TE044i004p00411.

J. Bartels, N. H. Heck, and H. F. Johnston. Geomagnetic three-hour-range indices for the years 1938 and 1939. *Terrestrial Magnetism and Atmospheric Electricity (Journal of Geophysical Research)*, 45(3):309, January 1940. doi: 10.1029/TE045i003p00309.

W. Baumjohann and R. A. Treumann. *Basic space plasma physics*. World Scientific, Singapore ; London, rev. ed. edition, 2012. ISBN 9781848168947.

R. F. Benson and M. D. Desch. Wideband noise observed at ground level in the auroral region. *Radio Science*, 26(4):943–948, Aug 1991. doi: 10.1029/91RS00450.

J. H. Binsack. Plasmapause observations with the M.I.T. experiment on IMP 2. *Journal of Geophysical Research*, 72(21):5231–5237, November 1967. doi: 10.1029/JZ072i021p05231.

P. D. Boakes, S. E. Milan, G. A. Abel, M. P. Freeman, G. Chisham, B. Hubert, and T. Sotirelis. On the use of IMAGE FUV for estimating the latitude of the open/closed magnetic field line boundary in the ionosphere. *Annales Geophysicae*, 26(9):2759–2769, September 2008. doi: 10.5194/angeo-26-2759-2008.

P. D. Boakes, S. E. Milan, G. A. Abel, M. P. Freeman, G. Chisham, and B. Hubert. A statistical study of the open magnetic flux content of the magnetosphere at the time of substorm onset. *Geophysical Research Letters*, 36(4):L04105, February 2009. doi: 10.1029/2008GL037059.

P. D. Boakes, S. E. Milan, G. A. Abel, M. P. Freeman, G. Chisham, and B. Hubert. A superposed epoch investigation of the relation between magnetospheric solar wind driving and substorm dynamics with geosynchronous particle injection signatures. *Journal of Geophysical Research (Space Physics)*, 116(A1):A01214, January 2011. doi: 10.1029/2010JA016007.

D. H. Boteler. A 21st Century View of the March 1989 Magnetic Storm. *Space Weather*, 17(10):1427–1441, October 2019. doi: 10.1029/2019SW002278.

G. Branduardi-Raymont, C. Wang, C. P. Escoubet, M. Adamovic, D. Agnolon, M. Berthomier, J. A. Carter, W. Chen, L. Colangeli, M. Collier, H. K. Connor, L. Dai, A. Dimmock, O. Djazovski, E. Donovan, J. P. Eastwood, G. Enno, F. Giannini, L. Huang, D. Kataria, K. Kuntz, H. Laakso, J. Li, L. Li, T. Lui, J. Loicq, A. Masson, J. Manuel, A. Parmar, T. Piekutowski, A. M. Read, A. Samsonov, Sembay S., Raab W., C. Ruciman, Shi J. K., D. G. Sibeck, E. L. Spanswick, T. Sun, K. Symonds, J. Tong, B. Walsh, F. Wei, D. Zhao, J. Zheng, X. Zhu, and Z. Zhu. Smile definition study report. Technical report, 2018.

G. W. Brier. Verification of Forecasts Expressed in Terms of Probability. *Monthly Weather Review*, 78, 1950. doi: 10.1175/1520-0493(1950)078⟨0001:VOFEIT⟩2.0.CO;2.

J. L. Burch. IMAGE mission overview. *Space Science Reviews*, 91:1–14, January 2000.

P. Cannon, M. Angling, L. Barclay, C. Curry, C. Dyer, R. Edwards, G. Greene, M. Hapgood, R. Horne, D. Jackson, C. Mitchell, J. Owen, A. Richards, C. Rogers, K. Ryden, S. Saunders, M. Sweeting, R. Tanner, A. Thomson, and C. Underwood. Extreme space weather: Impacts on engineered systems and infrastructure. Technical report, Royal Academy of Engineering, 2013.

J. F. Carbary. A Kp-based model of auroral boundaries. *Space Weather*, 3(10): S10001, October 2005. doi: 10.1029/2005SW000162.

J. F. Carbary, T. Sotirelis, P. T. Newell, and C. I. Meng. Auroral boundary correlations between UVI and DMSP. *Journal of Geophysics Research (Space Physics)*, 108(A1):1018, January 2003. doi: 10.1029/2002JA009378.

D. L. Carpenter. Whistler Evidence of a 'Knee' in the Magnetospheric Ionization Density Profile. *Journal of Geophysical Research*, 68(6):1675–1682, March 1963. doi: 10.1029/JZ068i006p01675.

D. L. Carpenter. Whistler studies of the plasmapause in the magnetosphere: 1. Temporal variations in the position of the knee and some evidence on plasma motions near the knee. *Journal of Geophysical Research*, 71(3):693–709, February 1966. doi: 10.1029/JZ071i003p00693.

D. L. Carpenter and R. R. Anderson. An ISEE/Whistler Model of Equatorial Electron Density in the Magnetosphere. *Journal of Geophysical Research*, 97(A2): 1097–1108, February 1992. doi: 10.1029/91JA01548.

D. L. Carpenter, B. L. Giles, C. R. Chappell, P. M. E. Décréau, R. R. Anderson, A. M. Persoon, A. J. Smith, Y. Corcuff, and P. Canu. Plasmasphere dynamics in the duskside bulge region: A new look at old topic. *Journal of Geophysical Research*, 98(A11):19,243–19,271, November 1993. doi: 10.1029/93JA00922.

N. A. Case, S. R. Marple, F. Honary, J. A. Wild, D. D. Billett, and A. Grocott. AuroraWatch UK: An Automated Aurora Alert System. *Earth and Space Science*, 4(12):746–754, December 2017. doi: 10.1002/2017EA000328.

S. Chapman and V. C. A. Ferraro. A new theory of magnetic storms. *Terrestrial Magnetism and Atmospheric Electricity (Journal of Geophysical Research)*, 36 (2):77, January 1931. doi: 10.1029/TE036i002p00077.

C. C. Chaston, J. W. Bonnell, C. W. Carlson, J. P. McFadden, R. E. Ergun, and R. J. Strangeway. Properties of small-scale Alfvén waves and accelerated electrons from FAST. *Journal of Geophysical Research (Space Physics)*, 108(A4):8003, April 2003. doi: 10.1029/2002JA009420.

G. Chisham. Auroral boundary derived from image satellite mission data (may 2000 - oct 2002), version 1.1. Polar Data Centre, Natural Environment Research Council, UK., 2017.

X. Chu, R. L. McPherron, T-S. Hsu, and V. Angelopoulos. Solar cycle dependence of substorm occurrence and duration: Implications for onset. *Journal of Geophysical Research (Space Physics)*, 120(4):2808–2818, April 2015. doi: 10.1002/2015JA021104.

L. B. N. Clausen, J. B. H. Baker, J. M. Ruohoniemi, S. E. Milan, and B. J. Anderson. Dynamics of the region 1 Birkeland current oval derived from the Active Magnetosphere and Planetary Electrodynamics Response Experiment (AMPERE). *Journal of Geophysical Research (Space Physics)*, 117(A6):A06233, June 2012. doi: 10.1029/2012JA017666.

L. B. N. Clausen, J. B. H. Baker, J. M. Ruohoniemi, S. E. Milan, J. C. Coxon, S. Wing, S. Ohtani, and B. J. Anderson. Temporal and spatial dynamics of the regions 1 and 2 Birkeland currents during substorms. *Journal of Geophysical Research (Space Physics)*, 118(6):3007–3016, June 2013. doi: 10.1002/jgra.50288.

V. Coumans, C. Blockx, J. C. GéRard, B. Hubert, and M. Connors. Global morphology of substorm growth phases observed by the IMAGE-SI12 imager. *Journal of Geophysical Research (Space Physics)*, 112(A11):A11211, November 2007. doi: 10.1029/2007JA012329.

S. W. H. Cowley and M. Lockwood. Excitation and decay of solar wind-driven flows in the magnetosphere-ionosphere system. *Annales Geophysicae*, 10(1-2): 103–115, Feb 1992.

J. C. Coxon, S. E. Milan, L. B. N. Clausen, B. J. Anderson, and H. Korth. A superposed epoch analysis of the regions 1 and 2 Birkeland currents observed by AMPERE during substorms. *Journal of Geophysical Research (Space Physics)*, 119(12):9834–9846, December 2014. doi: 10.1002/2014JA020500.

J. C. Coxon, I. J. Rae, C. Forsyth, C. M. Jackman, R. C. Fear, and B. J. Anderson. Birkeland currents during substorms: Statistical evidence for intensification of Regions 1 and 2 currents after onset and a localized signature of auroral dimming. *Journal of Geophysical Research (Space Physics)*, 122(6):6455–6468, June 2017. doi: 10.1002/2017JA023967.

J. C. Coxon, M. P. Freeman, C. M. Jackman, C. Forsyth, I. J. Rae, and R. C. Fear. Tailward Propagation of Magnetic Energy Density Variations With Respect to

Substorm Onset Times. *Journal of Geophysical Research (Space Physics)*, 123 (6):4741–4754, June 2018. doi: 10.1029/2017JA025147.

J. D. Craven, L. A. Frank, and S. I. Akasofu. Propagation of a westward traveling surge and the development of persistent auroral features. *Journal of Geophsical Research*, 94(A6):6961–6967, June 1989. doi: 10.1029/JA094iA06p06961.

I. A. Daglis, E. T. Sarris, and B. Wilken. AMPTE/CCE CHEM observations of the energetic ion population at geosynchronous altitudes. *Annales Geophysicae*, 11 (8):685–696, August 1993.

I. A. Daglis, R. M. Thorne, W. Baumjohann, and S. Orsini. The terrestrial ring current: Origin, formation, and decay. *Reviews of Geophysics*, 37(4):407–438, November 1999. doi: 10.1029/1999RG900009.

I. Dandouras. Detection of a plasmaspheric wind in the Earth's magnetosphere by the Cluster spacecraft. *Annales Geophysicae*, 31(7):1143–1153, July 2013. doi: 10.5194/angeo-31-1143-2013.

F. Darrouzet, D. L. Gallagher, N. André, D. L. Carpenter, I. Dandouras, P. M. E. Décréau, J. De Keyser, R. E. Denton, J. C. Foster, J. Goldstein, M. B. Moldwin, B. W. Reinisch, B. R. Sandel, and J. Tu. Plasmaspheric density structures and dynamics: Properties observed by the cluster and image missions. In F. Darrouzet, J. de Keyser, and V. Pierrard, editors, *The Earth's Plasmasphere*, chapter 4, pages 55–106. Springer, 2009. doi: 10.1007/978-1-4419-1323-4_4.

O. de La Beaujardiere, L. R. Lyons, J. M. Ruohoniemi, E. Friis-Christensen, C. Danielsen, F. J. Rich, and P. T. Newell. Quiet-time intensifications along the poleward auroral boundary near midnight. *Journal of Geophsical Research*, 99 (A1):287–298, January 1994. doi: 10.1029/93JA01947.

GL. Delzanno, J. E. Borovsky, M. G. Henderson, P. A Resendiz Lira, V. Roytershteyn, and D. T. Welling. The impact of cold electrons and cold ions in magnetospheric physics. *Journal of Atmospheric and Solar-Terrestrial Physics*, 220: 105599, September 2021. doi: 10.1016/j.jastp.2021.105599.

A. Dube, R. Ashrit, H. Singh, K. Arora, G. Iyengar, and E. N. Rajagopal. Evalutating the performance of two global ensemble forecasting sytems in predicting rainfall over india during the southwest monsoons. *Meteorological Applications*, 24:230–238, 2017. doi: 10.1002/met.1621.

J. W. Dungey. Interplanetary Magnetic Field and the Auroral Zones. *Physical Review Letters*, 6(2):47–48, January 1961. doi: 10.1103/PhysRevLett.6.47.

J. P. Eastwood, E. Biffis, M. A. Hapgood, L. Green, M. M. Bisi, R. D. Bentley, R. Wicks, L. A. McKinnell, M. Gibbs, and C. Burnett. The Economic Impact of Space Weather: Where Do We Stand? *Risk Analysis*, 37(2):206–218, February 2017. doi: 10.1111/risa.12765.

T. J. Elkins. A model for high frequency radar auroral clutter. Technical report, Rome Air Development Institution, Mar 1980.

I. Arslan Erinmez, John G. Kappenman, and William A. Radasky. Management of the geomagnetically induced current risks on the national grid company's electric power transmission system. *Journal of Atmospheric and Solar-Terrestrial Physics*, 64(5-6):743–756, March 2002. doi: 10.1016/S1364-6826(02)00036-6.

D. H. Fairfield. Average and unusual locations of the Earth's magnetopause and bow shock. *Journal of Geophysical Research*, 76(28):6700, January 1971. doi: 10.1029/JA076i028p06700.

D. H. Fairfield and A. F. Viñas. The inner edge of the plasma sheet and the diffuse aurora. *Journal of Geophysical Research*, 89(A2):841–854, February 1984. doi: 10.1029/JA089iA02p00841.

N. L. Farr, D. N. Baker, and M. Wiltberger. Using a global magnetohydrodynamic model to study the start of the substorm recovery phase. *Journal of Geophysical Research (Space Physics)*, 115(A12):A12237, December 2010. doi: 10.1029/2010JA015802.

Ia. I. Feldstein and Iu. I. Galperin. The auroral luminosity structure in the high-latitude upper atmosphere: its dynamics and relationship to the large-scale structure of the earth's magnetosphere. *Reviews of Geophysics*, 23:217–275, August 1985. doi: 10.1029/RG023i003p00217.

M. C. Fok, T. E. Moore, J. U. Kozyra, G. C. Ho, and D. C. Hamilton. Three-dimensional ring current decay model. *Journal of Geophysical Research*, 100 (A6):9619–9632, June 1995. doi: 10.1029/94JA03029.

M. C. Fok, R. A. Wolf, R. W. Spiro, and T. E. Moore. Comprehensive computational model of Earth's ring current. *Journal of Geophysical Research*, 106(A5):8417–8424, May 2001. doi: 10.1029/2000JA000235.

C. Forsyth, I. J. Rae, J. C. Coxon, M. P. Freeman, C. M. Jackman, J. Gjerloev, and A. N. Fazakerley. A new technique for determining Substorm Onsets and Phases from Indices of the Electrojet (SOPHIE). *Journal of Geophysical Research (Space Physics)*, 120(12):10,592–10,606, December 2015. doi: 10.1002/2015JA021343.

C. Forsyth, V. A. Sergeev, M. G. Henderson, Y. Nishimura, and B. Gallardo-Lacourt. Physical Processes of Meso-Scale, Dynamic Auroral Forms. *Space Science Reviews*, 216(4):46, April 2020a. doi: 10.1007/s11214-020-00665-y.

C. Forsyth, C. E. J. Watt, M. K. Mooney, I. J. Rae, S. D. Walton, M. Marsh, R. B. Horne, and J. Albert. Forecasting GOES 15 ¿ 2MeV electron fluxes from solar wind data and geomagnetic indices. *Space Weather*, June 2020b. doi: 10.1029/2019SW002416.

L. A. Frank. Relationship of the plasma sheet, ring current, trapping boundary, and plasmapause near the magnetic equator and local midnight. *Journal of Geophysical Research*, 76(10):2265, January 1971. doi: 10.1029/JA076i010p02265.

M. P. Freeman, C. Forsyth, and I. J. Rae. The Influence of Substorms on Extreme Rates of Change of the Surface Horizontal Magnetic Field in the United Kingdom. *Space Weather*, 17(6):827–844, June 2019. doi: 10.1029/2018SW002148.

H. Frey. Image fuv log, 2010. URL `https://web.archive.org/web/20100626145557/http://sprg.ssl.berkeley.edu/image/`.

H. U. Frey, S. B. Mende, V. Angelopoulos, and E. F. Donovan. Substorm onset observations by IMAGE-FUV. *Journal of Geophysical Research (Space Physics)*, 109(A10):A10304, October 2004. doi: 10.1029/2004JA010607.

Ryoichi Fujii and Takesi Iijima. Control of the ionospheric conductivities on large-scale birkeland current intensities under geomagnetic quiet conditions. *Journal of Geophysical Research*, 92(A5):4505–4514, May 1987. doi: 10.1029/JA092iA05p04505.

Yu. I. Galperin and Ya. I. Feldstein. Mapping of the Precipitation Regions to the Plasma Sheet. *Journal of Geomagnetism and Geoelectricity*, 48(5):857–875, January 1996. doi: 10.5636/jgg.48.857.

G. A. Germany, M. R. Torr, P. G. Richards, and D. G. Torr. The dependence of modeled 0I 1356 and N_2 Lyman Birge Hopfield auroral emissions on the neutral atmosphere. *Journal of Geophysical Research*, 95(A6):7725–7733, June 1990. doi: 10.1029/JA095iA06p07725.

J. W. Gjerloev, R. A. Hoffman, J. B. Sigwarth, and L. A. Frank. Statistical description of the bulge-type auroral substorm in the far ultraviolet. *Journal of Geophysical Research (Space Physics)*, 112(A7):A07213, July 2007. doi: 10.1029/2006JA012189.

J. Goldstein. Plasmasphere response: Tutorial and review of recent imaging results. In D. N. Baker, B. Klecker, S. J. Schwartz, R. Schwenn, and R. von Steiger, editors, *Solar Dynamics and Its Effects on the Heliosphere and Earth*, volume 22, chapter 14, pages 203–216. Springer, 2007. doi: 10.1007/978-0-387-69532-7_14.

J. Goldstein and B. R. Sandel. The Global Pattern of Evolution of Plasmaspheric Drainage Plumes. In Burch, James and Schulz, Michael and Spence, Harlan, editor, *Inner Magnetosphere Interactions: New Perspectives From Imaging*, volume

159. Washington DC American Geophysical Union Geophysical Monograph Series, 2005. doi: 10.1029/159GM02.

J. Goldstein, M. Spasojević, P. H. Reiff, B. R. Sandel, W. T. Forrester, D. L. Gallagher, and B. W. Reinisch. Identifying the plasmapause in IMAGE EUV data using IMAGE RPI in situ steep density gradients. *Journal of Geophysical Research (Space Physics)*, 108(A4):1147, April 2003. doi: 10.1029/2002JA009475.

J. Goldstein, B. R. Sandel, M. F. Thomsen, M. Spasojević, and P. H. Reiff. Simultaneous remote sensing and in situ observations of plasmaspheric drainage plumes. *Journal of Geophysical Research (Space Physics)*, 109(A3):A03202, March 2004a. doi: 10.1029/2003JA010281.

J. Goldstein, R. A. Wolf, B. R. Sandel, and P. H. Reiff. Electric fields deduced from plasmapause motion in IMAGE EUV images. *Geophysical Research Letters*, 31 (1):L01801, January 2004b. doi: 10.1029/2003GL018797.

E. M. Greenberg and J. LaBelle. Measurement and modeling of auroral absorption of HF radio waves using a single receiver. *Radio Science*, 37(2):1022, Mar 2002. doi: 10.1029/2000RS002550.

R. A. Greenwald, K. B. Baker, J. R. Dudeney, M. Pinnock, T. B. Jones, E. C. Thomas, J. P. Villain, J. C. Cerisier, C. Senior, C. Hanuise, R. D. Hunsucker, G. Sofko, J. Koehler, E. Nielsen, R. Pellinen, A. D. M. Walker, N. Sato, and H. Yamagishi. Darn/Superdarn: A Global View of the Dynamics of High-Latitude Convection. *Space Science Reviews*, 71(1-4):761–796, February 1995. doi: 10.1007/BF00751350.

R. S. Grew, F. W. Menk, M. A. Clilverd, and B. R. Sandel. Mass and electron densities in the inner magnetosphere during a prolonged disturbed interval. *Geophysical Research Letters*, 34(2):L02108, January 2007. doi: 10.1029/2006GL028254.

K. I. Gringauz, V. G. Kurt, V. I. Moroz, and I. S. Shklovskii. Results of Observations

of Charged Particles Observed Out to R = 100, 000 km, with the Aid of Charged-Particle Traps on Soviet Space Rockets. *Soviet Astronomy*, 4:680, February 1961.

A. Grocott, J. A. Wild, S. E. Milan, and T. K. Yeoman. Superposed epoch analysis of the ionospheric convection evolution during substorms: onset latitude dependence. *Annales Geophysicae*, 27(2):591–600, February 2009. doi: 10.5194/angeo-27-591-2009.

L Harang and W. Stroffregen. Echoversuche auf Ultrakurzwellen. *Hochfreq. Elektroakust*, 55:105–108, 1940.

D. A. Hardy, L. K. Schmitt, M. S. Gussenhoven, F. J. Marshall, and H. C. Yeh. Precipitating electron and ion detectors (SSJ/4) for the block 5D/Flights 6-10 DMSP (Defense Meteorological Satellite Program) satellites: Calibration and data presentation, November 1984.

D. A. Hardy, W. McNeil, M. S. Gussenhoven, and D. Brautigam. A statistical model of auroral ion precipitation. 2. Functional representation of the average patterns. *Journal of Geophysical Research*, 96(A4):5539–5547, April 1991. doi: 10.1029/90JA02451.

David A. Hardy, M. S. Gussenhoven, and E. Holeman. A statistical model of auroral electron precipitation. *Journal of Geophysics Research*, 90:4229–4248, 1985. doi: 10.1029/JA090iA05p04229.

Fei He, Rui-Long Guo, William R. Dunn, Zhong-Hua Yao, Hua-Sen Zhang, Yi-Xin Hao, Quan-Qi Shi, Zhao-Jin Rong, Jiang Liu, An-Min Tian, Xiao-Xin Zhang, Yong Wei, Yong-Liang Zhang, Qiu-Gang Zong, Zu-Yin Pu, and Wei-Xing Wan. Plasmapause surface wave oscillates the magnetosphere and diffuse aurora. *Nature Communications*, 11:1668, April 2020. doi: 10.1038/s41467-020-15506-3.

B. Heilig and H. Lühr. New plasmapause model derived from CHAMP field-aligned current signatures. *Annales Geophysicae*, 31(3):529–539, March 2013. doi: 10.5194/angeo-31-529-2013.

M. G. Henderson, E. F. Donovan, J. C. Foster, I. R. Mann, T. J. Immel, S. B. Mende, and J. B. Sigwarth. Start-to-end global imaging of a sunward propagating, SAPS-associated giant undulation event. *Journal of Geophysical Research (Space Physics)*, 115(A4):A04210, April 2010. doi: 10.1029/2009JA014106.

M. G. Henderson, S. K. Morley, and L. E. Kepko. SAPS-Associated Explosive Brightening on the Duskside: A New Type of Onset-Like Disturbance. *Journal of Geophysical Research (Space Physics)*, 123(1):197–210, January 2018. doi: 10.1002/2017JA024472.

R. H. Holzworth and C. I. Meng. Mathematical representation of the auroral oval. *Geophysical Research Letters*, 2(9):377–380, September 1975. doi: 10.1029/GL002i009p00377.

I. Horvath and B. C. Lovell. Subauroral flow channel structures and auroral undulations triggered by Kelvin-Helmholtz waves. *Journal of Geophysical Research, Space Physics*, June 2021. doi: 10.1029/2021JA029144.

J. L. Horwitz, W. K. Cobb, C. R. Baugher, C. R. Chappell, L. A. Frank, T. E. Eastman, R. R. Anderson, E. G. Shelley, and D. T. Young. On the relationship of the plasmapause to the equatorward boundary of the auroral oval and to the inner edge of the plasma sheet. *Journal of Geophysical Research*, 87(A11):9059–9070, November 1982. doi: 10.1029/JA087iA11p09059.

K. Hosokawa, Y. Miyoshi, M. Ozaki, S. I. Oyama, Y. Ogawa, S. Kurita, Y. Kasahara, Y. Kasaba, S. Yagitani, S. Matsuda, F. Tsuchiya, A. Kumamoto, R. Kataoka, K. Shiokawa, T. Raita, E. Turunen, T. Takashima, I. Shinohara, and R. Fujii. Multiple time-scale beats in aurora: precise orchestration via magnetospheric chorus waves. *Scientific Reports*, 10:3380, February 2020. doi: 10.1038/s41598-020-59642-8.

Keisuke Hosokawa, Yoshizumi Miyoshi, and Wen Li. Introduction to special section on pulsating aurora and related magnetospheric phenomena. *Journal*

of Geophysical Research (Space Physics), 120(7):5341–5343, July 2015. doi: 10.1002/2015JA021453.

W. Hsu and A. H. Murphy. The attributes diagram A geometrical framework for assessing the quality of probability forecasts. *International Journal of Forecasting*, 2(3):285–293, 1986. doi: 10.1016/0169-2070(86)90048-8.

B. Hubert, J. C. Gérard, D. S. Evans, M. Meurant, S. B. Mende, H. U. Frey, and T. J. Immel. Total electron and proton energy input during auroral substorms: Remote sensing with IMAGE-FUV. *Journal of Geophysical Research (Space Physics)*, 107(A8):1183, August 2002. doi: 10.1029/2001JA009229.

B. Hubert, S. E. Milan, A. Grocott, C. Blockx, S. W. H. Cowley, and J. C. GéRard. Dayside and nightside reconnection rates inferred from IMAGE FUV and Super Dual Auroral Radar Network data. *Journal of Geophysical Research (Space Physics)*, 111(A3):A03217, March 2006. doi: 10.1029/2005JA011140.

B. Hubert, J.-C. Gérard, S. E. Milan, and S. W. H. Cowley. Magnetic reconnection during steady magnetospheric convection and other magnetospheric modes. *Annales Geophysicae*, 35(3):505–524, March 2017. doi: 10.5194/angeo-35-505-2017.

IMAGE Failure Review Board. Image failure review board final report. Technical report, NASA Goddard Space Flight Center, 2006. URL `https://image.gsfc.nasa.gov/publication/document/IMAGE_FRB_Final_Report.pdf`.

R. K. Jaggi and R. A. Wolf. Self-consistent calculation of the motion of a sheet of ions in the magnetosphere. *Journal of Geophysical Research*, 78(16):2852, January 1973. doi: 10.1029/JA078i016p02852.

Ju Jing, Vasyl B. Yurchyshyn, Guo Yang, Yan Xu, and Haimin Wang. On the Relation between Filament Eruptions, Flares, and Coronal Mass Ejections. *Astrophysical Journal*, 614(2):1054–1062, October 2004. doi: 10.1086/423781.

I. T. Jolliffe and D. B Stephenson. *Forecast verification: A practitioner's guide in atmospheric science*. Wiley, 2 edition, 2012.

J. Jones, S. Sanders, B. Davis, C. Hedrick, E. J. Mitchell, and J. M. Cox. Research to Operations Transition of an Auroral Specification and Forecast Model. In *Advanced Maui Optical and Space Surveillance (AMOS) Technologies Conference*, page 94, 2017.

N. M. E. Kalmoni, I. J. Rae, C. E. J. Watt, K. R. Murphy, C. Forsyth, and C. J. Owen. Statistical characterization of the growth and spatial scales of the substorm onset arc. *Journal of Geophysical Research (Space Physics)*, 120(10):8503–8516, October 2015. doi: 10.1002/2015JA021470.

N. M. E. Kalmoni, I. J. Rae, K. R. Murphy, C. Forsyth, C. E. J. Watt, and C. J. Owen. Statistical azimuthal structuring of the substorm onset arc: Implications for the onset mechanism. *Geophysics Research Letters*, 44(5):2078–2087, March 2017. doi: 10.1002/2016GL071826.

R. M. Katus, D. L. Gallagher, M. W. Liemohn, A. M. Keesee, and L. K. Sarno-Smith. Statistical storm time examination of MLT-dependent plasmapause location derived from IMAGE EUV. *Journal of Geophysical Research (Space Physics)*, 120(7):5545–5559, July 2015. doi: 10.1002/2015JA021225.

K. Kauristie, J. Weygand, T. I. Pulkkinen, J. S. Murphree, and P. T. Newell. Size of the auroral oval: UV ovals and precipitation boundaries compared. *Journal of Geophysics Research*, 104(A2):2321–2332, February 1999. doi: 10.1029/1998JA900046.

S. R. Kidd and G. Rostoker. Distribution of auroral surges in the evening sector. *Journal of Geophysical Research*, 96(A4):5697–5706, April 1991. doi: 10.1029/90JA02627.

J. Kissinger, R. L. McPherron, T. S. Hsu, and V. Angelopoulos. Steady magnetospheric convection and stream interfaces: Relationship over a solar cycle. *Jour-*

nal of Geophysical Research (Space Physics), 116:A00I19, January 2011. doi: 10.1029/2010JA015763.

M. G. Kivelson and C. T. Russell. *Introduction to space physics*. Cambridge University Press, Cambridge, 1995. ISBN 0521451043.

E. A. Kronberg, M. Ashour-Abdalla, I. Dandouras, D. C. Delcourt, E. E. Grigorenko, L. M. Kistler, I. V. Kuzichev, J. Liao, R. Maggiolo, H. V. Malova, K. G. Orlova, V. Peroomian, D. R. Shklyar, Y. Y. Shprits, D. T. Welling, and L. M. Zelenyi. Circulation of Heavy Ions and Their Dynamical Effects in the Magnetosphere: Recent Observations and Models. *Space Science Reviews*, 184(1-4): 173–235, November 2014. doi: 10.1007/s11214-014-0104-0.

A. Kullen and T. Karlsson. On the relation between solar wind, pseudobreakups, and substorms. *Journal of Geophysical Research (Space Physics)*, 109(A12): A12218, December 2004. doi: 10.1029/2004JA010488.

A. Kullen, S. Ohtani, and T. Karlsson. Geomagnetic signatures of auroral substorms preceded by pseudobreakups. *Journal of Geophysical Research (Space Physics)*, 114(A4):A04201, April 2009. doi: 10.1029/2008JA013712.

C. Lane, A. Acebal, and Y. Zheng. Assessing predictive ability of three auroral precipitation models using DMSP energy flux. *Space Weather*, 13(1):61–71, January 2015. doi: 10.1002/2014SW001085.

B. A. Larsen, D. M. Klumpar, and C. Gurgiolo. Correlation between plasmapause position and solar wind parameters. *Journal of Atmospheric and Solar-Terrestrial Physics*, 69(3):334–340, March 2007. doi: 10.1016/j.jastp.2006.06.017.

D. S. Lauben, U. S. Inan, T. F. Bell, and D. A. Gurnett. Source characteristics of ELF/VLF chorus. *Journal of Geophysical Research (Space Physics)*, 107(A12): 1429, December 2002. doi: 10.1029/2000JA003019.

G. Le, C. Russell, and K. Takahashi. Morphology of the ring current derived

from magnetic field observations. *Annales Geophysicae*, 22(4):1267–1295, April 2004. doi: 10.5194/angeo-22-1267-2004.

J. F. Lemaire and K. I. Gringauz. *The Earth's Plasmasphere*. Cambridge University Press, 1998.

G. R. Linscott and M. W. J. Scourfield. Observations of the plasmapause and diffuse aurora. *Planetary and Space Science*, 24(3):299–300, March 1976. doi: 10.1016/0032-0633(76)90027-1.

N. Longden, G. Chisham, M. P. Freeman, G. A. Abel, and T. Sotirelis. Estimating the location of the open-closed magnetic field line boundary from auroral images. *Annales Geophysicae*, 28(9):1659–1678, September 2010. doi: 10.5194/angeo-28-1659-2010.

R. E. Lopez. The Current Sheet Disruption Model for Substorm Expansion Phase Onset: Background, Arguments, and Relationship to Global Substorm Evolution. *Advances in Space Research*, 25(7-8):1667–1677, January 2000. doi: 10.1016/S0273-1177(99)00682-1.

A. T. Y. Lui, C. I. Meng, and S. Ismail. Large amplitude undulations on the equatorward boundary of the diffuse aurora. *Journal of Geophysical Research*, 87(A4):2385–2400, April 1982. doi: 10.1029/JA087iA04p02385.

E. A. MacDonald, N. A. Case, J. H. Clayton, M. K. Hall, M. Heavner, N. Lalone, K. G. Patel, and A. Tapia. Aurorasaurus: A citizen science platform for viewing and reporting the aurora. *Space Weather*, 13(9):548–559, September 2015. doi: 10.1002/2015SW001214.

J. L. Machol, J. C. Green, R. J. Redmon, R. A. Viereck, and P. T. Newell. Evaluation of OVATION Prime as a forecast model for visible aurorae. *Space Weather*, 10, 2012. doi: 10.1029/2011SW000746.

G. T. Marklund, T. Karlsson, L. G. Blomberg, P. A. Lindqvist, C. G. Fälthammar, M. L. Johnson, J. S. Murphree, L. Andersson, L. Eliasson, H. J. Opgenoorth, and

L. J. Zanetti. Observations of the electric field fine structure associated with the westward traveling surge and large-scale auroral spirals. *Journal of Geophysical Research*, 103(A3):4125–4144, March 1998. doi: 10.1029/97JA00558.

G. T. Marklund, S. Sadeghi, T. Karlsson, P-A. Lindqvist, H. Nilsson, C. Forsyth, A. Fazakerley, E. A. Lucek, and J. Pickett. Altitude Distribution of the Auroral Acceleration Potential Determined from Cluster Satellite Data at Different Heights. *Physical Review Letters*, 106(5):055002, February 2011. doi: 10.1103/PhysRevLett.106.055002.

M. S. Marsh and M. K. Mooney. OVATION-PRIME-2013 Met Office Nowcast Verification Dataset, March 2021. URL `https://doi.org/10.5281/zenodo.4653288`.

I. Mason. A Model for Assessment of Weather Forecasts. *Australian Meteorological Magazine*, 30:291–303, 1982.

J. Matzka, O. Bronkalla, K. Tornow, K. Elger, and C. Stolle. Geomagnetic kp index. v. 1.0., 2021a. URL `https://doi.org/10.5880/Kp.0001`.

J. Matzka, C. Stolle, Y. Yamazaki, O. Bronkalla, and A. Morschhauser. The Geomagnetic Kp Index and Derived Indices of Geomagnetic Activity. *Space Weather*, 19(5):e02641, May 2021b. doi: 10.1029/2020SW002641.

R. M. McGranaghan, J. Ziegler, T. Bloch, S. Hatch, E. Camporeale, K. Lynch, M. Owens, J. Gjerloev, B. Zhang, and S. Skone. Toward a Next Generation Particle Precipitation Model: Mesoscale Prediction Through Machine Learning (a Case Study and Framework for Progress). *Space Weather*, 19(6):e02684, June 2021. doi: 10.1029/2020SW002684.

R. L. McPherron. Growth phase of magnetospheric substorms. *Journal of Geophysics Research*, 75:5592, 1970. doi: 10.1029/JA075i028p05592.

R. L. McPherron, C. T. Russell, and M. P. Aubry. Satellite studies of magnetospheric substorms on August 15, 1968: 9. Phenomenological model for sub-

storms. *Journal of Geophysics Research*, 78(16):3131, January 1973. doi: 10.1029/JA078i016p03131.

R. R. Meier and C. S. Weller. EUV resonance radiation from helium atoms and ions in the geocorona. *Journal of Geophysical Research*, 77(7):1190, January 1972. doi: 10.1029/JA077i007p01190.

S. B. Mende, H. Heetderks, H. U. Frey, M. Lampton, S. P. Geller, R. Abiad, O. H. W. Siegmund, A. S. Tremsin, J. Spann, H. Dougani, S. A. Fuselier, A. L. Magoncelli, M. B. Bumala, S. Murphree, and T. Trondsen. Far ultraviolet imaging from the IMAGE spacecraft. 2. Wideband FUV imaging. *Space Science Reviews*, 91:271–285, January 2000a. doi: 10.1023/A:1005227915363.

S. B. Mende, H. Heetderks, H. U. Frey, M. Lampton, S. P. Geller, S. Habraken, E. Renotte, C. Jamar, P. Rochus, J. Spann, S. A. Fuselier, J. C. Gerard, R. Gladstone, S. Murphree, and L. Cogger. Far ultraviolet imaging from the IMAGE spacecraft. 1. System design. *Space Science Reviews*, 91:243–270, January 2000b. doi: 10.1023/A:1005271728567.

S. B. Mende, H. Heetderks, H. U. Frey, J. M. Stock, M. Lampton, S. P. Geller, R. Abiad, O. H. W. Siegmund, S. Habraken, E. Renotte, C. Jamar, P. Rochus, J. C. Gerard, R. Sigler, and H. Lauche. Far ultraviolet imaging from the IMAGE spacecraft. 3. Spectral imaging of Lyman-α and OI 135.6 nm. *Space Science Reviews*, 91:287–318, January 2000c. doi: 10.1023/A:1005292301251.

S. B. Mende, H. U. Frey, B. J. Morsony, and T. J. Immel. Statistical behavior of proton and electron auroras during substorms. *Journal of Geophysics Research (Space Physics)*, 108(A9):1339, September 2003. doi: 10.1029/2002JA009751.

N. Meyer-Vernet. *Basics of the solar wind*. Cambridge atmospheric and space science series. Cambridge University Press, Cambridge, 2007. ISBN 0521814200.

S. E. Milan, M. Lester, S. W. H. Cowley, K. Oksavik, M. Brittnacher, R. A. Greenwald, G. Sofko, and J. P. Villain. Variations in the polar cap area during two

substorm cycles. *Annales Geophysicae*, 21(5):1121–1140, May 2003. doi: 10.5194/angeo-21-1121-2003.

S. E. Milan, S. W. H. Cowley, M. Lester, D. M. Wright, J. A. Slavin, M. Fillingim, C. W. Carlson, and H. J. Singer. Response of the magnetotail to changes in the open flux content of the magnetosphere. *Journal of Geophysical Research (Space Physics)*, 109(A4):A04220, April 2004. doi: 10.1029/2003JA010350.

S. E. Milan, G. Provan, and B. Hubert. Magnetic flux transport in the Dungey cycle: A survey of dayside and nightside reconnection rates. *Journal of Geophysical Research (Space Physics)*, 112(A1):A01209, January 2007. doi: 10.1029/2006JA011642.

S. E. Milan, P. D. Boakes, and B. Hubert. Response of the expanding/contracting polar cap to weak and strong solar wind driving: Implications for substorm onset. *Journal of Geophysical Research (Space Physics)*, 113(A9):A09215, September 2008. doi: 10.1029/2008JA013340.

S. E. Milan, A. Grocott, C. Forsyth, S. M. Imber, P. D. Boakes, and B. Hubert. A superposed epoch analysis of auroral evolution during substorm growth, onset and recovery: open magnetic flux control of substorm intensity. *Annales Geophysicae*, 27(2):659–668, February 2009a. doi: 10.5194/angeo-27-659-2009.

S. E. Milan, J. Hutchinson, P. D. Boakes, and B. Hubert. Influences on the radius of the auroral oval. *Annales Geophysicae*, 27(7):2913–2924, July 2009b. doi: 10.5194/angeo-27-2913-2009.

S. E. Milan, A. Grocott, and B. Hubert. A superposed epoch analysis of auroral evolution during substorms: Local time of onset region. *Journal of Geophysical Research (Space Physics)*, 115(A9):A00I04, October 2010. doi: 10.1029/2010JA015663.

S. E. Milan, J. A. Carter, H. Sangha, G. E. Bower, and B. J. Anderson. Magnetospheric Flux Throughput in the Dungey Cycle: Identification of Convection State

During 2010. *Journal of Geophysical Research (Space Physics)*, 126(2):e28437, February 2021. doi: 10.1029/2020JA028437.

E. J. Mitchell, P. T. Newell, J. W. Gjerloev, and K. Liou. OVATION-SM: A model of auroral precipitation based on SuperMAG generalized auroral electrojet and substorm onset times. *Journal of Geophysical Research (Space Physics)*, 118(6): 3747–3759, June 2013. doi: 10.1002/jgra.50343.

M. B. Moldwin, L. Downward, H. K. Rassoul, R. Amin, and R. R. Anderson. A new model of the location of the plasmapause: CRRES results. *Journal of Geophysical Research (Space Physics)*, 107(A11):1339, November 2002. doi: 10.1029/2001JA009211.

M. B. Moldwin, B. R. Sandel, M. F. Thomsen, and R. C. Elphic. Quantifying Global Plasmaspheric Images With in situ Observations. *Space Science Reviews*, 109(1): 47–61, October 2003. doi: 10.1023/B:SPAC.0000007512.69979.8f.

R. K. Moore. A VHF Propagation Phenomenon Associated with Aurora. *Journal of Geophysics Research*, March 1951.

J. P. Morelli, R. J. Bunting, S. W. H. Cowley, C. J. Farrugia, M. P. Freeman, E. Friis-Christensen, G. O. L. Jones, M. Lester, R. V. Lewis, H. Lühr, D. Orr, M. Pinnock, G. D. Reeves, P. J. S. Williams, and T. K. Yeoman. Radar observations of auroral zone flows during a multiple-onset substorm. *Annales Geophysicae*, 13(11): 1144–1163, November 1995. doi: 10.1007/s00585-995-1144-2.

T. Motoba, K. Takahashi, A. Ukhorskiy, M. Gkioulidou, D. G. Mitchell, L. J. Lanzerotti, G. I. Korotova, E. F. Donovan, J. R. Wygant, C. A. Kletzing, W. S. Kurth, and J. B. Blake. Link between premidnight second harmonic poloidal waves and auroral undulations: Conjugate observations with a Van Allen Probe spacecraft and a THEMIS all-sky imager. *Journal of Geophysical Research (Space Physics)*, 120(3):1814–1831, March 2015. doi: 10.1002/2014JA020863.

A. H. Murphy. A New Vector Partition of the Probability Score. *Journal of Ap-*

plied Meteorology, 12(4):595–600, June 1973. doi: 10.1175/1520-0450(1973)012⟨0595:ANVPOT⟩2.0.CO;2.

K. R. Murphy, I. J. Rae, I. R. Mann, A. P. Walsh, D. K. Milling, C. E. J. Watt, L. Ozeke, H. U. Frey, V. Angelopoulos, and C. T. Russell. Reply to comment by K. Liou and Y.-L. Zhang on "Wavelet-based ULF wave diagnosis of substorm expansion phase onset". *Journal of Geophysical Research (Space Physics)*, 114 (A10):A10207, October 2009. doi: 10.1029/2009JA014351.

K. R. Murphy, I. R. Mann, I. J. Rae, A. P. Walsh, and H. U. Frey. Inner magnetospheric onset preceding reconnection and tail dynamics during substorms: Can substorms initiate in two different regions? *Journal of Geophysical Research (Space Physics)*, 119(12):9684–9701, December 2014. doi: 10.1002/2014JA019795.

S. A. Murray, S. Bingham, M. Sharpe, and D. R. Jackson. Flare forecasting at the Met Office Space Weather Operations Centre. *Space Weather*, 15(4):577–588, April 2017. doi: 10.1002/2016SW001579.

R. Nakamura and T. Oguti. Drifts of auroral structures and magnetospheric electric fields. *Journal of Geophysical Research*, 92(A10):11241–11247, October 1987. doi: 10.1029/JA092iA10p11241.

R. Nakamura, W. Baumjohann, Y. Asano, A. Runov, A. Balogh, C. J. Owen, A. N. Fazakerley, M. Fujimoto, B. Klecker, and H. RèMe. Dynamics of thin current sheets associated with magnetotail reconnection. *Journal of Geophysical Research (Space Physics)*, 111(A11):A11206, November 2006. doi: 10.1029/2006JA011706.

P. T. Newell and C-I. Meng. Mapping the dayside ionosphere to the magnetosphere according to particle precipitation characteristics. *Geophysical Research Letters*, 19(6):609–612, March 1992. doi: 10.1029/92GL00404.

P. T. Newell, W. J. Burke, E. R. Sanchez, and M. E. Greenspan. Identification

and observations of the plasma mantle at low altitude. *Journal of Geophysical Research*, 96(A1):35–45, January 1991a. doi: 10.1029/90JA01760.

P. T. Newell, W. J. Burke, E. R. Sánchez, M. E. Greenspan, and C. R. Clauer. The low-latitude boundary layer and the boundary plasma sheet at low altitude: Prenoon precipitation regions and convection reversal boundaries. *Journal of Geophysical Research*, 96(A12):21013–21023, December 1991b. doi: 10.1029/91JA01818.

P. T. Newell, C-I. Meng, and K. M. Lyons. Suppression of discrete aurorae by sunlight. *Nature*, 381(6585):766–767, June 1996. doi: 10.1038/381766a0.

P. T. Newell, T. Sotirelis, J. M. Ruohoniemi, J. F. Carbary, K. Liou, J. P. Skura, C. I. Meng, C. Deehr, D. Wilkinson, and F. J. Rich. OVATION: Oval variation, assessment, tracking, intensity, and online nowcasting. *Annales Geophysicae*, 20 (7):1039–1047, July 2002. doi: 10.5194/angeo-20-1039-2002.

P. T. Newell, T. Sotirelis, K. Liou, C. I. Meng, and F. J. Rich. A nearly universal solar wind-magnetosphere coupling function inferred from 10 magnetospheric state variables. *Journal of Geophysics Research (Space Physics)*, 112(A1):A01206, January 2007. doi: 10.1029/2006JA012015.

P. T. Newell, T. Sotirelis, and S. Wing. Diffuse, monoenergetic, and broadband aurora: The global precipitation budget. *Journal of Geophysics Research (Space Physics)*, 114(A9):A09207, September 2009. doi: 10.1029/2009JA014326.

P. T. Newell, T. Sotirelis, K. Liou, A. R. Lee, S. Wing, J. Green, and R. Redmon. Predictive ability of four auroral precipitation models as evaluated using Polar UVI global images. *Space Weather*, 8(12):S12004, December 2010a. doi: 10.1029/2010SW000604.

P. T. Newell, T. Sotirelis, and S. Wing. Seasonal variations in diffuse, monoenergetic, and broadband aurora. *Journal of Geophysics Research (Space Physics)*, 115(A3):A03216, March 2010b. doi: 10.1029/2009JA014805.

P. T. Newell, K. Liou, Y. Zhang, T. Sotirelis, L. J. Paxton, and E. J. Mitchell. OVATION Prime-2013: Extension of auroral precipitation model to higher disturbance levels. *Space Weather*, 12(6):368–379, Jun 2014. doi: 10.1002/2014SW001056.

A. Nishida. Formation of plasmapause, or magnetospheric plasma knee, by the combined action of magnetospheric convection and plasma escape from the tail. *Journal of Geophysical Research*, 71(23):5669–5679, December 1966. doi: 10.1029/JZ071i023p05669.

YY. Niu, XX. Zhang, F. He, and Y. Jiang. Statistical characteristics of the equatorial boundary of the nightside auroral particle precipitation. *Science China Earth Sciences*, 58(9):1602–1608, September 2015. doi: 10.1007/s11430-015-5090-x.

T. P. O'Brien and M. B. Moldwin. Empirical plasmapause models from magnetic indices. *Geophysical Research Letters*, 30(4):1152, February 2003. doi: 10.1029/2002GL016007.

H. J. Opgenoorth, M. A. L. Persson, T. I. Pulkkinen, and R. J. Pellinen. Recovery phase of magnetospheric substorms and its association with morning-sector aurora. *Journal of Geophysical Research*, 99(A3):4115–4130, March 1994. doi: 10.1029/93JA01502.

L. Orr, S. C. Chapman, and J. W. Gjerloev. Directed Network of Substorms Using SuperMAG Ground-Based Magnetometer Data. *Geophysics Research Letters*, 46(12):6268–6278, June 2019. doi: 10.1029/2019GL082824.

M. Ozaki, S. Yagitani, K. Ishizaka, K. Shiokawa, Y. Miyoshi, A. Kadokura, H. Yamagishi, R. Kataoka, A. Ieda, Y. Ebihara, N. Sato, and I. Nagano. Observed correlation between pulsating aurora and chorus waves at Syowa Station in Antarctica: A case study. *Journal of Geophysical Research (Space Physics)*, 117(A8):A08211, August 2012. doi: 10.1029/2011JA017478.

M. Ozaki, S. Yagitani, K. Sawai, K. Shiokawa, Y. Miyoshi, R. Kataoka, A. Ieda, Y. Ebihara, M. Connors, I. Schofield, Y. Katoh, Y. Otsuka, N. Sunagawa, and

V. K. Jordanova. A direct link between chorus emissions and pulsating aurora on timescales from milliseconds to minutes: A case study at subauroral latitudes. *Journal of Geophysical Research (Space Physics)*, 120(11):9617–9631, November 2015. doi: 10.1002/2015JA021381.

E. N. Parker. Dynamics of the Interplanetary Gas and Magnetic Fields. *Astrophysical Journal*, 128:664, November 1958. doi: 10.1086/146579.

G. Paschmann. Recent in-situ observations of magnetic reconnection in near-Earth space. *Geophysical Research Letters*, 35(19):L19109, October 2008. doi: 10.1029/2008GL035297.

C. S. Peirce. The numerical measure of the success of predictions. *Science*, 4:453 – 454, 1884.

V. Pierrard and J. Cabrera. Comparisons between EUV/IMAGE observations and numerical simulations of the plasmapause formation. *Annales Geophysicae*, 23 (7):2635–2646, October 2005. doi: 10.5194/angeo-23-2635-2005.

G. Provan, M. Lester, S. Mende, and S. Milan. Statistical study of high-latitude plasma flow during magnetospheric substorms. *Annales Geophysicae*, 22(10): 3607–3624, October 2004. doi: 10.5194/angeo-22-3607-2004.

I. J. Rae, K. Kabin, R. Rankin, F. R. Fenrich, W. Liu, J. A. Wanliss, A. J. Ridley, T. I. Gombosi, and D. L. de Zeeuw. Comparison of photometer and global MHD determination of the open-closed field line boundary. *Journal of Geophysical Research (Space Physics)*, 109(A1):A01204, January 2004. doi: 10.1029/2003JA009968.

I. J. Rae, C. E. J. Watt, I. R. Mann, K. R. Murphy, J. C. Samson, K. Kabin, and V. Angelopoulos. Optical characterization of the growth and spatial structure of a substorm onset arc. *Journal of Geophysical Research (Space Physics)*, 115 (A10):A10222, October 2010. doi: 10.1029/2010JA015376.

R. J. Redmon, D. B. Seaton, R. Steenburgh, J. He, and J. V. Rodriguez. September 2017's Geoeffective Space Weather and Impacts to Caribbean Radio Communications During Hurricane Response. *Space Weather*, 16(9):1190–1201, September 2018. doi: 10.1029/2018SW001897.

C. T. Russell. The Configuration of the Magnetosphere. In E. R. Dyer, editor, *Critical Problems of Magnetospheric Physics*, January 1972.

B. R. Sandel, A. L. Broadfoot, C. C. Curtis, R. A. King, T. C. Stone, R. H. Hill, J. Chen, O. H. W. Siegmund, R. Raffanti, DAVID D. Allred, R. STEVEN Turley, and D. L. Gallagher. The Extreme Ultraviolet Imager Investigation for the IMAGE Mission. *Space Science Reviews*, 91:197–242, January 2000. doi: 10.1023/A:1005263510820.

B. R. Sandel, J. Goldstein, D. L. Gallagher, and M. Spasojevic. Extreme Ultraviolet Imager Observations of the Structure and Dynamics of the Plasmasphere. *Space Science Reviews*, 109(1):25–46, October 2003. doi: 10.1023/B:SPAC.0000007511.47727.5b.

J. K. Sandhu, I. J. Rae, M. P. Freeman, C. Forsyth, M. Gkioulidou, G. D. Reeves, H. E. Spence, C. M. Jackman, and M. M. Lam. Energization of the Ring Current by Substorms. *Journal of Geophysical Research (Space Physics)*, 123(10):8131–8148, October 2018. doi: 10.1029/2018JA025766.

J. K. Sandhu, I. J. Rae, and M. T. Walach. Challenging the Use of Ring Current Indices During Geomagnetic Storms. *Journal of Geophysical Research (Space Physics)*, 126(2):e28423, February 2021. doi: 10.1029/2020JA028423.

M. A. Schield and L. A. Frank. Electron observations between the inner edge of the plasma sheet and the plasmasphere. *Journal of Geophysical Research*, 75(28):5401, January 1970. doi: 10.1029/JA075i028p05401.

C. J. Schrijver, K. Kauristie, A. D. Aylward, C. M. Denardini, S. E. Gibson, A. Glover, N. Gopalswamy, M. Grande, M. Hapgood, D. Heynderickx,

N. Jakowski, V. V. Kalegaev, G. Lapenta, J. A. Linker, S. Liu, C. H. Mandrini, I. R. Mann, T. Nagatsuma, D. Nandy, T. Obara, P.T. O'Brien, T. Onsager, H. J. Opgenoorth, M. Terkildsen, C. E. Valladares, and N. Vilmer. Understanding space weather to shield society: A global road map for 2015-2025 commissioned by COSPAR and ILWS. *Advances in Space Research*, 55(12):2745–2807, June 2015. doi: 10.1016/j.asr.2015.03.023.

V. A. Sergeev, E. M. Sazhina, N. A. Tsyganenko, J. A. Lundblad, and F. Soraas. Pitch-angle scattering of energetic protons in the magnetotail current sheet as the dominant source of their isotropic precipitation into the nightside ionosphere. *Planetary and Space Science*, 31(10):1147–1155, October 1983. doi: 10.1016/0032-0633(83)90103-4.

M. A. Sharpe and S. A. Murray. Verification of Space Weather Forecasts Issued by the Met Office Space Weather Operations Centre. *Space Weather*, 15(10):1383–1395, October 2017. doi: 10.1002/2017SW001683.

G. L. Siscoe and T. S. Huang. Polar cap inflation and deflation. *Journal of Geophsical Research*, 90(A1):543–547, January 1985. doi: 10.1029/JA090iA01p00543.

A. W. Smith, M. P. Freeman, I. J. Rae, and C. Forsyth. The Influence of Sudden Commencements on the Rate of Change of the Surface Horizontal Magnetic Field in the United Kingdom. *Space Weather*, 17(11):1605–1617, November 2019. doi: 10.1029/2019SW002281.

A. W. Smith, I. J. Rae, C. Forsyth, D. M. Oliveira, M. P. Freeman, and D. R. Jackson. Probabilistic forecasts of storm sudden commencements from interplanetary shocks using machine learning. *Space Weather*, 2020. doi: 10.1029/2020sw002603.

P. Song and C. T. Russell. Model of the Formation of the Low-latitude Boundary Layer for Strongly Northward Interplanetary Magnetic Field. *Journal of Geophysical Research*, 97(A2):1411–1420, February 1992. doi: 10.1029/91JA02377.

T. Sotirelis and P. T. Newell. Boundary-oriented electron precipitation model. *Journal of Geophysical Research*, 105(A8):18,655–18,673, August 2000. doi: 10.1029/1999JA000269.

T. Sotirelis, H. Korth, S-Y. Hsieh, Y. Zhang, D. Morrison, and L. Paxton. Empirical relationship between electron precipitation and far-ultraviolet auroral emissions from DMSP observations. *Journal of Geophysical Research (Space Physics)*, 118 (3):1203–1209, March 2013. doi: 10.1002/jgra.50157.

M. Spasojević, J. Goldstein, D. L. Carpenter, U. S. Inan, B. R. Sandel, M. B. Moldwin, and B. W. Reinisch. Global response of the plasmasphere to a geomagnetic disturbance. *Journal of Geophysical Research (Space Physics)*, 108(A9):1340, September 2003. doi: 10.1029/2003JA009987.

J. A. Swets, W. P. Tanner, and Birdsall T. G. The evidence for a decision-making theory of visual detection. Technical report, Engineering Research Institute, University of Michigan, 1955.

John A. Swets. Measuring the Accuracy of Diagnostic Systems. *Science*, 240 (4857):1285–1293, June 1988. doi: 10.1126/science.3287615.

E. Tanskanen, T. I. Pulkkinen, H. E. J. Koskinen, and J. A. Slavin. Substorm energy budget during low and high solar activity: 1997 and 1999 compared. *Journal of Geophysical Research (Space Physics)*, 107(A6):1086, June 2002. doi: 10.1029/2001JA900153.

E. I. Tanskanen. A comprehensive high-throughput analysis of substorms observed by IMAGE magnetometer network: Years 1993-2003 examined. *Journal of Geophysical Research (Space Physics)*, 114(A5):A05204, May 2009. doi: 10.1029/2008JA013682.

E. G. Thomas and S. G. Shepherd. Statistical Patterns of Ionospheric Convection Derived From Mid-latitude, High-Latitude, and Polar SuperDARN HF Radar Observations. *Journal of Geophysical Research (Space Physics)*, 123(4):3196–3216, April 2018. doi: 10.1002/2018JA025280.

M. F. Thomsen. Why Kp is such a good measure of magnetospheric convection. *Space Weather*, 2(11):S11004, November 2004. doi: 10.1029/2004SW000089.

R. M. Thorne. Radiation belt dynamics: The importance of wave-particle interactions. *Geophysical Research Letters*, 37(22):L22107, November 2010. doi: 10.1029/2010GL044990.

R. M. Thorne, E. J. Smith, R. K. Burton, and R. E. Holzer. Plasmaspheric hiss. *Journal of Geophysical Research*, 78(10):1581–1596, April 1973. doi: 10.1029/JA078i010p01581.

G. Tóth, I. V. Sokolov, T. I. Gombosi, D. R. Chesney, C. R. Clauer, D. L. de Zeeuw, K. C. Hansen, K. J. Kane, W. B. Manchester, R. C. Oehmke, K. G. Powell, A. J. Ridley, I. I. Roussev, Q. F. Stout, O. Volberg, R. A. Wolf, S. Sazykin, A. Chan, B. Yu, and J. Kóta. Space Weather Modeling Framework: A new tool for the space science community. *Journal of Geophysical Research (Space Physics)*, 110(A12), December 2005. doi: 10.1029/2005JA011126.

K. Tsuruda, S. Machida, T. Oguti, S. Kokubun, K. Hayashi, T. Kitamura, O. Saka, and T. Watanabe. Correlations between the very low frequency chorus and pulsating aurora observed by low-light-level television at L $\approx$ 4.4. *Canadian Journal of Physics*, 59:1042, August 1981. doi: 10.1139/p81-137.

N. A. Tsyganenko. A magnetospheric magnetic field model with a warped tail current sheet. *Planetary and Space Science*, 37(1):5–20, January 1989. doi: 10.1016/0032-0633(89)90066-4.

N. A. Tsyganenko and D. P. Stern. Modeling the global magnetic field of the large-scale Birkeland current systems. *Journal of Geophysical Research*, 101(A12): 27187–27198, December 1996. doi: 10.1029/96JA02735.

A. Viljanen, A. Pulkkinen, R. Pirjola, K. Pajunpää, P. Posio, and A. Koistinen. Recordings of geomagnetically induced currents and a nowcasting service of the Finnish natural gas pipeline system. *Space Weather*, 4(10):S10004, October 2006. doi: 10.1029/2006SW000234.

M. T. Walach and S. E. Milan. Are steady magnetospheric convection events prolonged substorms? *Journal of Geophysical Research (Space Physics)*, 120(3): 1751–1758, March 2015. doi: 10.1002/2014JA020631.

M.-T. Walach, S. E. Milan, K. R. Murphy, J. A. Carter, B. A. Hubert, and A. Grocott. Comparative study of large-scale auroral signatures of substorms, steady magnetospheric convection events, and sawtooth events. *Journal of Geophysical Research (Space Physics)*, 122(6):6357–6373, June 2017. doi: 10.1002/2017JA023991.

A. P. Walsh, C. J. Owen, A. N. Fazakerley, C. Forsyth, and I. Dandouras. Average magnetotail electron and proton pitch angle distributions from Cluster PEACE and CIS observations. *Geophysical Research Letters*, 38(6):L06103, March 2011. doi: 10.1029/2011GL046770.

C. E. J. Watt and R. Rankin. Do magnetospheric shear Alfvén waves generate sufficient electron energy flux to power the aurora? *Journal of Geophysical Research (Space Physics)*, 115(A7):A07224, July 2010. doi: 10.1029/2009JA015185.

Daniel S. Wilks. *Statistical Methods in the Atmospheric Sciences*. Elsevier, 2 edition, 2006.

R. M. B. Young. Decomposition of the brier score for weighted forecast-verification pairs. *Quarterly Journal of the Royal Meteorological Society*, 136(650), July 2010. doi: 10.1002/qj.641.

Xiao-Xin Zhang, Fei He, Rui-Lin Lin, Mei-Ching Fok, Roxanne M. Katus, Michael W. Liemohn, Dennis L. Gallagher, and Shinya Nakano. A new solar wind-driven global dynamic plasmapause model: 1. Database and statistics. *Journal of Geophysical Research (Space Physics)*, 122(7):7153–7171, July 2017. doi: 10.1002/2017JA023912.